Winter 1-1-2012

Modulation of Cis-syn Cyclobutane Dimer Formation and Deamination at CpG sites by Nucleosome Particles and Its Implications for Deamination Bypass Mechanism for the Origin of C to T Mutations

Qian Song
Washington University in St. Louis

Recommended Citation

Song, Qian, "Modulation of Cis-syn Cyclobutane Dimer Formation and Deamination at CpG sites by Nucleosome Particles and Its Implications for Deamination Bypass Mechanism for the Origin of C to T Mutations" (2012). *All Theses and Dissertations (ETDs)*. 1020.
https://openscholarship.wustl.edu/etd/1020

WASHINGTON UNIVERSITY IN ST. LOUIS

Department of Chemistry

Dissertation Examination Committee:
John-Stephen Taylor, Chair
Peter M.J. Burgers
Sarah Elgin
Michael L. Gross
Liviu Mirica
Jay Ponder

Modulation of *Cis-syn* Cyclobutane Dimer Formation and Deamination at CpG Sites by Nucleosome Particles and Its Implications for Deamination Bypass Mechanism for the Origin of C to T Mutations

by

Qian Song

A dissertation presented to the
Graduate School of Arts and Sciences
of Washington University in
partial fulfillment of the
requirements for the degree
of Doctor of Philosophy

December 2012

Saint Louis, Missouri

Abstract

C-to-T mutations are a hallmark of UV light and, in humans, occur preferentially at methylated Py^{m}CG sites, which are also sites of preferential cyclobutane pyrimidine dimer (CPD) formation. CPDs containing C or 5-methylcytosine (^{m}C) are not stable and spontaneously deaminate to U or T at pH 7 and 37°C over a period of hours or days. Deamination of Cs or ^{m}Cs in CPDs is highly mutagenic because polymerase η will faithfully insert A opposite the resulting Us or Ts, thereby producing the observed C to T and CC to TT mutations (the deamination-bypass mechanism). In this thesis, we prepared a CPD of a T^{m}CG site, a known hotspot for C methylation, CPD formation, and UV light-induced C-to-T mutations found in the p53 gene of basal and squamous cell cancers. We show that both yeast and human pol η could synthesize past the 3'-^{m}C in T=^{m}C CPD in a >99% error-free manner by non-mutagenic insertion of G opposite the ^{m}C in the CPD. We also confirmed the error-free but mutagenic insertion of A opposite the resulting deaminated T.

Nucleosomes are the primary structural unit of chromatin in eukaryotic cells. UV preferentially induces the formation of CPDs in nucleosomes at sites where the phosphodiester backbone is positioned away from the histone surface and DNA bending is toward the major groove. Nucleosomes have also been found reduce the rate of nuclear excision repair to different extents depending on specific tissue and cell type. Although the frequency of CPD formation and repair is modestly modulated by its rotational positioning within a nucleosome, the effect of nucleosome rotational

positioning on the rate of deamination of ^{m}C in a CPD has not been previously studied. In this thesis, we investigated the deamination of CPDs in a chicken erythrocyte nucleosome core particle reconstituted with synthetic DNA. We found that the deamination of a $T^{m}C$ CPD whose sugar phosphate backbone is positioned against the histone core surface decreases by a factor of 4.7, whereas that of a $T^{m}C$ CPD positioned away from the surface increases by a factor of 8.9 when compared with unbound DNA. Considering that formation of the CPD positioned away from the surface is also enhanced by a factor of two, a $T^{m}CG$ site in this position might be expected to have up to an 84-fold higher probability of resulting in a UV-induced ^{m}C to T mutation than one positioned against the surface. We also determined the deamination rate for $T{=}^{m}C$ CPDs in all ten possible nucleosome rotational positions of a full periodic turn on the nucleosome core particle surface, at the same translational position. Three $T{=}^{m}CG$ CPDs positioned inside deaminated slower than the unbound DNA, whereas the seven positioned outside deaminated faster than the unbound sequence.

Many of researchers have relied on nucleosome core particles isolated directly from organisms for their *in vitro* studies. Although the isolation process is straightforward, it is generally time-consuming, and may contain modified histones. Recombinant histones offer the possibility to carefully study the structure activity relationships of nucleosome core particles containing DNA photoproducts, and in this thesis, we report the preparation and assembly of a nucleosome core particle from recombinant histones. A histone octamer was prepared from recombinant *Xenopus* histones expressed and purified from *E. coli*, based on minor modifications of previously described protocol. We also reconstituted the recombinant histone octamer with our synthetic 147-mer DNA duplex, and demonstrated that it assembled with a specific rotational and translational position.

Acknowledgements

First I would like to express my sincere gratitude for the help and support from my advisor, Dr. John-Stephen Taylor. I thank him for giving me the inspiration to explore the science I was interested in while at the same time always being there for help when I was in trouble. I do not believe I could walk out of the many frustrations during graduate school without him. He serves as a good model for me both as a scientist and as a family man. The lessons I learned from him extend far beyond what words can describe here.

My committee members, Dr. Robert Blankenship and Dr. Michael Gross, both gave helpful ideas that directed the course of my PhD research. I am thankful for their assistance in our yearly committee meetings, which made me a better scientist. I appreciate Dr. Jay Ponder, Dr. Liviu Mirica, Dr. Sarah Elgin and Dr. Peter Burgers for their willingness to bring their perspectives to my work by serving on my defense committee.

I thank all my wonderful group members, previous and current, for making the Taylor lab a pleasant place to work in. I am especially thankful to Dr. Vincent Cannistraro, who not only guided me into the biochemistry research area, helped me a lot on my experiment design, but also took care of me on my daily life.

I thank my parents and my beloved husband for their patience and unconditional support during this time. Their love gave me inspiration and was my driving force. This work would not be possible without them by my side. Finally, I would like to thank National Institute of Health for their financial support.

Table of Contents

Chapter 1

Introduction

Chapter 2

Preparation of Site-Specific T=^{m}CG *Cis-Syn* Cyclobutane Pyrimidine Dimer-Containing Template and Its Error-Free Bypass by Yeast and Human Polymerase Eta.

Chapter 3

Rotational Position of a 5-Methylcytosine-containing Cyclobutane Pyrimidine Dimer in a Nucleosome Greatly Affects Its Deamination Rate

Chapter 4

Modulation of T=^{m}C *Cis-Syn* CPD DNA Photoproduct Formation and Deamination Over a Full Helical Turn in a Reconstituted Nucleosome Core Particle

Chapter 5

Reconstitution of Nucleosome Core particle from Recombinant Histones and Synthetic DNA

Chapter 6

Conclusions and Future Directions

Appendix

Reconstitution of Nucleosome Core particle from Recombinant Histones and Synthetic DNA

List of Figures

Chapter 1

Introduction

Chapter 2

Preparation of Site-Specific T=^{m}CG *Cis-Syn* Cyclobutane Pyrimidine Dimer-Containing Template and Its Error-Free Bypass by Yeast and Human Polymerase Eta.

Chapter 3

Rotational Position of a 5-Methylcytosine-containing Cyclobutane Pyrimidine Dimer in a Nucleosome Greatly Affects Its Deamination Rate

Chapter 4

Modulation of T=^{m}C *Cis-Syn* CPD DNA Photoproduct Formation and Deamination Over a Full Helical Turn in a Reconstituted Nucleosome Core Particle

Chapter 5

Reconstitution of Nucleosome Core particle from Recombinant Histones and Synthetic DNA

Appendix

Reconstitution of Nucleosome Core particle from Recombinant Histones and Synthetic DNA

List of Tables

Chapter 2

Preparation of Site-Specific T=^{m}CG *Cis-Syn* Cyclobutane Pyrimidine Dimer-Containing Template and Its Error-Free Bypass by Yeast and Human Polymerase Eta.

Chapter 3

Rotational Position of a 5-Methylcytosine-containing Cyclobutane Pyrimidine Dimer in a Nucleosome Greatly Affects Its Deamination Rate

Chapter 4

Modulation of T=^{m}C *Cis-Syn* CPD DNA Photoproduct Formation and Deamination Over a Full Helical Turn in a Reconstituted Nucleosome Core Particle

Chapter 5

Reconstitution of Nucleosome Core particle from Recombinant Histones and Synthetic DNA

Appendix

Reconstitution of Nucleosome Core particle from Recombinant Histones and Synthetic DNA

Chapter 1

Introduction

1.1 General pathway leading to UV-induced skin cancer.

UV light is believed to be one of the major epidemiological factors for human skin cancer, especially non-melanoma skin cancer. Exposure of basal and squamous skin cells to UV irradiation can cause the formation of various types of DNA photoproducts in the genomic DNA. When these photoproducts form within crucial proto-oncogenes, such as the *ras* family genes, and tumor suppressor genes, such as the *p53* gene TP53, which are involved in cell cycle control, maintenance of gene integrity and cell proliferation and differentiation, there is the potential for inducing cancer (1-5). Of many types of DNA photoproducts, *cis-syn* cyclobutane pyrimidine dimers (CPD) and the pyrimidine (6-4) pyrimidone photoproducts [(6-4) photoproducts] of dipyrimidine sites are known to be most frequent DNA photo-lesions formed by UVB or UVC irradiation (6-9). CPDs are generated through the formation of a cyclobutane ring between the 5, 6-double bonds of the adjacent pyrimidine bases in the genome, which causes an approximately 7-9° deformation relative to the B-form DNA structure at the photo-lesion site. Compared with CPDs, (6-4) photoproducts have cause a much greater deformation of 44° which makes them more easily detected and repaired than CPDs (9). CPDs are formed at least 20-40 fold more frequently than (6-4) photoproducts (6), and given their slower rate of repair (9, 10), makes them a prime candidate for the mutagenic effects of light (11, 12).

Mutations at CpG sites. In mammalian cells, cytosine is often methylated during cell differentiation to give 5-methyl cytosine (^{m}C) which almost exclusively occurs at the CpG dinucleotide sites. MethylC sites are known mutational hotspots in cancer-related genes and are often mutated in genes associated with human genetic diseases. Sequencing of the tumor suppressor p53 gene in human skin cancers has revealed that about 35% of these mutations involve the tri-nucleotide sequence with 5-methyl cytosine, as 5'-Py^{m}CG, (Figure 1.1). Most of the mutations occurring at this methylated CpG sites are C→ T, ^{m}C→T or CC→TT mutations, which are generally considered as the molecular signature of UV light (1-4). Among the eight commonly observed hotspot mutations along p53 gene, five contain the methylated CpG sites, either with 5'-C^{m}CG or 5'-T^{m}CG (9, 13), as indicated by * in Figure 1.1. The enhanced mutation frequency at these sites has been attributed to the red shift in the absorption of UV light from λ_{max} = 267nm (cytosine) to λ_{max} = 273nm (5-methyl cytosine), as shown in Figure 1.2. This red shift results in an approximately 15-fold enhancement in the photoreactivity of ^{m}C compared with C to form the ^{m}C-containing CPDs at 5'-Py^{m}CG sites under UVB irradiation (280-320 nm) (9, 14-16).

Mechanisms for UV-induced C→T mutations. There are two principal mechanisms that have been proposed to explain how the UV induced C→T or ^{m}C→T transition mutations occur. One is called the "tautomer-bypass mechanism" in which the C or ^{m}C in a CPD adopts a tautomeric form that resembles T (18). Unlike T in native DNA or in a CPD, which is known to preferentially adopt the keto tautomeric state and base pair with A, a C or ^{m}C in a CPD could, in principal, adopt both amino and/or imino tautomeric forms with *E*- or *Z*-stereochemisty (the imino hydrogen is *trans* or *cis* with respect to N3), as shown in Figure 1.3. While the amino tautomer of

C or ^{m}C can base pair with G, the E-imino tautomer of C or ^{m}C has the same base pairing ability as T, which would direct the insertion of A during DNA replication thereby causing a C or ^{m}C to T mutation (17, 18). The possibility that C or ^{m}C could exist in an imino tautomeric form comes from early work demonstrating that dihydrocytosine adopts the amino tautomeric form in water but an imino tautomeric form in the much less polar solvent chloroform (19). Gas phase theoretical calculations have reproduced the preference for the imino tautomeric form in non-polar environments (20, 21) but failed to reproduce the preference for the amino form in water (21).

The other mechanism was proposed by our group, is the “deamination-bypass mechanism”. Unlike T=T CPDs which are chemically stable, the C-containing or (^{m}C)-containing CPDs are not, and deaminate to U or T respectively, within hours to days (22-27). The deamination process occurs under acidic conditions, with the C or ^{m}C first being protonated at the N3 position, followed by a water attack at C4, and the loss of ammonia resulting in the formation of U or T, as shown in Figure 1.4 for a T=^{m}C CPD. Spontaneous deamination of normal C or ^{m}C is very slow, with a half-life about 50,000 years (28, 29), while the formation of a CPD greatly accelerate this process, due to the disruption of the original aromatic system by the saturation of 5, 6-double bond.

DNA polymerase η. In response to UV irradiation, cells have adopted global genome and transcription-coupled nucleotide excision repair systems to specifically remove the UV-induced DNA lesion along the genome (30-32). It is believed however, that the CPDs are less efficiently repaired compared with (6-4) photoproducts, due to their moderate distortion on both the DNA structure and the duplex stability (34-37). For those unrepaired DNA photolesions, cells have evolved DNA damage bypass polymerases to carry out the trans-lesion synthesis (33). These DNA damage bypass polymerases generally belong to the Y family of DNA polymerases, of which polymerase η (Pol η) appears to be specifically adapted to synthesize past *cis-syn* CPDs (38-40). Pol η was first identified in yeast and was found to insert two A's opposite the the two T's of a T=T CPD (38). At about the same time it was shown that a defect pol η was responsible for the inability of XPV cells, which are proficient in the nucleotide excision repair, to replicate past UV-damaged DNA (41). The unique ability of Pol η to synthesize past CPDs comes from its unique structural features that were revealed in a crystal structure of the active site in Pol η complexed with a primer-template. Instead of only being able to accomodate one templating nucleotide in the active site as do replicative DNA polymerases, Pol η can accommodate both nucleotides of a CPD in its active site (42). As for a ^{m}C-containing CPD, we've been able to prove that yeast DNA Pol η can bypass a ^{m}C=T CPD in an error-free manner by inserting a G opposite the dimerized ^{m}C in the CPD (43).

In contrast to CPDs, bypass of (6-4) photoproducts by Pol η is very poor and can be error-prone. Pol η can not completely replicate past a (6-4) photoproduct and it will preferentially incorporate a G opposite the 3' pyrimidine of a (6-4) photoproduct followed by extension opposite the 5' pyrimidine by Pol ζ in an error-free manner

(44). So the overall consequence of bypassing (6-4) photoproduct would be error-free for a 3’ C or ^{m}C, whereas it would result in a T→ C mutation opposite a 3’ T.

Deamination of C-containing CPDs. Because we had found that DNA Pol η inserted A opposite the ^{m}C in ^{m}C=T CPD, it would appear that the ^{m}C has to deaminate to T to become mutagenic, as shown in Figure 1.5. We expected that this would also hold true for a T=^{m}CG dimer, and that the deaminated ^{m}C would similarly direct the insertion of A during the trans-lesion synthesis by Pol η in an error-free manner, leading the ^{m}C to T mutation at the CpG methylation site (43). Studies on ^{m}C deamination processes have been carried out both *in vitro* and *in vivo,* utilizing a various types of techniques, i.e., mass spectrometry, enzymatic assay, genetic analysis and ligation-mediated PCR (26, 45). Based on these results, the ^{m}C deamination rate was found to depend highly on the sequence context, pH, temperature, and the cell type, with a range of hours to weeks.

Previously, Dr. Cannistraro in our group developed a strategy to sensitively measure the ^{m}C deamination rate *in vitro* by use of an internally ^{32}P-radiolabled ^{m}C (46). According to this strategy, the ^{m}C was 5’-^{32}P radiolabeled, then ligated to another DNA fragment to fulfill the length and sequence context desired. After UVB irradiation, the ^{m}C-containing CPD was allowed to deaminate for specific times at a specific temperature and pH. Then the CPDs were photo-reverted to non-dimerized ^{m}C or T depending on the extent of deamination, by use of *E. coli* photolyase (47). Following that, the DNA was further degraded by Nuclease P1 to mononucleotides and the ^{32}P-dT and ^{32}P-^{m}dC were separated by two-step acrylamide gel electrophoresis. In the first step, ^{32}P-^{m}dC and ^{32}P-dT were separated from partially digested material and protein based on their size and charge by electrophoresis in an 10% acrylamide denaturing 7M urea, TBE gel. For the second step, the gel surrounding the radioactive band containing the mononucleotides was excised, and a second acrylamide gel containing 25 mM citric acid, pH 3.5, and 7M urea was poured around the remaining gel slice. Electrophoresis on this gel separated ^{32}P-^{m}dC from ^{32}P-dT with the ^{32}P-dT migrating the fastest. The deamination rate constant was obtained from the slope of a linear least squares fit of the log of the fraction of remaining T^{m}C CPD *versus* deamination time.

Factors affecting deamination of C-containing CPDs. When CPDs in a number of different sequence contexts were investigated, a number of factors were discovered to influence the ^{m}C deamination rate. Higher salt concentrations slowed down the deamination presumably by stabilizing the duplex and thereby inhibiting protonation of ^{m}C and addition of water. A 3'-^{m}C was found to deaminate faster than a 5'-^{m}C, and a G flanking the ^{m}C accelerated deamination in the duplex, by some process that appeared to involve the O6-carbonyl group of the G, since substitution of this O6-carbonyl group with other functional groups slowed down the deamination, as summarized in Figure 1.6 & 1.7 (46). Besides these factors, the methyl-C binding protein (MeCP2) was also found to enhance ^{m}C-containing CPD formation, while at the same time suppressing its deamination (48).

1.2 How does chromatin affect photochemistry of DNA in mammalian cells?

In eukaryotic cells, the DNA molecule is packaged into chromatin which can both protect the DNA from physical stresses or damage and package the genetic information within the nucleus of the cell (49-53). The packaging process is believed to involve several key steps: first of all, the genomic DNA will first form a “bead on a string” by assembling with histones, which results in a five to ten fold compaction of the DNA. In this process, the DNA wraps around histone octamers to form nucleosome core particles. The DNA between two consecutive nucleosome core particles is called the “linker DNA”, and varies in size between 20 to 60 bp, as shown in Figure 1.8. As demonstrated by high-resolution X-ray structural analysis, each nucleosome, which contains both the nucleosome core particle and the linker DNA, compacts around 200 bp of genomic DNA into almost two left-handed super-helical turns (51-55). The nucleosome has a cross-section diameter about 11 nm, and it is this 11 nm thick poly-nucleosome string that then condenses into a highly folded and compact structure called “30 nm chromatin fiber”. This fiber is believed to be stabilized by the binding of histone protein H1 to each nucleosome core particle and to the adjacent linker DNA and by divalent cations (56-59). The “30 nm chromatin fiber” results in a net compaction of about 50-fold. Various models have been proposed to explain the geometry of this fiber, and can be grouped into two classes. One model is the one-start solenoidal helix with linear coiled nucleosome arrays and bent linker DNA. The second is a two-start zig-zag helix with two stacks of helically arranged nucleosome arrays connected by straight linker DNA (60-64). This “30nm chromatin fiber” then further packs within the nucleus to form the chromosome structure, with the exact mechanism remaining unclear.

Nucleosome positioning. To better understand the role of chromatin structure in regulating various biological processes such as gene expression, DNA replication, transcription and repair, a lot of approaches have been developed to investigate the chromatin structure of specific cancer-related genes or even the whole genome by mapping of DNA-histone interactions, nucleosome occupancy and chromatin remodeling (65-68). With regards to UV carcinogenesis, Pfeifer and coworkers reported a high-resolution analysis of the chromatin structure along p53 gene in human fibroblast, using both DNaseI footprinting and Micrococcal nuclease (MNase) mapping (69). MNase preferentially cleaves chromatin in the linker DNA region, and was used to determine indicator the positions of nucleosomes along the p53 gene. They found that was there were two preferentially positioned nucleosomes between exon 5 and 6 along the p53 gene, one from the C-terminal of exon 5 to part of exon 5, and the other covering exon 6 and part of intron 6. They did not, however observe a clear nucleosome occupancy for exon 7 and 8. They tried to correlate the nucleosome positioning of the mutational hotspots located in exon 5 and 6 with the relative repair efficiency of photoproducts at these sites but failed, suggesting that different cellular machinery may have different bias towards specific chromatin structures.

Nucleosome structure. As the basic structural repeating unit, nucleosome core particle consists of a histone octamer and nucleosomal DNA with an average size of 147 bp, as shown in Figure 1.9, the nucleosome has a diameter about 7 nm and bears a 2-fold symmetry, based on the high-resolution X-ray structural analysis (51, 52). The histone core octamer is made up with two copies of each of the four histone proteins: H2A, H2B, H3 and H4, as shown in different colors in Figure 1.9, the octamer has a molecular weight about 108 kDa. Each histone protein has a central histone-fold motif and flanking tail or extensions, the structural motif consist of three α helices connected by two loops, generally dictated as α1-L1-α2-L2-α3. During the assembly of histone octamer, it is well believed that two H3-H4 dimers first form a tetramer though a 4-helix bundle between two H3 proteins. Then two H2A-H2B dimers will join and bind to the H3-H4 tetramer to form the histone octamer structure, through another 4-helix bundle between H2 and H4 proteins (51, 52). The 147 bp nucleosomal DNA is forms about 1.7 left-handed superhelical turns around the histone octamer, with the minor groove of DNA facing toward the histone octamer surface 14 times in the nucleosome core particle. It is believed that there are five types of histone-DNA interactions between the phosphodiester backbone of the DNA chain facing the histone octamer surface: (1) Electrostatic interactions between the positive charge from the amino-termini of α1 and α2 helix of the four histones and the phosphate group from the DNA backbone; (2) Hydrogen-bonding between the DNA phosphate group and the amide backbone nitrogen atoms from the amino acids located in the position of α1 and α2 helix that are close to the histone surface; (3) Insertion of an arginine side chain from either the histone-fold domain or the histone tail into the DNA minor groove; (4) Non-polar contacts between the deoxyribose groups of the DNA and non-polar amino acid side chains from the histone-fold surface; (5) Salt-bridges between the oxygen atoms from the DNA phosphate backbone and basic or hydroxyl side chains of the histone proteins on the surface.

Histone posttranslational modifications. Histone posttranslational modifications, or commonly viewed as the “histone code”, play a key role in regulating gene expression, epigenetic patterns, the stability of chromatin structure, etc (70-73). Histone modifications are believed to be reversible, and are not only confined to histone tails but also happen to structured histone folds, and include methylation, acetylation, phosphorylation and ubiquitylation of the basic amino acids, lysine and arginine (74-76). The specific “histone code” is read out by histone chaperons or chromatin remodeling complexes, to regulate DNA accessibility. For example, the methylation of Lys 9 in histone H3 can recruit the heterochromatin protein HP1 and stabilize the higher-order chromatin structure (77-79). Acetylation of Lys 14 in histone H3 can direct the binding of the ATP-dependent nucleosome-remodeling complex, thereby stimulating the gene activation (80, 81). Different cell types bear different histone modification patterns, especially in cancer development and progression, and could have unique hallmarks that are correlating with the specific type of carcinogenesis (82-86).

Nucleosomal DNA positions. The two key parameters commonly used to specify a DNA position in a nucleosome core particle are its translational and rotational position. In general, the 147 bp nucleosomal DNA binds the histone octamer with a central base pair falling at the pseudo-dyad, with the translational positioning being defined as the position of relative to the central base pair. The position is generally denoted in superhelical units with reference to the superhelix location zero, or SHL 0 with each superhelical turn containing 10 to 11 bp of the nucleosomal DNA (52). The 14 superhelical repeats of the nucleosomal DNA are thus divided into two 73-bp halves, with the translational positioning number increasing from SHL+1 to SHL+7 starting from the first superhelix on the right of pseudo-dyad, and continue clockwise towards the right 73-bp half. The superhelical positions on the left half decrease from SHL-1 to SHL-7 starting from the first superhelix on the left of pseudo-dyad, continuing counter clockwise for the remainder of the left 73-bp half.

The rotational position usually describes the orientation of a DNA phosphodiester backbone relative to the histone octamer surface. Rotataional positions can be categorized as either being “IN” in which the phosphodiester backbone of the DNA faces inside or toward the histone octamer surface, or “OUT” in which the phosphodiester backbone faces outside or away from the histone octamer surface. Generally, in one superhelical turn of the nucleosomal DNA, roughly three out of ten nucleotides adopt the “IN” rotational positioning, while the other seven nucleotides bearing the “OUT” rotational positioning. The key feature of nucleosome rotational positioning is that it represents the relative accessibility of the nucleosomal DNA to various DNA cleavage reagents, also other enzymes or cellular machinery that recognizes specific DNA sequence or structure to carry out important biological processes, i.e., DNA replication, transcription or DNA repair. It is well believed that both translational and rotational positioning of nucleosomal DNA can be modulated or changed to facilitate to cellular response to both endogenous and exogenous biological signals (87-91).

Nucleosome preparation. There are two general approaches to preparing nucleosome core particles, one involving the isolation and purification of nucleosome core particles directly from specific organisms (92-95), and the other involving reconstitution of a synthetic DNA with a histone octamer assembled from recombinant histones (96-100). For example, Smerdon, and coworkers developed a protocol for the isolation and purification of nucleosome core particles from chicken blood cells. Because chicken blood cells serve a very special function, most genes are silenced and the histones are largely unmodified. The overall procedure involves isolation of nuclei from chicken erythrocytes, chromatin digestion by Micrococcal Nuclease to generate nucleosomes, depletion of linker histone H1, purification of nucleosome core particle through ion-exchange chromatography and gel-filtration chromatography. The advantages of this isolation and purification method is that it is relatively easy to perform, nucleosome core particles could be obtained from different tissues or cell types, and the purified nucleosome core particles are stable and could be stored at 4ºC for more than a year.

The disadvantages of the isolation method, is that the overall procedure is relative time-consuming and restricted to the availability of sufficient quantities of the tissue or organism of interest, the presence of a heterogenous mix of post-translational histone modifications, depending on the chosen type of cell or organism. Also a great excess of the nucleosome core particle with respect to the

DNA to be reconstituted (more than 100-fold) is required. Perhaps the biggest drawback of this method is that only naturally occurring histones can be studied, which limits the ability of researchers to investigate the structure-function activities of histone mutants or variants (97, 99).

Recombinant histone core particles. To better understand the role of individual histone in modulating both the structure and function of nucleosome core particle or even chromatin structure, researchers have switched to preparing nucleosome core particle from recombinant histones (96-100). In particular, Luger and coworkers reported a detailed procedure for expressing and purifying four recombinant histones from Xenopus Oocyte in *E. coli*, and assembling them together to form the histone octamer. After that a synthetic DNA was reconstituted onto the histone octamer to generate the nucleosome core particle (99). Their procedure is based on the evidence that histone assembly occurs by H3 and H4 forming a tetramer first, followed by binding with two H2A-H2B dimers. By using this approach, researchers it becomes possible to construct nucleosome core particles containing specific histone modifications, histone mutants or variants, to study the effects of these alterations.

Nucleosomal DNA. Researchers have discovered that the binding affinity and position of DNA for the histone octamer is highly sequence-dependent (101-103). Several nucleosome positioning DNA motif or repeats have been found to play a great role in determining the specific DNA binding affinity and orientation of the DNA on the nucleosome core particle, such as TATA and, CA repeats, TG motifs, etc

(104-106). For example, Wrang and co-workers successfully utilized the TG motif to incorporate the glucocorticoid response element into 165 bp nucleosomal DNA with specific translational and rotational positioning relative to the histone octamer (107). Davey and coworkers crystallized the nucleosome core particles with the “601 DNA sequence” to give high-resolution crystal structures, demonstrating that this particular DNA sequence exhibited a strong preference for nucleosome positioning (108). To date, it is well accepted that the TG motif, $(A/T)_3NN(G/C)_3NN$, is one of the best nucleosome positioning motifs. The ten nucleotides make up one full nucleosomal helical turn, with the major groove of the G·C base pairs preferentially facing the histone octamer surface, which is consistent with their tendency to bend into the major groove. In contrast the minor groove of the A·T base pairs in this motif have a strong preference for facing the histone octamer surface, which is consistent with their tendency to bend into the minor groove. The bent nature of the minor groove of the A·T base pairs is also favorable for the insertion of single arginine side chain (52).

Probing DNA rotational position. Both chemical and enzymatic approaches have been developed to probe the DNA-histone interactions in nucleosome core particles or chromatin, especially for mapping the nucleosome positioning of synthetic or genomic DNA. Among these different approaches, DNase I mapping and hydroxyl radical footprinting are the two most commonly used techniques to determine the nucleosome rotational positioning, while Exonuclease III is used to determine translational positioning (109-111). Both DNase I and hydroxyl radical show a preference for cutting nucleosomal DNA backbone that faces OUT, though hydroxyl radicals exhibit much less sequence specificity and thus can probe the DNA backbone at a single nucleotide level (112-114). The hydroxyl radical can be easily generated by the Fenton reaction: $[Fe(EDTA)]^{2-} + H_2O_2 \rightarrow [Fe(EDTA)]^{1-} + \cdot OH + OH^-$, and is believed to mainly attack the hydrogen at the C5'-position of the sugar ring of DNA, and 2–5-fold less at other sugar sites in the order C4' > C3' > C2'> C1'(115). The principle cleavage products that result are a nucleotide 5'-phosphate, a nucleotide 3'- phosphate and a nucleotide 3'- phosphoglycolate, as shown in Figure 1.10 (116). When nucleosomal DNA is exposed to hydroxyl radical, the outside facing positions are more accessible to attack compared with inside facing positions, resulting in a darker band on a DNA sequencing gel. Since the rotational position of the nucleotides is repeated every 10-11 bp, the hydroxyl radical cleavage patter of nucleosomal DNA is characterized by a pronounced 10-11 bp periodicity.

Probing DNA translational position. Exonuclease III is used to determine the translational positioning of a given nucleosome-bound DNA duplex, because of its ability to specifically cleave the ends of DNA that are not bound to the histones at the “entry” and “exit” ends of the nucleosome-bound DNA (110, 111). The resulting cleavage bands serve to map out the DNA region that is tightly bound to the histone octamer with the central base pair falling on the pseudo-dyad axis to form the 2-fold symmetrical nucleosome core particle.

Nucleosome dynamics. Although there are interactions between the DNA and histone octamer surface that result in fairly well-defined rotational and translational positioning of the DNA, it is believed that the nucleosome is not completely static. It appears that the nucleosome can undergo a series of dynamic processes that alter both the structure and the function of nucleosome or chromatin (117-119). The three main classes of nucleosome dynamics that have been identified are: nucleosome breathing, nucleosome sliding or rearrangement, and chromatin remodeling (117). Nucleosome breathing is characterized by a transient site-exposure of the “entry” or “exit” region of the nucleosomal DNA through unwrapping and re-wrapping between the histone octamer and the end of the nucleosomal DNA. This short-live exposure is supported by the observation that transcription factors exhibit a relative higher binding affinity for the DNA in the regions located close to the ends of nucleosomal DNA. Since both the “entry” and “exit” site are close to the dyad of the nucleosome, the nucleosome breathing could also facilitate the recognition between the DNA sequences around the dyad and the specific nucleosome binding proteins (120, 121). Nucleosome sliding is defined as the movement of the histone octamer with respect to the nucleosomal DNA, which can free up the previously bound DNA sequences and increase the accessibility of the nucleosomal DNA. Nucleosome sliding or histone octamer sliding process is found to be temperature-dependent, directly reflecting the stability of the translational positions of the nucleosomal DNA. At certain temperatures, other cellular machinery like histone chaperons or chromatin remodeling complexes can specifically bind to the nucleosome and carry out the rearrangement process (122, 123). The chromatin remodeling process is usually ATP-dependent, and various chromatin remodeling factors are believed to function in this process, generating different “remodeled” substrates, depending to some extent on the specific type of ATPase involved (124-126).

There are a number of factors that play roles in regulating nucleosome dynamics. First of all, the sequence of the nucleosomal DNA can greatly affect both the translational and rotational positioning in the nucleosome, which determines the stability of the nucleosome. The stronger the nucleosome positioning sequences in the nucleosomal DNA, the more “rigid” the nucleosome structure, and the less dynamics. Secondly, histone modifications can drastically change the properties of specific amino acids. Depending on the location of the amino acid, the modification could either alter the charge and shape of histone octamer structure and its interactions with nucleosomal DNA, both of which can affect the stability of the nucleosome (73-74, 127). Thirdly, histone tails are of particular interest in controlling nucleosome dynamics, not only because they contribute many of the binding sites between nucleosomal DNA and histone octamer, but also because they are involved in inter-nucleosome cross-talk through by interacting with other nucleosomes at the histone octamer surface. Removal of histone tails has been found to lower the energy barrier for repositioning nucleosomes and chromatin (128, 129). Last but not least, histone variants have different sequences with more conserved sequences in their structural motif domain and can interfere with nucleosome structure and function in several ways (130-133). They can interfere with the interactions between nucleosomal DNA and histone octamer thereby affecting nucleosome stability. Specific histone variants can also induce or repress DNA transcription through histone eviction, or interfere with recognition by ATP-dependent chromatin remodeling complexes.

Probes for nucleosome dynamics. A series of techniques have been developed to probe nucleosome dynamics, especially structural fluctuations and short-lived dynamical states, among which Exonuclease III (Exo III) digest and Fluorescence resonance energy transfer (FRET) are the two most commonly utilized methods (134-139). In a mono-nucleosome, nucleosome array or chromatin structure, Exo III can preferentially digest the linker DNA in a 3’ to 5’ direction until it is blocked by the bulky nucleosome core particle. Because of nucleosome dynamics, the transiently exposed “entry” and “exit” sites of the nucleosomal DNA could be accessible to Exo III digestion, revealing the frequency of nucleosome breathing. Likewise both histone octamer sliding and chromatin remodeling processes can be detected by Exo III, as these nucleosome dynamics can result in different exposure of the nucleosomal DNA Exo III digestion both *in vitro* and *in vivo* (134-136).

Compared with Exo III, FRET measurements are confined to *in vitro* studies using a donor-acceptor pair of flurophores incorporated in the nucleosome structure that can probe conformational changes during nucleosome dynamics (137-139). Generally, two approaches are commonly used for FRET studies of nucleosome dynamics. In one approach the two fluorophores are incorporated into the nucleosomal DNA, with one located at the dyad region, the other one at either the “entry” or the “exit” site of nucleosomal DNA. Using this design, the FRET measurements can detect nucleosome breathing processes, since in the unwrapped state, the two fluorophores are not close enough to generate the FRET signal, while they are in the wrapped state. In another approach, one fluorophore is placed in the nucleosomal DNA, while the other one is incorporated at specific site a of histone protein. By monitoring the distance between particular site of the nucleosomal DNA and certain position of the histone octamer by FRET, one can determine the extent of nucleosome sliding and chromatin remodeling.

1.3 How is DNA damage and repair modulated by the nucleosome?

DNA damage can be generated either endogenously or exogenously. Endogenous reactions mainly involve reactive oxygen species (ROS) from metabolic byproducts, like hydroxyl radicals, which can cause different types of DNA damages, i.e., oxidation of DNA base (8-oxoG), strand cleavage, and formation of base adducts, as well as spontaneous reactions such as depurination, and deamination (140-143). Exogenous reactions could arise from different sources, such as UV irradiation which induces various type of DNA photoproducts such as the CPD and (6-4) products as the two predominant forms(6-9), ionizing radiation which can generate single-strand break (SSB), double-strand break (DSB) or even inter-strand crosslink (144-147). Other DNA damaging chemicals, such as cisplatin or etoposide, can contribute to the overall number of DNA lesions by creating different DNA base adducts or distortion to the DNA structure (148-149). In response to DNA damage, cells undergo DNA repair, cell cycle arrest, and apoptosis, but significant amounts of unrepaired DNA damage could lead to DNA mutations, which can lead to cancer (150-154).

Photoproduct formation in nucleosomes. In eukaryotic cells, it is well believed that both formation and processing of DNA damage could be modulated by numerous factors, among which nucleosome and chromatin structure serve as a general platform since most of the genomic DNA is wrapped around the histone octamer to form the higher-ordered chromatin structure. As one of the main exogenous DNA damaging agent, UV irradiation can still induce both CPD and (6-4) photoproducts formation within the chromatin environment, with the (6-4) photoproducts largely confined to the linker DNA region, compared with CPDs which form in both linker and nucleosomal DNA. UV irradiation of the nucleosomal DNA results in CPD DNA photoproducts which vary with the rotational position, compared with the relatively uniform distribution in the linker DNA region. Formation of CPDs show a slight preference for sites where the DNA phosphodiester backbone is positioned away from the histone octamer surface (9, 155-157). The broadly accepted explanation for this preference is that the nucleosomal DNA at the facing OUT region has a higher decompression and rotational flexibility which allows the adjacent pyridimines additional freedom to adopt a more favorable photoreactive orientation for forming CPDs. Since the formation of CPDs causes a 7-9° structural distortion onto the DNA, the facing OUT position can accommodate this distortion better than the facing IN region, where the DNA conformation is more compressed and rigid. This point of view is furthered supported by the observation that the similar preference was also detected from the loop DNA or bent DNA that is not in contact with a protein, and unfolding of nucleosomes under low ionic strength condition yields a CPD distribution pattern similar to naked DNA (158-161).

When DNA containing randomly distributed CPDs is reconstituted into nucleosomes, the CPDs greatly influence nucleosome rotational positioning, since they favor the orientation where the phosphodiester backbone is facing OUT. On the other hand, the formation of CPDs could also interfere with the translational positioning in nucleosome as the CPDs show a preference for being located in the central three superhelical turns around the pseudo-dyad axis, where the nucleosomal DNA is almost exclusively bound by histone H3-H4 tetramers. This is probably due to the relative larger space between the nucleosomal DNA and the histone octamer surface which can better accommodate the local distortions induced by the CPD structure (161-163).

Although the formation of CPDs can cause local distortions in nucleosomal DNA, it doesn’t block the reconstitution of the nucleosome with DNA containing CPDs with different rotational or translational positionings. A number of studies have reported the successful preparation and isolation of nucleosome core particles bearing CPDs at either specific positions or when randomly distributed along the nucleosomal DNA (164-166). Smerdon’s laboratory developed a method for incorporating a T=T CPD DNA photoproduct into specific sites within a synthetic DNA duplex containing multiple TG motifs (164). After a DNA exchange reaction with nucleosome core particles isolated and purified from chicken blood cells, they managed to reconstitute the T=T CPD containing DNA duplex into a nucleosome core particle. By comparing the hydroxyl radical footprinting pattern between the nucleosomal DNA containing the T=T CPD with the nucleosomal DNA containing a non-dimerized TT sequence, they could determine the rotational positioning of the specific T=T CPD site. They were able to use hydroxyl radical footprinting to confirm the position of the CPD as shown in Figure 1.10. Due to the formation of the four-member ring in the CPD structure, the breakage of the phosphodiester bond between the T and T, which should create a footprinting band for the 3’-T in a non-dimerized TT sequence, won’t generate the cleavage site along the nucleosomal DNA. This is because the cleaved fragment is still connected to the rest of the DNA duplex through the four-member ring, as showed in Figure 1.10, *B*, thereby generating a “missing band” corresponding to the position of the 3’-T of the T=T CPD on the footprinting pattern.

If the CPD DNA photoproducts are not directly incorporated into the nucleosomal DNA sequences, but generated by UV irradiation of the reconstituted nucleosome, the hydroxyl radical footprinting method can still work to identify the rotational positioning of a specific CPD, but in this case, there won’t be a clear “missing band” on the footprinting pattern of the UV-irradiated nucleosomal DNA. In this case, there will be a change in the cleavage intensity at the footprinting band depending on the yield of the CPD. The rotational position could then be determined by comparing the intensity change between the UV-irradiated nucleosomal DNA footprinting pattern with the one of non-UV-irradiated nucleosomal DNA.

Repair of DNA photodamage in nucleosomes. When it comes to UV-induced DNA damage, photoreversal by photolyase and nucleotide excision repair are considered as the two main pathways leading to the removal or repair of UV-induced DNA photoproducts, the former is modulated by the accessibility of the

DNA lesion to the monomeric enzyme photolyase, whereas the latter relies on a stepwise assembly of multiple proteins onto the DNA lesion to form the complicate repair system. Nucleosomes have been found to play an important role in modulating these DNA repair process both *in vitro* and *in vivo* (167-172). Photolyase photoreverts CPDs by bending the DNA and flipping out the pyrimidine dimer from the double helix into the active site of the enzyme (173, 174). The repaired pyrimidines are then released from the enzymatic pocket and the photolyase dissociates from the DNA. It has been reported that a reconstituted nucleosome core particle inhibits repair of CPDs in the core DNA by photolyase compared with the linker DNA region. On the other hand, repair of a CPD at the ends of the nucleosomal DNA is greater than one in the core DNA, indicating that transient unwrapping of the DNA is taking place (175, 176).

In vivo studies of photoproduct repair in nucleosomes. In living cells, the presence of nucleosomes slows down CPD repair by photolyase, with a gradually increased rate from the center of the nucleosome toward the ends, where the accessibility of the CPDs to photolyase is higher. This could be attributed to the dynamic properties of nucleosome *in vivo*, such as transient unwrapping or sliding of the histone octamer thereby making the CPD accessible to photolyase (177-180). It has also been shown that the yeast SWI/SNF remodeling complex can accelerate photolyase repair of a CPD in a reconstituted nucleosome core particle presumably by destabilizing the nucleosome core particle (176).

Nucleosomes have also been shown to interfere with the nucleotide excision repair (NER) in different ways. NER comprises two sub-pathways: global genome repair (GGR) and transcription-coupled repair (TCR), with the GGR accounting for the removal of the majority of DNA lesions in nucleosomes (181, 183). In living cells, NER repair initially occurs at the ends of nucleosomal DNA and becomes more evenly distributed later on and sometimes results in nucleosome rearrangement. This observation could be explained by transient unwrapping and histone octamer sliding which would free up both the end and core regions of the nucleosomal DNA (186, 184). An alternate explanation is involves histone eviction or displacement in the beginning of NER repair followed by reassembly of the original histones to restore the nucleosome structure and encoded epigenetic information. Such a process may be aided by chromatin remodeling complexes (185-188).

In vitro studies of photoproduct repair in nucleosomes. *In vitro* studies with various nucleosome substrates and NER competent cell extracts also demonstrate the inhibitory effect of nucleosomes on the NER of UV-induced DNA lesions, with CPDs repaired much more slowly than (6-4) DNA photoproducts and other types of photo lesions (189-194). The presence of nucleosome was found to reduce the NER of CPDs by 6-9 fold compared with free DNA, using cellular extracts of human fibroblasts (189). In a study of a human nucleosome containing a site-specific CPD, the NER repair rate was slowed down by 10 fold, and was not affected by the yeast SWI/SNF chromatin remodeling complex which could stimulate the NER of a (6-4) DNA photoproduct (193, 194).

Smerdon and coworkers laboratory studied the nucleosome’s effect on the

NER rate of a T=T CPD photoproduct in two different nucleosome rotational positioning, using *Xenopus* nuclear extracts. As shown in Figure 1.11, the green color highlights the positions of the two T=T CPD DNA photoproduct sites in the nucleosome core particle, one IN, and the other OUT. They found that the OUR facing T=T CPD was repaired about 1.5-fold faster compared with the IN facing T=T CPD, and that both were repaired a 2-3 times slower than in naked DNA (165).

1.4 Goals of this thesis.

The major goal of this thesis was to continue the study of the deamination bypass mechanism with a focus on T=^{m}CG CPDs. Though we had previously established that a ^{m}C=T CPD was bypassed in an almost completely error free manner by yeast polymerase η, we did not know how the biologically relevant T=^{m}CG CPD would be bypassed by human as well as yeast polymerase η. Thus in chapter 2 we describe the preparation, characterization and in vitro bypass of a T=^{m}CG CPD, and show that it is bypassed in a similar error-free manner by both yeast and human polymerase η. Because this was the case, the ^{m}C of the T=^{m}CG CPD would have to deaminate first, followed by error-free bypass by polymerase η to efficiently produce a C to T mutation. It therefore became of great interest to see how this deamination process would be modulated in mammalian cells.

Prior *in vivo* studies with uracil DNA glycosylase-deficient cells have showed that the deamination of C-containing CPDs did occurs at a significant rate with an estimated half-life from a few hours to 120 hours (195-198). Futhermore, research on

UV-irradiated human fibroblasts revealed that C or ^{m}C-containing CPDs deaminate in a sequence and time-dependent manner, with about 10 to 60% deamination after 24 hours (199). However, none of these studies tried to correlate the C or ^{m}C deamination in the CPD with the nucleosome occupancy or nucleosome positioning. Most recently, it has been reported that nucleosome occupancy greatly suppresses the spontaneous deamination of C, with a nearly 50% decrease in the rate of C to T mutation in nucleosomal DNA in yeast (200). Thus it would appear that the nucleosome position of a C or ^{m}C-containing CPD could affect the deamination rate.

Therefore, in Chapter 3, we examined the effect of nucleosome rotational position on T^{m}CG CPD deamination by preparing a nucleosome core particle with the same 150-mer DNA sequence as used by the Smerdon group (165) and substituted the TTN (N: any nucleotide) site with T^{m}CG, to have a CPD site facing inside (IN) and one facing outside (OUT) relative to the histone core surface. We found that a T^{m}C CPD positioned against the surface could deaminate 4.7 times slower than the unbound sequence, whereas a T^{m}C CPD facing out deaminated 8.9 times faster than the unbound sequence, corresponding to an overall 42-fold difference in rate (201). In Chapter 4, we went on to examine the deamination rate of T=^{m}CG CPDs in all ten possible nucleosome rotational positioning in one full periodic turn at the same translational positioning site, and found a similar effect.

In chapter 5, we expressed and purified histones H2A, H2B, H3 and H4 from Xenopus Oocyte in *E. Coli*, reassembled the histone octamer based on the previously reported method (99). Through nucleosome reconstitution with the synthetic 147-mer

DNA sequences as used in Chapter 4, we were able to prove the nucleosome positioning pattern via hydroxyl radical footprinting, although with some difference compared with chicken nucleosome core particle.

In the appendix, we described a hydroxyl radical footprinting method followed by the ligation-mediated PCR (LMPCR) detection to probe the nucleosome positioning along p53 gene in both HeLa cells and human primary keratinocyte. Consistently with earlier results using DNase I footprinting (69), we were able to identify a clear nucleosome positioning pattern in exon 5 and 6 along p53 gene.

References

1. Bickers, D. R.; Lim, H. W.; Margolis, D.; Weinstock, M. A.; Goodman, C.; Faulkner, E.; Gould, C.; Gemmen, E.; Dall, T. The burden of skin diseases: 2004 a joint project of the American Academy of Dermatology Association and the Society for Investigative Dermatology. *J Am Acad Dermatol.* **2006,** *55,* 490-500.

2. D.E. Brash, J.A. Rudolph, J.A. Simon, A. Lin, G.J. McKenna, H.P. Baden, A.J. Halperin, J. Pont´en,Arole for sunlight in skin cancer: UV-induced p53 mutations in squamous cell carcinoma. *Proc. Natl. Acad. Sci. U.S.A.* **1991,** *88*, 10124–10128.

3. N. Dumaz, C. Drougard, A. Sarasin, L. Daya-Grosjean, Specific UV- induced mutation spectrum in the p53 gene of skin tumors from DNA-repair-deficient xeroderma pigmentosum patients. *Proc. Natl. Acad. Sci. U.S.A.* **1993,** *90*, 10529–10533.

4. A. Ziegler, D.J. Leffell, S. Kunala, H.W. Sharma, M. Gailani, J.A. Simon, A.J. Halperin, H.P. Baden, P.E. Shapiro, A.E. Bale, D.E. Brash, Mutation hot spots due to sunlight in the p53 gene of nonmelanoma skin cancers. *Proc. Natl. Acad. Sci. U.S.A.* **1993,** *90*, 4216–4220.

5. G. Giglia-Mari, A. Sarasin, TP53 mutations in human skin cancers. *Hum. Mutat.* **2003,** *21*, 217–228.

6. Yoon, J. H., Lee, C. S., O'Connor, T. R., Yasui, A., and Pfeifer, G. P. The DNA damage spectrum produced by simulated sunlight. *J. Mol. Biol.* **2000,** *299,* 681–693.

7. Cadet, J., Sage, E., and Douki, T. Ultraviolet radiation-mediated damage to cellular DNA *Mutat. Res.* **2005,** *571,* 3–17.

8. Douki, T., and Cadet, J. Individual determination of the yield of the main UV-induced dimeric pyrimidine photoproducts in DNA suggests a high mutagenicity of CC photolesions. *Biochemistry.* **2001,** *40*, 2495–2501.

9. G.P. Pfeifer, Formation and processing of UV photoproducts: effects of DNA sequence and chromatin environment. *Photochem. Photobiol.* **1997,** *65*, 270–283.

10. D.L. Mitchell, R.S. Nairn, The biology of the (6-4) photoproduct. Photochem. Photobiol. **1989,** *49,* 805–819.

11. W.A. Franklin and W.A. Haseltine, The role of the (6-4) photoproduct in ultraviolet light-induced transition mutations in *E. Coli*. *Mutat. Res.* **1986,** *165*, 1-7.

12. Beukers, R., Eker, A.P. and Lohman, P.H. 50 years thymin dimer. *DNA Repair*

(Amst). **2008,** *7*, 530-543.

13. Pfeifer, G. P., You, Y. H. and Besaratinia, A. Mutations induced by ultraviolet light. *Mutat. Res.* **2005,** *571*, 19-31.

14. Mitchell, D. L., Jen, J and Cleaver, J. E. Sequence specificity of cyclobutane pyrimidine dimers in DNA treated with solar (ultraviolet B) radiation. *Nucleic Acids Res.* **1992,** *20*, 225-229.

15. You, Y., Li, C. and Pfeifer, G. P. Involvement of 5-methylcytosine in sunlight-induced mutagenesis. *J. Mol. Biol.* **1999,** *293*, 493–503.

16. Shugar, D., and Fox, J. J. Spectrophotometric studies of nucleic acid derivatives and related compounds as a function of pH. *Biochim. Biophys. Acta,* **1952,** *9*, 199-218.

17. Jiang, N., and Taylor, J. S. *In vivo* evidence that UV-induced C→ T mutations at dipyrimidine sites could result from the replicative bypass of *cis-syn* cyclobutane dimers or their deamination products. *Biochemistry.* **1993,** *32*, 472–481.

18. Danilo, V. I., Les, A., and Alderfer, J. L. A theoretical study of the *cis-syn* pyrimidine dimers in the gas phase and water cluster and a tautomer bypass mechanism for the origin of UV-induced mutations. *J. Biomol. Struct. Dyn.* **2001,** *19,* 179–191.

19. Brown, D. M., and Hewlins, M. J. Dihydrocytosine and related compounds. *J. Chem. Soc. C.* **1968,** 2050–2055.

20. Dupuy-Mamelle, N., and Pullman, B. No. 61.-Recherches theoriques sur la structure electronique des purine et pyrimidines bilogiques. IV. Les pyrimidines saturees sur la liaison 5–6. *J. Chim. Phys. Phys. Chim. Biol.* **1967,** *64,* 708–712.

21. Danilov, V. I., Stewart, J. J. P., Les, A., and Alderfer, J. L. A theoretical study of pyrimidine photohydrates and a proposed mechanism for the mutagenic effect of ultraviolet light. *Chem. Phys. Lett.* **2000,** 328, 75–82.

22. Setlow, R. B., Carrier, W. L., and Bollum, F. J. Pyrimidine dimers in UV-irradiated poly dI:dC. *Proc. Natl. Acad. Sci. U.S.A.* **1965,** *53,* 1111–1118.

23. Liu, F. T., and Yang, N. C. Photochemistry of cytosine derivatives. 1. Photochemistry of thymidylyl-(3'→5')-deoxycytidine. *Biochemistry.* **1978,** *17,* 4865–4876.

24. Fix, D., and Bockrath, R. Thermal resistance to photoreactivation of specific mutations potentiated in *E. coli* B/r ung by ultraviolet light. *Mol. Gen. Genet.* **1981,** *182*, 7–11.

25. Lemaire, D. G., and Ruzsicska, B. P. Kinetic analysis of the deamination reactions of cyclobutane dimers of thymidylyl-3’,5’-2’-deoxycytidine and 2’-deoxycytidylyl-3’,5’-thymidine. *Biochemistry.* **1993,** *32*, 2525–2533.

26. Barak, Y., Cohen-Fix, O., and Livneh, Z. Deamination of cytosine containing pyrimidine photodimers in UV-irradiated DNA. Significance for UV light mutagenesis. *J. Biol. Chem.* **1995,** *270*, 24174–24179.

27. Peng, W., and Shaw, B. R. Accelerated deamination of cytosine residues in UV-induced cyclobutane pyrimidine dimers leads to CC → TT transitions. *Biochemistry.* **1996,** *35*, 10172–10181.

28. Frederico, L. A., Kunkel, T. A., and Shaw, B. R. A sensitive genetic assay for the detection of cytosine deamination: determination of rate constants and the activation energy. *Biochemistry.* **1990,** *29*, 2532–2537.

29. Shen, J. C., Rideout, W. M., 3rd, and Jones, P. A. The rate of hydrolytic deamination of 5-methylcytosine in double-stranded DNA. *Nucleic. Acids. Res.* **1994,** *22*, 972–976.

30. Nouspikel, T. DNA repair in mammalian cells: nucleotide excision repair: variations on versatility. *Cell. Mol. Life Sci.* **2009,** *66*, 994–1009.

31. Tornaletti, S. DNA repair in mammalian cells: transcription-coupled DNA repair: directing your effort where it’s most needed. *Cell. Mol. Life Sci.* **2009,** *66*, 1010–1020.

32. Lagerwerf, S., Vrouwe, M. G., Overmeer, R. M., Fousteri, M. I., and Mullenders, L. H. DNA damage response and transcription. *DNA Repair Repair.* **2011,** *10*, 743–750.

33. Waters, L. S., Minesinger, B. K., Wiltrout, M. E., D’Souza, S., Woodruff, R. V., and Walker, G. C. Eukaryotic translesion polymerases and their roles and regulation in DNA damage tolerance. *Microbiol. Mol. Biol. Rev.* **2009,** *73*, 134–154.

34. Wang, C. I., and Taylor, J. S. Site-specific effect of thymine dimer formation on $dA_n\cdot dT_n$ tract bending and its biological implications. *Proc. Natl. Acad. Sci. U.S.A.* **1991,** *88*, 9072–9076.

35. Jing, Y., Kao, J. F., and Taylor, J. S. Thermodynamic and base pairing studies of matched and mismatched DNA dodecamer duplexes containing *cis-syn*, (6-4), and Dewar photoproducts of TT. *Nucleic Acids Res.* **1998,** *26*, 3845–3853.

36. Park, H., Zhang, K., Ren, Y., Nadji, S., Sinha, N., Taylor, J. S., and Kang, C. Crystal structure of a DNA decamer containing a *cis-syn* thymine dimer. *Proc. Natl. Acad. Sci. U.S.A.* **2002,** *99*, 15965–15970.

37. Huang, J. C., Hsu, D. S., Kazantsev, A., and Sancar, A. Substrate spectrum of human excinuclease: repair of abasic sites, methylated bases, mismatches, and bulky adducts. *Proc. Natl. Acad. Sci. U.S.A.* **1994,** *91*, 12213–12217.

38. Johnson, R. E., Prakash, S., and Prakash, L. Efficient bypass of a thymine-thymine dimer by yeast DNA polymerase, pol η. *Science.* **1999,** *283*, 1001–1004.

39. Masutani, C., Kusumoto, R., Yamada, A., Dohmae, N., Yokoi, M., Yuasa, M., Araki, M., Iwai, S., Takio, K., and Hanaoka, F. The XPV (xeroderma pigmentosum variant) gene encodes human DNA polymerase η. *Nature.* **1999,** *399*, 700–704.

40. Prakash, S., Johnson, R. E., and Prakash, L. Eukaryotic translesion synthesis DNA polymerases: specificity of structure and function. *Annu. Rev. Biochem.* **2005**, *74*, 317–353.

41. Lehmann, A. R., Kirk-Bell, S., Arlett, C. F., Paterson, M. C., Lohman, P.H. et al. Xeroderma pigmentosum cells with normal levels of excision repair have a defect in DNA synthesis after UV-irradiation. *Proc. Natl. Acad. Sci. U.S.A.* **1975,** *72*, 219–223.

42. Trincao, J., Johnson, R. E., Escalante, C. R., Prakash, S. and Aggarwal, A. K. Structure of the catalytic core of *S. cerevisiae* DNA polymerase eta: implications for translesion DNA synthesis. *Mol. Cell.* **2001,** *8*, 417-426.

43. Vu, B., Cannistraro, V.J., Sun, L.P. and Taylor, J. S. DNA synthesis past a 5-methylC-containing cis-syn-cyclobutane pyrimidine diemr by yeast pol η is highly nonmutagenic. *Biochemistry.* **2006,** *45*, 9327–9335.

44. Johnson, R. E., Haracska, L., Prakash, S. and Prakash, L. Role of DNA polymerase zeta in the bypass of a (6-4) TT photoproduct. *Mol. Cell. Biol.* **2001,** *21*, 3558-3563.

45. Tu Y, Dammann R, Pfeifer GP. Sequence and time-dependent deamination of cytosine bases in UVB- induced cyclobutane pyrimidine dimers *in vivo*. *J. Mol. Biol.* **1998,** *284*, 297–311.

46. Cannistraro, V. J., and Taylor, J. S. Acceleration of 5-methylcytosine deamination in cyclobutane dimers by G and its implications for UV-induced C-to-T mutation hotspots. *J. Mol. Biol.* **2009,** *392*, 1145–1157.

47. Sancar GB, Sancar A. Purification and characterization of DNA photolyases. *Methods Enzymol.* **2006,** *408*, 121–156.

48. Cannistraro, V. J., and Taylor, J. S. Methyl CpG binding protein 2 (MeCP2) enhances photodimer formation at methyl-CpG sites but suppresses dimer deamination. *Nucleic. Acids. Res.* **2010,** *38*, 6943–6955.

49. Kornberg, R. D. Structure of chromatin. *Annu. Rev. Biochem*. **1977,** *46*, 931-954

50. Widom, J. Structure, dynamics, and function of chromatin *in vitro*. *Annu. Rev. Biophys. Biomol. Struct.* **1998,** *27,* 285-327.

51. Davey, C. A., Sargent, D. F., Luger, K., Maeder, A. W. and Richmond, T. J. Solvent mediated interactions in the structure of the nucleosome core particle at 1.9 A resolution. *J. Mol. Biol.* **2002,** *319*, 1097-1013.

52. Luger, K., Mader, A. W., Richmond, R. K., Sargent, D. E. and Richmond, T. J. Crystal structure of the nucleosome core particle at 2.8 A resolution. *Nature.* **1997,** *389*, 251-60.

53. Kornberg, R. D. and Lorch, Y. Twenty-five years of the nucleosome, fundamental particle of the eukaryote chromosome. *Cell.* **1999,** *98*, 285-294.

54. Kornberg, R. D. Chromatin structure: a repeating unit of histones and DNA. *Science.* **1974,** *184*, 868-871.

55. Felsenfeld, G. and Groudine, M. Controlling the double helix. *Nature.* **2003,** *421*, 448-453.

56. Van Holde, K. E. Chromatin*, Springer-Verlag, New York,* **1988**

57. Wolffe, A. P. Chromatin structure and function. *Academic Press, Londer,* **1998**.

58. Finch, J. T. and Klug, A. Solenoidal model for superstructure in chromatin. *Proc. Natl. Acad. Sci. U.S.A.* **1976,** *73*, 1897–1901.

59. Thoma, F., Koller, T. and Klug, A. Involvement of histone H1 in the organization of the nucleosome and the salt-dependent superstructures of chromatin. *J. Cell. Biol.* **1979,** *83*, 403-427.

60. Van Holde, K. and Zlatanova, J. What determines the folding of the chromatin fiber? *Proc. Natl. Acad. Sci. U.S.A.* **1996,** *93*, 10548–10555.

61. Dorigo, B., Schalch, T., Kulangara, A., Duda, S., Schroeder, R. R. And Richmond, T. J. Nucleosome arrays reveal the two-start organization of the chromatin fibers. *Science,* **2004,** *306*, 1571-1573.

62. Robinson, P., Fairall, L., Huynh, V. and Rhodes, D. EM measurements define the dimensions of the "30-nm" chromatin fibre: evidence for a compact, interdigitated structures, *Proc. Natl. Acad. Sci. U.S.A.* **2006,** *103*, 6506–6511.

63. Woodcock, C., Frado, L. and Rattner, J. The higher-order structure of chromatin: evidence for a helical ribbon arrangement. *J. Cell. Biol.* **1984,** *99*, 42-52.

64. Schalch, T., Duda, S. Sargent, D.F. and Richmond, T. J. X-ray structure of a tetranucleosome and its implications for the chromatin fibre. *Nature,* **2005,** *436*, 138-141.

65. Sekinger, E. A., Moqtaderi, Z. and Struhl, K. Intrinsic histone-DNA interactions and low nucleosome density are important for preferential accessibility of promoter regions in yeast. *Mol. Cell.* **2005,** *18*, 735-748.

66. Young, D. and Carroll, D. Regular arrangement of nucleosomes on 5S rRNA genes in *Xenopus laevis*. *Mol. Cell. Biol.* **1983,** *3*, 720-730.

67. Ioshikhes, I. P., Albert, I., Anton, S. J. and Pugh, B. F. Nucleosome positions predicted through comparative genomics. *Nat. Genet.* **2006,** *442*, 772-778.

68. Rando, O. J. and Chang, H. Y. Genome-wide views of chromatin structure. *Annu. Rev. Biochem.* **2009,** *78,* 245-271.

69. Tornaletti, S., Bates, S. and Pfeifer, G. P. A high-resolution analysis of chromatin structure along p53 sequences. *Mol. Carcinog.* **1996,** *17*, 192-201.

70. Fischle, W., Wang, Y. and Allis, C. D. Binary switches and modifications cassettes in histone biology and beyond. *Nature,* **2003,** *15,* 172-183.

71. Jenuwein, T. and Allis, C. D. Translating the histone code. *Science,* **2001,** *293*, 1074-1080.

72. Strahl, B. D. and Allis, C. D. The language of covalent histone modifications. *Nature,* **2000,** *403*, 41-45.

73. Cosgrove, M. S. and Wolberger, C. How does the histone code work? *Biochem. Cell. Biol.* **2005,** *83*, 468-476.

74. Freitas, M. A., Sklenar, A. R. and Parthun, M. R. Application of mass spectrometry to the identification and quantification of histone post-translational modifications. *J. Cell. Biochem,* **2004,** *92,* 691-700.

75. Shi, Y., Lan, F. and Matson, C. Histone demethylation mediated by the nuclear amine oxidase homolog LSD1. *Cell,* **2004,** *119,* 941-953.

76. Wysocka, J., Milne, T. A. and Allis, C. D. Taking LSD 1 to a new high. *Cell,* **2005**, *122,* 654-658.

77. Bannister, A. J., Zegerman, P., Partridge, J. F., Miska, E. A., Thomas, J. O., Allshire, R. C. and Kouzarides, T. Selective recognition of methylated lysine 9 on histone H3 by the HP1 chromo domain. *Nature,* **2001,** *410,* 120-124.

78. Lachner, M., O'Carroll, D., Rea, S., Mechtler, K. and Jenuwein, T. Methylation of histone H3 lysine 9 creates a binding site for HP1 proteins. *Nature*, **2001,** *410,* 116-120.

79. Jenuwein, T. Re-SET-ting heterochromatin by histone methyltransferases. *Trends. Cell. Biol.* **2001,** *11*, 266-273.

80. Kasten, M., Szerlong, H., Erdjument-Bromage, H., Tempst, P., Werner, M. and Cairns, B. R. Tandem bromodomains in the chromatin remodeler RSC recognized acetylated histone H3 Lys 14. *EMBO. J,* **2004,** *23*, 1348-1359.

81. Pray-Grant, M. G., Daniel, J. A., Schieltz, D., Yates, J. R. and Grant, P. A. Chd1 chromodomain links histone H3 methylation with SAGA- and SLIK-dependent acetylation. *Nature*, **2005,** *433*, 434-438.

82. Sharma, S., Kelly, T. K and Jones, P. A. Epigenetics in cancer. *Carcinogenesis.* **2010,** *31*, 27-36.

83. Fraga, M. F., Ballestar, E., Villar-Garea, A., Boix-Chornet, M., Espada, J., Ropero, S. And Petrie, K. Loss of acetylation at Lys 16 and trimethylation at Lys 20 of histone H4 is a common hallmark of human cancer. *Nat. Genet.* **2005,** *37*, 391-400.

84. Manuyakorn, A., Paulus, R., Farrell, J., Dawson, N. A., Reber, H., Seligson, D. B. and Horvath, S. Cellular histone modification patterns predict prognosis and treatment response in resectable pancreatic adenocarcinoma: Results from RTOG 9704. *J. Clin. Oncol.* **2010,** *28*, 1358-1365.

85. Seligson, D. B., Horvath, S., McBrian, M. A., Mah, V., Chia, D., Goodglick, L. and Kurdistani, S. K. Global levels of histone modifications predict prognosis in different cancers. *Am. J. Pathol.* **2009,** *174*, 1619-1628.

86. Van Den Broeck, A., Brambilla, E., Moro-Sibilot, D., Khochbin, S. and Gazzeri, S. Loss of histone H4K20 trimethylation occurs in preneoplasia and influences prognosis of non-small cell lung cancer. *Clin. Cancer. Res.* **2008,** *14*, 7237-7245.

87. Todd, R. C. and Lippard, S. J. Consequences of cisplatin binding on nucleosome structure and dynamics. *Chem. Biol.* **2010,** *17*, 1334-1343.

88. Sahu, G., Wang, D., Chen, C. B., Zhurkin, V. B., Harrington, R. E., Appella, E. and Nagaich, A. K. p53 binding to nucleosomal DNA depends on the rotational positioning of DNA response element. *J. Biol. Chem.* **2010,** *285*, 1321-1332.

89. Vinayachandran, V., Pusarla, R. H. and Bhargava, P. Multiple sequence-directed possibilities provide a pool of nucleosome position choices in different states of activity of a gene. *Epigenetics. Chromatin*. **2009,** *2*, 4.

90. Albert, I., Mavrich, T. N., Tomsho, L. P., Zanton, S. J., Schuster, S. C. and Pugh, B. F. Translational and rotational settings of H2A.Z nucleosome across the *Saccharomyces cerevisiae* genome. *Nature,* **2007,** *446*, 572-576.

91. Caserta, M., Agricolam E., Churcher, M., Hiriart E., Verdone, L., Di Mauro, E. And Travers, A. A translational signature for nucleosome positioning *in vivo*. *Nucleic. Acids. Res.* **2009,** *16*, 5309-5321.

92. Schnitzler, G. R. Isolation of histones and nucleosome cores from mamalian cells. *Curr. Protoc. Mol. Biol.* **2001,** *21*, 21.5.

93. Kasai, K., Hayashi, H. and Iwai, K. Nucleosome core particles of calf thymus, tetrahymena, and the reconstituted hybrid. Their structure reflects the nature of histone octamer. *J. Biochem.* **1986,** *1*, 91-98.

94. Caiafa, P., Scarpati-Cioffari, M. R., Allegra, P., Lonigro, R. And Turano, C. Tightly bound non-histone proteins in nucleosomes from pig-liver chromatin. *Eur. J. Biochem.* **1981,** *121*, 15-19.

95. Fukuma, M., Hiraoka, Y., Sakurai, H. and Fukasawa, T. Purification of yeast histones competent for nucleosome assembly *in vitro*. *Yeast.* **1994,** *3*, 319-331.

96. Gelbart, M. E., Rechsteiner, T., Richmond, T. J. and Tsukiyama, T. Interactions of Isw2 chromatin remodeling complex with nucleosomal arrays: analyses using recombinant yeast histones and immobilized templates. *Mol. Cell. Biol.* **2001,** *6*,

2098-2106.

97. Nightingale, K. P. and Becker, P. B. Structural and functional analysis of chromatin assembled from defined histones. *Methods.* **1998,** *4,* 343-353.

98. Ruiz-Carrillo, A., Jorcano, J. L., Eder, G. And Lurz. R. *In vitro* core particle and nucleosome assembly at physiological ionic strength. *Proc. Natl. Acad. Sci. U.S.A.* **1979,** *76,* 3284–3288.

99. Luger, K., Rechsteiner, T. J. And Richmond, T. J. Expression and purification of recombinant histones and nucleosome reconstitution. *Methods. Mol. Biol.* **1999,** *119,* 1-16.

100. Luger, K., Rechsteiner, T. J. And Richmond, T. J. Preparation of nucleosome core particle from recombinant histones. *Methods. Enzymol.* **1999,** *304,* 3-19.

101. Zhang, Y., Moqtaderi, Z., Rattner, B. P, Euskirchen, G., Snyder, M. and Kadonago, J. T. Intrinsic histone-DNA interactions are not the major determinant of nucleosome positions *in vitro*. *Nat. Struct. Mol. Biol.* **2009,** *16,* 847-852.

102. Travers, A., Caserta, M., Chucher, M., Hiriart, E. and Di Mauro, E. Nucleosome positioning – what do we really know? *Mol. Biosyst.* **2009,** *5,* 1582-1592.

103. Stein, A., Takasuka, T. E. and Collings, C. K. Are nucleosome positions in vivo primarily determined by histone-DNA sequence preferences? *Nucleic. Acids. Res.* **2010,** *38,* 709-719.

104. Widlund, H. R., Cao, H., Simonsson, S., Magnusson, E., Simonsson, T. and Nielsen, P. E. Identification and characterization of genomic nucleosome-positioning sequences. *J. Mol. Biol.* **1997,** *267,* 807-817.

105. Virstedt, J., Berge, T., Henderson, R. M, Waring, M. J. and Travers, A. A. The influence of DNA stiffness upon nucleosome formation. *J. Struct. Biol.* **2004,** *148,* 66-85.

106. Shrader, T. E. and Crothers. D. M. Artificial nucleosome positioning sequences. *Proc. Natl. Acad. Sci. U.S.A.* **1989,** *86,* 7418–7422.

107. Li, Q. and Wrange, O. Translational positioning of a nucleosomal glucocorticoid response element modulates glucocorticoid receptor affinity. *Genes Dev.* **1993,** *12A,* 2471-2482.

108. Vasudevan, D., Chua, E. Y. and Davey, C. A. Crystal structure of nucleosome core particles containing the “601” strong positioning sequence. *J. Mol. Biol.* **2010,**

403, 1-10.

109. Vitolo, J. M., Thiriet, C. and Hayes, J. J. DNase I and hydroxyl radical characterization of chromatin complexes. *Curr. Protoc. Mol. Biol.* **2001,** *21*, 21.4.

110. Ober, M and Lippard, S. J. Cisplatin damage overrides the predefined rotational setting of positioned nucleosomes. *J. Am. Chem. Soc.* **2007,** *129*, 6278-6286.

111. Danford, A. J., Wang, D., Wang, Q., Tullius. T. D. and Lippard, S. J. Platinum anticancer drug damage enforces a particular rotational setting of DNA in nucleosomes. *Proc. Natl. Acad. Sci. U.S.A.* **2005,** *102*, 12311–12316.

112. Hampshire, A. J., Rusling, D. A., Broughton-Head, V. J. and Fox, K. R. Footprinting: a method for determining the sequence selectivity, affinity and kinetics of DNA-binding ligands. *Methods.* **2007,** *42*, 128-140.

113. Tullius, T. D. and Dombroski, B. A. Hydroxyl radical "footprinting": high-resolution information about DNA-protein contacts and application to lambda repressor and Cro protein. *Proc. Natl. Acad. Sci. U.S.A.* **1986,** *83*, 5469–5473.

114. Tullius, T. D. DNA footprinting with hydroxyl radical. *Nature.* **1988,** *332*, 663-664.

115. Balasubramanian, B., Pogozelski, W. K., and Tullius, T. D. DNA strand breaking by the hydroxyl radical is governed by the accessible surface areas of the hydrogen atoms of the DNA backbone. *Proc. Natl. Acad. Sci. U.S.A.* **1998,** *95*, 9738–9743.

116. Pogozelski, W. K. and Tullius, T. D. Oxidative strand scission of nucleic acids: Routes initiated by hydrogen abstraction from the sugar moiety. *Chem. Rev*. **1998,** *98*, 1089-1108.

117. Luger, K. Dynamic nucleosomes. *Chromosome Res.* **2006,** *14*, 5-16.

118. Blossey, R. and Schiessel, H. The dynamics of the nucleosome: thermal effects, external forces and ATP. *FEBS. J.* **2011,** *278*, 3619-3632.

119. Choy, J. S. and Lee, T. H. Structural dynamics of nucleosomes at single-molecule resolution. *Trends. Biochem. Sci.* **2012,** 1-11.

120. Anderson, J. D. and Widom, J. Sequence and position-dependence of the equilibrium accessibility of nucleosomal DNA target sites. *J. Mol. Biol.* **2000,** *296*, 979-987.

121. Li, G. and Widom, J. Nucleosome facilitate their own invasion. *Nat. Struct. Mol. Biol.* **2004,** *11*, 763-769.

122. Pennings, S., Meersseman, G. and Bradbury, EM. Mobility of positioned nucleosomes on 5S rDNA. *J. Mol. Biol.* **1991,** *220*, 101-110.

123. Flaus, A., Rencurel, C., Ferreira, H., Wiechens, N. and Owen-Hughes, T. Sin mutations alter inherent nucleosome mobility. *EMBO. J*, **2004,** *23*, 343-353.

124. Peterson, C. L. and Tamkun, J. W. The SWI-SNF complex: a chromatin remodeling machine? *Trends. Biochem. Sci.* **1995,** *20*, 143-146.

125. Fan, H. Y., Rangasamy, D., Luger, K. and Tremethick, D. J. H2A.Z alters the nucleosome surface to promote HP1alpha-mediated chromatin fiber folding. Mol. *Cell.* **2004,** *16*, 655-661.

126. Hamiche, A., Sandaltzopoulos, R., Gdula, D. A. And Wu, C. ATP-dependent histone octamer sliding mediated by the chromatin remodeling complex NURF. *Cell.* **1999,** *97*, 833-842.

127. Wright, D. E., Wang, C. Y. and Kao, C. F. Histone ubiquitylation and chromatin dynamics. *Front. Biosci.* 2012, 17, 1051-1078.

128. Gottesfeld, J. M. Melander, C., Suto, R. K., Ravio, H., Luger, K. And Dervan, P. B. Sequence-specific recognition of DNA in the nucleosome by pyrrole-imidazole polyamides. *J. Mol. Biol.* **2001,** *309*, 625-639.

129. Polach, K. J., Lowary, P. T. and Widom. J. Effects of core histone tail domains on the equilibrium constants for dynamic DNA site accessibility in nucleosomes. *J. Mol. Biol.* **2000,** *298*, 211-223.

130. Chakravarthy, S., Bao, Y., Roberts, V. A., Tremethick, D. J. and Luger, K. Structural characterisation of histone H2A variants. *Cold Spring Harb Symp Quant Biol.* **2004,** *69*, 227-234.

131. Bao, Y., Konesky, K. and Park, Y. J. Nucleosomes containing the histone variant H2A.Bbd organize only 118 base pairs of DNA. *EMBO. J.* **2004,** *23*, 3314-3324.

132. Zhang, H., Roberts, D. N. and Cairns, B. R. Genome-wide dynamics of Htz1, a histone H2A variant that poises repressed/basal promoters for activation through histone loss. *Cell.* **2005,** *123*, 219-231.

133. Angelov, D., Charra, M., Seve, M., Cote, J., Khochbin, S. and Dimitrov, S.

Differential remodeling of the HIV-1 nucleosome upon transcription activators and SWI/SNF complex binding. *J. Mol. Biol.* **2000,** *302*, 315-326.

134. Archer, T. K. and Ricci, A. R. Exonuclease III as a probe of chromatin structure *in vivo*. *Methods. Enzymol.* **1999,** *304*, 584-599.

135. Roberts, M. S., Fragoso, G. and Hager, G. L. Nucleosomes reconstituted in vitro on mouse mammary tumor virus B region DNA occupy multiple translational and rotational frames. *Biochemistry.* **1995,** *34*, 12470-12480.

136. Archer, T. K. and Lee, H. L. Visualization of multicomponent transcription factor complexes on chromatin and nonnucleosomal templates *in vivo*. *Methods.* **1997,** *11*, 235-245.

137. Koopmans, W. J., Buning, R. and Van Noort, J. Engineering mononucleosomes for single-pair FRET experiments. *Methods. Mol. Biol.* **2011,** *749*, 291-303.

138. Deindl, S. and Zhuang, X. Monitoring conformational dynamics with single-molecule fluorescence energy transfer: applications in nucleosome remodeling. *Methods. Enzymol.* **2012,** *513*, 59-86.

139. Koopmans, W. J., Brehm, A., Logie, C., Schmidt, T. and van Noort. J. Single-pair FRET microscopy reveals mononucleosome dynamics. *J. Fluoresc.* **2007,** *17*, 785-795.

140. Wang, D., Kreutzer, D. A. and Essigmann, J. M. Mutagenicity and repair of oxidative DNA damage: insights from studies using defined lesions. *Mutat. Rev.* **1998,** *400*, 99-115.

141. Aruoma, O. I., Halliwell, B. and Dizdaroglu, M. Iron ion-dependent modification of bases in DNA by the superoxide radical-generating system hyposanthine / xanthine oxidase. *J. Biol. Chem.* **1989,** *264*, 13024-13028.

142. Breen, A. P. and Murphy, J. A. Reactions of oxyl radicals with DNA. *Free. Radic. Bio. Med.* **1995,** *18*, 1033-1077.

143. Floyd, R. A. and Carney, J. M. Free radical damage to protein and DNA: mechanisms involved and relevant observations on brain undergoing oxidative stress. *Ann. Neurol.* **1992,** *32*, 22-27.

144. Jeggo, P.A. and Lobrich, M. DNA double-strand breaks: their cellular and clinical impact? *Oncogene.* **2007,** *26*, 7717-7719.

145. Jeggo, P. and Lobrich, M. Radiation-induced DNA damage responses. *Radiat.*

Prot. Dosimetry. **2006,** *122*, 124-127.

146. Noll, D. M., Mason, T. M, and Miller, P. S. Formation and repair of interstrand cross-links in DNA. *Chem. Rev.* **2006,** *106*, 277-301.

147. Dextraze, M. E., Gantchev, T., Girouard, S. Hunting, D. DNA interstrand cross-links induced by ionizing radication: An unsung lesion. *Mutat. Res.* **2010,** *704*, 101-107.

148. Doi, K. Mechanisms of neurotoxicity induced in the developing brain of mice and rats by DNA-damaging chemicals. *J. Toxicol. Sci.* **2011,** *36*, 695-712.

149. Galluzzi, L., Senovilla, L., Vitale, I., Michels, J. Martins, I., Castedo, M. And Kroemer, G. Molecular mechanisms of cisplatin resistance. *Oncogene.* **2012,** *31*, 1869-1883.

150. Roos, W. P. And Kaina, B. DNA damage-induced apoptosis: From specific DNA lesions to the DNA damage response and apoptosis. *Cancer. Lett.* **2012,** Epub ahead of print.

151. Ames, B. N., Shigenaga, M. K. and Gold, L. S. DNA lesions, inducible DNA repair and cell division: three key factors in mutagenesis and carcinogenesis. *Environ. Health. Perspect.* **1993,** *101*, 35-44.

152. Stone, M. P., Huang, H., Brown, K. L. and Shanmugam, G. Chemistry and structural biology of DNA damage and biological consequences. *Chem. Biodivers.* **2011,** *8*, 1571-1615.

153. Klaunig, J. E. Wang, Z. and Zhou, S. Oxidative stress and oxidative damage in chemical carcinogenesis. *Toxicol. Appl. Pharmacol.* **2011,** *254*, 86-99.

154. Nakanishi, M., Niida, H., Murakami, H. and Shimada, M. DNA damage responses in skin biology: implications in tumor prevention and aging acceleration. *J. Dermatol. Sci.* **2009,** *56*, 76-81.

155. Gale, J. M., Nissen, K. A., and Smerdon, M. J. UV-induced formation of pyrimidine dimers in nucleosome core DNA is strongly modulated with a period of 10.3 bases. *Proc. Natl. Acad. Sci. U.S.A.* **1987,** *84*, 6644–6648.

156. Pehrson, J. R. Thymine dimer formation as a probe of the path of DNA in and between nucleosomes in intact chromatin. *Proc. Natl. Acad. Sci. U.S.A.* **1989,** *86*, 9149–9153.

157. Pehrson, J. R. Probing the conformation of nucleosome linker DNA *in situ* with

pyrimidine dimer formation. *J. Biol. Chem.* **1995,** *270*, 22440-22444.

158. Pehrson, J. R., and Cohen, L. H. Effects of DNA looping on pyrimidine dimer formation. *Nucleic. Acids Res.* **1992,** *20*, 1321–1324.

159. Becker, M. M., and Wang, Z. Origin of ultraviolet damage in DNA. *J. Mol. Biol.* **1989,** *210*, 429–438.

160. Brown, D. W., Libertini, L. J. Suquet, C., Small, E. W. and Smerdon, M. J. Unfolding of nucleosome cores dramatically changes the distribution of ultraviolet photoproducts in DNA. *Biochemistry.* **1993,** *32*, 10527-10531.

161. Suquet, C., and Smerdon, M. J. UV damage to DNA strongly influences its rotational setting on the histone surface of reconstituted nucleosomes. *J. Biol. Chem.* **1993,** *268*, 23755–23757.

162. Liu, X., Mann, D. B., Suquet, C., Springer, D. L. and Smerdon, M. J. Ultraviolet damdage and nucleosome folding of the 5S ribosomal RNA gene. *Biochemistry.* **2000,** *39*, 557-566.

163. Schieferstein, U. and Thoma, F. Modulation of cyclobutane pyrimidine dimer formation in a positioned nucleosome containing poly (dA.dT) tracts. *Biochemistry.* **1996,** *35*, 7705-7714.

164. Kosmoski, J. V., and Smerdon, M. J. Synthesis and nucleosome structure of DNA containing a UV photoproduct at a specific site. *Biochemistry.* **1999,** *38*, 9485–9494.

165. Kosmoski, J. V., Ackerman, E. J., and Smerdon, M. J. DNA repair of a single UV photoproduct in a designed nucleosome. *Proc. Natl. Acad. Sci. U.S.A.* **2001,** *98*, 10113–10118.

166. Svedruziћ Z. M., Wang, C., Kosmoski, J. V., and Smerdon, M. J. Accommodation and repair of a UV photoproduct in DNA at different rotational settings on the nucleosome surface. *J. Biol. Chem.* **2005,** *280*, 40051–40057; Correction. *J. Biol. Chem.* **2010,** *285*, 39574.

167. Thoma, F. Repair of UV lesions in nucleosomes – intrinsic properties and remodeling. *DNA repair.* **2005,** *4*, 855-869.

168. Smerdon, M. J. and Conconi, A. Modulation of DNA damage and DNA repair in chromatin. *Prog. Nucl. Acid. Res. Mol. Biol.* **1999,** *62*, 227-255.

169. Peterson, C. L. and Cote, J. Cellular machineries for chromosomal DNA repair.

Genes. Dev. **2004,** *18,* 602-616.

170. Tremblay, M., Toussaint, M., D’Amours, A. and Conconi, A. Nucleotide excision repair and photolyase repair of UV photoproducts in nucleosomes: assessing the existence of nucleosome and non-nucleosome rDNA chromatin *in vivo*. *Biochem. Cell. Biol.* **2009,** *87,* 337-346.

171. Morrison A. J. and Shen, X. DNA repair in the context of chromatin. *Cell. Cycle.* **2005,** *4*, 568-571.

172. Osley, M. A., Tsukuda, T. and Nickoloff, J. A. ATP-dependent chromatin remodeling factors and DNA damage repair. *Mutat. Res.* **2007,** *618*, 65-80.

173. Mees, A., Klar, T., Gnau, P., Hennecke, U., Eker, A. P., Carell, T. and Essen, L. O. Crystal structure of a photolyase bound to a CPD-like DNA lesion after *in situ* repair. *Science,* **2004,** *306*, 1789-1793.

174. Carell, T., Burgdorf, L. T., Kundu, L. M. and Cichon, M. The mechanism of action of DNA photolyase. *Curr. Opin. Chem. Biol.* **2001,** *5*, 491-498.

175. Schieferstein, U. and Thoma, F. Site-specific repair of cyclobutane pyrimidine dimers in a positioned nucleosome by photolyase and T4 endonuclease V *in vitro*. *EMBO. J.* **1998,** *17*, 306-316.

176. Gaillard, H., Fitzgerald, D. J., Smith, C. J., Peterson, C. L. and Thoma, F. Chromatin remodeling activities act on UV-damaged nucleosomes and modulate DNA damage accessibility to photolyase. *J. Biol. Chem.* **2003,** *278*, 17655-17663.

177. Suter, B., Livingstone-Zatchej, M. and Thoma. F. Chromatin structure modulates DNA repair by photolyase *in vivo*. *EMBO. J.* **1997,** *16*, 2150-2160.

178. Schul, W., Jans, J., Rijksen, Y. M., Klemann, K. H., Eker, A. P., Dewit, J., Nikaido, O., Nakjima, S. and van der Horst, G. T. Enhanced repair of cyclobutane pyrimidine dimers and improved UV resistance in photolyase transgenic mice. *EMBO. J.* **2002,** *21*, 4719-4729.

179. Suter, B. and Thoma, F. DNA-repair by photolyase reveals dynamic properties of nucleosome positioning *in vivo*. *J. Mol. Biol.* **2002,** *319*, 395-406.

180. Morse, N. R., Meniel, V. and Waters, R. Photoreactivation of UV-induced cyclobutane pyrimidine dimers in the MFA2 gene of *Saccharomyces cerevisiae. Nucl. Acids. Res.* **2002,** *30,* 1799-1807.

181. Hoeijmakers, J. H. Genome maintenance mechanisms for preventing cancer.

Nature. **2001,** *411*, 366-374.

182. Hanawalt, P. C. Subpathways of nucleotide excision repair and their regulation. *Oncogene.* **2002,** *21*, 8949-8956.

183. Nissen, K. A., Lan, S. Y. and Smerdon, M. J. Stability of nucleosome placement in newly repaired regions of DNA. *J. Biol. Chem.* **1986,** *261*, 8585-8588.

184. Jensen, K. A. and Smerdon, M. J. DNA repair within nucleosome cores of UV-irradiated human cells. *Biochemistry*, **1990,** *29*, 4773-4782.

185. Gontijo, A. M., Green, C. M. and Almouzni, G. Repairing DNA damage in chromatin. *Biochimie.* **2003,** *85*, 1133-1147.

186. Gaillard, P. H., Martini, E. M., Kaufman, P. D., Stillman, B. and Almouzni, G. Chromatin assembly coupled to DNA repair: a new role for chromatin assembly factor I. *Cell.* **1996,** *86*, 887-896.

187. Tyler, J. K., Adams, C. R., Chen, S. R., Kobayashi, R. and Kadonaga, J. T. The RCAF complex mediates chromatin assembly during DNA replication and repair. *Nature.* **1999,** *402*, 555-560.

188. Lan, L., Nakajima, S., Kapetanaki, M. G., Hsieh, C. L., Fagerbur, M., Thickman, K,. Leuba, S. H. and Rapic-Otrin, V. Monoubiquitinated histone-H2A destabilizes photolesion-containing nucleosomes with concomitant release of UV-damaged DNA-binding protein E3 ligase. *J. Biol. Chem.* **2012,** *287*, 12036-12049.

189. Wang, Z. G., Wu, X. H., and Friedberg, E. C. Nucleotide excision repair of DNA by human cell extracts is suppressed in reconstituted nucleosomes. *J. Biol. Chem.* **1991,** *266*, 22472–22478.

190. Araki, M., Masutani, C., Maekawa, T., Watanabe, Y., Yamada, A. Sakai, D., Ohkuma, Y. and Hanaoka, F. Reconstitution of damage DNA excision reaction from SV40 minichromosomes with purified nucleotide excision repair proteins. *Mutat. Res.* **2000,** *459*, 147-160.

191. Liu, X., and Smerdon, M. J. Nucleotide excision repair of the 5 S ribosomal RNA gene assembled into a nucleosome. *J. Biol. Chem.* **2000,** *275*, 23729–23735.

192. Ura, K., Araki, M., Saeki, H., Masutani, C., Iwai, S., Mizukoshi, T., Kaneda, Y. and Hanaoka, F. ATP-dependent chromatin remodeling facilitates nucleotide excision repair of UV-induced DNA lesions in synthetic dinucleosomes. *EMBO. J.* **2001,** *20*, 2004-2014.

193. Hara, R., and Sancar, A. Effect of damage type on stimulation of human excision nuclease by SWI/SNF chromatin remodeling factor. *Mol. Cell. Biol.* **2003,** *23,* 4121–4125.

194. Hara, R., and Sancar, A. The SWI/SNF chromatin-remodeling factor stimulates repair by human excision nuclease in the mononucleosome core particle. *Mol. Cell. Biol.* **2002,** *22,* 6779–6787.

195. Fix, D.F. Thermal resistance of UV-mutagenesis to photoreactivation in *E. Coli* B/r uvrA ung: estimate of activation energy and further analysis. *Mol. Gel. Genet.* **1986,** *204*, 452-456.

196. Ruiz-Rubio, M. and Bockrath, R. On the possible role of cytosine deamination in delayed photoreversal mutagenesis targeted at thymine-cytosine dimers in *E. Coli. Mutat. Res.* **1989,** *210*, 93-102.

197. Barak, Y. Cohen-Fix, O. and Livneh, Z. Deamination of cytosine-containing pyrimidine photodimers in UV-irradiated DNA. *J. Biol. Chem.* **1995,** *270,* 24174-24179.

198. Peng, W. and Ramsay, S. B. Accelerated deamination of cytosine residues in UV-induced cyclobutane pyrimidine dimers leads to CC to TT transitions. *Biochemistry.* **1996,** *35*, 10172-10181.

199. Tu, Y., Dammann, R. and Pfeifer, G. P. Sequence and time-dependent deamination of cytosine bases in UVB-induced cyclobutane pyrimidine dimers *in vivo. J. Mol. Biol.* **1998,** *284*, 297-311.

200. Chen, X., Chen, Z., Chen, H., Su, Z., Yang, J., Lin, F., Shi, S. and He, X. Nucleosomes suppress spontaneous mutations base-specifically in eukaryotes. *Science.* **2012,** *335*, 1235-1238.

201. Song, Q., Cannistraro, V. J. and Taylor, J. S. Rotational position of a 5-methylcytosine-containing cyclobutane pyrimidine dimer in a nucleosome greatly affects its deamination rate. *J. Biol. Chem.* **2011,** *286*, 6329-6335.

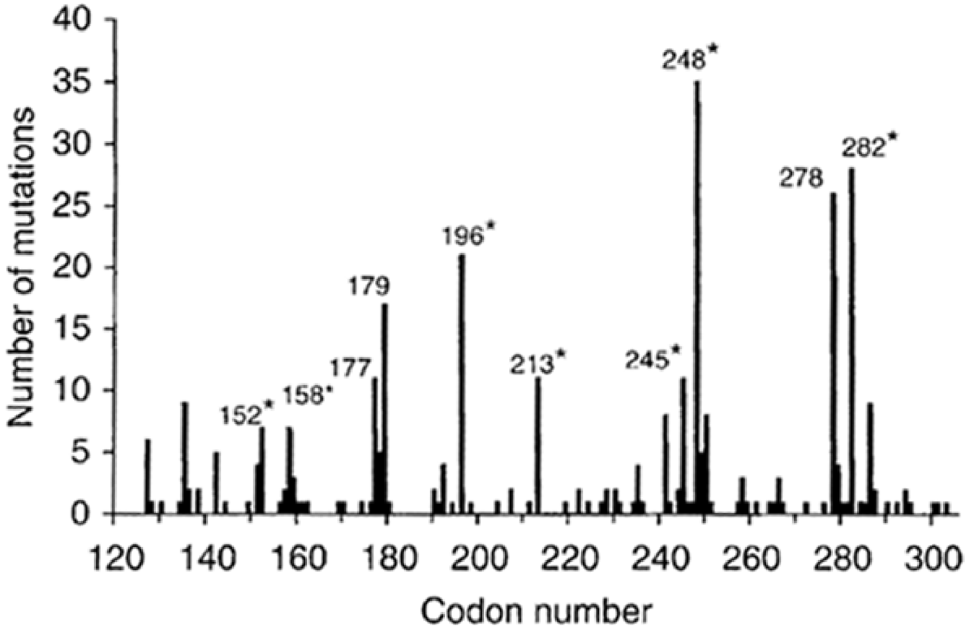

Figure 1.1 Mutation spectrum of the p53 gene in human non-melanoma skin cancers. * Sites that are asterisked correspond to C to T mutations at methylated CpG sites.

* The picture was adapted from Ref. 13 with permission.

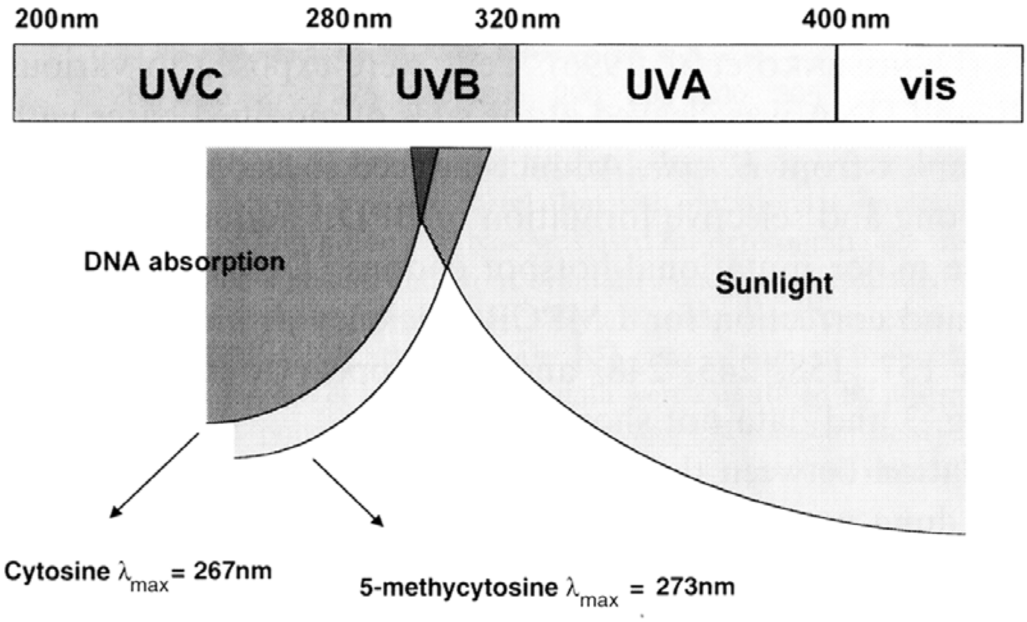

Figure 1.2 Origin of 5-methyl cytosine enhancement of photoproduct formation in UVB light. * Methylation of C causes a red shift in its absorption spectrum which can then better absorb UVB light.

---

* The picture was adapted from Ref. 15 with permission.

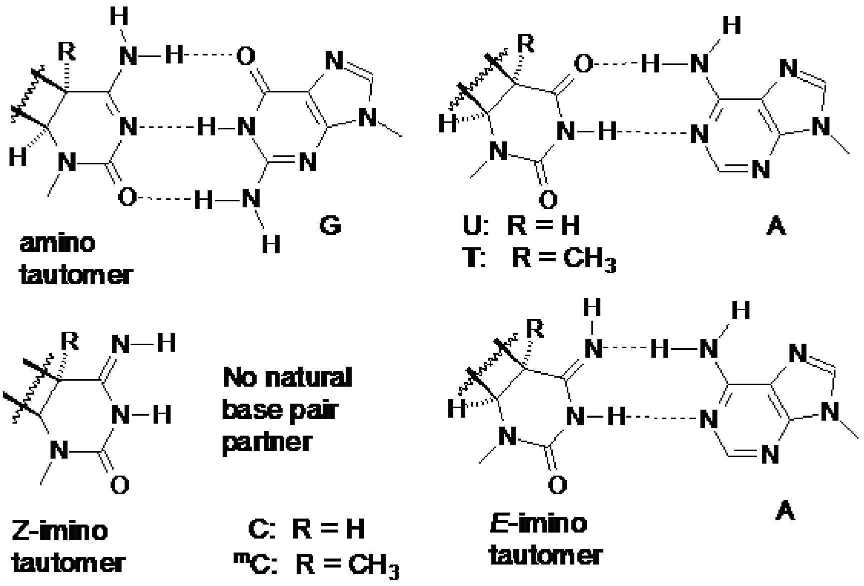

Figure 1.3 Coding properties of tautomers of C-containing CPD relevant to the tautomer-bypass mechanism for C or ^{m}C to T transition mutations.

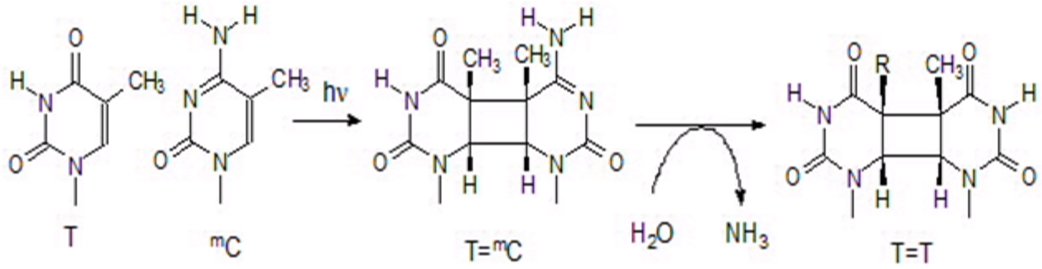

Figure 1.4 Deamination of the C in CPDs relevant to the deamination-bypass mechanism for C or ^{m}C to T transition mutations.

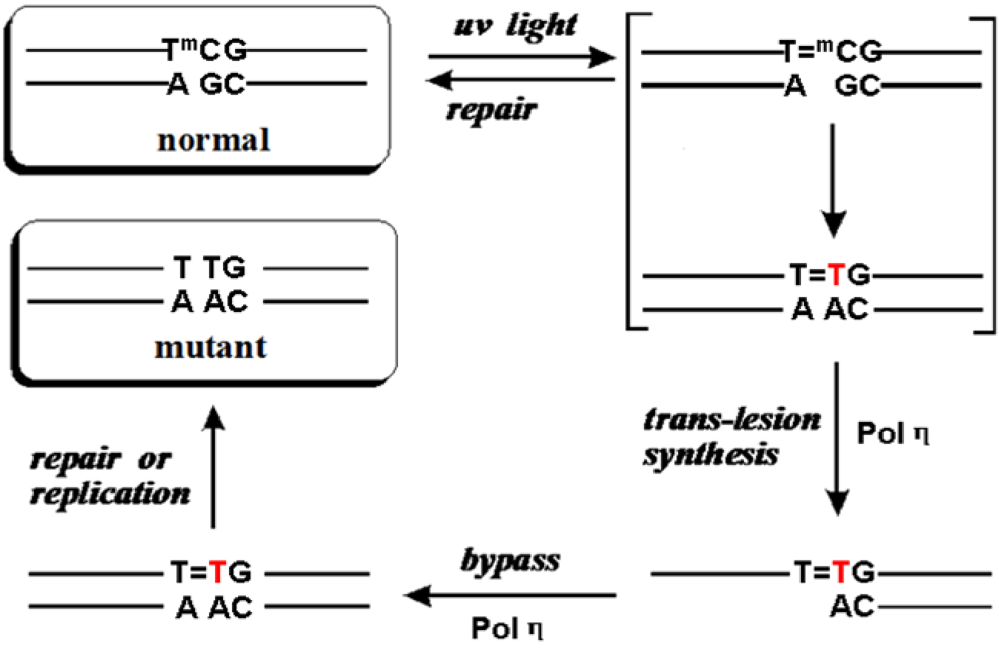

Figure 1.5 Deamination-bypass mechanism for UV-induced ^{m}C to T transition mutations at CpG methylation sites.

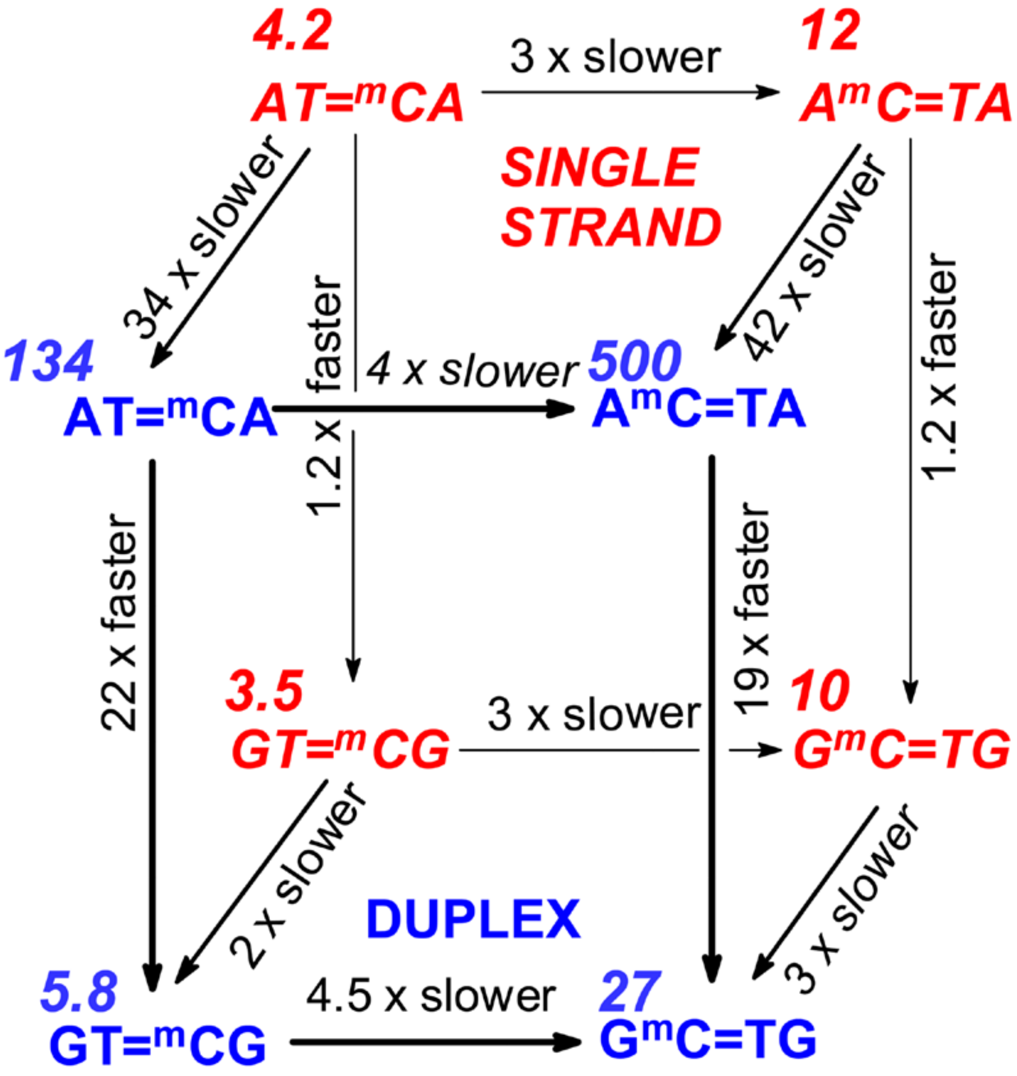

Figure 1.6 Effect of sequence context and duplex formation on deamination rate.* Sequences in italic and red on the back face of the cube refer to the single stranded form. Sequences in bold and blue on the front face of the cube refer to the double stranded form. Numbers in italics are the deamination half lives in hours.

---

* The picture was adapted from Ref. 46 with permission.

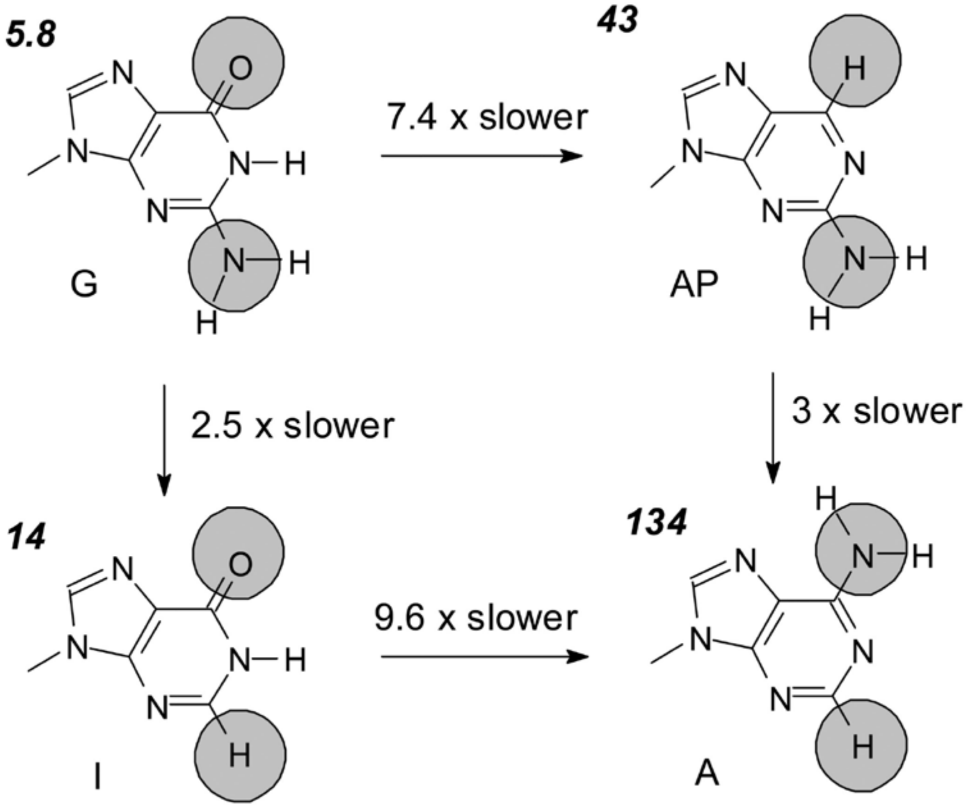

Figure 1.7 Influence of individual functional groups of a 3'-G on the deamination rate of the 3'-C of the dimer in tGT=^{m}CGtc. Values in italics are the half lives in hours at 37°C. *

---

* The picture was adapted from Ref. 46 with permission.

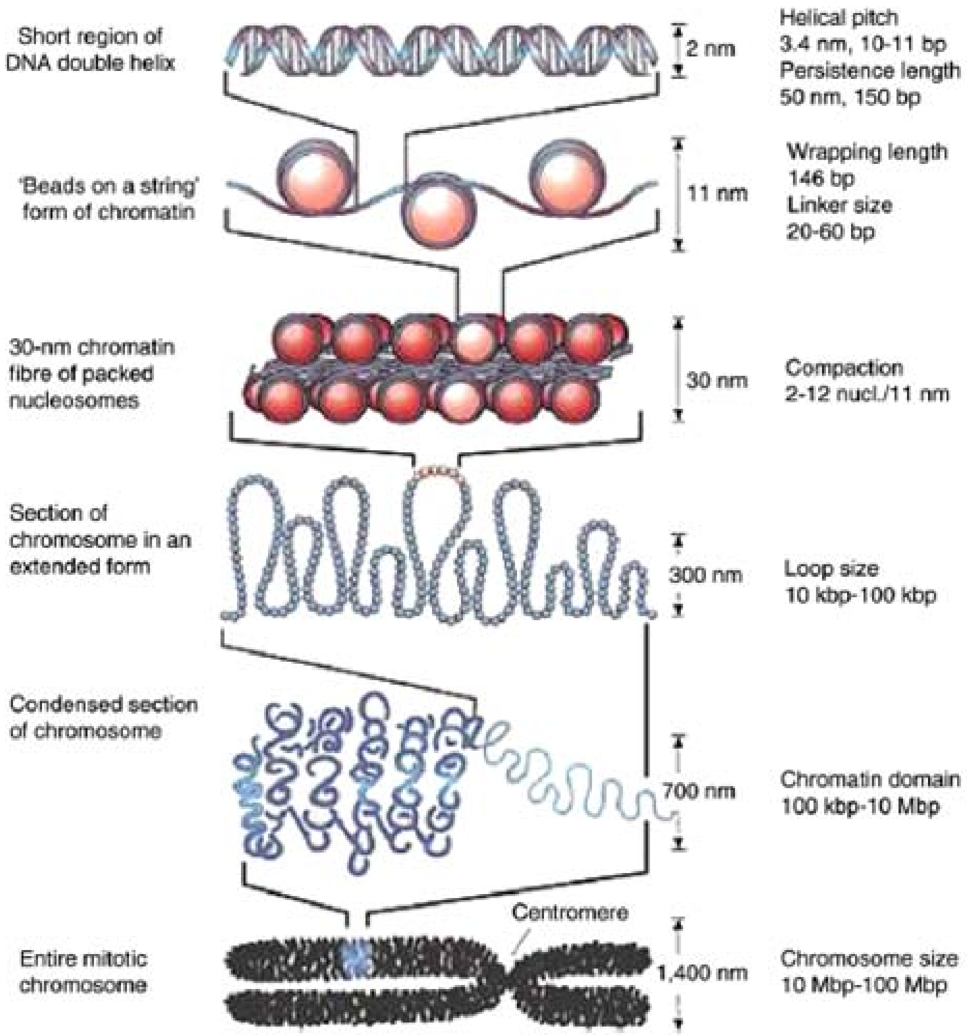

Figure 1.8 Assembly process of DNA in cells to form chromosomes in eukaryotic cells. *

* The picture was adapted from Ref. 55 with permission.

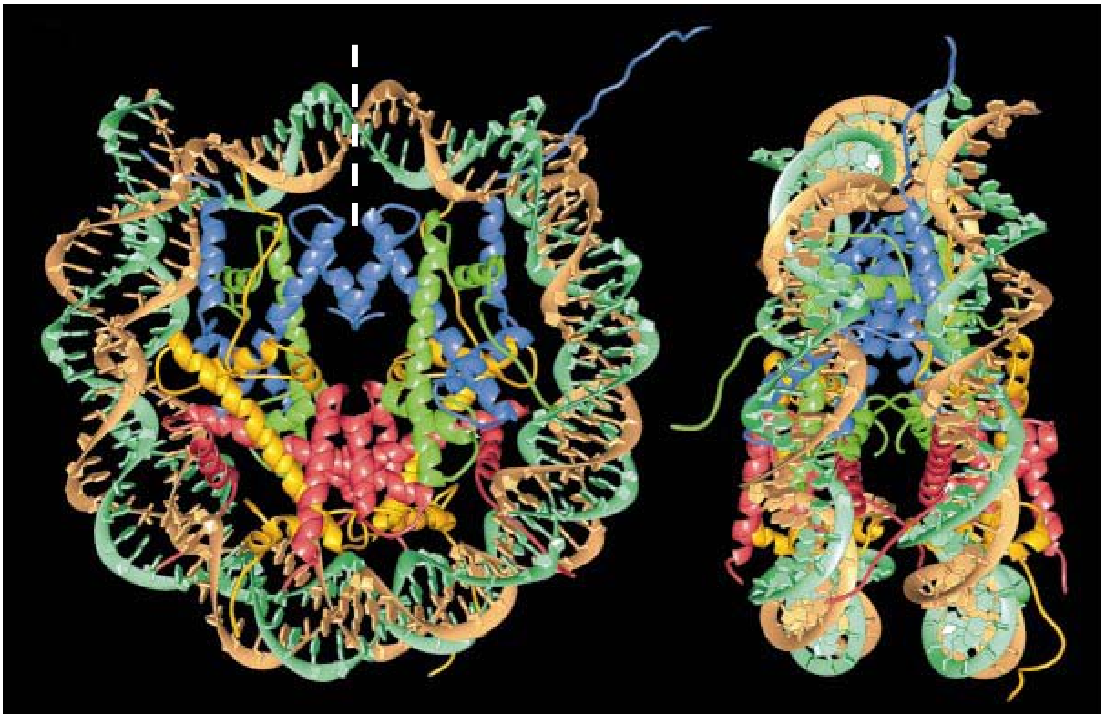

Figure 1.9 Crystal structure of nucleosome core particle. * Nucleosome core particle is shown with the 146-bp DNA phosphodiester backbones in brown and turquoise, and the eight histone protein main chains in blue for H3, green for H4, yellow for H2A and red for H2B. The views are shown down the DNA superhelix axis for the left panel and perpendicular to it for the right panel. For both views, , the pseudo-twofold axis is aligned vertically with the DNA center at the top.

* The picture was adapted from Ref. 52 with permission.

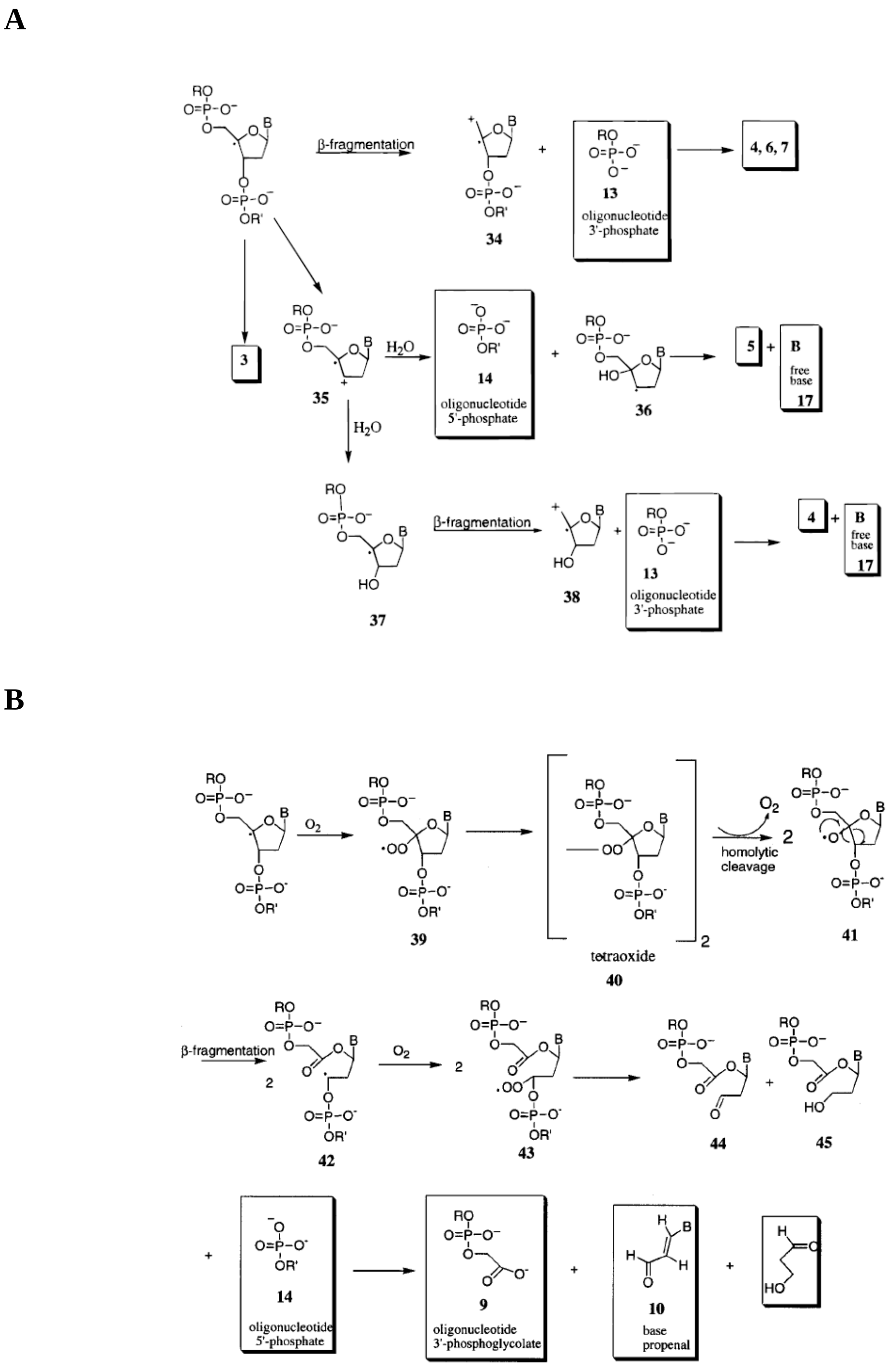

Figure 1.10 Proposed H-4'-abstraction pathway for DNA strand scission by gamma radiolysis. * A, anaerobic conditions. B, aerobic conditions.

* The picture was adapted from Ref. 116 with permission.

A

B

Figure 1.11 Mechanism of hydroxyl radical backbone cleavage of DNA at a normal TT site, and a dimerized site. A, hydroxyl radical attack on H4’ of 3’-T in normal 5’TT3’ sequence. B, hydroxyl radical attack at H4’ of 3’-T in dimerized 5’T=T3’ sequence, showing that the latter backbone cleavage does not lead to strand cleavage.

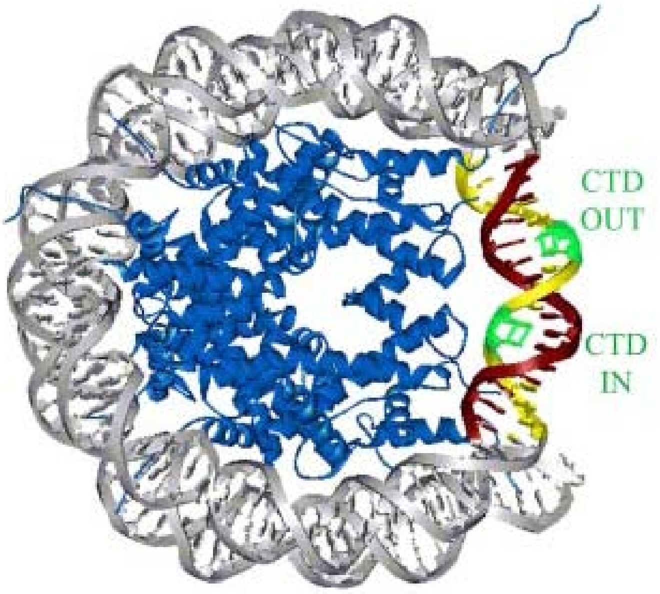

Figure 1.12 Structure of nucleosome core particle containing two T=T CPD DNA photoproducts with different rotational positionings. * Grey color represents the DNA duplex wrapping around the histone octamer surface. Blue color indicates the histone core octamer. Green color highlights the CPDs. IN and OUT refers to position facing against or inside the histone core particle surface and facing away or outside the histone core particle surface, respectively.

* The picture was adapted from Ref. 166 with permission.

Chapter 2

Preparation of A Site-Specific T=^{m}CG *Cis-Syn* Cyclobutane Pyrimidine Dimer-Containing Template and Its Error-Free Bypass by Yeast and Human Polymerase Eta *

---

* The chapter was adapted from Ref. 51 with permission.

Abstract

C-to-T mutations are a hallmark of UV light and, in humans, occur preferentially at methylated Py^{m}CG sites, which are also sites of preferential cyclobutane pyrimidine dimer (CPD) formation. In response, cells have evolved DNA damage bypass polymerases, of which polymerase η (pol η) appears to be specifically adapted to synthesize past *cis-syn* CPDs. Although T=T CPDs are stable, CPDs containing C or 5-methylcytosine (^{m}C) are not and spontaneously deaminate to U or T at pH 7 and 37°C over a period of hours or days, making their preparation and study difficult. Furthermore, there is evidence to suggest that, depending on solvent polarity, a C or an ^{m}C in a CPD can adopt three tautomeric forms, one of which could code as T. Although many *in vitro* studies have established that synthesis past T or U in a CPD by pol η occurs in a highly error-free manner, the only *in vitro* evidence that synthesis past C or ^{m}C in a CPD also occurs in an error-free manner is for an ^{m}C in the 5'-position of an ^{m}C=T CPD. Here in this chapter, we describe the preparation and characterization of an oligodeoxynucleotide containing a CPD of a T^{m}CG site, one of the major sites of C methylation and C-to-T mutations found in the p53 gene of basal and squamous cell cancers. We also demonstrate that both yeast and human pol η synthesize past the 3'-^{m}C CPD in a >99% error-free manner, consistent with the highly water-exposed nature of the active site.

Introduction

One of the primary causes of basal and squamous cell skin cancer is exposure to sunlight. Sequencing of the p53 gene of these skin cancers has revealed a predominance of C-to-T and CC-to-TT mutations at methylated dipyrimidine sites, Py^{m}CG (1, 2). These sites are also hotspots for *cis-syn* cyclobutane pyrimidine dimer (CPD) formation induced by the UV in sunlight (3, 4). Unlike CPDs of TT sites, C- or 5-methylcytosine (^{m}C)-containing CPDs are unstable and deaminate to U or T (5–11). The major responses to UV damage are global genome and transcription-coupled nucleotide excision repair (12–14) and translesion synthesis (15). CPDs do not distort DNA structure or duplex stability greatly (16–18), making them difficult to be detected and repaired by nucleotide excision repair (19). Although they block RNA polymerases and can thus be removed by transcription-coupled repair, this cannot occur for the non-transcribed strand or in either strand of inactive genes. Thus, many CPDs may go unrepaired before replication is initiated, and because they block replicative polymerases, DNA damage bypass polymerases are recruited to carry out translesion synthesis. Of these, polymerase η (pol η) is the most efficient at synthesizing past CPDs and appears to be the principal polymerase involved in CPD translesion synthesis (20–22). Early *in vitro* studies showed that pol η could synthesize past a T=T CPD in an essentially error-free manner, suggesting that the two Ts of the CPD were capable of directing the insertion of As. It was only by investigating DNA synthesis past N^3-methyl derivatives of T=T CPDs that it was possible to demonstrate that both the 5'- and

3'-Ts of the CPD were directing the insertion of As and that the As were not being inserted by a non-templated mechanism, otherwise known as the "A rule" (23). Furthermore, studies with 7-deaza-ATP demonstrated that a Watson-Crick like intermediate was being used to direct the insertion of the A, and not a Hoogsteen-type base pair as found in the crystal structure of another Y-family polymerase (24). These conclusions were later confirmed through x-ray crystallography of intermediates in the synthesis past a T=T CPD by human pol η (25).

Unlike T in native DNA or in a CPD, which is known to preferentially adopt a keto tautomer and base pair with A, a C or an ^{m}C in a CPD could, in principal, adopt amino and/or imino tautomeric forms with *E*- or *Z*-stereochemisty (the imino hydrogen is *trans* or *cis* with respect to N3), some of which could thereby direct the insertion of G and/or A (Figure 2.1) (26, 27). The possibility that C or ^{m}C could exist in an imino tautomeric form comes from early work demonstrating that dihydrocytosine adopts the amino tautomeric form in water but an imino tautomeric form in the much less polar solvent chloroform (28). Gas phase theoretical calculations have reproduced the preference for the imino tautomeric form in non-polar environments (29, 30) but failed to reproduce the preference for the amino form in water (30). The same type of calculations also predicted that the Cs in CPD should exist almost exclusively in the imino tautomeric state in water (27). However, evidence that Cs in CPDs exist in their amino tautomeric state comes from them highly preferential insertion of G opposite the Cs by pol η from various genetic experiments in yeast and human cells (31, 32) and from an *in vitro* translesion experiment with an ^{m}C=T CPD-containing template and yeast pol η (33). No work has yet been carried out on a site-specific CPD of an ^{m}CG site. Because we have previously observed that the deamination rate of an ^{m}C in a CPD is 3–4 times slower for Pu^{m}CTPu than for PuT^{m}CPu (where Pu = A or G) and depends on flanking sequence (34), it was possible that the relative proportion of tautomers may likewise depend on position and flanking sequence.

Part of the difficulty in working with C- or ^{m}C-containing CPDs *in vitro* or *in vivo* is their spontaneous deamination to U or T within hours to days (34) compared with ~ 50,000 years for canonical C or ^{m}C in duplex DNA (35, 36). This lability has also impeded the development of a phosphoramidite building block for site-specific incorporation of C-containing CPDs into DNA templates by automated synthesis. At the moment, the only route to such templates involves UV irradiation of an oligodeoxynucleotide (ODN) followed by HPLC purification, as was originally developed for the preparation of a T=C CPD-containing 11-mer (37).We used this approach to prepare a 14-mer containing the CPD of an ^{m}CTA site (33). An ^{m}CTA site was chosen for our initial studies because the CPD was found to have a much lower deamination rate and to be produced in a higher yield than at the more biologically relevant T^{m}CG site (34). Herein, we report the preparation and characterization of a CPD of a T^{m}CGsite, a known hotspot for C methylation, CPD formation, and UV light-induced C-to-T mutations, and demonstrate the highly error-free, non-mutagenic insertion of G opposite the ^{m}C in the CPD by yeast and human pol η. We also report the deamination rate of the ^{m}C in the CPD and confirm the error-free but mutagenic insertion of A opposite the resulting T.

Experimental Procedures

Enzymes, Substrates, and Equipment

T4 polynucleotide kinase was purchased from New England Biolabs, [γ-^{32}P]ATP from Amersham Biosciences, and dNTPs from Invitrogen. The catalytic core of yeast pol η with an N-terminal His$_6$ tag was prepared as described previously (38). Full-length human pol η with a C-terminal His$_6$ tag was also prepared as described previously (39). The ^{m}C-containing template ODN and primer ODNs were synthesized by Integrated DNA Technologies, Inc. Mass spectrometry was carried out on an LCQ Classic ion trap mass spectrometer (Thermo Finnigan, San Jose, CA).

Preparation and Deamination of cis-syn T=^{m}C CPD-containing 14-mer DNA Template

100 µg of T^{m}C 14-mer in 200 µl of 20mM Tris (pH 8.8) on a piece of Saran Wrap was irradiated for 1 h on top of a 302-nm transilluminator (~1.9 milliwatts/ cm^2) at 4°C in a cold room. HPLC purification was carried out with 50mM triethylamine acetate at pH 8.5 to minimize deamination to yield ~ 5.2 µg of the *cis-syn* dimer eluting in 1 mL of ~ 10% acetonitrile. This sample was immediately stored at -80°C prior to use. A sample was also completely deaminated by adjusting the pH of the T=^{m}C 14-mer sample to pH 6.5 by adding 0.5M Mes buffer and heated overnight at 67°C.

DNA Photoproduct Identification and Characterization by HPLC and Mass Spectrometry

The fractions corresponding to the major photoproduct peaks from the HPLC of the T^{m}C 14-mer irradiation mixture, with and without heating, were analyzed by an enzyme-coupled mass spectrometry assay. In a typical assay, 1µL of a 1 unit/µL aqueous solution of nuclease P1 was added to a 10-µL aliquot of the ODN sample, incubated at room temperature for 3 min, cooled on ice, and immediately analyzed by electrospray ionization coupled to MS/MS. MS/MS data were acquired on the selected [M - H] ions. To select both the deaminated and undeaminated components for fragmentation, the mass width for precursor selection was set at 5–6 *m*/*z* units.

Single-hit Competitive Nucleotide Insertion Assay

In a cold room (4°C), a 5-µL aliquot of the T=^{m}C 14-mer template (120nM) was added to 5 µL of 40nM 5'-^{32}P end-labeled primer, 20mM Tris-HCl (pH 7.5), and 10mM DTT, and allowed to anneal for 10 min before the addition of pol η (500nM). Each sample was incubated for an additional 7 min before initiating single-hit synthesis by the addition of 30 µL of all dNTPs (200µM each) containing 10mM $MgCl_2$, 10mM Tris-HCl (pH 7.5), and 10mg/mL sonicated/denatured salmon sperm DNA as a polymerase trap. The synthesis reaction was quenched after 10 s by the addition of 80 µL of formamide containing 0.1% xylene cyanol, 0.2% SDS, 25mM EDTA, and 1 µg of unlabeled primer (stop mixture). The samples were then heated at 100°C for 10 min before loading onto a 10% polyacrylamide gel (40 cm×0.8mm) containing 25mM citrate (pH 3.5), which was the same as the reservoir buffer. The gel was polymerized by adding 1.3 mL of ferrous sulfate (250 mg/100 mL), 1.3 mL of 10% ascorbate, and 300µL of 3% hydrogen peroxide. The gel was run at

2000Vuntil the xylene cyanol dye marker reached 25 cm (~ 3 h). For biased pool experiments, the dNTP of interest was held at 100μM while the dGTP concentration was varied as indicated.

Multiple-hit Competitive Nucleotide Insertion Assays

In a cold room (4°C), primer-templates were prepared by annealing 20nM primer with 60nM template, to which 200μM of each dNTP, 10mM $MgCl_2$, 5mM DTT, 10mMTris-HCl (pH 7.5), and 500nM pol η were added. After 2 min, a 10-μL aliquot was removed and added to a tube containing 300 μg of sonicated and denatured salmon sperm DNA before quenching the reaction with 80μL of stop mixture. Aliquots from extension times that yielded almost exclusively full-length product were then assayed by electrophoresis on a 20% polyacrylamide gel containing 25mM citrate (pH 3.5).

Deamination Rates by Nucleotide Insertion Assay

The T=^{m}C 14-mer template (120nM) was adjusted to pH 7.5 with Mes buffer (0.5M) and incubated at 37 or 50°C. Aliquots (5 μL) were removed at various times and quickly frozen on dry ice before storing overnight at -80°C. All subsequent steps were performed in a cold room (4°C). To each of the 5-μL aliquots was added 5μL of 40nM 5'-^{32}P end-labeled primer, 1mM of each dNTP, 20mM Tris-HCl (pH 7.5), and 10mM DTT, followed by annealing for 10 min before the addition of yeast pol η (500nM). Each sample was incubated for an additional 5 min to complete multiple-hit synthesis, after which 300μg of sonicated and denatured salmon sperm DNA was added before quenching the reaction with 80μL of stop mixture. The samples were then heated at 95°C for 10 min before loading onto a 25% polyacrylamide gel (40 cm ×0.8 mm) containing 25mM citrate (pH 3.5), which was the same as the reservoir buffer, and the gel was run at 2000Vuntil the xylene cyanol dye marker reached 18 cm (~ 4 h). The gel had been polymerized by adding 1.3 ml of ferrous sulfate (250 mg/100 mL), 1.3 mL of 10% ascorbate, and 300μL of 3% hydrogen peroxide.

Analysis of Deamination Rate Data

The deamination rate constant was obtained from the slope of a nonlinear least squares fit of the natural log of the fraction of dGMP inserted, G/(G + A), *versus* time to $\ln(G/(G + A))_0{}^{-k*t}$ where $(G/(G + A))_0$ equals the fraction of dGMP inserted at time 0.

Results

Template Design

Because there is still no phosphoramidite building block available for incorporating a T=^{m}C CPD into an ODN, we resorted to preparing the T=^{m}C CPD-containing template by UV irradiation of an ODN. On the basis of prior experience with the preparation of an ^{m}C=TA CPD-containing 14-mer (33), we designed the T^{m}C-14-mer (Table 2.1 and Figure 2.2). This sequence is devoid of other dipyrimidine sites, so the T=^{m}C CPD-containing product could be cleanly separated from other photoproducts of the T^{m}C site and unreacted ODN by reverse phase HPLC. The sequence was long enough, however, to accommodate a 10-mer for primer extension reactions by positioning the T^{m}C site toward the 5’-end. However, the exact sequence was modified from what was used before to accommodate the

T^{m}CG sequence and to optimize separation of the expected primer extension products by citrate-PAGE according to which nucleotides were inserted opposite the CPD by pol *η* (Figure 2.2).

Preparation and Characterization of CPD-containing 14-mer Templates

The T^{m}C-14-mer was irradiated with 302 nm light at 4°C at pH 8.5 to suppress deamination for 1 h, after which half of the sample was allowed to completely deaminate by heating at 67°C for 3 h at pH 6.5. The reaction mixtures were then subjected to reverse phase HPLC to separate the different photoproducts from the starting T^{m}C-14-mer. The fractions collected by HPLC were immediately cooled on dry ice to suppress deamination prior to further analysis and use. The desired *cis*-*syn* CPD-containing product, T[*c*,*s*]^{m}C-14-mer, was initially identified by its conversion to its deamination product, T[*c*,*s*]T-14-mer, which eluted with a longer retention time. Thus, UV irradiation of the T^{m}C-14-mer resulted in one major product peak with a retention time of 30.5 min (Figure 2.3), which shifted to a peak with a retention time of 33.2 min after heating to effect deamination (Figure 2.4). To further confirm the assignment of the T=^{m}C-14-mer as the *cis*-*syn* cyclobutane dimer, we analyzed the sample by nuclease P1-coupled electrospray ionization-MS. Nuclease P1 digests CPD-containing DNA to mononucleotides and a CPD containing trinucleotide, pPy=PyN, which results in a major fragment, pPy=Pyab, corresponding to loss of the base from the 3’-nucleotide to yield an abasic site (ab) (40). MS/MS of the nuclease P1 digestion products of the HPLC fraction that eluted at 30.5 min showed an ion at *m*/*z* 953.4, corresponding to a pT=^{m}CG photoproduct, which fragmented to a major ion at *m*/*z* 802 (Figure 2.5), corresponding to pT[*c*,*s*]^{m}Cab. MS/MS of the digestion products of the fraction eluting at 33.2 min showed an ion at *m*/*z* 954.3, corresponding to pT=TG, which fragmented to an ion at *m*/*z* 803, corresponding to pT[*c*,*s*]Tab (Figure 2.6).

Single-hit Competitive Nucleotide Insertion Assay Opposite CPDs by pol η

To determine the extent to which the ^{m}C in the T=^{m}C CPD codes as C or T, we first carried out a single-hit competition assay with dATP and dGTP. In this assay, yeast pol *η* was first incubated with the 9-mer primer-T*X* 14-mer templates and then added to a solution containing equimolar dATP and dGTP and a large excess of sonicated and denatured salmon sperm DNA to trap the polymerase once it dissociated from the primer-template. To resolve the products of insertion, we used of a 25mM citrate gel (pH 3.5), which can easily separate products according to their nucleotide composition as evidenced from the independently synthesized standards in Figure 2.7. Primer extension under these single-hit conditions yielded primarily the products in which the primer was extended by two nucleotides, corresponding to the almost exclusive extension by G followed by A for the native and CPD-containing T^{m}C templates and to extension by AA for the TT templates.

Multiple-hit Competitive Nucleotide Insertion Assay Opposite CPDs

We also examined insertion opposite the ^{m}C site in the T=^{m}C CPD using a multiple-hit competition assay in which the full-length translesion synthesis products could also be separated according to nucleotide composition on a low pH citrate gel. In this assay, primer extension was carried out by both yeast and human pol *η* on the

T=^{m}C-14-mer template in the presence of equal amounts of all dNTPs. The primer extension products were then electrophoresed on a 20% Tris/borate/EDTA - polyacrylamide gel to identify the full-length synthesis products in comparison with authentic 14-mer standards AA-14-mer and GA-14-mer, corresponding to insertion of dAMP or dGMP opposite the ^{m}C site, respectively. We found that both yeast and human pol η were able to fully extend the primer to the end of the T=^{m}C and T=T-14-mer templates and that the full-length products had the same mobility on a denaturing polyacrylamide gel as the primer extension products opposite the undimerized T^{m}C and TT-14-mer templates and both the GA-14-mer and AA-14-mer standards (Figure 2.8). To determine the nucleotide insertion selectivity opposite the dipyrimidine sites, we used a 20% citrate-polyacrylamide gel to separate the full-length 14-mer synthesis products according to sequence composition (Figure 2.9). As shown, the full-length synthesis products from both yeast and human pol η opposite the T=^{m}C-14-mer were found to have the same gel mobility as those opposite the undimerized T^{m}C-14-mer, as well as an authentic 14-mer ODN containing G (Figure 2.9, *lanes 1–3*), indicating the preferential insertion of G opposite the ^{m}C of the CPD. Conversely, the full-length synthesis product opposite the completely deaminated T=^{m}C-14-mer had the same mobility as that opposite the undimerized TT template and the authentic 14-mer product containing A (Figure 2.9, *lanes 1*, *2*, and *5*). These results demonstrate that the T=^{m}C-14-mer template did not undergo any detectable deamination during its purification and subsequent handling, which would have resulted in the production of an A-containing 14-mer bypass product.

Selectivity of Nucleotide Insertion Opposite T=^{m}CG CPD

To determine the selectivity of nucleotide insertion opposite the ^{m}C of the dimer in comparison with undamaged DNA, we carried out the single-hit primer extension experiment in the presence of a biased nucleotide pool in which the indicated nucleotide was present in a 32-fold excess over dGTP (Figure 2.10). As shown, the 9-mer primer was extended only by G opposite both T^{m}C and T=^{m}C by both yeast and human pol η, even in the presence of 32-fold excess dCTP or dTTP. Extension of the primer by C or T would have produced bands moving slower than the 9-mer and faster than 9G, respectively (33), which was not observed. On the other hand, in the presence of 32-fold excess dATP, a small amount of a band corresponding to extension by AA opposite T=^{m}C was observed in addition to extension by GA. This band was not observed for the undamaged T^{m}C site, suggesting that insertion opposite the ^{m}C in a dimer proceeds with a lower fidelity of insertion than that opposite an undamaged ^{m}C. To more accurately determine the selectivity of nucleotide insertion, primer extension was carried out with different ratios of dATP to dGTP (Figure 2.11). The selectivity of an A insertion relative to G could then be determined accurately from the slope of a linear fit of the ratio of the primer extension product incorporating A compared with G *versus* the ratio of the concentrations of dATP *versus* dGTP. Both yeast and human pol η showed similar selectivities for A *versus* G insertion of 6.6×10^{-3} and 6.1×10^{-3}, respectively, corresponding to G *versus* A selectivities of 152 ± 7 and 165 ± 6. The non-zero intercepts of 0.012 ± 0.008 and 0.007 ± 0.006 for yeast and human pol η suggest the presence of ~ 1% of the deaminated T=^{m}C CPD and/or the *E*-imino tautomer (Selectivity data are the average of those calculated from linear least squares fits to three independent sets, with the error shown derived from propagation of the standard deviations for each fit.).

Deamination Kinetics of T=^{m}C CPD

The ability of pol η to faithfully insert A opposite T and G opposite ^{m}C in a CPD was then used to study the deamination kinetics of the T=^{m}C CPD at two temperatures. The fraction of ^{m}C remaining in the CPD as a function time was determined by monitoring the fraction of G inserted opposite the ^{m}C by pol η in the full-length primer extension reaction (Figure 2.12). The rate constants were then determined from the slope of linear fits of the data to a first-order rate process (Figure 2.13). In this way, the deamination rate constants were determined to be 0.0014 min^{-1} at 37°C and 0.0054 min^{-1} at 50°C, corresponding to deamination half-lives of 8.25 and 2.1 h, respectively.

Discussion

In this chapter, we have demonstrated that DNA synthesis by both yeast and human polymerase η opposite an ^{m}C in a *cis-syn* CPD of a T^{m}CG site proceeds in a >99% error-free and hence non-mutagenic manner. Our original expectation was that the ^{m}C might also exist in an imino tautomeric form based on an early study showing that 5,6-dihydrocytosine could exist in either an amino or imino tautomeric form depending on the solvent (28). In the relatively non-polar solvent chloroform, dihydrocytosine was found to exist primarily in an imino tautomeric form (*E* and/or *Z*), whereas in water, it was found to exist primarily in the amino tautomeric form. If a polymerase were to surround the nascent base pair involving C or ^{m}C of a CPD and exclude water, as it does for a representative replicative polymerase, yeast pol δ (Figure 2.14, A) (41), one might expect an increased preference for an imino tautomer.

The observation of only a dGMP insertion opposite the ^{m}C of the T^{m}C CPD by either yeast or human pol *η* in the presence of equal concentrations of all four dNTPs indicates that the ^{m}C is not adopting a significant amount of the *E*-imino tautomer form, which would have templated the insertion of dAMP (Figure 2.1). An upper limit to the amount of the *E*-imino tautomer comes from the non-zero intercept of ~ 1% observed in the plots of dAMP *versus* dGMP insertion as a function of [dATP]/ [dGTP], which could also more likely be attributed to the presence of the deaminated T=^{m}C CPD. We do not have any direct way of knowing whether or not any of the *Z*-imino tautomer is present, as it is not Watson-Crick complementary to any of the canonical DNA bases. If it is present, it is either very poor at directing nucleotide insertion or directs the insertion of only G. Results from the single-hit primer extension experiments (Figure 2.7) did not show any premature dissociation from the template compared with the undamaged template that would be indicative of significant impediment to nucleotide insertion. If the *Z*-imino isomer were directing insertion of G, it would likely be occurring via the equivalent of a G· T wobble base pair. Both insertion and extension of a G opposite the 3’-T of a T=T CPD by yeast pol η are known, however, to be much less efficient than for a Watson-Crick base-paired A (42, 43). Thus, the comparably efficient extension opposite the 3’-^{m}C in the dimer and the undamaged template observed in the single-hit primer extension reaction suggest that insertion is occurring largely if not exclusively via the amino tautomer in the CPD.

The selectivity of dGMP insertion relative to dAMP by yeast and human pol *η* opposite the ^{m}C of the T=^{m}C CPD is less, however, than that opposite an undamaged ^{m}C, as shown in Figure 2.10 , in which 32-fold excess of dATP over dGTP was used. In Figure 2.10, a band for dAMP insertion opposite the ^{m}C in the dimer is clearly seen, whereas it is not seen for undamaged ^{m}C. This is consistent with experiments that determined that the selectivity for dGMP insertion relative to dAMP opposite a C in undamaged DNA was 960 for the same yeast pol η used in these experiments (44) and 909 for human pol *η* (45) compared with 152 and 165, respectively, which we observed for insertion opposite the ^{m}C in the T=^{m}C CPD. The lower fidelity may have to do with the greater ability of an ^{m}C in a CPD to adopt the *E*-imino tautomer compared with an undamaged mC due to the loss of aromatic stabilization of the amino tautomer (27, 29, 30). Interestingly, we had observed a selectivity of only 120 for insertion opposite the ^{m}C in a ^{m}C=T CPD (33), suggesting that the 5’-^{m}C may be more prone to tautomerization or that insertion opposite the amino tautomer is less specific opposite the 5’-^{m}C of a CPD.

The almost exclusive presence of the amino tautomeric form of the ^{m}C in the CPD during nucleotide insertion suggests that it is in a polar and/or aqueous environment (28), which is in accord with a recent crystal structure of a ternary complex of human pol η with dATP opposite the 3'-T of a T=T CPD (25). In this structure, the O4 carbonyl of the 3'-T of the T=T CPD, corresponding to the position of the N4 of the 3'-C of a Py=^{m}C CPD, is completely exposed to water during insertion of dATP (Figure 2.14, B). Likewise, the O4 carbonyl of the 5'-T of the CPD, corresponding to the 5'-^{m}C of a ^{m}C=Py CPD, is also highly exposed to water during dATP insertion (Figure 2.14, C). The 5'-^{m}C of a ^{m}C=T CPD would therefore also be expected to adopt the amino tautomeric form, in accord with our previous study showing that only dGMP is inserted opposite this ^{m}C in the presence of a equal concentration of A (33). These results suggest that pol η may have evolved to bypass CPDs in an error-free manner by increasing the exposure of the N4 of a C or an ^{m}C in either or both of the 3'- and 5'-sites of a *cis-syn* CPD to maximize the amount of the amino tautomer.

The active site of pol η also had to evolve to accommodate the 5'-pyrimidine of the CPD when the 3'-pyrimidine of the CPD is in the templating position, otherwise the 3'-pyrimidine could not template insertion of the complementary nucleotide. Replicative polymerases achieve high selectivity for canonical bases in part by extensive contacts with the 5'-face of the templating nucleotide (Figure 2.14, A), which would prevent the CPD from entering the active site when insertion opposite the 3'-pyrimidine of the CPD is to take place. As a result, the polymerase would become arrested at a CPD, which would allow for the recruitment of DNA damage bypass polymerases. It has been shown, however, that in the absence of other polymerases, the replicative T7 DNA polymerase will preferentially insert A opposite the 3'-pyrimidine of all types of dipyrimidine photoproducts, irrespective of their base pairing properties, by a non-template mechanism (46-48). If non-template insertion were to occur opposite the 3'-C or ^{m}C of a CPD, a C-to-T mutation would result and may represent an alternate pathway for UV light-induced C-to-T mutations. Thus, the T=^{m}C CPD could serve as a useful probe for determining if a polymerase synthesizes past CPDs by a template or non-template mechanism.

Although bypass of a C- or an ^{m}C-containing CPD by pol η occurs in an error-free and hence non-mutagenic manner, once the C or ^{m}C in a CPD deaminates, error-free insertion by pol η opposite the resulting U or T leads to a mutation. Thus, the mutagenicity of pol η bypass of a CPD will depend on the presence and deamination rate of a C or an ^{m}C within the dimer, which we have recently shown to be highly dependent on sequence (34), protein binding (49), and nucleosome position (50). As we have shown herein, the T^{m}C CPD in a single-strand AT^{m}CG sequence context deaminates with a half-life of 7.1 h at 37 °C, which is not much different from what we previously found for a CPD with the same flanking sequence in duplex DNA at low salt concentration (7.7 h) (34). On the other hand, the methyl-CpG-binding protein MeCP2 was found to completely suppress deamination of a T=^{m}CG CPD (49) and hence the mutagenic potential of the CPD if bypassed by pol η. In a nucleosome core particle, the deamination rate of a T=^{m}CG CPD whose backbone faced away from the histone surface was accelerated by a factor of 9, whereas one whose backbone faced toward the surface was retarded by ~ 5-fold (50).

Thus, as long as pol η synthesizes past a C/^{m}C-containing CPD prior to deamination, the bypass event will be non-mutagenic, but as soon as the CPD deaminates, the bypass will be mutagenic. Therefore, although pol η synthesizes past CPDs in an error-free manner, in the sense of faithfully inserting nucleotides that are complementary to the pyrimidines present in the CPD, if a U or T arises from deamination of a C or an ^{m}C, trans-lesion synthesis will be mutagenic and can explain the origin of UV light-induced C-to-T mutations.

Conclusions

We prepared and characterized an 14-mer DNA oligodeoxynucleotide containing a T=^{m}C CPD at a T^{m}CG site, which is one of the major sites of C methylation and C-to-T mutations found in the p53 gene of basal and squamous cell cancers. We demonstrated that both yeast and human pol η could synthesize past the 3'-^{m}C in the T=^{m}C CPD in a >99% error-free manner, consistent with the highly water-exposed nature of the active site. We also report the deamination rate of the ^{m}C in the T=^{m}C CPD at T^{m}CG site and confirm the error-free bypass at the dimer site but mutagenic insertion of A opposite the resulting T.

Acknowledgment

We thank Dr. Dian Su for acquiring the mass spectral data.

References

1. Brash, D. E., Rudolph, J. A., Simon, J. A., Lin, A., McKenna, G. J., Baden, H. P., Halperin, A. J., and Pontén, J. A role for sunlight in skin cancer: UV-induced p53 mutations in squamous cell carcinoma. *Proc. Natl. Acad. Sci. U.S.A.* **1991,** *88*, 10124–10128.

2. Ziegler, A., Leffell, D. J., Kunala, S., Sharma, H. W., Gailani, M., Simon, J. A., Halperin, A. J., Baden, H. P., Shapiro, P. E., and Bale, A. E. Mutation hotspots due to sunlight in the p53 gene of non-melanoma skin cancers. *Proc. Natl. Acad. Sci. U.S.A.* **1993**, *90*, 4216–4220.

3. You, Y. H., Li, C., and Pfeifer, G. P. Involvement of 5-methylcytosine in sunlight-induced mutagenesis. *J. Mol. Biol.* **1999,** *293*, 493–5034.

4. You, Y. H., Szabó, P. E., and Pfeifer, G. P. Cyclobutane pyrimidine dimers form preferentially at the major p53 mutational hotspot in UVB induced mouse skin tumors. *Carcinogenesis.* **2000,** *21*, 2113–2117.

5. Setlow, R. B., Carrier, W. L., and Bollum, F. J. (1965) Pyrimidine dimers in UV-irradiated poly dI:dC. *Proc. Natl. Acad. Sci. U.S.A.* 53, 1111–1118.

6. Liu, F. T., and Yang, N. C. Photochemistry of cytosine derivatives. 1. Photochemistry of thymidylyl-(3’ → 5’)-deoxycytidine. *Biochemistry.* **1978,** *17*, 4865–4876.

7. Fix, D., and Bockrath, R. Thermal resistance to photoreactivation of specific mutations potentiated in *E. coli* B/r ung by ultraviolet light. *Mol. Gen. Genet.* **1981,** *182*, 7–11.

8. Lemaire, D. G., and Ruzsicska, B. P. Kinetic analysis of the deamination reactions of cyclobutane dimers of thymidylyl-3’,5’-2’-deoxycytidine and 2’-deoxycytidylyl-3’,5’-thymidine. *Biochemistry.* **1993,** *32*, 2525–2533.

9. Barak, Y., Cohen-Fix, O., and Livneh, Z. Deamination of cytosine containing pyrimidine photodimers in UV-irradiated DNA. Significance for UV light mutagenesis. *J. Biol. Chem.* **1995,** *270*, 24174–24179.

10. Peng, W., and Shaw, B. R. Accelerated deamination of cytosine residues in UV-induced cyclobutane pyrimidine dimers leads to CC → TT transitions. *Biochemistry.* **1996,** *35*, 10172–10181.

11. Tu, Y., Dammann, R., and Pfeifer, G. P. Sequence- and time-dependent deamination of cytosine bases in UVB-induced cyclobutane pyrimidine dimers *in vivo*. *J. Mol. Biol.* **1998,** *284*, 297–311.

12. Nouspikel, T. DNA repair in mammalian cells: nucleotide excision repair: variations on versatility. *Cell. Mol. Life Sci.* **2009,** *66,* 994–1009.

13. Tornaletti, S. DNA repair in mammalian cells: transcription-coupled DNA repair: directing your effort where it's most needed. *Cell. Mol. Life Sci.* **2009,** *66,* 1010–1020.

14. Lagerwerf, S., Vrouwe, M. G., Overmeer, R. M., Fousteri, M. I., and Mullenders, L. H. DNA damage response and transcription. *DNA Repair Repair.* **2011,** *10,* 743–750.

15. Waters, L. S., Minesinger, B. K., Wiltrout, M. E., D'Souza, S., Woodruff, R. V., and Walker, G. C. Eukaryotic translesion polymerases and their roles and regulation in DNA damage tolerance. *Microbiol. Mol. Biol. Rev.* **2009,** *73*, 134–154.

16. Wang, C. I., and Taylor, J. S. Site-specific effect of thymine dimer formation on $dA_n \cdot dT_n$ tract bending and its biological implications. *Proc. Natl. Acad. Sci. U.S.A.* **1991,** *88*, 9072–9076.

17. Jing, Y., Kao, J. F., and Taylor, J. S. Thermodynamic and base pairing studies of matched and mismatched DNA dodecamer duplexes containing *cis-syn*, (6-4), and Dewar photoproducts of TT. *Nucleic Acids Res.* **1998,** *26*, 3845–3853.

18. Park, H., Zhang, K., Ren, Y., Nadji, S., Sinha, N., Taylor, J. S., and Kang, C. Crystal structure of a DNA decamer containing a *cis-syn* thymine dimer. *Proc. Natl. Acad. Sci. U.S.A.* **2002,** *99*, 15965–15970.

19. Huang, J. C., Hsu, D. S., Kazantsev, A., and Sancar, A. Substrate spectrum of human excinuclease: repair of abasic sites, methylated bases, mismatches, and bulky adducts. *Proc. Natl. Acad. Sci. U.S.A.* **1994,** *91*, 12213–12217.

20. Johnson, R. E., Prakash, S., and Prakash, L. Efficient bypass of a thymine-thymine dimer by yeast DNA polymerase, pol η. *Science.* **1999,** *283,* 1001–1004.

21. Masutani, C., Kusumoto, R., Yamada, A., Dohmae, N., Yokoi, M., Yuasa, M., Araki, M., Iwai, S., Takio, K., and Hanaoka, F. The XPV (xeroderma pigmentosum variant) gene encodes human DNA polymerase η. *Nature.* **1999,** *399*, 700–704.

22. Prakash, S., Johnson, R. E., and Prakash, L. Eukaryotic translesion synthesis DNA polymerases: specificity of structure and function. *Annu. Rev. Biochem.* **2005**, *74*, 317–353.

23. Sun, L., Zhang, K., Zhou, L., Hohler, P., Kool, E. T., Yuan, F., Wang, Z., and Taylor, J. S. Yeast pol *η* holds a *cis-syn* thymine dimer loosely in the active site during elongation opposite the 3'-T of the dimer, but tightly opposite the 5'-T. *Biochemistry*. **2003,** *42*, 9431–9437.

24. Hwang, H., and Taylor, J. S. Evidence for Watson-Crick and not Hoogsteen or wobble base pairing in the selection of nucleotides for insertion opposite pyrimidines and a thymine dimer by yeast DNA pol η. *Biochemistry.* **2005**, *44*, 4850–4860.

25. Biertümpfel, C., Zhao, Y., Kondo, Y., Ramón-Maiques, S., Gregory, M., Lee, J. Y., Masutani, C., Lehmann, A. R., Hanaoka, F., and Yang, W. Structure and mechanism of human DNA polymerase η. *Nature.* **2010,** *465*, 1044–1048.

26. Jiang, N., and Taylor, J. S. *In vivo* evidence that UV-induced C→ T mutations at dipyrimidine sites could result from the replicative bypass of *cis-syn* cyclobutane dimers or their deamination products. *Biochemistry.* **1993,** *32*, 472–481.

27. Danilo, V. I., Les, A., and Alderfer, J. L. A theoretical study of the *cis-syn* pyrimidine dimers in the gas phase and water cluster and a tautomer bypass mechanism for the origin of UV-induced mutations. *J. Biomol. Struct. Dyn.* **2001,** *19,* 179–191.

28. Brown, D. M., and Hewlins, M. J. Dihydrocytosine and related compounds. *J. Chem. Soc. C.* **1968,** 2050–2055.

29. Dupuy-Mamelle, N., and Pullman, B. No. 61.-Recherches theoriques sur la structure electronique des purine et pyrimidines bilogiques. IV. Les pyrimidines saturees sur la liaison 5–6. *J. Chim. Phys. Phys. Chim. Biol.* **1967,** *64,* 708–712.

30. Danilov, V. I., Stewart, J. J. P., Les, A., and Alderfer, J. L. A theoretical study of pyrimidine photohydrates and a proposed mechanism for the mutagenic effect of ultraviolet light. *Chem. Phys. Lett.* **2000,** 328, 75–82.

31. Yu, S. L., Johnson, R. E., Prakash, S., and Prakash, L. Requirement of DNA polymerase η for error-free bypass of UV-induced CC and TC photoproducts. *Mol. Cell. Biol.* **2001,** *21*, 185–188.

32. Yoon, J. H., Prakash, L., and Prakash, S. Highly error-free role of DNA polymerase η in the replicative bypass of UV-induced pyrimidine dimers in mouse

and human cells. *Proc. Natl. Acad. Sci. U.S.A.* **2009,** *106*, 18219–18224.

33. Vu, B., Cannistraro, V. J., Sun, L., and Taylor, J. S. DNA synthesis past a 5-methyl-C-containing *cis-syn* cyclobutane pyrimidine dimer by yeast pol η is highly non-mutagenic. *Biochemistry.* **2006,** *45*, 9327–9335.

34. Cannistraro, V. J., and Taylor, J. S. Acceleration of 5-methylcytosine deamination in cyclobutane dimers by G and its implications for UV-induced C-to-T mutation hotspots. *J. Mol. Biol.* **2009,** *392*, 1145–1157.

35. Frederico, L. A., Kunkel, T. A., and Shaw, B. R. A sensitive genetic assay for the detection of cytosine deamination: determination of rate constants and the activation energy. *Biochemistry.* **1990,** *29*, 2532–2537.

36. Shen, J. C., Rideout, W. M., 3rd, and Jones, P. A. The rate of hydrolytic deamination of 5-methylcytosine in double-stranded DNA. *Nucleic Acids Res.* **1994,** *22*, 972–976.

37. Horsfall, M. J., Borden, A., and Lawrence, C. W. Mutagenic properties of the T-C cyclobutane dimer. *J. Bacteriol.* **1997,** *179*, 2835–2839.

38. Cannistraro, V. J., and Taylor, J. S. DNA-thumb interactions and processivity of T7 DNA polymerase in comparison to yeast polymerase *η*. *J. Biol. Chem.* **2004,** *279*, 18288–18295.

39. Sherrer, S. M., Fiala, K. A., Fowler, J. D., Newmister, S. A., Pryor, J. M., and Suo, Z. Quantitative analysis of the efficiency and mutagenic spectra of abasic lesion bypass catalyzed by human Y-family DNA polymerases. *Nucleic Acids Res.* **2011,** *39*, 609–622.

40. Wang, Y., Taylor, J. S., and Gross, M. L. Nuclease P1 digestion combined with tandem mass spectrometry for the structure determination of DNA photoproducts. *Chem. Res. Toxicol.* **1999,** *12*, 1077–1082.

41. Swan, M. K., Johnson, R. E., Prakash, L., Prakash, S., and Aggarwal, A. K. Structural basis of high fidelity DNA synthesis by yeast DNA polymerase η. *Nat. Struct. Mol. Biol.* **2009,** *16*, 979–986.

42. Washington, M. T., Johnson, R. E., Prakash, S., and Prakash, L. Accuracy of thymine-thymine dimer bypass by *Saccharomyces cerevisiae* DNA polymerase η. *Proc. Natl. Acad. Sci. U.S.A.* **2000,** 97, 3094–3099.

43. Washington, M. T., Johnson, R. E., Prakash, L., and Prakash, S. Accuracy of lesion bypass by yeast and human DNA polymerase η. *Proc. Natl. Acad. Sci. U.S.A.*

2001, *98,* 8355–8360.

44. Brown, J. A., Zhang, L., Sherrer, S. M., Taylor, J. S., Burgers, P. M., and Suo, Z. Pre-Steady-State Kinetic Analysis of Truncated and Full-Length Saccharomyces cerevisiae DNA Polymerase Eta. *J. Nucleic Acids,* ***2010,*** *25,* 871939.

45. Johnson, R. E., Washington, M. T., Prakash, S., and Prakash, L. Fidelity of human DNA polymerase η. *J. Biol. Chem.* **2000,** *275*, 7447–7450.

46. Smith, C. A., Baeten, J., and Taylor, J. S. The ability of a variety of polymerases to synthesize past site-specific *cis-syn*, *trans-syn*-II, (6-4), and Dewar photoproducts of thymidylyl-(3’→5’)-thymidine. *J. Biol. Chem.* **1998,** *273*, 21933–21940.

47. Sun, L., Wang, M., Kool, E. T., and Taylor, J. S. Pyrene nucleotide as a mechanistic probe: evidence for a transient abasic site-like intermediate in the bypass of dipyrimidine photoproducts by T7 DNA polymerase. *Biochemistry*. **2000,** *39,* 14603–14610.

48 Taylor, J. S. New structural and mechanistic insight into the A rule and the instructional and non-instructional behavior of DNA photoproducts and other lesions. *Mutat. Res.* **2002,** *510*, 55–70.

49. Cannistraro, V. J., and Taylor, J. S. Methyl CpG-binding protein 2 (MeCP2) enhances photodimer formation at methyl-CpG sites but suppresses dimer deamination. *Nucleic Acids Res.* **2010,** *38,* 6943–6955.

50. Song, Q., Cannistraro, V. J., and Taylor, J. S. Rotational position of a 5-methylcytosine-containing cyclobutane pyrimidine dimer in a nucleosome greatly affects its deamination rate. *J. Biol. Chem.* **2011,** *286,* 6329–6335.

51. Song, Q., Sherrer, S. M., Suo, Z. and Taylor, J. S. Preparation of site-specific T=^{m}CG *cis-syn* cyclobutane dimer-containing template and its error-free bypass by yeast and human polymerase *η*. *J. Biol. Chem.* **2012,** *287,* 8021–8028.

Table 2.1 Oligodeoxynucleotides (ODN) used in this study.

ODN	Sequence
9-mer	5’-GCTCGTCAC-3’
9A-mer	5’-GCTCGTCAC**A**-3’
9AA-mer	5’-GCTCGTCAC**AA**-3’
9G-mer	5’-GCTCGTCAC**G**-3’
9GA-mer	5’-GCTCGTCAC**GA**-3’
AA-14-mer	5’-GCTCGTCAC**AA**T AC-3’
GA-14-mer	5’-GCTCGTCAC**GA**T AC-3’
T^{m}C-14-mer	5’-GTA**T^{m}C**GTGACGAGC-3’
T=^{m}C-14-mer	5’-GTA**T=^{m}C**GTGACGAGC-3’
TT-14-mer	5’-GTA**TT**GTGACGAGC-3’
T=T-14-mer	5’-GTA**T=T**GTGACGAGC-3’

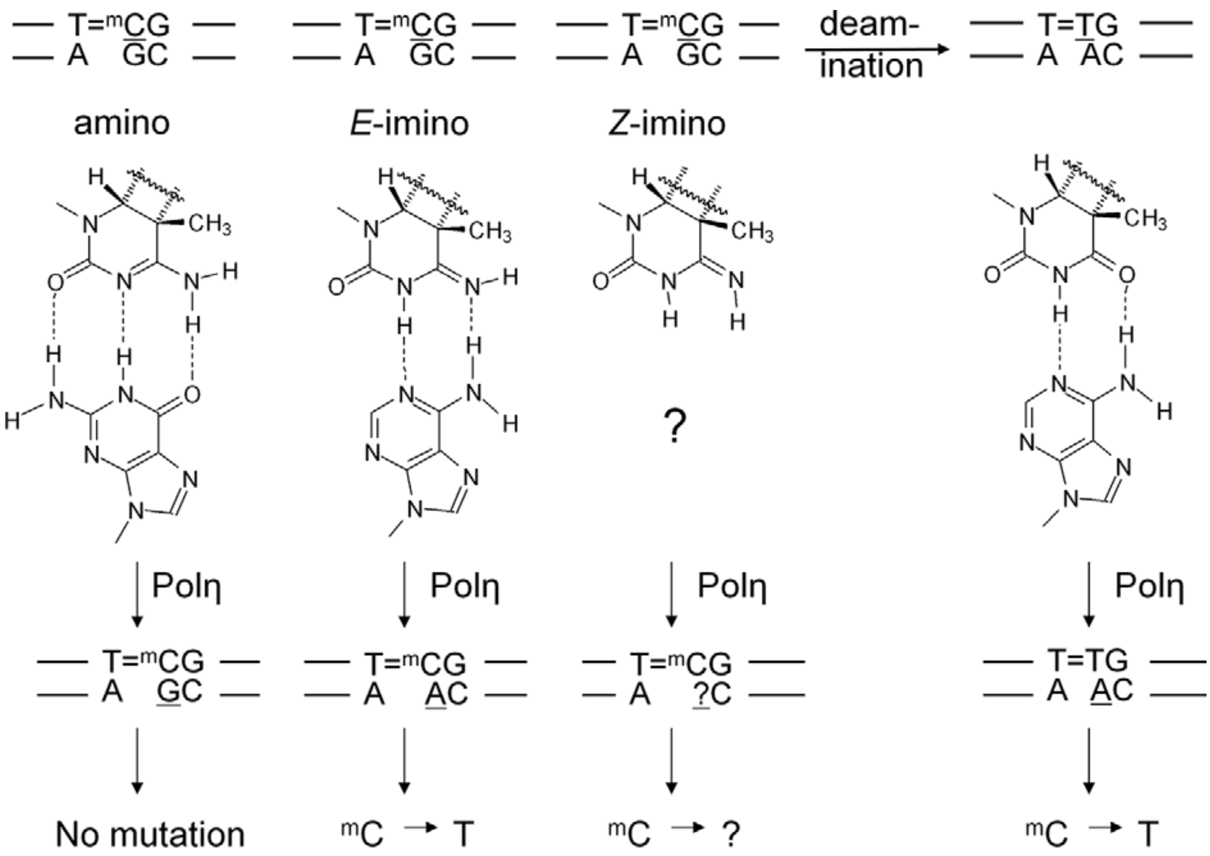

Figure 2.1 Mutagenic properties of ^{m}C and its deamination product, T, in *cis-syn* cyclobutane pyrimidine dimer.

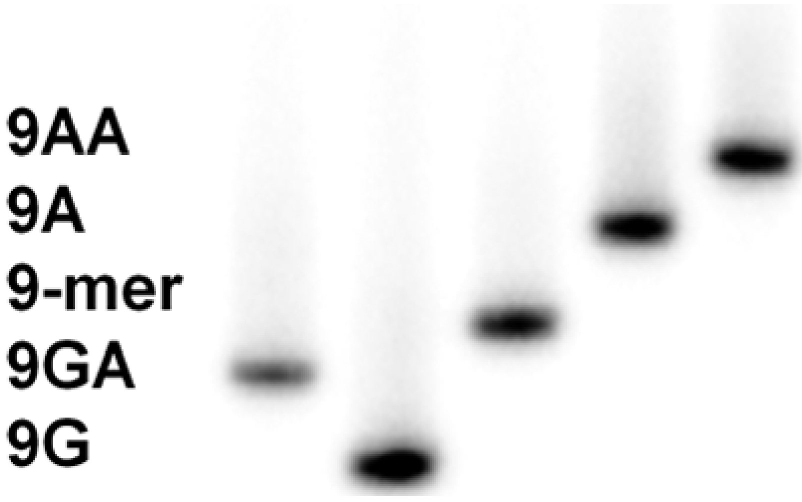

Figure 2.2 Oligodeoxynucleotides on citrate PAGE gel.

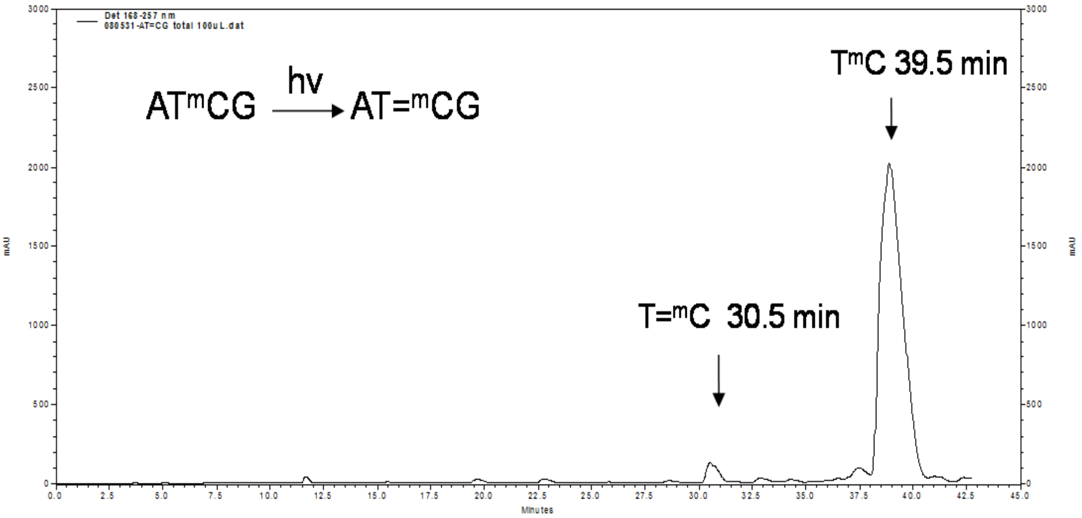

Figure 2.3. Analysis of the UV irradiation products of T^{m}C-14-mer before deamination. HPLC trace of T^{m}C-14-mer after UV irradiation at 4°C for 1 hour at pH 8.5.

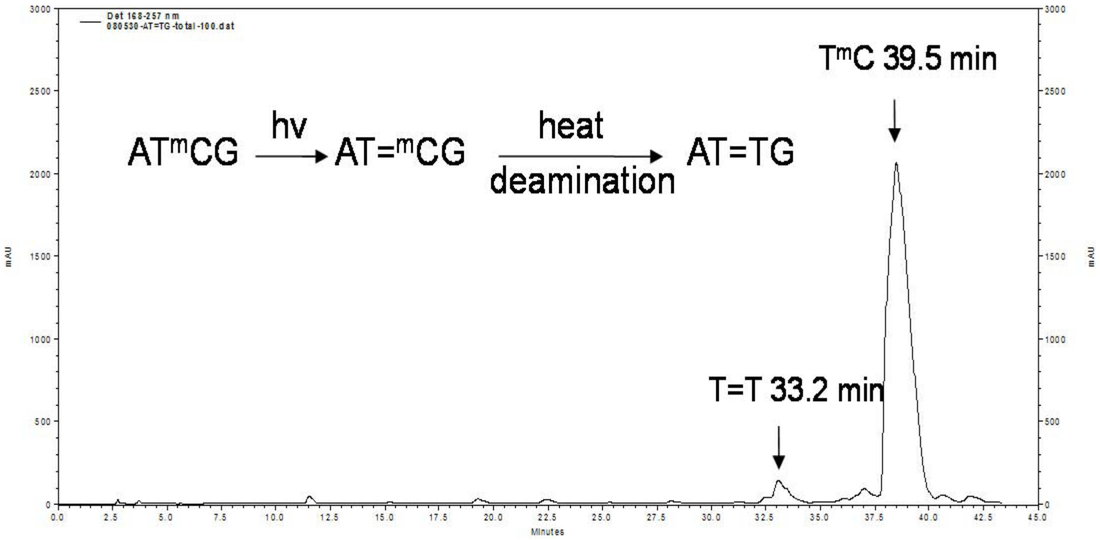

Figure 2.4 Analysis of the UV irradiation products of T^{m}C-14-mer after deamination. HPLC trace of T^{m}C-14-mer after UV irradiation at 4°C for 1 h followed by 3 h at 67°C and pH 6.5.

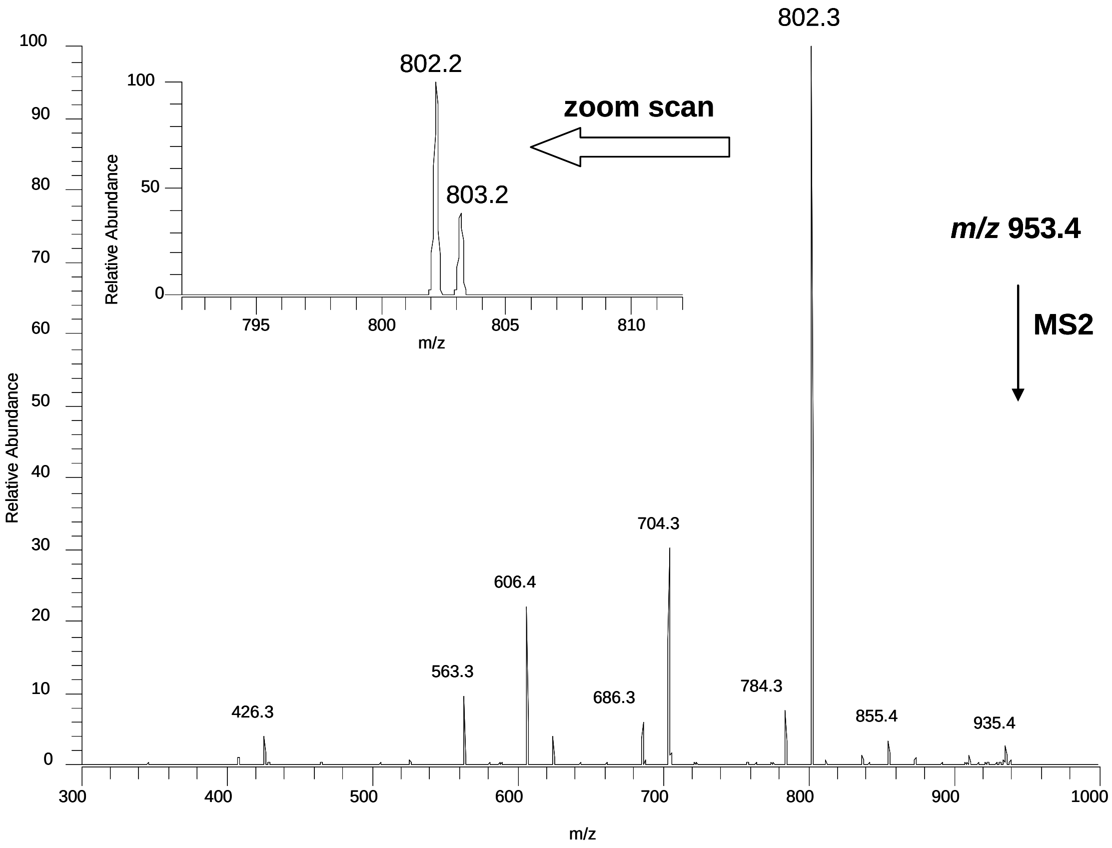

Figure 2.5 Nuclease P1-coupled ESI-MS/MS analysis of T=^{m}C-14-mer. MS/MS of nuclease P1 digestion products of the HPLC peak corresponding to the cis-syn CPD of TmC-14-mer (A1: parent ion *m*/*z*: 953, full MS; A2: zoom scan at *m*/*z*: 802). The 953 parent ion corresponds to [pT=^{m}CG-H]$^{-}$.

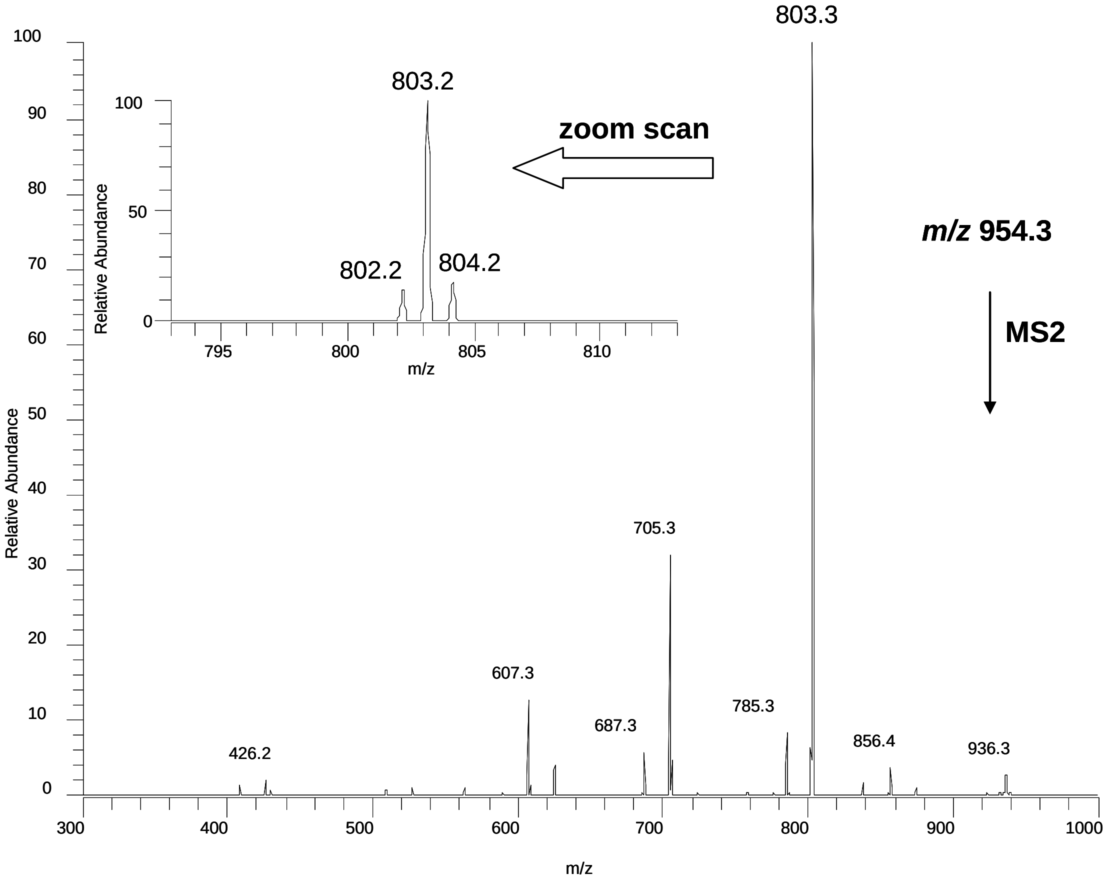

Figure 2.6 Nuclease P1-coupled ESI-MS/MS analysis of the deamination products of T=^{m}C-14-mer. Spectra of the nuclease P1 digested HPLC peak corresponding to the deaminated product of cis-syn CPD TmC-14-mer (A1: parent ion *m*/*z*: 954, full MS; A2: zoom scan at *m*/*z*: 803). The 954 parent ion corresponds to [pT=TG-H]$^{-}$.

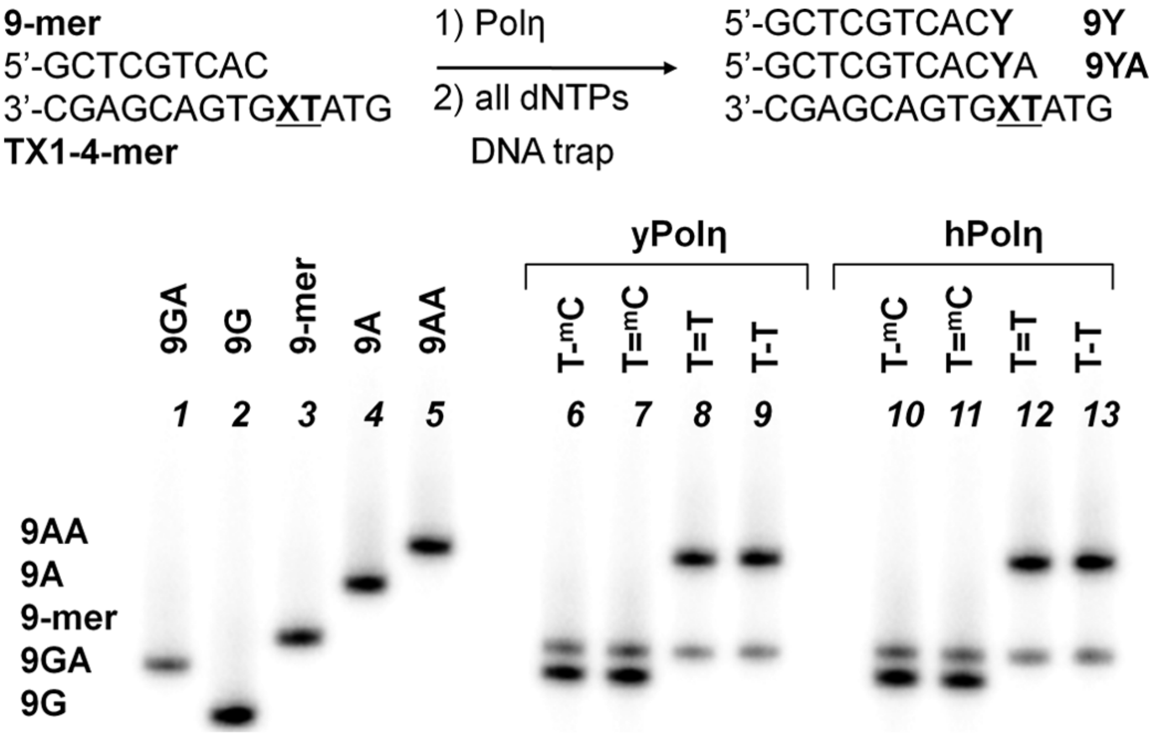

Figure 2.7 Single-hit primer extension competition experiment opposite 14-mer templates. An equimolar mixture of all dNTPs (200μM each) together with sonicated/denatured salmon sperm DNA was added to a preincubated mixture of the indicated 9-mer primer-14-mer template and pol η. The reactions were terminated after 10 s with EDTA and unlabeled primer, and the products were electrophoresed on a citrate (pH 3.5)-10% polyacrylamide gel. The standards corresponding to extension of the 9-mer by A or G were prepared by automated synthesis. *yPolη*: yeast Pol η; *hPolη*: human Pol η.

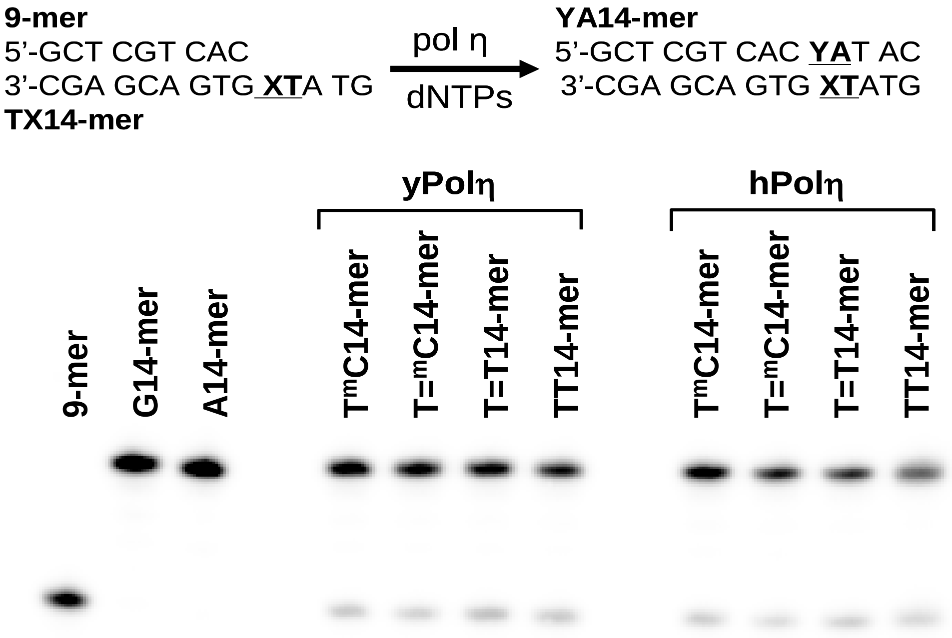

Figure 2.8 Multiple hit full length primer-extension experiment (TBE PAGE). The 9-mer primer/14-templates were incubated with Pol η and 100 μM of each dNTP until complete extension was achieved. Denaturing electrophoresis gel (20% TBE PAGE) showed production of full-length primer extension products under the reaction conditions.

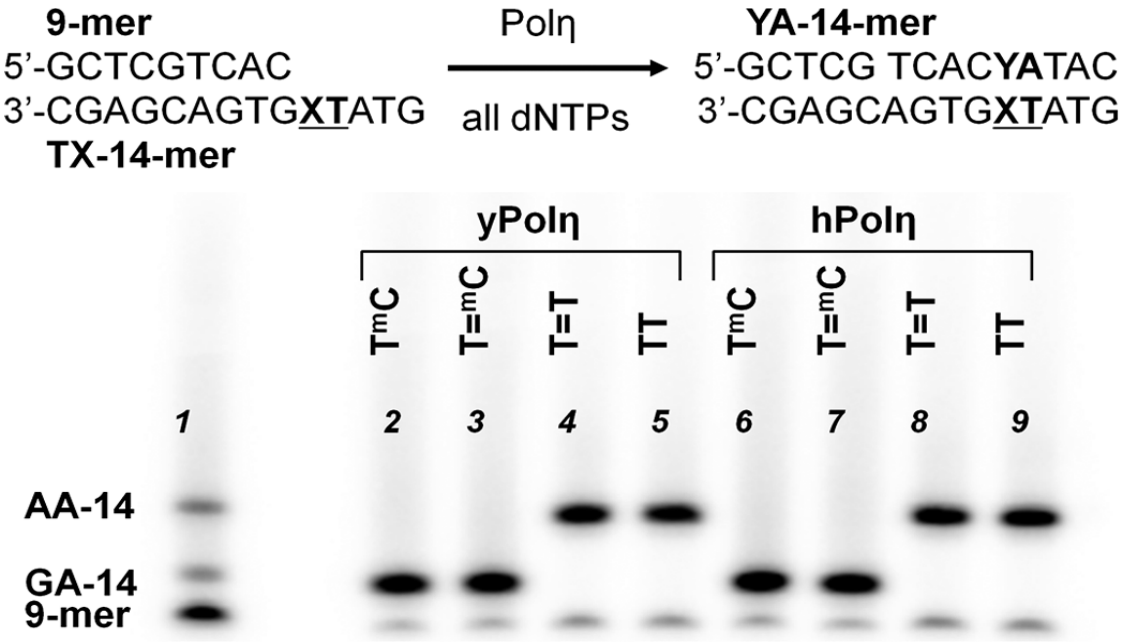

Figure 2.9 Multiple hit full length primer-extension experiment (Citrate PAGE gel). The indicated 9-mer primer-14-mer templates were incubated with pol η and 200μM each dNTP for 2 min, and the products were electrophoresed on a citrate (pH 3.5)-20% polyacrylamide denaturing gel in comparison with standards. *yPolη*: yeast pol η; *hPolη*: human pol η.

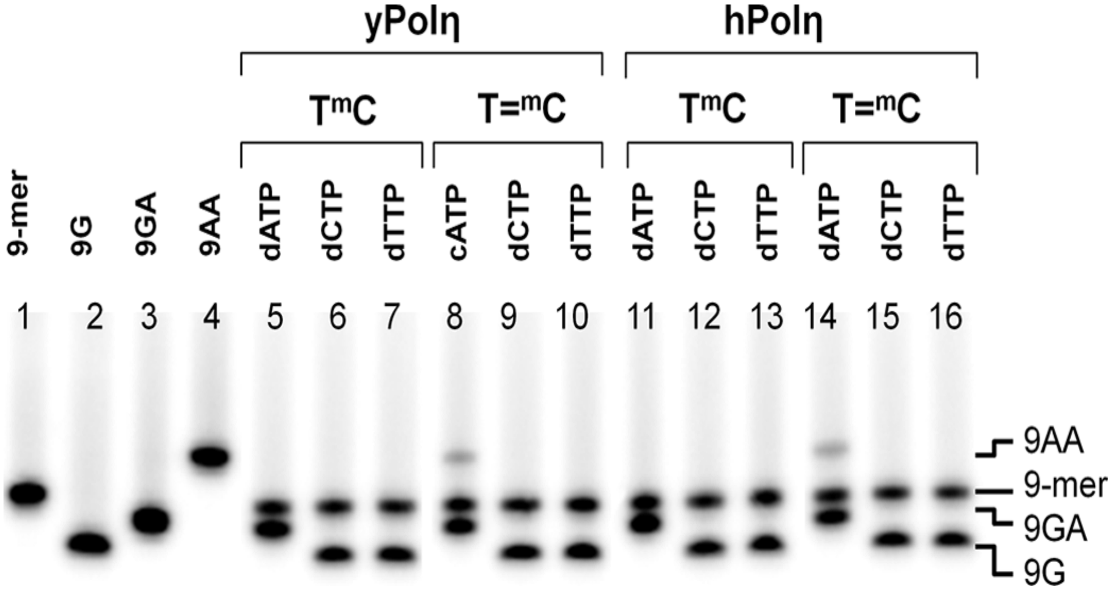

Figure 2.10 Single-hit primer extension biased nucleotide pool competition experiment opposite 14-mer templates. A 32:1 mixture of the indicated dNTP/dGTP (100 μM in the dNTP) together with sonicated/denatured salmon sperm DNA was added to a preincubated mixture of the indicated 9-mer primer-14-mer template and pol η. The reaction was terminated after 10 s with EDTA and unlabeled primer, and the products were electrophoresed on a citrate (pH 3.5)-10% polyacrylamide gel. The standards corresponding to extension of the 9-mer by A or G were prepared by automated synthesis. *yPolη*: yeast pol η; *hPolη*: human pol η.

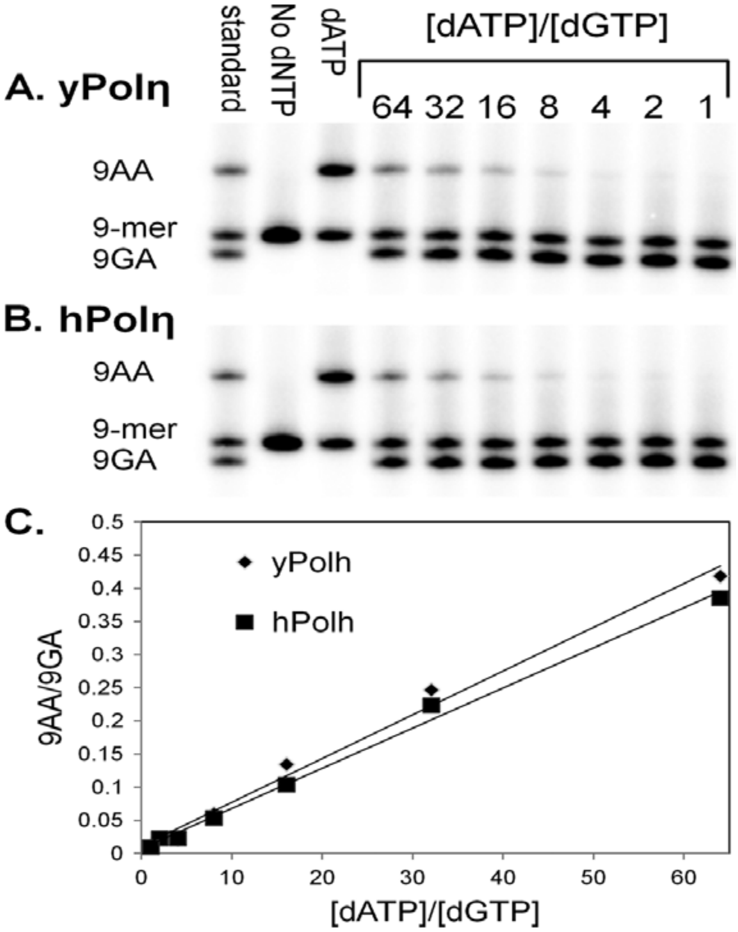

Figure 2.11 Selectivity of dGMP *versus* dAMP insertion opposite $^{\mathrm{m}}$C of T=$^{\mathrm{m}}$C CPD via single-hit assay. Varying ratios of dATP to dGTP (with dATP fixed at 100 μM) together with sonicated/denatured salmon sperm DNA were added to a preincubated mixture of the 9-mer primer-14-mer template and pol η. The reaction was terminated after 10 s with EDTA and unlabeled primer, and the products were electrophoresed on a citrate (pH 3.5)-10% polyacrylamide gel. The standards corresponding to extension of the 9-mer by A or G were prepared by automated synthesis. *yPolη*: yeast pol η; *hPolη*: human pol η.

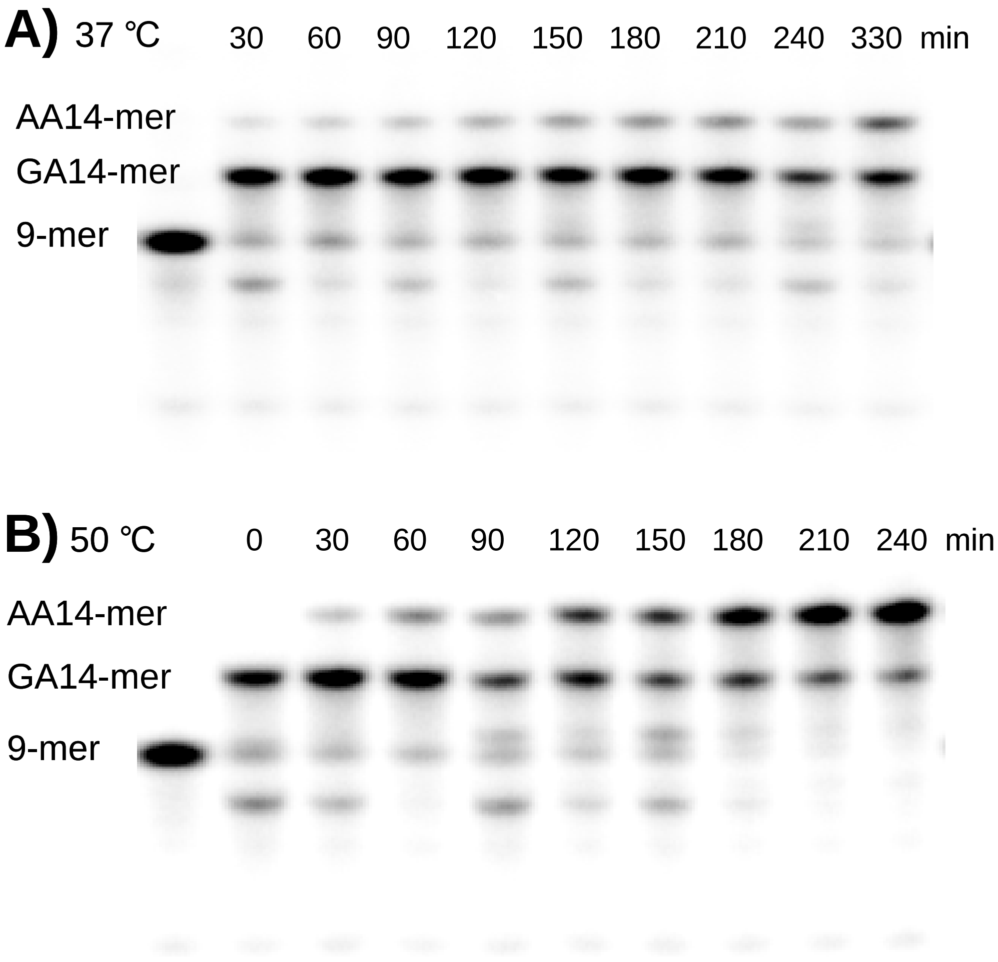

Figure 2.12 Temperature dependence of ^{m}C deamination in T=^{m}C-14-mer CPD at pH 7.5. Multiple-hit nucleotide insertion competition assay carried out with 100 μM of each dNTP at 37°C and 50°C and electrophoresed on a 25% polyacrylamide, pH 3.5, citrate gel.

A) Deamination of T=^{m}C14-mer at 37^{o}C

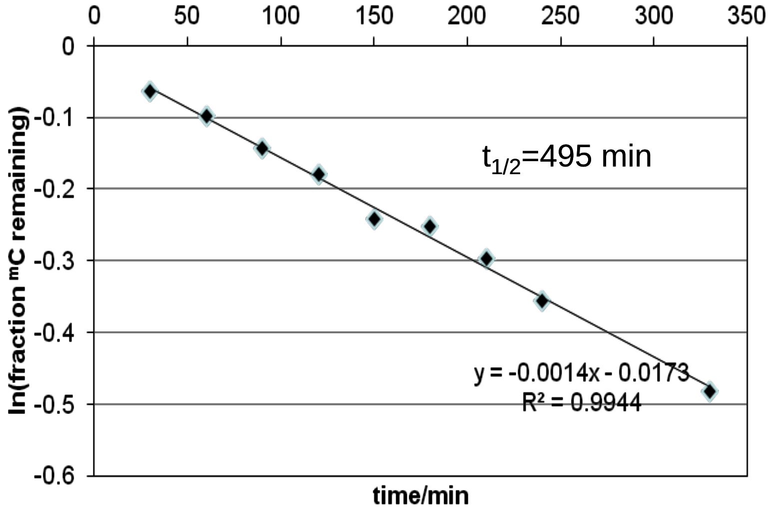

B) Deamination of T=^{m}C14-mer at 50^{o}C

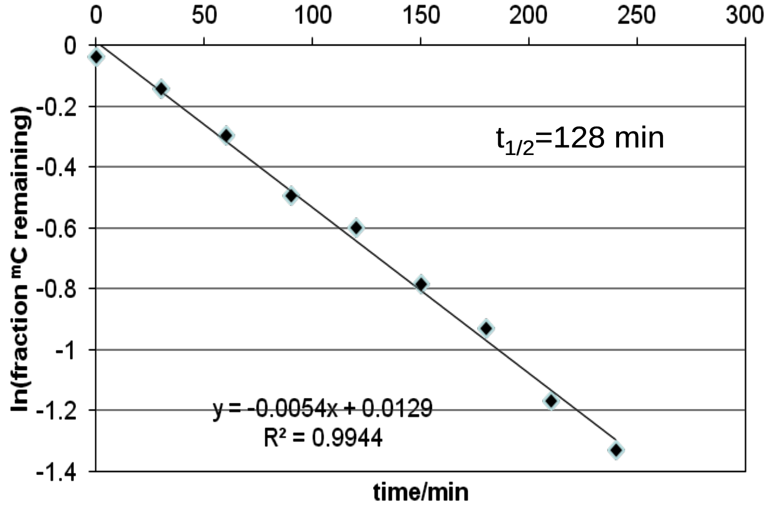

Figure 2.13 Deamination rate constant determinations. Least squares fit to a plot of the natural log of the fraction of mC remaining in the T^{m}CG-14-mer CPD versus deamination time at two different temperatures. The fraction of ^{m}C remaining equals the fraction of G inserted, G/(G + A), opposite the ^{m}C of the T=^{m}C 14-mer by yPol η.

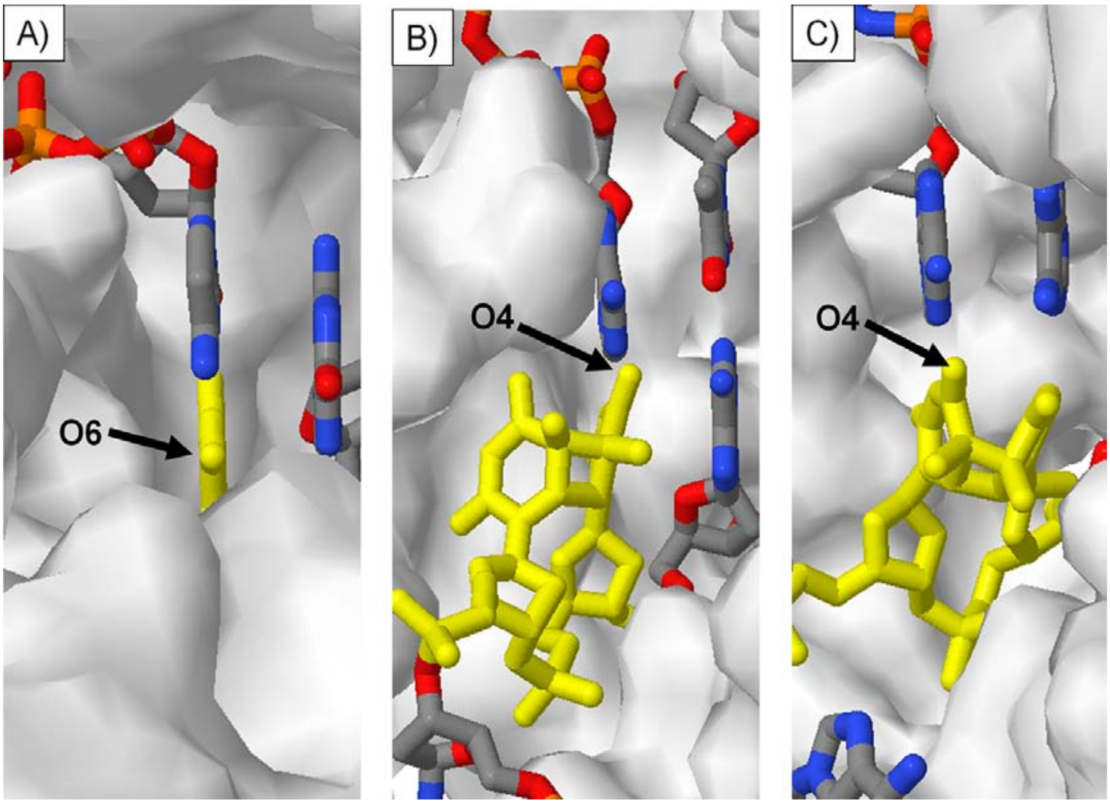

Figure 2.14 Visual comparison of water accessibility of O6 of template guanine (*yellow*) inactive site of yeast pol δ (Protein Data Bank code 3IAY) (*A*) and of O4 of template 3'-T (*B*) and template 5'-T (*C*) of *cis-syn* TT CPD (*yellow*) in active site of human pol η (code 3MR4).

Chapter 3

Rotational Position of a 5-Methylcytosine-containing Cyclobutane Pyrimidine Dimer in a Nucleosome Greatly Affects Its Deamination Rate*

---

* The chapter was adapted from Ref. 57 with permission.

Abstract

C to T mutation hotspots in skin cancers occur primarily at methylated CpG sites that coincide with sites of UV-induced cyclobutane pyrimidine dimer (CPD) formation. These mutations are proposed to arise from the insertion of A by DNA polymerase η opposite the T resulting from deamination of the methylC (^{m}C) within the CPD. Although the frequency of CPD formation and repair is modestly modulated by its rotational positioning within a nucleosome, the effect of nucleosome rotational positioning on the rate of ^{m}C deamination in a CPD has not been previously studied. We now report that deamination of a T^{m}C CPD whose sugar phosphate backbone is positioned against the histone core surface decreases by a factor of 4.7, whereas that of a T^{m}C CPD positioned away from the surface increases by a factor of 8.9 when compared with unbound DNA. Because the ^{m}Cs undergoing deamination are in similar steric environments, the difference in rate appears to be a consequence of a difference in the flexibility and compression of the two sites due to DNA bending. Considering that formation of the CPD positioned away from the surface is also enhanced by a factor of two, a T^{m}CG site in this position might be expected to have up to an 84-fold higher probability of resulting in a UV-induced ^{m}C to T mutation than one positioned against the surface. These results indicate that rotational position may play an important role in the formation of UV-induced C to T mutation hotspots, as well as in the mutagenic mechanism of other DNA lesions.

Introduction

Sunlight is a major epidemiological factor for the induction of skin cancer. In basal and squamous cell carcinomas, the p53 tumor suppressor gene exhibits a very high percentage of C to T transition mutations at dipyrimidine sites, including the tandem CC to TT mutation (1–4). The UVB wavelengths in sunlight induce the formation of many types of photoproducts at dipyrimidine sites in DNA, the majority of which are cyclobutane pyrimidine dimers, which are normally abbreviated as CPDs (5–8). Methylation of C at 5’-PyCG sites further enhances formation of CPDs 15- fold in sunlight (9, 10), and most C to T mutation hotspots occur at methylated 5’-PyCG sites (10–12). It has been found that 5-methylcytosine is involved in 25–40% of sunlight-induced mutations of the *cII* and *lacI* transgenes as well as the p53 gene in skin tumors and that CPDs are responsible for a significant fraction of these mutations (6, 13).

The initially formed cyclobutane pyrimidine dimers are not significantly mutagenic, however, because of the DNA damage bypass polymerase η, which can efficiently bypass T- and C/^{m}C-containing dimers in an essentially error-free manner (14–17). Although the T in a CPD is stable, the C and ^{m}C are not, and they deaminate to U and T in a matter of hours or days (18–24) (Figure 3.1), unlike their canonical forms, which deaminate with a half-life of about 50,000 years (25, 26). Deamination of Cs or ^{m}Cs in CPDs is highly mutagenic because polymerase η will faithfully insert A opposite the resulting Us or Ts, thereby producing the observed C to T and CC to TT mutations (the deamination-bypass mechanism) (3, 4, 27–29). The frequency of C to T and CC to TT mutations will depend, however, on the rate of formation of C-containing dimers, their rate of repair, deamination, and bypass by polymerases. All of these processes are expected to be modulated by sequence context, protein interactions, as well as the secondary and tertiary structure of DNA. A detailed understanding of all these processes and interactions may lead to a better understanding of the origin of UV mutation hotspots.

Nucleosomes are the primary structural unit of chromatin in eukaryotic cells (30). Nucleosome core particles contain about 150 bp of DNA, which wrap 1.7 times around a histone octamer, made up of two H2A, H2B, H3, and H4 histones (31). UV preferentially induces the formation of CPDs in nucleosomes at sites where the phosphodiester backbone is positioned away from the histone surface and DNA bending is toward the major groove (32, 33). This preference is also seen for bent DNA that is not in contact with a protein (34) and has been attributed to the greater degree of rotational freedom in the phosphate backbone, making it easier to for adjacent pyrimidines to adopt a photoreactive conformation (35, 36). When DNA containing randomly distributed CPDs is assembled into nucleosomes, the CPDs also favor positions away from the surface (37), which is consistent with the 30° bend that they make toward the major grove of DNA (38). Despite the distortion of DNA caused by CPDs, nucleosome core particles containing CPDs in different rotational settings can be readily prepared and isolated (39–41).

Nucleosomes have also been found to affect the repair of CPDs (42). *In vitro* studies with human fibroblast extracts found that nucleosomes reduce the rate of nucleotide excision repair of CPDs by 6–9-fold relative to free DNA (43). A similar 10-fold reduction in excision repair has been observed for a site-specific CPD reconstituted with human nucleosome core particles (44). With *Xenopus* nuclear extracts, the nucleotide excision repair rates of rotationally positioned CPDs were only 2–3 times lower in nucleosomes and no more than 1.5-fold greater when a CPD was positioned away from the histone surface when compared with against the surface (41). In an earlier study with a 5S rRNA gene, no correlation was observed with rotational positioning of the CPD (45).

Although the effects of nucleosome positioning on the rates of CPD formation and repair have been studied, the effects on the deamination rates of C- and ^{m}C-containing CPDs have not. The purpose of this study was to determine the extent to which the rotational position of the CPD relative to the histone surface affects the rate of ^{m}C to T deamination, and hence, its potential mutagenicity by a deamination bypass mechanism. To address this question, we determined the deamination rate of a T^{m}CG CPD in two different orientations in a nucleosome core particle. We find that a T^{m}C CPD positioned against the surface deaminates 4.7 times slower than the unbound sequence, whereas a T^{m}C CPD facing out deaminates 8.9 times faster than the unbound sequence, corresponding to an overall 42-fold difference in rate.

Experimental Procedures

DNA Substrates

Oligodeoxynucleotides (ODN) with or without 5’-terminal phosphates were purchased from Integrated DNA Technologies and purified by denaturing gel electrophoresis prior to ligation with T4 DNA ligase and ATP in the presence of complementary 20-mer ligation scaffolds (Table 3.1 to 3.4, Figure 3.3). The 150-mer single strand products were purified by denaturing PAGE. Complementary 150-mers were then annealed to form the 150-mer duplexes and purified by native PAGE (Figure 3.4).

Nucleosome Reconstitution

Nucleosome core particles were isolated and purified from chicken erythrocytes following a detailed procedure provided by the Dr. Michael Smerdon laboratory. Each 150-mer DNA duplex (ds-IN, ds-OUT, and ds-control) was reconstituted with the chicken nucleosome core particles by slow dialysis from high to low salt as described previously (46). Briefly, about 10nM 150-mer duplex was incubated with an increasing amount of nucleosome core particles (from 100 to 500nM) in a total volume of 500μL, containing 2M NaCl, 10mM Tris-HCl, 5mM EDTA at pH 7.5 and room temperature for 2 h, and then dialyzed against 50mM NaCl, 10mM Tris-HCl, pH 7.5, at 4°C, overnight. Finally, the reconstituted particles were recovered from the dialysis tubing and equilibrated at 55°C for 2 h to fix the nucleosome phasing. The reconstituted particles were assayed by native PAGE (6% acrylamide, 0.2% bisacrylamide in TBE), and the ratio of nucleosome-bound DNA to free DNA was quantified by the Quantity One software (Figure 3.5).

Hydroxyl Radical Foot-printing and Dimethylsulfate Mapping

Hydroxyl radical footprinting was performed as described previously (46). Briefly, a 15-μL aliquot of 10mM sodium ascorbate, a 15-μL aliquot containing 1mM

$Fe(NH_4)_2(SO_4)_2 \cdot 6H_2O$ and 2mM EDTA, and 15μL of a 0.12% (w/w) H_2O_2 solution were premixed and added within 5 s to 105μL of the nucleosome-bound DNA sample. The reaction was incubated for 120 s at room temperature and stopped by the addition of 16μL of 50% (v/v) glycerol and 4μL of a 500mM EDTA solution. The samples were electrophoresed on a native gel (6% acrylamide, 0.2% bisacrylamide in TBE), and the nucleosome bands were electroeluted in TBE. The proteins were extracted with phenol:chloroform:isopropyl alcohol 25:24:1, and the DNA was precipitated with ethanol. The free ds-control was treated in a similar way, except that the reaction was quenched with a solution containing 1M sodium acetate, 120mM thiourea, 300μg/ml salmon sperm DNA, and 60mM EDTA at pH 6.5 and then ethanol-precipitated. A Maxam-Gilbert G sequencing reaction was also carried out on the free ds-control in 50mM cacodylate, 50mM NaCl, 5mM EDTA in the presence of 10nM ds-control. For a 50-μL reaction, 0.5μL of dimethyl sulfate was added to initiate the reaction, and 10-μL aliquots were removed over time and quenched by the addition of 50μL of 1.5M sodium acetate, 1M mercaptoethanol and 50μg of denatured salmon sperm DNA. The samples were ethanol-precipitated twice, and the resulting pellets were vacuum-dried and then solubilized in 100μL of 1M piperidine. The samples were then heated at 90°C in 1M piperidine for 30 min and then evaporated to dryness at 60°C.

Deamination Rate Assay by Two-dimensional Gel Electrophoresis

The deamination rate was determined by adapting a previously described method (24). The free and nucleosome-bound internally ^{32}P-labeled 150-mer ds-IN and ds-OUT were irradiated with 302 nm UVB light at 4°C for 1 h and then adjusted to pH 7.2 with Mes buffer (0.5M) and incubated at 37°C. Aliquots (10-µL) were removed at various times and quickly frozen on dry ice before storing overnight at -80°C. The remaining sample was adjusted to pH 6.5 with Mes buffer (0.5M) and heated at 67°C overnight to complete the deamination. The aliquots were then warmed to room temperature, extracted with phenol:chloroform:isopropyl alcohol 25:24:1, ethanol-precipitated, redissolved in buffer containing 10mM Tris-HCl, pH 7.5, 50mM NaCl, 5mM DTT, and photoreverted with photolyase and 365 nm light for 1 h. After photoreversion, the aliquots were treated with nuclease P1 to degrade the DNA to mononucleotides containing either $^{32}P^{m}dC$ or ^{32}P-dT, depending on the extent of deamination, and separated by two-dimensional gel electrophoresis. In the first dimension, electrophoresis on a 7M urea, a TBE gel was used to separate ^{32}P-^{m}dC and ^{32}P-dT, which co-migrate, from partially digested material and protein. For the second dimension, the gel surrounding the radioactive band containing the mononucleotides was excised, and a second gel containing 25mM citric acid, pH 3.5, and 7M urea was poured around the remaining gel slice. Electrophoresis on this gel separated $^{32}P^{m}dC$ from ^{32}P-dT with the ^{32}P-T migrating the fastest. The deamination rate constant was obtained from the slope of a linear least squares fit of the log of the fraction of remaining T^{m}C CPD *versus* deamination time. The fraction of T^{m}C CPD remaining was calculated as $1- (T/(T + {}^{m}C))/(T_{\infty}/(T_{\infty} + {}^{m}C))$ where $T_{\infty}/(T_{\infty} + {}^{m}C_{\infty})$ is the fraction $T/(T + {}^{m}C)$ in the fully deaminated sample. The yield of CPD photoproduct was calculated as the $T_{\infty}/(T_{\infty} + {}^{m}C_{\infty}) - T_0/(T_0 + {}^{m}C_0)$, where $T_0/(T_0 +$

${}^{m}C_0$) is the fraction T/(T + ^{m}C) at time 0.

Results

Design and Synthesis of DNA Substrates

The substrate for study was adapted from a previously described 150-mer DNA duplex sequence that was shown by hydroxyl radical foot-printing to position a TT CPD near the nucleosome dyad axis with an inside (IN) or outside (OUT) orientation relative to the histone core surface (41). The CPDs were oriented by flanking the dimer-containing sequence with multiple TG motifs $(T/A)_3NN(G/C)_3$ that had been shown to position a glucocorticoid hormone-response element (GRE) with different orientations relative to the histone surface (47, 48). To study the effect of nucleosome rotational positioning on the deamination of cyclobutane pyrimidine dimers of T^{m}CG sites, we simply replaced the ATTA (OUT) and GTTC (IN) CPD sites in the original 150-mer DNA sequence with AT^{m}CG and GT^{m}CG sites respectively (Figure 3.6, *top right*).

To determine the deamination rates of the T^{m}C CPDs, we used a previously developed method that requires the ^{m}C to be 5’-^{32}P-end-labeled (Figure 3.2) (24). We therefore prepared the two internally ^{32}P-labeled duplex 150-mers, ds-IN and ds-OUT, along with a 5’-end-labeled control duplex, ds-control. The duplexes were prepared by annealing complementary single strand 150-mers that were prepared by ligating four ODNs together with T4 ligase and ATP in the presence of complementary ligation scaffolds (Figure 3.2). For ds-IN and ds- OUT, the second and third ODNs of the top strand were designed so that the ^{m}C of interest would be at the 5’-end of the third fragment so that the ^{m}C could be 5'-^{32}P-end-labeled prior to ligation (Table 3.1 to 3.4, Figure 3.3). Thus, ds-IN was ^{32}P-labeled at the ^{m}C of the GT^{m}CG site, ds-OUT was labeled at the ^{m}C of the AT^{m}CG site, and ds-control was labeled at the 5'-end of the 150-mer of the top strand. Each single strand 150-mer was purified by denaturing PAGE, and the final 150-mer duplexes were purified by native PAGE (Figure 3.4).

Nucleosome Core Particle Reconstitution with the 150-mer DNA Duplexes

The 150-mer duplexes, ds-IN, ds-OUT, and ds-control, were assembled into nucleosome core particles according to a previously described procedure that involves exchanging the DNA with that from chicken erythrocyte nucleosome core particles (NCPs) (39). The 150-mer duplexes were titrated with the NCPs and electrophoresed on a native gel to determine the NCP concentration needed to achieve maximal incorporation of the DNA into the NCP (Figure 3.5). We found that about 90% of 10nM 150-mer DNA duplexes could be incorporated into 500nM nucleosome core particles.

Orientation of the Two TmC Sites on the Nucleosome Core Particle

To verify the IN and OUT positions of the GT^{m}CG and AT^{m}CG sites, the nucleosomes were analyzed by hydroxyl radical foot-printing. The hydroxyl radical cleavage intensity on the nucleosome-bound ds-control with and without UVB irradiation exhibited very pronounced 10–11-bp periodicity with the same phasing as described previously for the ATTA and GTTC sites within the same 150-mer sequence (41) (Figure 3.6, *lanes 2* and *3*) when compared with the free ds-control (Figure 3.6, *lane 1*). The cleavage sites were mapped onto the sequence by alignment with the Maxam Gilbert G sequencing reaction bands (Figure 3.6, *lane 4*). Hydroxyl radicals primarily attack the H5’5’’ and H4’ hydrogens that are present on the minor groove side of the DNA (49). The ^{m}C of the AT^{m}CG CPD site is in the center of a region of maximal cleavage, indicating that its phosphodiester backbone is facing out (Figure 3.6, *boxed section*). The ^{m}C of the GT^{m}CG CPD site, which is half a turn from the first site, is at a site of minimal cleavage, indicating that its backbone is facing toward the histone surface.

The similar hydroxyl radical cleavage pattern in the presence and absence of UVB irradiation suggests that the UVB photoproducts do not disrupt the phasing. Furthermore, the decrease of the intensity of the ^{m}C band and increase in that of the flanking G at the AT^{m}CG site following UVB radiation is consistent with the formation of a significant amount of CPD photoproduct (Figure 3.6, *boxed section*). It has been previously observed that hydroxyl radical cleavage is suppressed at the 3’-T of a TT CPD and increased at the nucleotide immediately following the 3’-T (41).

Deamination Rates of the Two T=^{m}C CPDs

The deamination rates for the IN and OUT T=^{m}C CPDs when compared with free DNA were determined by following the conversion of ^{32}P-^{m}dC to ^{32}P-dT in the dimer by an enzyme-coupled two dimensional gel electrophoresis assay (24). In the first step, free or NCP complexed ds-IN and ds-OUT were irradiated with 302 nm light to produce the *cis-syn*-cyclobutane pyrimidine dimers (CPD) of the AT^{m}CG and GT^{m}CG sites, along with other photoproducts, at 4°C to suppress deamination. The samples were then incubated at 37°C and pH 7.2 to allow for deamination for various times, and one was made to undergo complete deamination by lowering the pH down to pH 6.5 and heating at 67°C, overnight. The aliquots were then incubated with *Escherichia coli* photolyase and visible light to specifically photorevert the *cis-syn*-CPDs and then treated with nuclease P1 to degrade all of the undamaged and photoreverted DNA to mononucleotides. Non-photorevertible dipyrimidine photoproducts, such as (6-4) and Dewar DNA photoproducts, would only be digested to trinucleotides. The mononucleotides were then isolated by electrophoresis on a denaturing gel and subjected to a second electrophoresis on a pH 3.5 citrate gel (Figure 3.7) that separates the deaminated ^{32}P-T from the undeaminated ^{32}P-^{m}dC and quantified by radioisotopic imaging analysis.

The rate constants for deamination were then determined from the slopes of lines fit to the log of the fraction of remaining T^{m}C CPD (Figure 3.10 & 3.11) as described under “Experimental Procedures” for multiple experiments and then averaged. The photoproduct yields were determined from the increase in the initial amount of radio-labeled T following complete deamination. The initial amount of T was non-zero in many cases and could be attributed to unintended labeling of the T at the 5’-end of the 150-mer resulting from incomplete heat deactivation of the kinase used to label the ^{m}C-containing ODN prior to ligation. Table 3.5 shows the deamination half-lives and yields of the T=^{m}C CPDs in the IN and OUT positions of free and nucleosome-bound DNA. When compared with the free DNA, the nucleosome decreases the rate of deamination of the facing IN CPD by a factor of 4.7, whereas it increases the rate of deamination of the facing OUT CPD by a factor of 8.9.

We also determined that although the nucleosome did not affect the efficiency of forming the facing inside CPD, it did enhance the formation of the facing outside CPD by a factor of two.

Discussion

The goal of this study was to determine whether or not the nucleosome rotational positioning of a *cis*-*syn*-cyclobutane pyrimidine dimer (CPD) of a T^{m}CG site on a nucleosome would affect its deamination rate and thereby contribute to its relative UV-induced mutagenicity via a deamination bypass mechanism. Two nucleosome rotational positionings were studied, one with the phosphodiester backbone of the T=^{m}C CPD positioned against or facing inside the histone core surface (IN) and one with the backbone of the T=^{m}C CPD positioned away or facing outside from the surface (OUT). These positions can be mapped onto a crystal structure of the nucleosome core particle as shown in Figure 3.12. Because the facing outside CPD site precedes the facing inside CPD site when going in the 5'- to 3'-direction, the two sites must lie to one side of the nucleosome pseudo dyad axis.

The different photoreactivity of the two sites in free DNA (Table 3.5) was consistent with an earlier study of ours showing that an AT^{m}CG site is about 2-fold more photoreactive than a GT^{m}CG site (5.4 *versus* 12% yield) due to the quenching effect of flanking Gs (24). Complexing the DNA to the histone core particle did not affect the photoreactivity of the inside GT^{m}CG site but enhanced the photoreactivity of the outside AT^{m}CG site 2-fold to give a 26% yield of the CPD when compared with 5.5% for the inside site. The enhanced photoreactivity of the facing outside position is in accord with the higher photoreactivity previously noted for dipyrimidine sites positioning away from the histone surface (32, 33).

In contrast to their photoreactivity, the deamination rates of the two T=^{m}C CPD sites in the nucleosome were dramatically different from those in the free DNA, with the T=^{m}C CPD positioned against or facing inside the histone core surface deaminating 4.7 times slower than the free DNA, whereas the T=^{m}C CPD positioned away or facing outside from the histone core particle surface deaminating 8.9 times faster compared with the free DNA (Table 3.5). The relative reactivity of the two T=^{m}C CPDs toward deamination parallels the relative reactivity of the two T=^{m}C CPD sites to hydroxyl radical cleavage, but we believe for a different reason. Although hydroxyl radical cleavage of DNA results mainly from initial abstraction of the hydrogens on the sugar backbone of DNA (49), deamination of an ^{m}C in a *cis*-*syn*-cyclobutane pyridimine dimer involves attack of water on the C4 carbon (20), which lies in the major groove of the DNA.

Hydroxyl radical cleavage mainly involves attack at the C5'position and 2–5-fold less at the other sugar sites in the order C4' > C3' > C2'> C1' (49). Maximum inhibition occurs when these hydrogens face toward the histone core surface, which sterically blocks the approach of the hydroxyl radical. Conversely, maximum cleavage is observed when the sugar hydrogens face out toward the solvent. When hydroxyl radical cleavage at a CPD is minimal (inside position), the sugar phosphate backbone faces the histone surface, but the C4 carbon of the ^{m}C faces in a direction parallel with the surface (Figure 3.13). On the other hand, when hydroxyl radical cleavage at the CPD is maximal (outside position), the sugar phosphate backbone faces away from the histone surface, but the C4 position of the ^{m}C faces in a direction parallel with the surface but in an opposite direction when compared with the CPD in the inside position (Figure 3.13).

Analysis of the crystal structure of a nucleosome core particle shows that the C4 position of what would be the ^{m}C of both the IN and the OUT CPDs is unobstructed by protein within a radius of 8.5 A (1KX5.pdb) (50). The same would be expected to hold true for the CPDs as the 3’-pyrimidine of a CPD has been found to adopt roughly the same position as it does in the undamaged DNA (38). Thus, the C4 position of the ^{m}C of both the facing inside and the facing outside T=^{m}C CPDs would appear to be in a similar, unobstructed environment, suggesting that factors other than steric interference by the histone proteins must play a role in inhibiting or enhancing the ^{m}C deamination of the T=^{m}C CPDs.

Previous studies of the deamination of C have found that deamination can be both inhibited and enhanced by protein binding. In one case, the α/β-type small, acid-soluble proteins of *Bacillus subtilis* spores have been found to suppress deamination by as much as 10-fold (51). It was suggested that the protein might be inhibiting deamination by a variety of means, such as restricting the “breathing” of the DNA, excluding water from the DNA, or enforcing an A conformation on the DNA. In a subsequent study, a restriction enzyme was found to both suppress and enhance deamination of Cs within its binding site by 7- and 15-fold, respectively (52). The large enhancement was proposed to arise from enzyme-mediated flipping of one of the Cs out of the helix. In addition, we recently showed that the methyl CpG binding domain of MeCP2 drastically inhibited deamination of a T=^{m}CG CPD, most probably by restricting attack of water on the CPD (53).

In the case of the nucleosome, it may be that the same factors that increase CPD formation at outside positions also increase the deamination rate. It has been shown that CPD dimers form preferentially in outside positions in protein-free DNA loops, demonstrating that a DNA curvature rather than protein-DNA contact is controlling reactivity (34). It was suggested that the facing inside positions of curved DNA are more compressed and less mobile, whereas the facing outside positions are less compressed and more mobile. Thus, although the C4 positions of the ^{m}C in the facing inside and facing outside CPDs may be in similar steric environments, the increased flexibility and/or more open conformation of the outside position may facilitate protonation of N3 and/or attack by water at C4. Conversely, protonation of N3 or attack of water on C4 might be inhibited by restricted movements and the compressed nature of a facing inside CPD site. It is interesting to note that the observed rate of deamination of the facing outside CPD is very similar to if not faster than what we observed for a CPD with the same flanking bases in single strand DNA ($t_{1/2}$ = 1.57h *versus* 3.5 h). This could indicate that CPD might be able to flip out of the helix or is being held in a favorable conformation for deamination. A more detailed study of CPDs in different rotational and translational positions will be required to sort out these effects, which would be elucidated in following chapters.

The 8.9-fold increase in the rate of deamination of an outside T^{m}CG dimer when compared with a 4.7-fold decrease for the inside dimer corresponds to an overall 42-fold difference in rate. When one couples the difference in deamination rate with a 2-fold enhancement of outside CPD formation, there would appear to be an 84-fold higher propensity for a UVB induced ^{m}C to T mutation at an outside TmCG site when compared with an inside site. Given that little difference has been observed in excision repair rates between inside and outside TT CPDs (41), the large difference in deamination rates could explain, at least in part, the origin of UV mutation hotspots and cold spots in phased nucleosomes that would arise following polymerase η bypass. On the other hand, deamination of an ^{m}C-containing CPD will result in a T/G mismatch, which has been shown to destabilize the DNA duplex by 0.7 kcal/mol (54). This duplex destabilization may be able to further destabilize the nucleosome, which has already been shown to be destabilized by 0.14–0.24 kcal/mol by a TT CPD (41), and facilitate recognition by histone modification and/or excision repair systems. The extent of nucleosome destabilization, and hence recognition, may depend, however, on the nucleosome rotational position of the mismatch. Deaminated C-containing CPDs have been shown to be much more readily detected and repaired than TT CPDs (55, 56).

In a word, we have found that the nucleosome rotational positioning of a T^{m}CG CPD in a nucleosome greatly affects its deamination rate, and this may explain at least in part the origin of UV mutation hotspots and coldspots in phased nucleosomes. Deamination of CPDs may also be accelerated in unphased nucleosomes if the CPDs are in dynamic exchange with outside positions. It remains to been seen how the nucleosome affects the deamination rate of C^{m}CG CPDs, which are much more slowly deaminated than T^{m}CG CPDs in free DNA (24), as well as the deamination of (6-4) and Dewar DNA photoproducts, which also form at this site (22). Nucleosome rotational positioning is also expected to affect the spontaneous deamination of C and ^{m}C and their more readily deaminated oxidized products, as well as the chemistry of many other bases and adducts.

Conclusions

We have found that the rotational position of a T^{m}CG CPD in a nucleosome greatly affects its deamination rate, and this may explain at least in part the origin of UV mutation hotspots and coldspots in phased nucleosomes. Deamination of CPDs may also be accelerated in unphased nucleosomes if the CPDs are in dynamic exchange with outside positions. It remains to been seen how the nucleosome affects the deamination rate of C^{m}CG CPDs, which are much more slowly deaminated than T^{m}CG CPDs in free DNA, as well as the deamination of (6-4) and Dewar DNA photoproducts, which also form at this site. Rotational positioning is also expected to affect the spontaneous deamination of C and ^{m}C and their more readily deaminated oxidized products, as well as the chemistry of many other bases and adducts.

Acknowledgment

We thank Aziz Sancar for a gift of photolyase, Stephen Lloyd for a gift of T4 endonuclease V, and Michael Smerdon for a detailed protocol for preparation of the nucleosome core particles. We also thank John Hinz and Zeljko Svedruzic for helpful discussions on the design of the substrates.

References

1. Brash, D. E., Rudolph, J. A., Simon, J. A., Lin, A., McKenna, G. J., Baden, H. P., Halperin, A. J., and Pontén, J. A role for sunlight in skin cancer: UV-induced p53 mutations in squamous cell carcinoma. *Proc. Natl. Acad. Sci. U.S.A.* **1991,** *88*, 10124–10128.

2. Ziegler, A., Leffell, D. J., Kunala, S., Sharma, H. W., Gailani, M., Simon, J. A., Halperin, A. J., Baden, H. P., Shapiro, P. E., Bale, A. E., and Brash, D. E. Mutation hotspots due to sunlight in the p53 gene of non-melanoma skin cancers. *Proc. Natl. Acad. Sci. U.S.A.* **1993,** *90*, 4216–4220.

3. Giglia-Mari, G., and Sarasin, A. TP53 mutations in human skin cancers. *Hum. Mutat.* **2003,** *21*, 217–228.

4. Pfeifer, G. P., You, Y. H., and Besaratinia, A. Mutations induced by ultraviolet light. *Mutat. Res.* **2005,** *571*, 19–31.

5. Yoon, J. H., Lee, C. S., O'Connor, T. R., Yasui, A., and Pfeifer, G. P. The DNA damage spectrum produced by simulated sunlight. *J. Mol. Biol.* **2000,** *299*, 681–693.

6. You, Y. H., and Pfeifer, G. P. Similarities in sunlight-induced mutational spectra of CpG-methylated transgenes and the p53 gene in skin cancer point to an important role of 5-methylcytosine residues in solar UV mutagenesis. *J. Mol. Biol.* **2001,** *305*, 389–399.

7. Cadet, J., Sage, E., and Douki, T. Ultraviolet radiation-mediated damage to cellular DNA *Mutat. Res.* **2005,** *571*, 3–17.

8. Douki, T., and Cadet, J. Individual determination of the yield of the main UV-induced dimeric pyrimidine photoproducts in DNA suggests a high mutagenicity of CC photolesions. *Biochemistry.* **2001,** *40*, 2495–2501.

9. Tommasi, S., Denissenko, M. F., and Pfeifer, G. P. Sunlight induces pyrimidine dimers preferentially at 5-methylcytosine bases. *Cancer Res.* **1997,** *57*, 4727–4730.

10. Drouin, R., and Therrien, J. P. UVB-induced cyclobutane pyrimidine dimer frequency correlates with skin cancer mutational hotspots in p53. *Photochem. Photobiol.* **1997,** *66*, 719–726.

11. You, Y. H., Li, C., and Pfeifer, G. P. Involvement of 5-methylcytosine in sunlight-induced mutagenesis. *J. Mol. Biol.* **1999,** *293*, 493–503.

12. You, Y. H., Szabó, P. E., and Pfeifer, G. P. Cyclobutane pyrimidine dimers form

preferentially at the major p53 mutational hotspot in UVB-induced mouse skin tumors. *Carcinogenesis.* **2000,** *21*, 2113–2117.

13. You, Y. H., Lee, D. H., Yoon, J. H., Nakajima, S., Yasui, A., and Pfeifer, G. P. Cyclobutane pyrimidine dimers are responsible for the vast majority of mutations induced by UVB irradiation in mammalian cells. *J. Biol. Chem.* **2001,** *276*, 44688–44694.

14. Washington, M. T., Johnson, R. E., Prakash, S., and Prakash, L. Accuracy of thymine-thymine dimer bypass by *Saccharomyces cerevisiae* DNA polymerase eta. *Proc. Natl. Acad. Sci. U.S.A.* **2000,** *97*, 3094–3099.

15. Yu, S. L., Johnson, R. E., Prakash, S., and Prakash, L. Requirement of DNA polymerase eta for error-free bypass of UV-induced CC and TC photoproducts. *Mol. Cell. Biol.* **2001,** *21*, 185–188.

16. McCulloch, S. D., Kokoska, R. J., Masutani, C., Iwai, S., Hanaoka, F., and Kunkel, T. A. Preferential *cis-syn* thymine dimer bypass by DNA polymerase eta occurs with biased fidelity. *Nature.* **2004,** *428*, 97–100.

17. Vu, B., Cannistraro, V. J., Sun, L., and Taylor, J. S. DNA synthesis past a 5-methylC-containing *cis-syn* cyclobutane pyrimidine dimer by yeast pol eta is highly nonmutagenic. *Biochemistry.* **2006,** *45*, 9327–9335.

18. Setlow, R. B. Cyclobutane-type pyrimidine dimers in polynucleotides. *Science.* **1966,** *153*, 379–386.

19. Fix, D., and Bockrath, R. Thermal resistance to photoreactivation of specific mutations potentiated in E. coli B/r ung by ultraviolet light. *Mol. Gen. Genet.* **1981,** *182*, 7–11.

20. Lemaire, D. G., and Ruzsicska, B. P. Kinetic analysis of the deamination reactions of cyclobutane dimers of thymidylyl-3',5'-2'-deoxycytidine and 2'-deoxycytidylyl-3',5'-thymidine. *Biochemistry.* **1993,** *32*, 2525–2533.

21. Tu, Y., Dammann, R., and Pfeifer, G. P. Sequence and time-dependent deamination of cytosine bases in UVB-induced cyclobutane pyrimidine dimers *in vivo*. *J. Mol. Biol.* **1998,** *284*, 297–311.

22. Douki, T., and Cadet, J. Formation of cyclobutane dimers and (6-4) photoproducts upon far-UV photolysis of 5-methylcytosine-containing dinucleotide monophosphates. *Biochemistry.* **1994,** *33*, 11942–11950.

23. Celewicz, L., Mayer, M., and Shetlar, M. D. The photochemistry of

thymidylyl-(3'-5')-5-methyl-2'-deoxycytidine in aqueous solution. *Photochem. Photobiol.* **2005,** *81*, 404–418.

24. Cannistraro, V. J., and Taylor, J. S. Acceleration of 5-methylcytosine deamination in cyclobutane dimers by G and its implications for UV-induced C-to-T mutation hotspots. *J. Mol. Biol.* **2009,** *392*, 1145–1157.

25. Frederico, L. A., Kunkel, T. A., and Shaw, B. R. A sensitive genetic assay for the detection of cytosine deamination: determination of rate constants and the activation energy. *Biochemistry.* **1990,** *29*, 2532–2537.

26. Shen, J. C., Rideout, W. M., 3rd, and Jones, P. A. The rate of hydrolytic deamination of 5-methylcytosine in double-stranded DNA. *Nucleic. Acids. Res.* **1994,** *22*, 972–976.

27. Taylor, J. S., and O'Day, C. L. *Cis-syn* thymine dimers are not absolute blocks to replication by DNA polymerase I of Escherichia coli in vitro. *Biochemistry.* **1990,** *29*, 1624–1632.

28. Jiang, N., and Taylor, J. S. *In vivo* evidence that UV-induced C-->T mutations at dipyrimidine sites could result from the replicative bypass of cis-syn cyclobutane dimers or their deamination products. *Biochemistry.* **1993,** *32*, 472–481.

29. Lee, D. H., and Pfeifer, G. P. Deamination of 5-methylcytosines within cyclobutane pyrimidine dimers is an important component of UVB mutagenesis. *J. Biol. Chem.* **2003,** *278*, 10314–10321.

30. Luger, K. Dynamic nucleosomes. *Chromosome Res.* **2006,** *14*, 5–16.

31. Luger, K., Ma¨der, A. W., Richmond, R. K., Sargent, D. F., and Richmond, T. J. Crystal structure of the nucleosome core particle at 2.8 A resolution. *Nature.* **1997,** *389*, 251–260.

32. Gale, J. M., Nissen, K. A., and Smerdon, M. J. UV-induced formation of pyrimidine dimers in nucleosome core DNA is strongly modulated with a period of 10.3 bases. *Proc. Natl. Acad. Sci. U.S.A.* **1987,** *84*, 6644–6648.

33. Pehrson, J. R. Thymine dimer formation as a probe of the path of DNA in and between nucleosomes in intact chromatin. *Proc. Natl. Acad. Sci. U.S.A.* **1989,** *86*, 9149–9153.

34. Pehrson, J. R., and Cohen, L. H. Effects of DNA looping on pyrimidine dimer formation. *Nucleic. Acids Res.* **1992,** *20*, 1321–1324.

35. Becker, M. M., and Wang, Z. Origin of ultraviolet damage in DNA. *J. Mol. Biol.* **1989,** *210*, 429–438.

36. Pfeifer, G. P. Formation and processing of UV photoproducts: effects of DNA sequence and chromatin environment. *Photochem. Photobiol.* **1997,** *65*, 270–283.

37. Suquet, C., and Smerdon, M. J. UV damage to DNA strongly influences its rotational setting on the histone surface of reconstituted nucleosomes. *J. Biol. Chem.* **1993,** *268*, 23755–23757.

38. Park, H., Zhang, K., Ren, Y., Nadji, S., Sinha, N., Taylor, J. S., and Kang, C. Crystal structure of a DNA decamer containing a *cis-syn* thymine dimer. *Proc. Natl. Acad. Sci. U.S.A.* **2002,** *99*, 15965–15970.

39. Kosmoski, J. V., and Smerdon, M. J. Synthesis and nucleosome structure of DNA containing a UV photoproduct at a specific site. *Biochemistry.* **1999,** *38*, 9485–9494.

40. Kosmoski, J. V., Ackerman, E. J., and Smerdon, M. J. DNA repair of a single UV photoproduct in a designed nucleosome. *Proc. Natl. Acad. Sci. U.S.A.* **2001,** *98*, 10113–10118.

41. Svedruziʹç Z. M., Wang, C., Kosmoski, J. V., and Smerdon, M. J. Accommodation and repair of a UV photoproduct in DNA at different rotational settings on the nucleosome surface. *J. Biol. Chem.* **2005,** *280*, 40051–40057; Correction. *J. Biol. Chem.* **2010,** *285*, 39574.

42. Thoma, F. Repair of UV lesions in nucleosomes--intrinsic properties and remodeling. *DNA Repair.* **2005,** *4*, 855–869.

43. Wang, Z. G., Wu, X. H., and Friedberg, E. C. Nucleotide excision repair of DNA by human cell extracts is suppressed in reconstituted nucleosomes. *J. Biol. Chem.* **1991,** *266*, 22472–22478.

44. Hara, R., and Sancar, A. Effect of damage type on stimulation of human excision nuclease by SWI/SNF chromatin remodeling factor. *Mol. Cell. Biol.* **2003,** *23*, 4121–4125.

45. Liu, X., and Smerdon, M. J. Nucleotide excision repair of the 5 S ribosomal RNA gene assembled into a nucleosome. *J. Biol. Chem.* **2000,** *275*, 23729–23735.

46. Ober, M., and Lippard, S. J. Cisplatin damage overrides the predefined rotational setting of positioned nucleosomes. *J. Am. Chem. Soc.* **2007,** *129*, 6278–6286.

47. Li, Q., and Wrange, O. Translational positioning of a nucleosomal glucocorticoid

response element modulates glucocorticoid receptor affinity. *Genes Dev.* **1993,** *7*, 2471–2482.

48. Li, Q., and Wrange, O. Accessibility of a glucocorticoid response element in a nucleosome depends on its rotational positioning. *Mol. Cell. Biol.* **1995,** *15*, 4375–4384.

49. Balasubramanian, B., Pogozelski, W. K., and Tullius, T. D. DNA strand breaking by the hydroxyl radical is governed by the accessible surface areas of the hydrogen atoms of the DNA backbone. *Proc. Natl. Acad. Sci. U.S.A.* **1998,** *95*, 9738–9743.

50. Davey, C. A., Sargent, D. F., Luger, K., Maeder, A. W., and Richmond, T. J. Solvent mediated interactions in the structure of the nucleosome core particle at 1.9 a resolution. *J. Mol. Biol.* **2002,** *319*, 1097–1113.

51. Sohail, A., Hayes, C. S., Divvela, P., Setlow, P., and Bhagwat, A. S. Protection of DNA by alpha/beta-type small, acid-soluble proteins from Bacillus subtilis spores against cytosine deamination. *Biochemistry.* **2002,** *41*, 11325–11330.

52. Carpenter, M., Divvela, P., Pingoud, V., Bujnicki, J., and Bhagwat, A. S. Sequence-dependent enhancement of hydrolytic deamination of cytosines in DNA by the restriction enzyme PspGI. *Nucleic Acids Res.* **2006,** *34*, 3762–3770.

53. Cannistraro, V. J., and Taylor, J. S. Methyl CpG binding protein 2 (MeCP2) enhances photodimer formation at methyl-CpG sites but suppresses dimer deamination. *Nucleic. Acids. Res.* **2010,** *38*, 6943–6955.

54. Jing, Y., Kao, J. F., and Taylor, J. S. Thermodynamic and base-pairing studies of matched and mismatched DNA dodecamer duplexes containing *cis-syn*, (6-4) and Dewar photoproducts of TT. *Nucleic. Acids. Res.* **1998,** *26*, 3845–3853.

55. Mu, D., Tursun, M., Duckett, D. R., Drummond, J. T., Modrich, P., and Sancar, A. Recognition and repair of compound DNA lesions (base damage and mismatch) by human mismatch repair and excision repair systems. *Mol. Cell. Biol.* **1997,** *17*, 760–769.

56. Sugasawa, K., Okamoto, T., Shimizu, Y., Masutani, C., Iwai, S., and Hanaoka, F. A multistep damage recognition mechanism for global genomic nucleotide excision repair. *Genes Dev.* **2001,** *15*, 507–521.

57. Song, Q., Cannistraro, V. J., and Taylor, J. S. Rotational position of a 5-methylcytosine-containing cyclobutane pyrimidine dimer in a nucleosome greatly affects its deamination rate. *J. Biol. Chem.* **2011,** *286*, 6329–6335.

Table 3.1 Sequences used to assemble the 150-mer top strand for ds-IN.

ds-IN top strand	
ODN	Sequence
ts1	TGT TAG AGC CTG TAA CTC GGT GTT AGA GCC TGT AAC TCG
ts2_IN	GTG TTA GAG CCT GTA ACT CGG TGA TTG TAC AT^{M}C GTG T
ts3_IN	^{M}**C**G TAG CCT GTA ACA GCC TGT TAG AGC CTG TAA CTC
ts4	GGT GTT AGA GCC TGT AAC TCG GTG TTA GAG CCT GTA ACT
ts12	GCT CTA ACA CCG AGT TAC AG
ts23_IN	ACA GGC TAC GAC ACG ATG TA
ts4	CTC TAA CAC CGA GTT ACA GG

Table 3.2 Sequences used to assemble the 150-mer top strand for ds-OUT.

ds-OUT top strand	
ODN	Sequence
ts1	TGT TAG AGC CTG TAA CTC GGT GTT AGA GCC TGT AAC TCG
ts2_OUT	GTG TTA GAG CCT GTA ACT CGG TGA TTG TAC AT
ts3_OUT	$^{\mathrm{M}}$**C**G TGT $^{\mathrm{M}}$CG TAG CCT GTA ACA GCC TGT TAG AGC CTG TAA CTC
ts4	GGT GTT AGA GCC TGT AAC TCG GTG TTA GAG CCT GTA ACT
ts12	GCT CTA ACA CCG AGT TAC AG
ts23_OUT	ACA GGC TAC GAC ACG ATG TA
ts4	CTC TAA CAC CGA GTT ACA GG

Table 3.3 Sequences used to assemble the 150-mer top strand for ds-Control.

ds-Control top strand	
ODN	Sequence
ts1	**T**GT TAG AGC CTG TAA CTC GGT GTT AGA GCC TGT AAC TCG
ts2_Control	GTG TTA GAG CCT GTA ACT CGG TGA TTG TAC AT^{M}C GTG T
ts3_Control	^{M}CG TAG CCT GTA ACA GCC TGT TAG AGC CTG TAA CTC
ts4	GGT GTT AGA GCC TGT AAC TCG GTG TTA GAG CCT GTA ACT
ts12	GCT CTA ACA CCG AGT TAC AG
ts23_Control	ACA GGC TAC GAC ACG ATG TA
ts4	CTC TAA CAC CGA GTT ACA GG

Table 3.4 Sequences used to assemble the 150-mer top bottom strands for ds-IN, ds-OUT and ds-Control.

ds-IN, ds-OUT and ds-Control bottom strand	
ODN	Sequence
cs1	AGT TAC AGG CTC TAA CAC CGA GTT ACA GGC TCT AA
cs2	CAC CGA GTT ACA GGC TCT AAC AGG CTG TTA CAG GCT ACG
cs3	ACA CGA TGT ACA ATC ACC GAG TTA CAG GCT CTA ACA C
cs4	CGA GTT ACA GGC TCT AAC ACC GAG TTA CAG GCT CTA ACA
cs12	TAA CTC GGT GTT AGA GCC TG
cs23	TAC ATC GTG TCG TAG CCT GT
cs4	CTG TAA CTC GGT GTT AGA GC

Table 3.5 Yields and deamination half lives of the T^{m}C CPDs in free and nucleosome-bound DNA (37°C, 50mM NaCl).

	Facing in yield [a] (%)	Facing out yield [a] (%)	Facing in half-life [b] $t_{1/2}$ (h)	Facing out half-life [b] $t_{1/2}$ (h)
Free	5.5, 5.5	13, 12	12.2 ± 0.9	14.0 ± 1.3
Nucleosome-bound	6.0 ± 0.5	26 ± 4	57.8 ± 5.1	1.57 ± 0.13
Fold change	1.1	2.1	4.7	0.11(1/8.9)

[a] Photoproduct yields for free DNA are from two independent experiments, and for nucleosome DNA, yields are the average of three independent experiments with the standard deviations shown.

[b] Deamination half-lives were the average of those calculated from linear least squares fits to two (free DNA) or three (nucleosome DNA) independent sets of deamination data (7–9 time points each), with the error shown derived from propagation of the standard deviations for each fit.

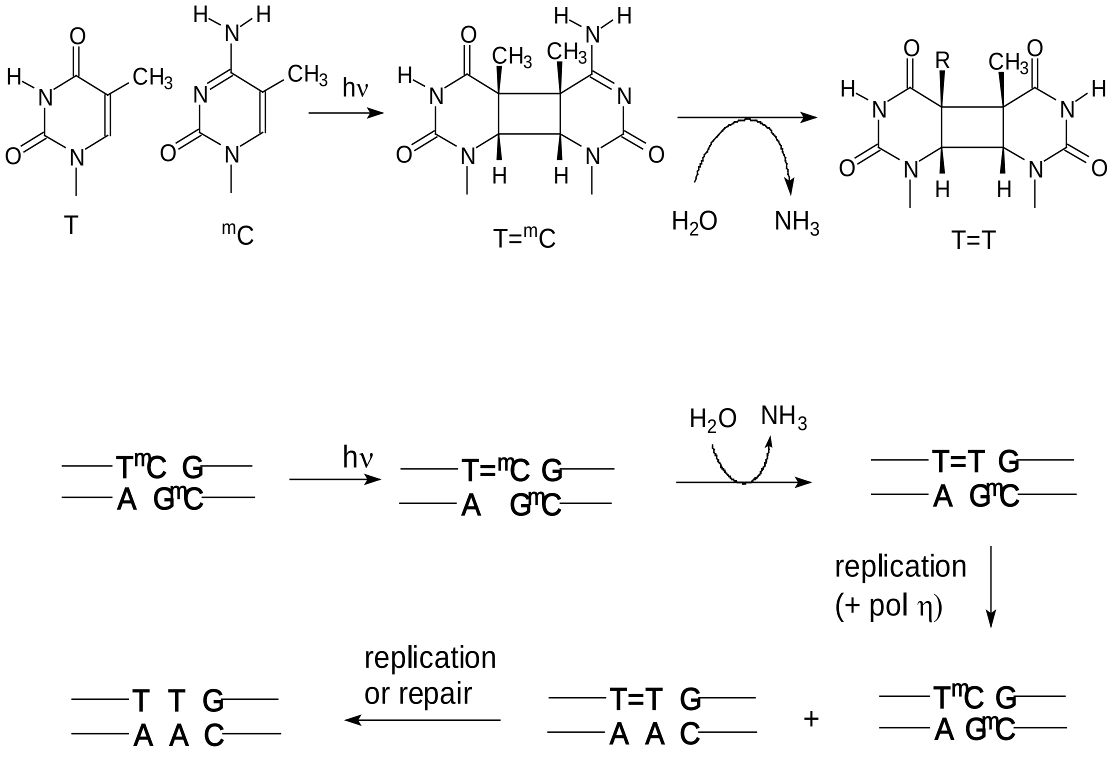

Figure 3.1 Mutagenic properties of ^{m}C-containing *cis-syn*-cyclobutane pyrimidine dimers and their deamination products.

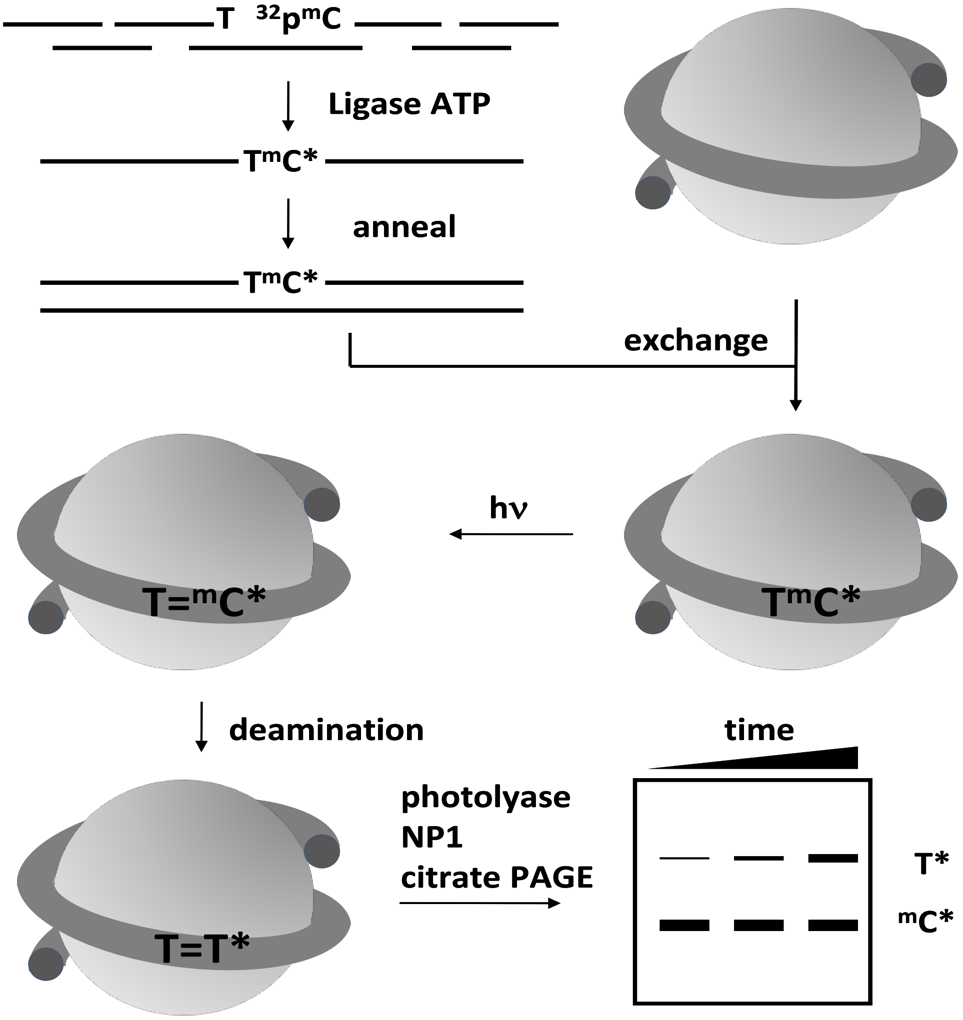

Figure 3.2 Strategy for determining the deamination rates of T^{m}CG CPDs in a nucleosome core particle.

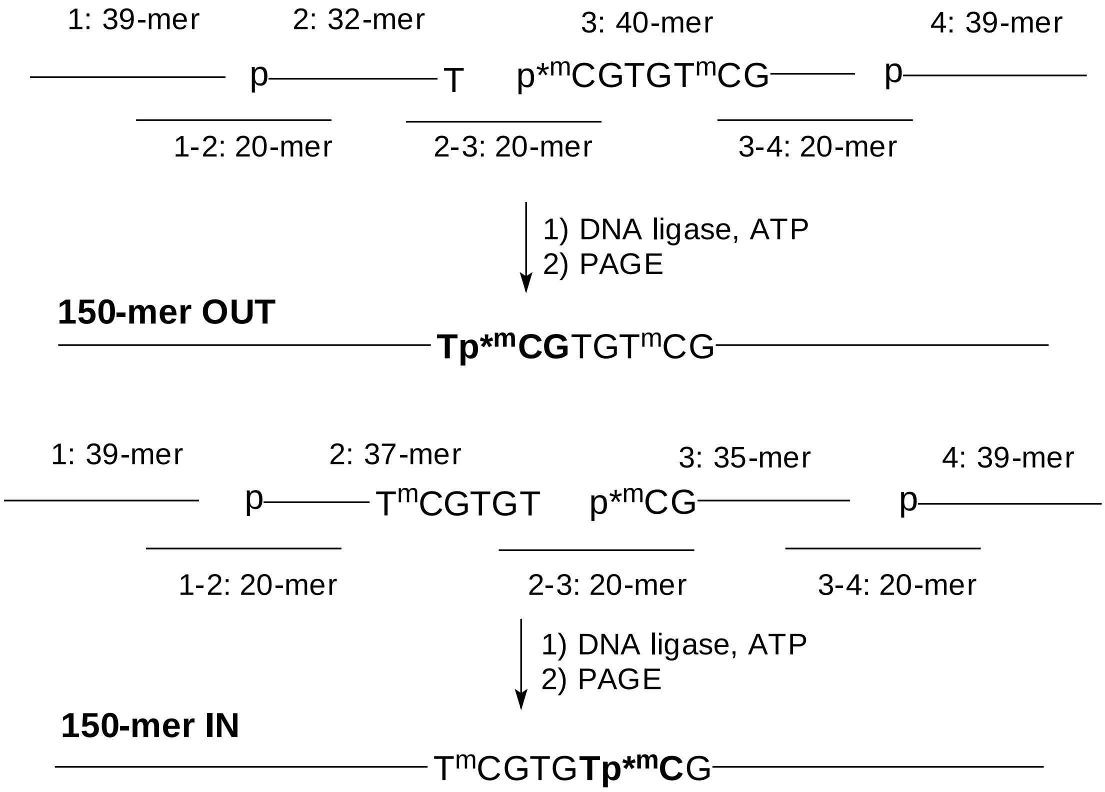

Figure 3.3 Ligation strategy for assembly of the 150-mer top strand substrates.

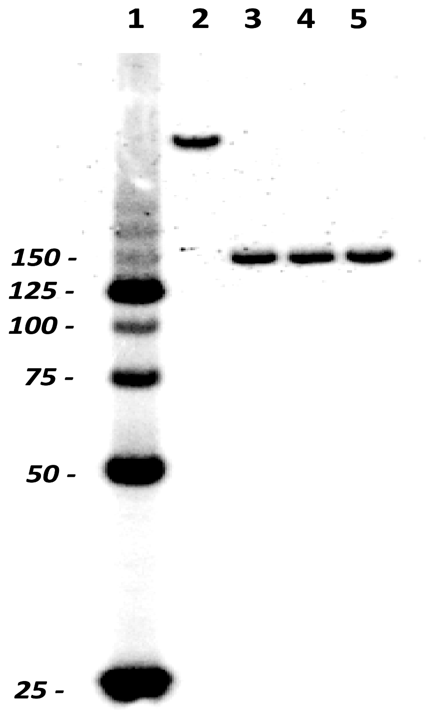

Lane 1: **25 bp DNA ladder**
Lane 2: **ss-control**
Lane 3: **ds-in**
Lane 4: **ds-out**
Lane 5: **ds-control**

Figure 3.4 Characterization and purification of the 150-mer DNA duplexes by native PAGE. The PAGE-purified single strand 150-mer substrates were annealed together to form duplexes and characterized by native gel electrophoresis on a 10% acrylamide, 0.3% bisacrylamide polyacrylamide gel in TBE. Lane 1: 25 bp DNA ladder, lane 2: 5’-endlabeled single strand 150-mer, lane 3: 150-mer duplex with internally ^{32}P-labeled facing out ^{m}C, lane 4: 150-mer duplex with internally ^{32}P-labeled facing in ^{m}C, lane 5: 5’-end labeled 150-mer. Each duplex substrate was isolated from the gel for further studies.

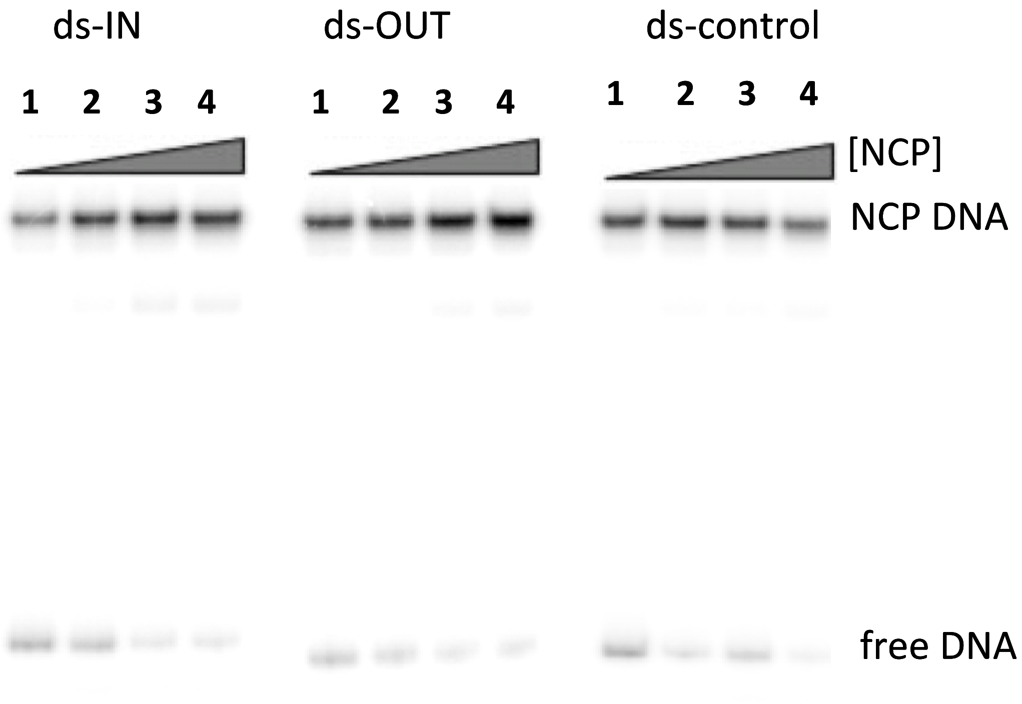

Figure 3.5 Reconstitution of the nucleosome core particles with the 150-merr DNA duplexes. The 150-mer DNA duplexes (10 nM) were incubated with increasing amounts of chicken erythrocyte nucleosome core particles (NCP) (lanes 1-4: 100, 200, 300, 500 nM) at room temperature in 2M NaCl at pH 7.5 for 2 h followed by dialysis overnight at 4°C in 50mM NaCl, with final equilibration at 55°C for 2 h. The reconstituted NCP were then electrophoresed on a native polyacrylamide gel (6% acrylamide, 0.2% bisacrylamide in TBE).

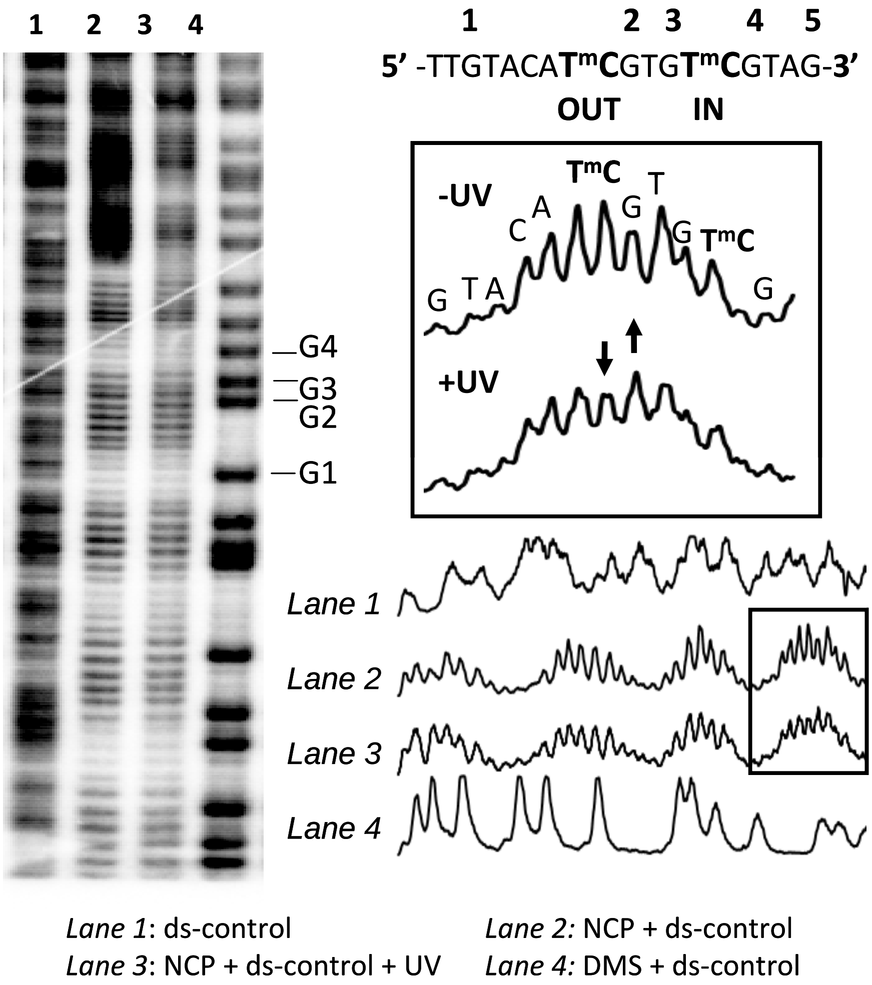

Figure 3.6 Hydroxyl radical footprinting of the reconstituted nucleosome core particles to determine phasing. The nucleosome core particle reconstituted with 5’-end-labeled 150-mer duplex DNA was subjected to hydroxyl radical footprinting and electrophoresed on a 7M urea, 10% acrylamide, 0.3% bisacrylamide denaturing gel. Lane 1, hydroxyl radical footprinting of the free DNA duplex; lane 2, hydroxyl radical footprinting of the nucleosome-bound DNA duplex; lane 3, hydroxyl radical footprinting of the nucleosome-bound duplex DNA after 1 h of irradiation at 302 nm at 4°C; lane 4, Maxam Gilbert G reaction on the free duplex. DMS: dimethyl sulfate.

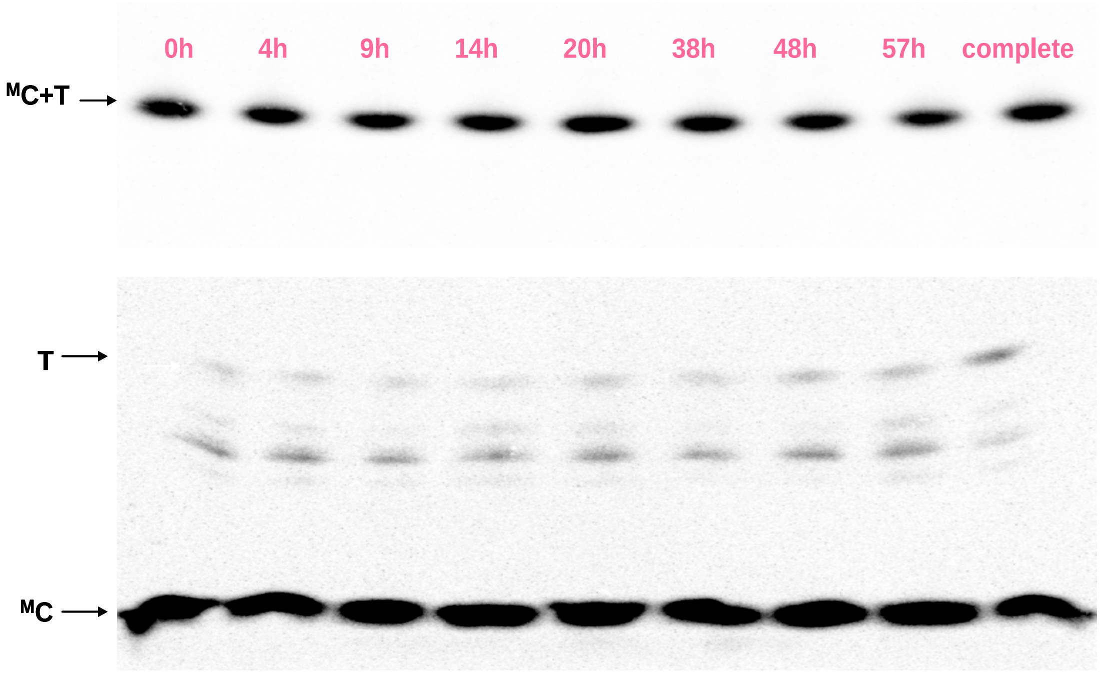

Figure 3.7 Deamination rate of T=^{m}C CPD in nucleosome-bound ds-IN using two-dimensional gel electrophoresis.

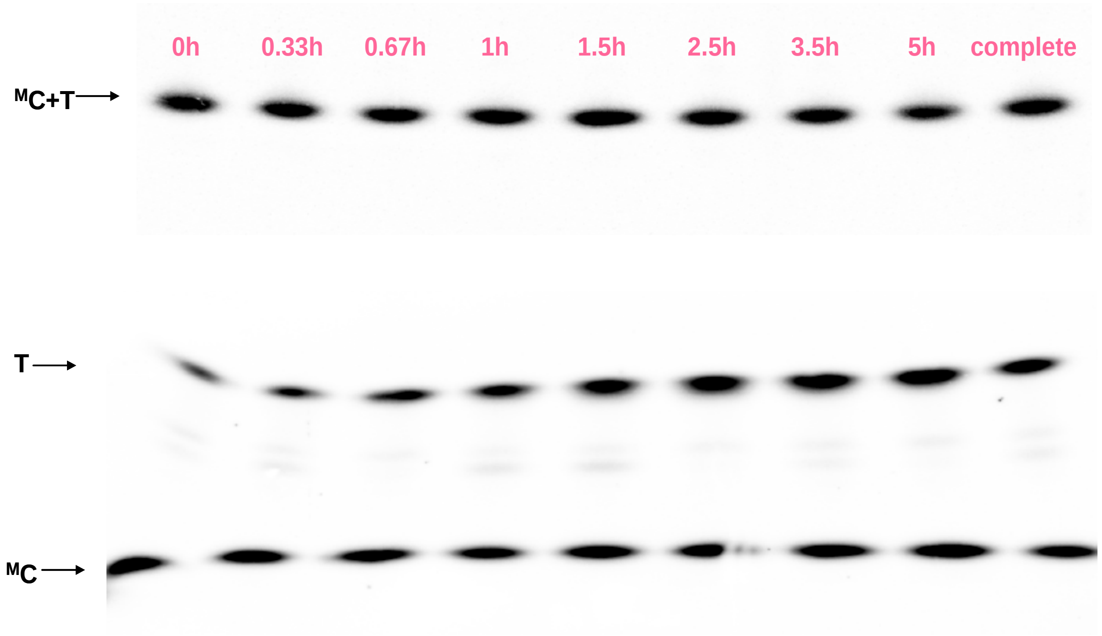

Figure 3.8 Deamination rate of T=^{m}C CPD in nucleosome-bound ds-OUT using two-dimensional gel electrophoresis.

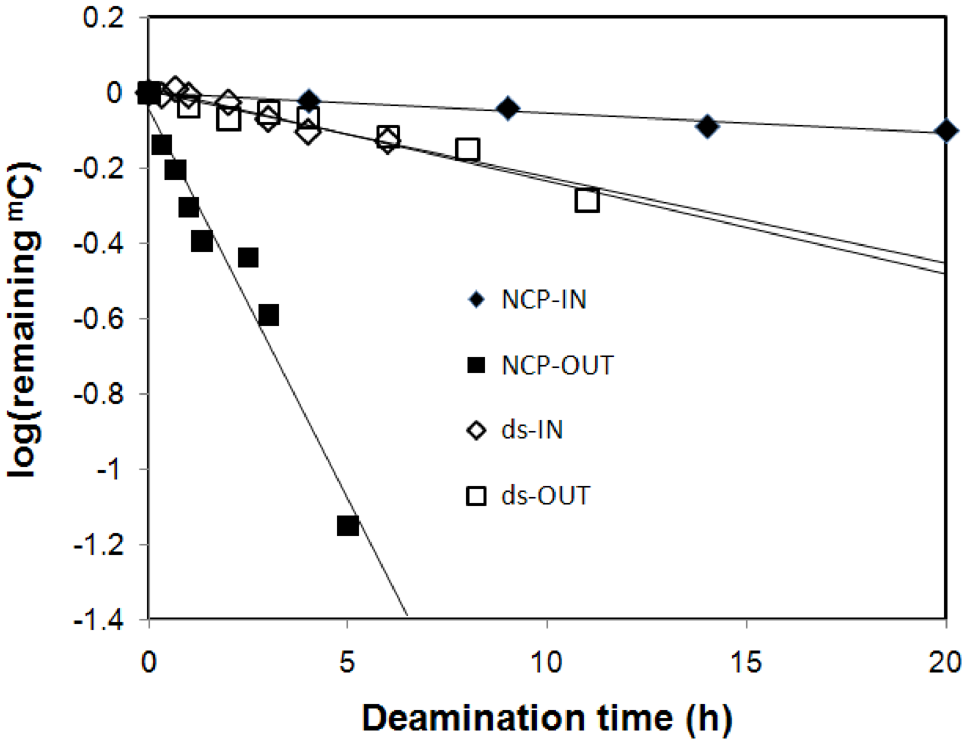

Figure 3.9 Deamination of the T=^{m}C CPDs in the free and nucleosome-bound 150-mer DNA duplexes. Plots of log (fraction of T=^{m}C CPD remaining) as a function of different deamination times for the gels shown in **Figure 3.6.1** and **Figure 3.6.2** and for the free 150-mer ds substrates, after correcting for background ^{32}P-T. Plots for other sets of independent measurements are given in **Figure 3.6.4** and **Figure 3.6.5**. The intermediate bands in the gels shown in **Figure 3.6.1** and **Figure 3.6.2** are due to non-photorevertible photoproduct-containing trinucleotides and incomplete digestion products and do not significantly affect the rate measurements.

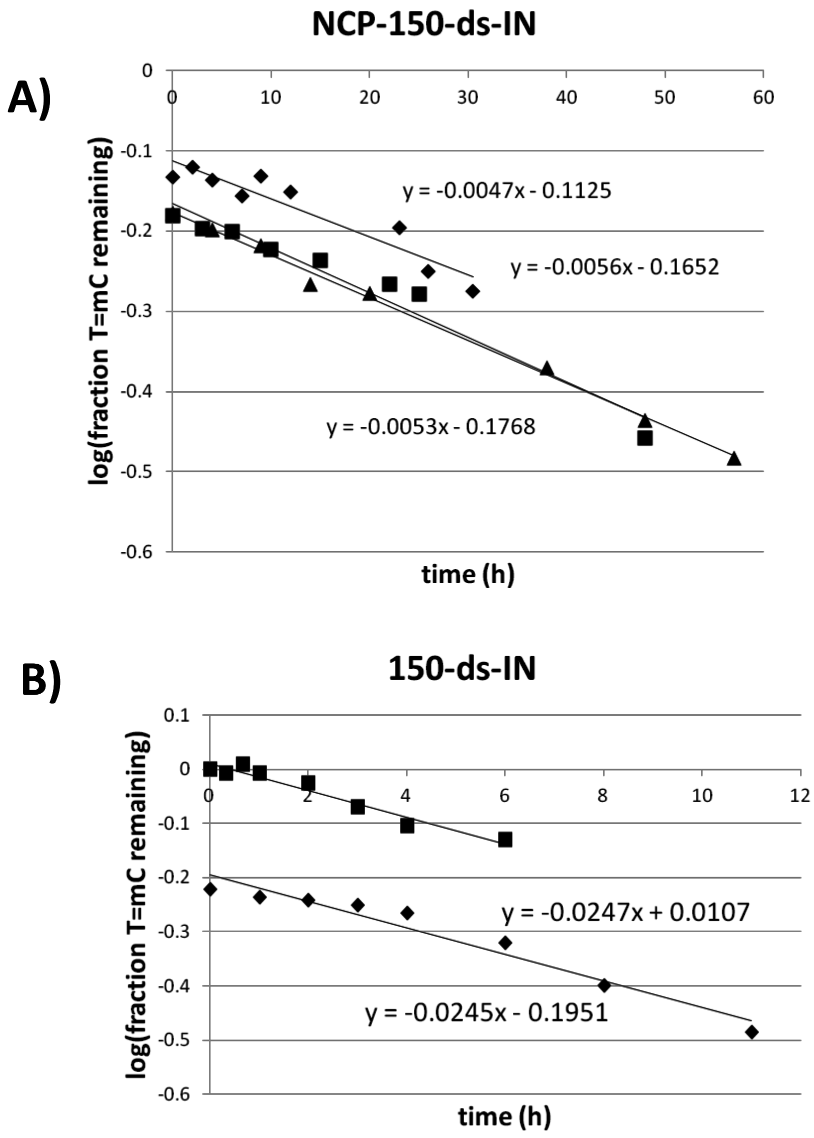

Figure 3.10 Linear regression analysis of the deamination rate data for GT^{m}CG CPD-IN. Plots of the individual deamination rate data as log (fraction T=^{m}C remaining) vs time for A): the nucleosome-bound ds-IN (NCP-150-ds-IN), and B): free 150-ds-IN. The non-zero intercept is due to contamination from ^{32}p-dT resulting from labeling the 5'-end of the DNA 150-mer as a result of incomplete heat inactivation of the kinase prior to ligation.

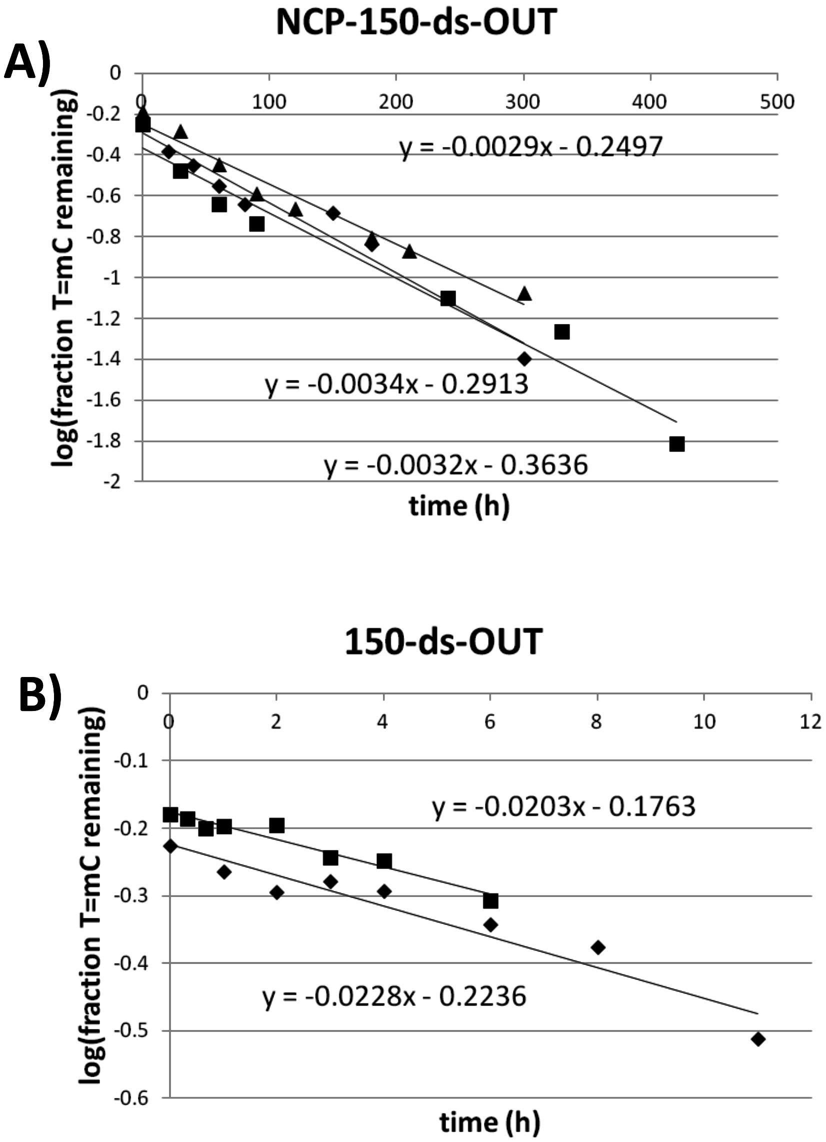

Figure 3.11 Linear regression analysis of the deamination rate data for AT^{m}CG CPD-OUT. Plots of the individual deamination rate data as log (fraction T=^{m}C remaining) vs time for A): the nucleosome-bound ds-OUT (NCP-150-ds-OUT), and B): free 150-ds-OUT. The non-zero intercept is due to contamination from ^{32}p-dT resulting from labeling the 5’-end of the DNA 150-mer as a result of incomplete heat inactivation of the kinase prior to ligation.

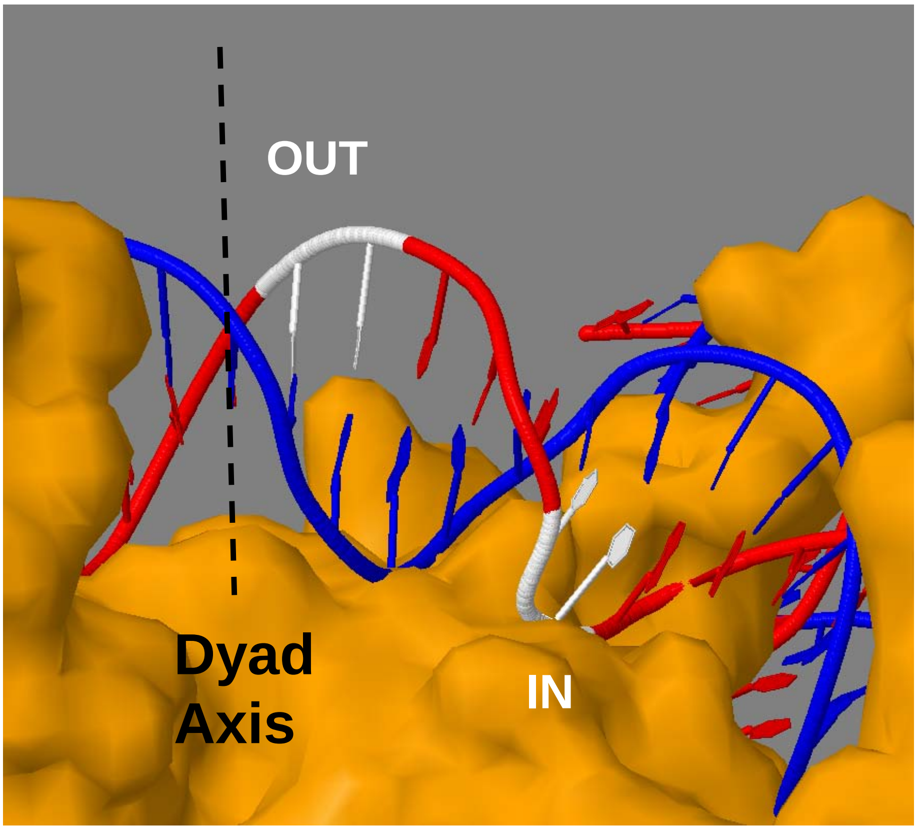

Figure 3.12 Nucleosome core particle structure highlighting in white the positions of the facing inside and outside T=^{m}CG CPD sites that are consistent with the hydroxyl radical foot-printing data. Brown color represents the histone proteins, red and blue color indicate the DNA duplex wrapping around the histone octamer surface. Black dashed line points out the dyad axis of the nucleosome core particle. White color highlights the two specific nucleosome rotational positionings.

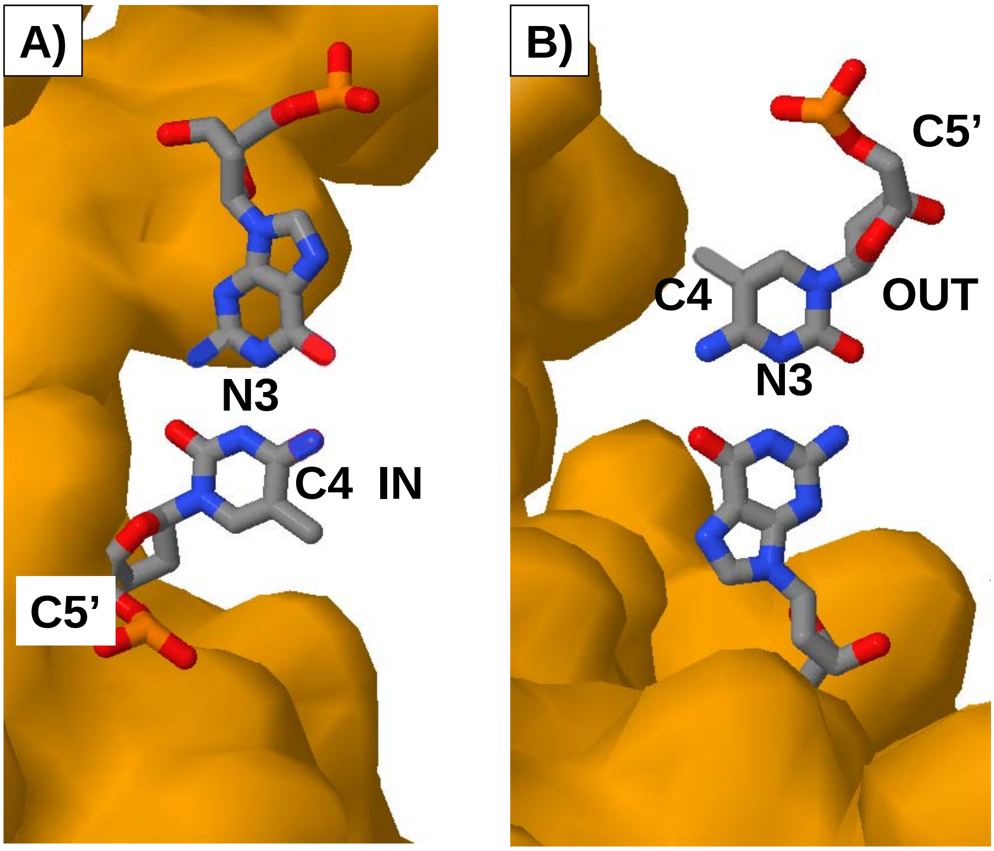

Figure 3.13 orientation of the ^{m}C:G base pair for the inside (*A*) and outside (*B*) T=^{m}C CPD sites. The structure was rendered from 1KX5.pdb (50) with Jmol using T1C2 and C6T7 of chain J to represent the outside and inside CPD sites with editing to produce the ^{m}C:G base pair.

Chapter 4

Modulation of T=^{m}C *Cis-Syn* CPD DNA Photoproduct Formation and Deamination Over a Full Helical Turn in a Reconstituted Nucleosome Core Particle

Abstract

C to T mutation hotspots in skin cancers occur primarily at methylated CpG sites that coincide with sites of UV-induced cyclobutane pyrimidine dimer (CPD) formation. We have previously shown a 45-fold greater deamination rate of a T=^{m}CG CPD with sugar phosphate backbone positioned away from the histone core surface than one positioned against the surface. We do not yet know if this represents the extremes of the range, or how the rate may vary in other positions, so in this chapter, we report the deamination rate of T=^{m}CG CPDs in one full helical turn at the dyad axis of the nucleosome core particle. We find that three out of the ten T=^{m}CG CPDs positioned inside the nucleosome core particle surface deaminated slower than the unbound sequence, with a maximum decrease in rate of 3.1-fold, whereas the other seven T=^{m}CG CPDs positioned outside the core particle surface deaminated faster than the unbound sequence, with a maximum increase in rate of 3.8-fold, corresponding to an overall 12-fold difference in deamination rate. We also replaced the G with A at two positions and surprisingly found that although the facing outside T=^{m}CA CPD still deaminated faster than the unbound sequence, the CPD facing inside only exhibited a 1.3-fold decrease in deamination rate. This discovery indicates that nucleosome rotational positioning could interfere with the accelerating function of the G at T=^{m}CG CPD, with the inside facing positioning greatly hindering the accelerating ability of flanking G on the deamination rate.

Introduction

Nucleosomes are the primary structural unit of chromatin in eukaryotic cells (1). Nucleosome core particles contain about 147 bp of DNA duplex, which wrap 1.7 times around a histone octamer, which is made up of two H2A, H2B, H3, and H4 histones (2). UV light preferentially induces the formation of CPD DNA photoproducts in nucleosomes at sites where the phosphodiester backbone is positioned away from the histone core particle surface and DNA bending is toward the major groove (3, 4). This preference is also seen for bent DNA that is not in contact with a protein (5) and has been attributed to the greater degree of rotational freedom in the phosphate backbone, making it easier for adjacent pyrimidines to adopt a photoreactive conformation (6, 7). When DNA containing randomly distributed CPDs is assembled into nucleosomes, the CPDs also favor positions away from the surface (8), which is consistent with the 30° bending that they make toward the major grove of DNA (9). Despite the distortion of DNA caused by CPDs, nucleosome core particles containing CPDs in different rotational settings can be readily prepared and isolated (10-12).

In Chapter 3, we have already determined the deamination rates for two T=^{m}CG CPDs with sugar phosphate backbones positioned against or away from the histone core surface and found a 45-fold difference in ^{m}C deamination rate (13). We do not yet know if this represents the extremes of the range, so in this chapter, we examined the deamination rate of T=^{m}CG CPDs in a full turn of the helix nucleosome core particle surface at the dyad axis. In chapter 3, we used a method for preparing IN and OUT facing CPDs (14, 15) that made use of nucleosome core particles isolated from chicken erythrocytes and a rotationally positioned 150-mer DNA based on a sequence by Li and Wrange (16). The 150-mer DNA substrate was prepared by ligation and contained repeating $(T/A)_3NN(G/C)_3NN$ sequences that insured a particular rotational setting of the DNA on the histone surface which was verified by hydroxyl radical foot-printing with EDTA. However, this 150-mer sequence appears to have been modified from the originally reported sequence (16) by the insertion of 3 extra nucleotides that puts the 3'-side slightly out of phase with the 5'-side. So in this chapter, we adapted the originally designed 147-mer sequence (14, 16), and made the center of the sequence coincide with the pseudodyad axis, so these 10 $T{=}^{m}CG$ sites would flank the pseudodyad axis on the nucleosome core particle surface.

The purpose of this study was to determine the full extent to which the rotational positioning of the $T{=}^{m}C$ CPD relative to the histone core particle surface affects the rate of ^{m}C to T deamination, and hence, its potential mutagenicity by a deamination bypass mechanism. To answer this question, we determined the deamination rate of a $T{=}^{m}CG$ CPD in ten different positions in a nucleosome core particle. We find that in a full turn of the nucleosome core particle surface, three out the ten $T{=}^{m}CG$ CPDs positioned against the nucleosome core particle surface deaminated more slowly than the unbound sequence, with a maximal decrease of 3.1-fold. The other seven $T{=}^{m}CG$ CPDs positioned away or outside the core particle surface, on the other hand, deaminated faster than the unbound sequence, with a maximum increase of 3.8-fold, corresponding to an overall 12-fold difference in terms of ^{m}C deamination rate, and not the 45-fold observed before.

Since we had previously observed that a G flanking the ^{m}C of a T^{m}C CPD site could increase the deamination rate in duplex DNA 40-fold compared with a flanking A, we also investigated the extent to which nucleosome rotational positioning would have on this rate. To study this we simply replaced the T^{m}CG with T^{m}CA in two 147-mer DNA duplexes corresponding to inside and outside facing positions. Surprisingly, we found that while the facing outside AT=^{m}CA DNA photoproduct still deaminated 3.1-fold faster than in the free DNA control, the inside facing AT=^{m}CA, didn't show a significant decrease in deamination rate like the AT=^{m}CG DNA photoproduct, This phenomenon indicates that nucleosome rotational positioning could interfere with the accelerating function of flanking G, with the inside facing position greatly hindering the accelerating effect of the flanking G on ^{m}C deamination rate.

Experimental Procedures

DNA Substrates

Similar to chapter 3, oligodeoxynucleotides (ODN) with or without 5'-terminal phosphates used in this chapter were purchased from Integrated DNA Technologies and purified by denaturing gel electrophoresis prior to ligation with T4 DNA ligase and ATP in the presence of complementary 20-mer ligation scaffolds (Table 4.1 to 4.12, Figure 4.1 to 4.5). The 147-mer single strand products were purified by denaturing PAGE. Complementary 147-mers were then annealed to form the 150-mer duplexes and purified by native PAGE (Figure 4.6).

Nucleosome Reconstitution

Nucleosome core particles were isolated and purified from chicken erythrocytes following a detailed procedure provided by the Dr. Michael Smerdon laboratory as described in Chapter 3. An equimolar ratio mixture of the ten 147-mer DNA duplexes ds-1, ds-2 to ds-10, and also individual 147-mer DNA duplexes NCP-1, NCP-2 to NCP-10, were reconstituted with the chicken nucleosome core particles by slow dialysis from high to low salt. Briefly, 10 nM 147-mer duplexes were incubated with an increasing amounts of nucleosome core particles (from 100 to 1000 nM) in a total volume of 500 µl, containing 2 M NaCl, 10mM Tris-HCl, 5 mM DTT, and 5 mM EDTA at pH 7.5 and room temperature for 2 h, and then dialyzed against 50 mM NaCl, 10 mM Tris-HCl, 1 mM DTT, pH 7.5, at 4°C, overnight. Finally, the reconstituted particles were recovered from the dialysis tubing and equilibrated at 55°C for 2 h to fix the nucleosome phasing. The reconstituted particles were assayed by native PAGE (6% acrylamide, 0.2% bisacrylamide in TBE), and the ratio of nucleosome-bound DNA to free DNA was quantified by the Quantity One software (Figure 4.6).

Hydroxyl Radical Foot-printing and Dimethylsulfate Mapping

Hydroxyl radical foot-printing was performed as described previously (17). Briefly, a 15 µL aliquot of 10mM sodium ascorbate, a 15 µL aliquot containing 1 mM $Fe(NH_4)_2(SO_4)_2\cdot 6H_2O$ and 2 mM EDTA, and 15 µL of a 0.12 % (w/w) H_2O_2 solution were premixed and added within 5 s to 105 µL of the nucleosome separately reconstituted with the equimolar ratio mixture of the 147-mer DNA duplexes ds-1 to ds-10. The reaction was incubated for 120 s at room temperature and stopped by the addition of 16µL of 50% (v/v) glycerol and 4µL of a 500mM EDTA solution. The samples were electrophoresed on a native gel (6 % acrylamide, 0.2 % bisacrylamide in TBE), and the nucleosome bands were electroeluted in TBE. The proteins were extracted with phenol:chloroform:isopropyl alcohol 25:24:1, and the DNA was precipitated with ethanol. The free ds-control was treated in a similar way, except that the reaction was quenched with a solution containing 1M sodium acetate, 120 mM thiourea, 300 µg/ml salmon sperm DNA, and 60 mM EDTA at pH 6.5 and then ethanol-precipitated. A Maxam-Gilbert G sequencing reaction was carried out on each 147-mer DNA duplex ds-1 to ds-10 in 50 mM cacodylate, 50 mM NaCl, 5 mM EDTA in the presence of 10 nM ds-control. For a 50 µL reaction, 0.5 µL of dimethyl sulfate was added to initiate the reaction, and 10 µL aliquots were removed over time and quenched by the addition of 50 µL of 1.5 M sodium acetate, 1 M mercaptoethanol and 50 µg of denatured salmon sperm DNA. The samples were ethanol-precipitated twice, and the resulting pellets were vacuum-dried and then solubilized in 100 µL of 1 M piperidine. The samples were then heated at 90°C in 1 M piperidine for 30 min and then evaporated to dryness at 60°C.

Deamination Rate Assay by Two-dimensional Gel Electrophoresis

The deamination rate was determined by adapting a previously described method (18). The equimolar ration mixture of free ds-1 to ds-10 and the individual nucleosome-bound internally ^{32}P-labeled 147-mer NCP-1 to NCP-10, and 147-mer NCP-1A, NCP-6A were irradiated with 302 nm UVB light at 4°C for 1 h and then adjusted to pH 7.2 with Mes buffer (0.5 M) and incubated at 37°C. Aliquots (10 µL) were removed at various times and quickly frozen on dry ice before storing overnight at -80°C. The remaining sample was adjusted to pH 6.5 with Mes buffer (0.5 M) and heated at 67°C overnight to complete the deamination. The aliquots were then warmed to room temperature, extracted with phenol:chloroform:isopropyl alcohol 25:24:1, ethanol-precipitated, redissolved in buffer containing 10 mM Tris-HCl, pH 7.5, 50 mM NaCl, 5 mM DTT, and photoreverted with photolyase and 365 nm light for 1 h. After photoreversion, the aliquots were treated with nuclease P1 to degrade the DNA to mononucleotides containing either $^{32}P^{m}dC$ or ^{32}P-dT, depending on the extent of deamination, and separated by two-dimensional gel electrophoresis. In the first dimension, electrophoresis on a 7M urea, a TBE gel was used to separate ^{32}P-^{m}dC and ^{32}P-dT, which co-migrate, from partially digested material and protein. For the second dimension, the gel surrounding the radioactive band containing the mononucleotides was excised, and a second gel containing 25 mM citric acid, pH 3.5, and 7 M urea was poured around the remaining gel slice. Electrophoresis on this gel separated $^{32}P^{m}dC$ from ^{32}P-dT with the ^{32}P-T migrating the fastest. The deamination rate constant for each nucleosome-bound NCP- 1 to 10 was obtained from the slope of a linear least squares fit of the log of the fraction of remaining $T^{m}C$ CPD *versus* deamination time. The fraction of $T^{m}C$ CPD remaining was calculated as 1- $(T/(T + {}^{m}C))/(T_{\infty}/(T_{\infty} + {}^{m}C))$ where $T_{\infty}/(T_{\infty} + {}^{m}C_{\infty})$ is the fraction $T/(T + {}^{m}C)$ in the fully deaminated sample. The yield of CPD photoproduct was calculated as the $T_{\infty}/(T_{\infty} + {}^{m}C_{\infty}) - T_0/(T_0 + {}^{m}C_0)$, where $T_0/(T_0 + {}^{m}C_0)$ is the fraction $T/(T + {}^{m}C)$ at time 0.

Results

Design and Synthesis of DNA Substrates

The substrate for this study was adapted from a previously described 147-mer sequence that was shown by hydroxyl radical foot-printing to have a well defined nucleosome translational and rotational positioning relative to the histone core surface.[12] The T=^{m}C CPDs were oriented by flanking the dimer-containing sequence with multiple TG motifs $(T/A)_3NN(G/C)_3$ that had been shown to position a glucocorticoid hormone-response element (GRE) with different orientations relative to the histone surface (20, 21). To study the effect of nucleosome rotational positioning on the deamination of T=^{m}C CPD on a full turn of the helix, we constructed ten 147-mer DNA duplexes, which contained ten T^{m}CG sites, varying from the first position in a 10-nucleotide nucleosomal turn to the 10th position in the turn.

To determine the deamination rates of the T^{m}C CPD at T^{m}CG and T^{m}C sites, we used the previously described method that requires that the ^{m}C to be 5’-^{32}P-end-labeled (Fig 4.1 to 4.5) (18). We therefore prepared the ten internally ^{32}P-labeled 147-mer DNA duplexes, NCP-1 to NCP-10, along with ten 5’-^{32}P-end-labeled control duplexes, ds-1 to ds-10. We also prepared the internally ^{32}P-labeled 147-mer DNA duplexes NCP-1A and NCP-6A in the same way. The duplexes were prepared by annealing the complementary 147-mer single strands that were prepared by ligating four oligodeoxynucleotides (ODN) together with T4 ligase and ATP in the presence of complementary ligation scaffolds (Figure 4.1 to 4.5). For

NCP-1 to NCP-10, NCP-1A and NCP-6A, the third ODN of the top strand was designed so that the ^{m}C could be 5'-^{32}P-end-labeled prior to ligation, and for ds-1 to ds-10, the first ODN of the top strand was 5'-^{32}P-end-labeled prior to ligation (Table 4.1 to 4.10).

Nucleosome Core Particle Reconstitution with the 147-mer DNA Duplexes

An equimolar ratio mixture of the ten 147-mer DNA duplexes ds-1, ds-2 to ds-10, and also individual 147-mer DNA duplexes NCP-1 to NCP-10, NCP-1A, NCP-6A were assembled into nucleosome core particles according to a previously described procedure that involves exchanging the DNA with that from chicken erythrocyte nucleosome core particles (NCPs) (10). The equimolar ratio mixture of ten 147-mer DNA duplexes were titrated with the NCPs and electrophoresed on a native gel to determine the NCP concentration needed to achieve maximal incorporation of the DNA into the NCP (Figure 4.7). We found that about 95% of 10 nM 147-mer DNA duplexes could be incorporated into 1000 nM nucleosome core particles.

Orientation of the T^{m}C Sites on the Nucleosome Core Particle

The hydroxyl radical cleavage intensity on the nucleosome core particle reconstituted with the mixture of ten 147-mer DNA duplexes ds-1 to ds-10 exhibited a very pronounced 10–11 bp periodicity (Figure 4.9). The cleavage sites were mapped onto the sequence by alignment with the DMS mapping on ds-1, ds-2 to ds-10 (Figure 4.9) and with the 10 bp DNA ladder (Figure 4.10). The ^{m}C of NCP-1, NCP-2 and NCP-10, which corresponded to 71, 72 and 80-mers in terms of length on ds-1, ds-2, and ds-10, were located in the minimal cleavage region, indicating that phosphodiester backbones of these three ^{m}Cs were facing inside (Figure 4.10, *boxed section*). The ^{m}C of NCP-3 through NCP-9, which corresponded to 73 to 79-mers in length on ds-3 through ds-9, were located in the maximal cleavage region, indicating that the phosphodiester backbones of these seven ^{m}Cs were facing outside (Figure 4.10, *boxed section*).

Deamination Rates of the T=^{m}C CPDs

The deamination rates for the three inside facing and seven outside facing T=^{m}CG CPDs were determined by following the conversion of ^{32}P-^{m}dC to ^{32}P-dT in the CPD by our enzyme-coupled two dimensional gel electrophoresis assay (18). In the first step, free or nucleosome-bound 147-mer DNA duplexes were irradiated with 302 nm light to produce the *cis-syn*-cyclobutane pyrimidine dimers (CPD) at the AT^{m}CG sites, along with other photoproducts, at 4°C to suppress deamination. The samples were then incubated at 37°C and pH 7.2 to allow for deamination for various times, and one was made to undergo complete deamination by lowering the pH to 6.5 and heating at 67°C, overnight. The aliquots were then incubated with *Escherichia coli* photolyase and visible light to specifically photorevert the *cis-syn*-CPDs and then treated with nuclease P1 to degrade all of the undamaged and photoreverted DNAs to mononucleotides. Non-photorevertible dipyrimidine photoproducts, such as (6-4) and Dewar DNA photoproducts, would only be digested to trinucleotides. The mononucleotides were then isolated by electrophoresis on a denaturing gel and subjected to a second electrophoresis on a pH 3.5 citrate gel (Figure 4.11 to 4.21, *top* *pictur*e) that separates the deaminated ^{32}P-T from the undeaminated ^{32}P-^{m}dC and quantified by radioisotopic imaging analysis.

The rate constants for ^{m}C deamination were then determined from the slopes of lines fit to the log of the fraction of remaining T^{m}CG CPD (Figure 4.11 to 4.21, *bottom picture*) as described in the Experimental Procedures section. The photoproduct yields were determined from the increase in the initial amount of radio-labeled T following complete deamination. The initial amount of T was non-zero in many cases and could be attributed to unwanted small fraction of deamination during the DNA purification through PCI (phenol:chloroform:isopropyl alcohol 25:24:1) extract and ethanol precipitation. Table 4.13 summarizes the deamination half-lives and yields of the T=^{m}CG CPDs in the ten different nucleosome rotational positions and in the free DNA format. When compared with the free DNA, the nucleosome decreases the rate of deamination of the in facing T=^{m}CG CPDs by a maximum factor of 3.1, whereas it increases the rate of deamination of the out facing T=^{m}C CPDs by a maximal factor of 3.8. When it comes to the photoproduct yield, the nucleosome decreases the formation of the inside T=^{m}CG CPDs by a maximal factor of 1.7 and enhanced the formation of the outside T=^{m}CG CPDs by a maximal factor of 1.9.

Deamination of the two T=^{m}CA CPDs did not behave in the same way as the corresponding T=^{m}CG CPDs. As shown in Figure 4.22 to 4.25, the deamination half-lives of ^{m}C in T=^{m}CA were calculated in the same way as for the T=^{m}CG CPDs, and is summarized in Table 4.14. While the out facing AT=^{m}CA DNA photoproduct deaminating 3.1-fold faster than in free DNA, the in facing AT=^{m}CA, unlike the corresponding AT=^{m}CG DNA photoproduct, didn't show any significant decrease in deamination rate, compared to free DNA. Compared with the 12-fold difference in deamination rate between in and out facing T=^{m}CG CPDs, the T=^{m}CA CPDs only exhibited a 4-fold difference in deamination rate.

Discussion

As mentioned earlier, we had already determined that there was a 45-fold effect on the deamination of ^{m}C to T in in and out facing T=^{m}CG CPDs (17). The goal of this study was to determine the effect of nucleosome positioning on the deamination rate of T=^{m}C CPD in a periodic full turn of DNA at the dyad axis. In order to achieve this goal, ten T=^{m}C CPDs which made up a full periodic turn on the histone core surface were prepared and studied. Three out of the ten CPDs were shown to have the phosphodiester backbone of the CPD facing against the histone core surface (IN) by hydroxyl radical footprinting, and the other seven CPDs were shown to have the backbone facing away from the surface (OUT). These ten positionings can be mapped onto a crystal structure of the nucleosome core particle as shown in Figure 4.29.

The photoreactivity of the ten T=^{m}CG sites in nucleosome-bound DNA duplexes (Table 4.13 & Figure 4.26) were partially consistent with the previous study as shown in Chapter 3. The out facing T=^{m}CG sites showed a maximum 1.8-fold increase when compared with the free DNA duplexes (22% vs 12% yield). However, instead of no effect as found in Chapter 3, the in facing T=^{m}CG sites exhibited a maximal 1.7-fold decrease when compared with the free DNA duplexes (6.9% vs 11.8%). A possible explanation for this difference could be that the in facing CPD sequence used in Chapter 3 was GT=^{m}CG , which only produced 5.5% CPD, which could make a small decrease in the nucleosome difficult to detect, compared to the AT=^{m}CG sequence, which produced 11.8% CPD in free DNA. The enhanced photoreactivity of the out facing positions is in agreement with the higher photoreactivity previously noted for dipyrimidine sites positioned away from the histone surface (3, 4).

On the other hand, the deamination rates of the ten T=^{m}CG CPD sites in the nucleosome were dramatically different from those in the free DNA. Consistent with the results in Chapter 3, T=^{m}CG CPDs positioned inside or against the nucleosome core particle deaminated much slower than in free DNA, with a maximum decrease of about 3.1-fold. The T=^{m}CG CPDs positioned outside or away from the nucleosome core particle deaminated faster than in free DNA, with a maximum increase about 3.7-fold (Table 4.13 & Figure 4.27). Interestingly, we did not observe as gradual change in ^{m}C deamination rates as observed for hydroxyl radical cleavage. Instead, there was a consistently high rate of ^{m}C deamination, with seven out of the ten T=^{m}CG sites having the deamination half-life ranging from 3.5 h to 15 h, as shown in Table 4.13, while the three innermost positions deaminated with half-lives between 36 h to 41 h. The biggest difference in ^{m}C deamination rates between the innermost and outmost positions was a factor of 12.

As mentioned in Chapter 3, hydroxyl radical cleavage of DNA results mainly from initial abstraction of the hydrogens from the sugar backbone of DNA (21), whereas deamination of an ^{m}C in a *cis-syn* cyclobutane pyrimidine dimer involves attack of water on the C4 carbon (22), which lies in the major groove of the DNA. Analysis of the crystal structure of a nucleosome core particle shows that the C4 position of what would be the ^{m}C of both the IN and the OUT CPDs is unobstructed by protein within a radius of 8.5 A (1KX5.pdb) (23). Thus, the C4 position of the ^{m}C in T=^{m}C CPDs of both the facing inside and facing outside positions would appear to be in a similar, unobstructed environment, suggesting other factors, but not steric interference by the histone proteins might play a role in inhibiting or enhancing deamination of the T=^{m}C CPDs. In the reconstituted nucleosome. It may be that the same factors that increase CPD formation at outside positions also enhance the deamination rate. CPD DNA photoproducts also form preferentially in outside positions in protein-free DNA loops, demonstrating that a DNA curvature rather than protein-DNA contact is controlling the DNA photo-reactivity (5). It was suggested that the inside positions of curved DNA could be more compressed and less mobile, whereas the outside positions were less compressed and more mobile. In this case, although the steric environment of C4 positions of the ^{m}C in both the inside and outside T=^{m}C CPDs might be similar, the facing outside positions might have an increased flexibility and/or more open conformation, which could facilitate N3 protonation and subsequent water attack at C4 position of the ^{m}C. On the other hand, protonation of N3 or attack of water on C4 of ^{m}C might be inhibited by restricted movements and the compressed nature of a facing inside T=^{m}C CPD.

When considering the large difference between the effect of flanking G and flanking A on the deamination rate of T=^{m}C CPD, it is possible that the nucleosome rotational positioning could interfere with the accelerating effect previously observed for flanking G in free DNA. Since the facing inside positions are more compressed and less mobile, it is possible that the interaction between ^{m}C and flanking G might not be in the optimal orientation could diminish the potential accelerating effect of the flanking G.

Conclusions

In this chapter, we have determined that the rotational position of T^{m}CG CPDs in a full turn of nucleosome greatly affects their deamination rate, and this may explain at least in part the origin of UV mutation hotspots and coldspots in phased nucleosomes. Three out of the ten T=^{m}CG CPDs positioned against or inside the nucleosome core particle surface deaminated slower than the free sequences, with a maximum decrease in rate of 3.1-fold. The other seven T=^{m}CG CPDs positioned away or outside the core particle surface deaminated faster than the free sequences, with a maximum increase of 3.8-fold, resuling in a maximum difference in rates between outside and inside positions of 12-fold. Surprisingly, after we replaced the G with A at the fastest and slowest deamination sites, the inside facing AT=^{m}CA CPD, unlike the AT=^{m}CG DNA photoproduct, didn’t show a significant decrease in deamination rate, whereas the outside facing AT=^{m}CA CPD deaminated 3.1-fold faster than the free DNA control. This result may indicate that nucleosome rotational positioning could interfere with the accelerating function of flanking G at T=^{m}C CPD, with the inside facing position greatly hindering the accelerating ability of flanking G in terms of ${}^{m}C$ deamination rate.

Acknowledgment

We thank Aziz Sancar for a gift of photolyase, Stephen Lloyd for a gift of T4 endonuclease V, and Michael Smerdon for a detailed protocol for preparation of the nucleosome core particles.

References

1. Luger, K. Dynamic nucleosomes. *Chromosome Res.* **2006,** *14*, 5–16.

2. Luger, K., Ma¨der, A. W., Richmond, R. K., Sargent, D. F., and Richmond, T. J. Crystal structure of the nucleosome core particle at 2.8 A resolution. *Nature.* **1997,** *389*, 251–260..

3. Gale, J. M., Nissen, K. A., and Smerdon, M. J. UV-induced formation of pyrimidine dimers in nucleosome core DNA is strongly modulated with a period of 10.3 bases. *Proc. Natl. Acad. Sci. U.S.A.* **1987,** *84*, 6644–6648.

4. Pehrson, J. R. Thymine dimer formation as a probe of the path of DNA in and between nucleosomes in intact chromatin. *Proc. Natl. Acad. Sci. U.S.A.* **1989,** *86*, 9149–9153.

5. Pehrson, J. R., and Cohen, L. H. Effects of DNA looping on pyrimidine dimer formation. *Nucleic. Acids Res.* **1992,** *20*, 1321–1324.

6. Becker, M. M., and Wang, Z. Origin of ultraviolet damage in DNA. *J. Mol. Biol.* **1989,** *210*, 429–438.

7. Pfeifer, G. P. Formation and processing of UV photoproducts: effects of DNA sequence and chromatin environment. *Photochem. Photobiol.* **1997,** *65*, 270–283.

8. Suquet, C., and Smerdon, M. J. UV damage to DNA strongly influences its rotational setting on the histone surface of reconstituted nucleosomes. *J. Biol. Chem.* **1993,** *268*, 23755–23757.

9. Park, H., Zhang, K., Ren, Y., Nadji, S., Sinha, N., Taylor, J. S., and Kang, C. Crystal structure of a DNA decamer containing a *cis-syn* thymine dimer. *Proc. Natl. Acad. Sci. U.S.A.* **2002,** *99*, 15965–15970.

10. Kosmoski, J. V., and Smerdon, M. J. Synthesis and nucleosome structure of DNA containing a UV photoproduct at a specific site. *Biochemistry.* **1999,** *38*, 9485–9494.

11. Kosmoski, J. V., Ackerman, E. J., and Smerdon, M. J. DNA repair of a single UV photoproduct in a designed nucleosome. *Proc. Natl. Acad. Sci. U.S.A.* **2001,** *98*, 10113–10118.

12. Svedruzi'ç Z. M., Wang, C., Kosmoski, J . V., and Smerdon, M. J. Accommodation and repair of a UV photoproduct in DNA at different rotational settings on the nucleosome surface. *J. Biol. Chem.* **2005,** *280*, 40051–40057; Correction, *J. Biol. Chem.* **2010,** *285*, 39574.

13. Song, Q., Cannistraro, V. J., and Taylor, J. S. Rotational position of a 5-methylcytosine-containing cyclobutane pyrimidine dimer in a nucleosome greatly affects its deamination rate. *J. Biol. Chem.* **2011,** *286,* 6329–6335.

14. Thoma, F. Repair of UV lesions in nucleosomes--intrinsic properties and remodeling. *DNA Repair.* **2005,** *4,* 855–869.

15. Wang, Z. G., Wu, X. H., and Friedberg, E. C. Nucleotide excision repair of DNA by human cell extracts is suppressed in reconstituted nucleosomes. *J. Biol. Chem.* **1991,** *266,* 22472–22478.

16. Hara, R., and Sancar, A. Effect of damage type on stimulation of human excision nuclease by SWI/SNF chromatin remodeling factor. *Mol. Cell. Biol.* **2003,** *23,* 4121–4125.

17. Ober, M., and Lippard, S. J. Cisplatin damage overrides the predefined rotational setting of positioned nucleosomes. *J. Am. Chem. Soc.* **2007,** *129,* 6278–6286.

18. Cannistraro, V. J., and Taylor, J. S. Acceleration of 5-methylcytosine deamination in cyclobutane dimers by G and its implications for UV-induced C-to-T mutation hotspots. *J. Mol. Biol.* **2009,** *392,* 1145–1157.

19. Li, Q., and Wrange, O. Translational positioning of a nucleosomal glucocorticoid response element modulates glucocorticoid receptor affinity. *Genes Dev.* **1993,** *7,* 2471–2482.

20. Li, Q., and Wrange, O. Accessibility of a glucocorticoid response element in a nucleosome depends on its rotational positioning. *Mol. Cell. Biol.* **1995,** *15,* 4375–4384.

21. Balasubramanian, B., Pogozelski, W. K., and Tullius, T. D. DNA strand breaking by the hydroxyl radical is governed by the accessible surface areas of the hydrogen atoms of the DNA backbone. *Proc. Natl. Acad. Sci. U.S.A.* **1998,** *95,* 9738–9743.

22. Lemaire, D. G., and Ruzsicska, B. P. Kinetic analysis of the deamination reactions of cyclobutane dimers of thymidylyl-3',5'-2'-deoxycytidine and 2'-deoxycytidylyl-3',5'-thymidine. *Biochemistry.* **1993,** *32,* 2525–2533.

23. Davey, C. A., Sargent, D. F., Luger, K., Maeder, A. W., and Richmond, T. J. Solvent mediated interactions in the structure of the nucleosome core particle at 1.9 a resolution. *J. Mol. Biol.* **2002,** *319,* 1097–1113.

Table 4.1 Oligonucleotide sequences used for 147-mer NCP-1.

NCP-1 top strand

ODN	Sequence
ts1	AGT TAT GTT AGA GCC TGT AAC TCG GTG TTA GAG CCT
ts2_1	GTA ACT CGG TGT TAG AGC CTG TAA CTC GGT GTA T
ts3_1	$^{\mathbf{M}}$**C**G ATG GTA TAG AGC CTG TAA CAG AAT GTT AGA GCC TGT AAC T
ts4	CGG TGT TAG AGC CTG TAA CTC GGT GTT AGA GCC TG
ts12	ACC GAG TTA CAG GCT CTA AC
ts23_1	TAT ACC ATC GAT ACA CCG AG
ts4	TCT AAC ACC GAG TTA CAG GC

NCP-1 bottom strand

ODN	Sequence
cs1	CAG GCT CTA ACA CCG AGT TAC AGG CTC TAA CAC CGA GTT
cs2_1	ACA GGC TCT AAC ATT CTG TTA CAG GCT CTA TAC CAT CGA TA
cs3	CAC CGA GTT ACA GGC TCT AAC ACC GAG TT
cs4	ACA GGC TCT AAC ACC GAG TTA CAG GCT CTA ACA TAA CT
cs12	TAG AGC CTG TAA CTC GGT GT
cs23_1	TAA CTC GGT GTA TCG ATG GT
cs4	TAG AGC CTG TAA CTC GGT GT

Table 4.2 Oligonucleotide sequences used for 147-mer NCP-2.

NCP-2 top strand	
ODN	Sequence
ts1	AGT TAT GTT AGA GCC TGT AAC TCG GTG TTA GAG CCT
ts2_2	GTA ACT CGG TGT TAG AGC CTG TAA CTC GGT GAT AT
ts3_2	^{M}**C**G ATA TGT ATA GCC TGT AAC AGA ATG TTA GAG CCT GTA ACT
ts4	CGG TGT TAG AGC CTG TAA CTC GGT GTT AGA GCC TG
ts12	ACC GAG TTA CAG GCT CTA AC
ts23_2	ATA CAT ATC GAT TAC ACC GA
ts4	TCT AAC ACC GAG TTA CAG GC

NCP-2 bottom strand	
ODN	Sequence
cs1	CAG GCT CTA ACA CCG AGT TAC AGG CTC TAA CAC CGA GTT
cs2_2	ACA GGC TCT AAC ATT CTG TTA CAG GCT ATA CAT ATC GAT AT
cs3	CAC CGA GTT ACA GGC TCT AAC ACC GAG TT
cs4	ACA GGC TCT AAC ACC GAG TTA CAG GCT CTA ACA TAA CT
cs12	TAG AGC CTG TAA CTC GGT GT
cs23_2	TAA CTC GGT GAT ATC GAT TA
cs4	TAG AGC CTG TAA CTC GGT GT

Table 4.3 Oligonucleotide (ODN) sequences used for 147-mer NCP-3.

NCP-3 top strand

ODN	Sequence
ts1	AGT TAT GTT AGA GCC TGT AAC TCG GTG TTA GAG CCT
ts2_3	GTA ACT CGG TGT TAG AGC CTG TAA CTC GGT GTA TAT
ts3_3	$^{\mathrm{M}}$**C**G ATA TGT AAG CCT GTA ACA GCC TGT TAG AGC CTG TAA CT
ts4	CGG TGT TAG AGC CTG TAA CTC GGT GTT AGA GCC TG
ts12	ACC GAG TTA CAG GCT CTA AC
ts23_3	TTA CAT ATC GAT ATA CAC CG
ts4	TCT AAC ACC GAG TTA CAG GC

NCP-3 bottom strand

ODN	Sequence
cs1	CAG GCT CTA ACA CCG AGT TAC AGG CTC TAA CAC CGA GTT
cs2_3	ACA GGC TCT AAC AGG CTG TTA CAG GCT TAC ATA TCG ATA TA
cs3	CAC CGA GTT ACA GGC TCT AAC ACC GAG TT
cs4	ACA GGC TCT AAC ACC GAG TTA CAG GCT CTA ACA TAA CT
cs12	TAG AGC CTG TAA CTC GGT GT
cs23_3	TAA CTC GGT GTA TAT CGA TA
cs4	TAG AGC CTG TAA CTC GGT GT

Table 4.4 Oligonucleotide (ODN) sequences used for 147-mer NCP-4.

NCP-4 top strand

ODN	Sequence
ts1	AGT TAT GTT AGA GCC TGT AAC TCG GTG TTA GAG CCT
ts2_4	GTA ACT CGG TGT TAG AGC CTG TAA CTC GGT GAT ACA T
ts3_4	$^{\mathbf{M}}$**C**G TGT ATG AGC CTG TAA CAG CCT GTT AGA GCC TGT AAC T
ts4	CGG TGT TAG AGC CTG TAA CTC GGT GTT AGA GCC TG
ts12	ACC GAG TTA CAG GCT CTA AC
ts23_4	CAC ATA CAC GAT GTA TCA CC
ts4	TCT AAC ACC GAG TTA CAG GC

NCP-4 bottom strand

ODN	Sequence
cs1	CAG GCT CTA ACA CCG AGT TAC AGG CTC TAA CAC CGA GTT
cs2_4	ACA GGC TCT AAC AGG CTG TTA CAG GCT CAT ACA CGA TGT AT
cs3	CAC CGA GTT ACA GGC TCT AAC ACC GAG TT
cs4	ACA GGC TCT AAC ACC GAG TTA CAG GCT CTA ACA TAA CT
cs12	TAG AGC CTG TAA CTC GGT GT
cs23_4	TAA CTC GGT GAT ACA TCG TG
cs4	TAG AGC CTG TAA CTC GGT GT

Table 4.5 Oligonucleotide (ODN) sequences used for 147-mer NCP-5.

NCP-5 top strand

ODN	Sequence
ts1	AGT TAT GTT AGA GCC TGT AAC TCG GTG TTA GAG CCT
ts2_5	GTA ACT CGG TGT TAG AGC CTG TAA CTC GGT GTA TGT AT
ts3_5	$^{\mathbf{M}}$**C**G ATA GTA GCC TGT AAC AGC CTG TTA GAG CCT GTA ACT
ts4	CGG TGT TAG AGC CTG TAA CTC GGT GTT AGA GCC TG
ts12	ACC GAG TTA CAG GCT CTA AC
ts23_5	GCT ACT ATC GAT ACA TAC AC
ts4	TCT AAC ACC GAG TTA CAG GC

NCP-5 bottom strand

ODN	Sequence
cs1	CAG GCT CTA ACA CCG AGT TAC AGG CTC TAA CAC CGA GTT
cs2_5	ACA GGC TCT AAC AGG CTG TTA CAG GCT ACT ATC GAT ACA TA
cs3	CAC CGA GTT ACA GGC TCT AAC ACC GAG TT
cs4	ACA GGC TCT AAC ACC GAG TTA CAG GCT CTA ACA TAA CT
cs12	TAG AGC CTG TAA CTC GGT GT
cs23_5	TAA CTC GGT GTA TGT ATC GA
cs4	TAG AGC CTG TAA CTC GGT GT

Table 4.6 Oligonucleotide (ODN) sequences used for 147-mer NCP-6.

NCP-6 top strand	
ODN	Sequence
ts1	AGT TAT GTT AGA GCC TGT AAC TCG GTG TTA GAG CCT
ts2_6	GTA ACT CGG TGT TAG AGC CTG TAA CTC GGT GAT GAT GAT
ts3_6	$^{\mathbf{M}}$**C**G TAT GAG CCT GTA ACA GCC TGT TAG AGC CTG TAA CT
ts4	CGG TGT TAG AGC CTG TAA CTC GGT GTT AGA GCC TG
ts12	ACC GAG TTA CAG GCT CTA AC
ts23_6	GGC TCA TAC GAT CAT CAT CA
ts4	TCT AAC ACC GAG TTA CAG GC

NCP-6 bottom strand	
ODN	Sequence
cs1	CAG GCT CTA ACA CCG AGT TAC AGG CTC TAA CAC CGA GTT
cs2_6	ACA GGC TCT AAC AGG CTG TTA CAG GCT CAT ACG ATC ATC AT
cs3	CAC CGA GTT ACA GGC TCT AAC ACC GAG TT
cs4	ACA GGC TCT AAC ACC GAG TTA CAG GCT CTA ACA TAA CT
cs12	TAG AGC CTG TAA CTC GGT GT
cs23_6	TAA CTC GGT GAT GAT GAT CG
cs4	TAG AGC CTG TAA CTC GGT GT

Table 4.7 Oligonucleotide (ODN) sequences used for 147-mer NCP-7.

NCP-7 top strand

ODN	Sequence
ts1	AGT TAT GTT AGA GCC TGT AAC TCG GTG TTA GAG CCT
ts2_7	GTA ACT CGG TGT TAG AGC CTG TAA CTC GGT GTA TAT GCA T
ts3_7	^{M}**C**G TAC AGC CTG TAA CAG CCT GTT AGA GCC TGT AAC T
ts4	CGG TGT TAG AGC CTG TAA CTC GGT GTT AGA GCC TG
ts12	ACC GAG TTA CAG GCT CTA AC
ts23_7	AGG CTG TAC GAT GCA TAT AC
ts4	TCT AAC ACC GAG TTA CAG GC

NCP-7 bottom strand

ODN	Sequence
cs1	CAG GCT CTA ACA CCG AGT TAC AGG CTC TAA CAC CGA GTT
cs2_7	ACA GGC TCT AAC AGG CTG TTA CAG GCT GTA CGA TGC ATA TA
cs3	CAC CGA GTT ACA GGC TCT AAC ACC GAG TT
cs4	ACA GGC TCT AAC ACC GAG TTA CAG GCT CTA ACA TAA CT
cs12	TAG AGC CTG TAA CTC GGT GT
cs23_7	TAA CTC GGT GTA TAT GCA TC
cs4	TAG AGC CTG TAA CTC GGT GT

Table 4.8 Oligonucleotide (ODN) sequences used for 147-mer NCP-8.

NCP-8 top strand

ODN	Sequence
ts1	AGT TAT GTT AGA GCC TGT AAC TCG GTG TTA GAG CCT
ts2_8	GTA ACT CGG TGT TAG AGC CTG TAA CTC GGT GAT ACG CACA T
ts3_8	$^{\mathbf{M}}$**C**G TAA GCC TGT AAC AGC CTG TTA GAG CCT GTA ACT
ts4	CGG TGT TAG AGC CTG TAA CTC GGT GTT AGA GCC TG
ts12	ACC GAG TTA CAG GCT CTA AC
ts23_8	CAG GCT TAC GAT GTG CGT AT
ts4	TCT AAC ACC GAG TTA CAG GC

NCP-8 bottom strand

ODN	Sequence
cs1	CAG GCT CTA ACA CCG AGT TAC AGG CTC TAA CAC CGA GTT
cs2_8	ACA GGC TCT AAC AGG CTG TTA CAG GCT TAC GAT GTG CGT AT
cs3	CAC CGA GTT ACA GGC TCT AAC ACC GAG TT
cs4	ACA GGC TCT AAC ACC GAG TTA CAG GCT CTA ACA TAA CT
cs12	TAG AGC CTG TAA CTC GGT GT
cs23_8	TAA CTC GGT GAT ACG CAC AT
cs4	TAG AGC CTG TAA CTC GGT GT

Table 4.9 Oligonucleotide (ODN) sequences used for 147-mer NCP-9.

NCP-9 top strand	
ODN	Sequence
ts1	AGT TAT GTT AGA GCC TGT AAC TCG GTG TTA GAG CCT
ts2_9	GTA ACT CGG TGT TAG AGC CTG TAA CTC GGT GTA TGT AGA CAT
ts3_9	$^{\mathbf{M}}$**C**G CAG CCT GTA ACA GCC TGT TAG AGC CTG TAA CT
ts4	CGG TGT TAG AGC CTG TAA CTC GGT GTT AGA GCC TG
ts12	ACC GAG TTA CAG GCT CTA AC
ts23_9	ACA GGC TGC GAT GTC TAC AT
ts4	TCT AAC ACC GAG TTA CAG GC

NCP-9 bottom strand	
ODN	Sequence
cs1	CAG GCT CTA ACA CCG AGT TAC AGG CTC TAA CAC CGA GTT
cs2_9	ACA GGC TCT AAC AGG CTG TTA CAG GCT GCG ATG TCT ACA TA
cs3	CAC CGA GTT ACA GGC TCT AAC ACC GAG TT
cs4	ACA GGC TCT AAC ACC GAG TTA CAG GCT CTA ACA TAA CT
cs12	TAG AGC CTG TAA CTC GGT GT
cs23_9	TAA CTC GGT GTA TGT AGA CA
cs4	TAG AGC CTG TAA CTC GGT GT

Table 4.10 Oligonucleotide (ODN) sequences used for 147-mer NCP-10.

NCP-10 top strand

ODN	Sequence
ts1	AGT TAT GTT AGA GCC TGT AAC TCG GTG TTA GAG CCT
ts2_10	GTA ACT CGG TGT TAG AGC CTG TAA CTC GGT GAT ACG CAC GTA T
ts3_10	$^{\mathrm{M}}$**C**G AGC CTG TAA CAG CCT GTT AGA GCC TGT AAC T
ts4	CGG TGT TAG AGC CTG TAA CTC GGT GTT AGA GCC TG
ts12	ACC GAG TTA CAG GCT CTA AC
ts23_10	TAC AGG CTC GAT ACG TGC GT
ts4	TCT AAC ACC GAG TTA CAG GC

NCP-10 bottom strand

ODN	Sequence
cs1	CAG GCT CTA ACA CCG AGT TAC AGG CTC TAA CAC CGA GTT
cs2_10	ACA GGC TCT AAC AGG CTG TTA CAG GCT CGA TAC GTG CGT AT
cs3	CAC CGA GTT ACA GGC TCT AAC ACC GAG TT
cs4	ACA GGC TCT AAC ACC GAG TTA CAG GCT CTA ACA TAA CT
cs12	TAG AGC CTG TAA CTC GGT GT
cs23_10	TAA CTC GGT GAT ACG CAC GT
cs4	TAG AGC CTG TAA CTC GGT GT

Table 4.11 Oligonucleotide (ODN) sequences used for 147-mer NCP-1A

NCP-1A top strand

ODN	Sequence
ts1	AGT TAT GTT AGA GCC TGT AAC TCG GTG TTA GAG CCT
ts2_1A	GTA ACT CGG TGT TAG AGC CTG TAA CTC GGT GTA T
ts3_1A	**^{M}C**A ATG GTA TAG AGC CTG TAA CAG AAT GTT AGA GCC TGT AAC T
ts4	CGG TGT TAG AGC CTG TAA CTC GGT GTT AGA GCC TG
ts12	ACC GAG TTA CAG GCT CTA AC
ts23_1A	TAT ACC ATT GAT ACA CCG AG
ts4	TCT AAC ACC GAG TTA CAG GC

NCP-1A bottom strand

ODN	Sequence
cs1	CAG GCT CTA ACA CCG AGT TAC AGG CTC TAA CAC CGA GTT
cs2_1A	ACA GGC TCT AAC ATT CTG TTA CAG GCT CTA TAC CAT TGA TA
cs3	CAC CGA GTT ACA GGC TCT AAC ACC GAG TT
cs4	ACA GGC TCT AAC ACC GAG TTA CAG GCT CTA ACA TAA CT
cs12	TAG AGC CTG TAA CTC GGT GT
cs23_1A	TAA CTC GGT GTA TCA ATG GT
cs4	TAG AGC CTG TAA CTC GGT GT

Table 4.12 Oligonucleotide (ODN) sequences used for 147-mer NCP-6A

NCP-6A top strand

ODN	Sequence
ts1	AGT TAT GTT AGA GCC TGT AAC TCG GTG TTA GAG CCT
ts2_6A	GTA ACT CGG TGT TAG AGC CTG TAA CTC GGT GAT GAT GAT
ts3_6A	$^{\mathbf{M}}$**C**A TAT GAG CCT GTA ACA GCC TGT TAG AGC CTG TAA CT
ts4	CGG TGT TAG AGC CTG TAA CTC GGT GTT AGA GCC TG
ts12	ACC GAG TTA CAG GCT CTA AC
ts23_6A	GGC TCA TAT GAT CAT CAT CA
ts4	TCT AAC ACC GAG TTA CAG GC

NCP-6 bottom strand

ODN	Sequence
cs1	CAG GCT CTA ACA CCG AGT TAC AGG CTC TAA CAC CGA GTT
cs2_6	ACA GGC TCT AAC AGG CTG TTA CAG GCT CAT ATG ATC ATC AT
cs3	CAC CGA GTT ACA GGC TCT AAC ACC GAG TT
cs4	ACA GGC TCT AAC ACC GAG TTA CAG GCT CTA ACA TAA CT
cs12	TAG AGC CTG TAA CTC GGT GT
cs23_6	TAA CTC GGT GAT GAT GAT CA
cs4	TAG AGC CTG TAA CTC GGT GT

Table 4.13 Nucleosome rotational positioning effect on T=^{m}CG CPD photoproduct yield and deamination.

	T=^{m}C yield (%)	Fold change	Deamination half-life (h)	Fold change
Free NCP 1-10	**11.8**	**-**	**13.1**	**-**
Nucleosome-bound NCP-1	**6.9**	**0.59**	**40.8**	**3.1**
Nucleosome-bound NCP-2	**7.6**	**0.64**	**38.5**	**2.9**
Nucleosome-bound NCP-3	**13.2**	**1.1**	**14.9**	**1.1**
Nucleosome-bound NCP-4	**14.4**	**1.2**	**8.8**	**0.67**
Nucleosome-bound NCP-5	**19.2**	**1.6**	**5.1**	**0.39**
Nucleosome-bound NCP-6	**21.9**	**1.9**	**3.5**	**0.26**
Nucleosome-bound NCP-7	**19.9**	**1.7**	**3.6**	**0.28**
Nucleosome-bound NCP-8	**13.8**	**1.2**	**10.2**	**0.78**
Nucleosome-bound NCP-9	**12.2**	**1.0**	**12.1**	**0.92**
Nucleosome-bound NCP-10	**8.4**	**0.71**	**35.9**	**2.7**

Table 4.14 Nucleosome rotational positioning effect on T=^{m}CA CPD photoproduct yield and deamination.

	T=^{m}C yield (%)	Fold change	Deamination half-life (h)	Fold change
Free NCP-1A	**13.8**	**-**	**86**	**-**
Nucleosome-bound NCP-1A	**11.6**	**0.84**	**113**	**1.3**
Free NCP-6A	**14.0**	**-**	**90**	**-**
Nucleosome-bound NCP-6A	**23.7**	**1.7**	**29**	**0.32**

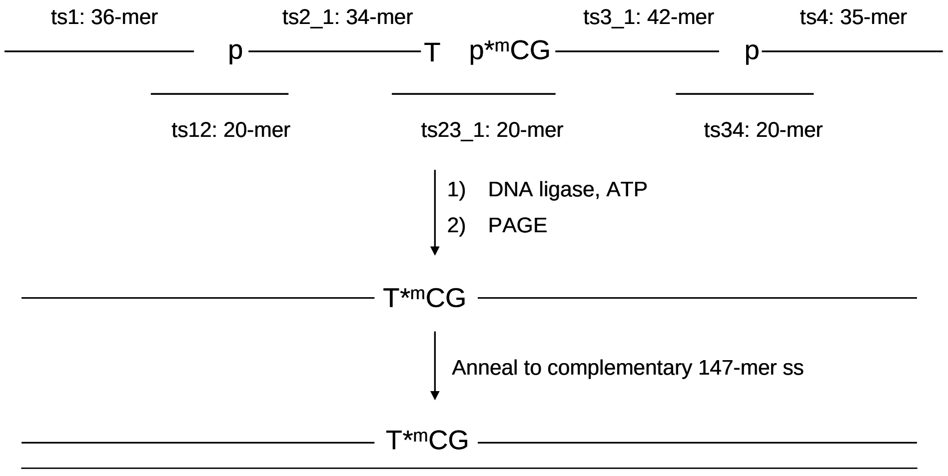

147-mer DNA duplex: NCP-1

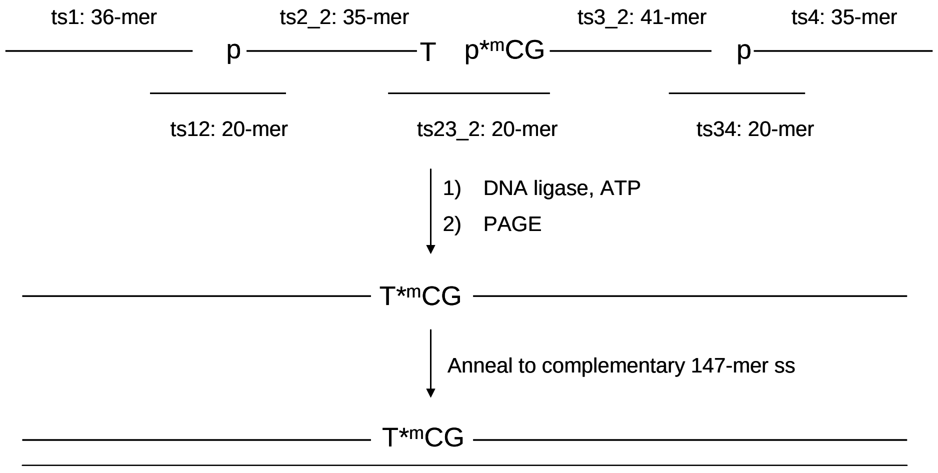

147-mer DNA duplex: NCP-2

Figure 4.1 Ligation strategy for assembly of the 147-mer NCP-1 and NCP-2 substrate.

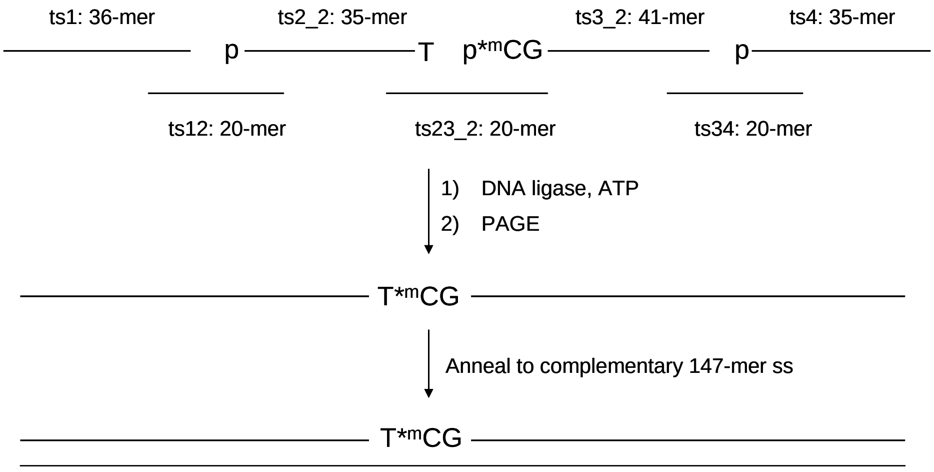

147-mer DNA duplex: NCP-2

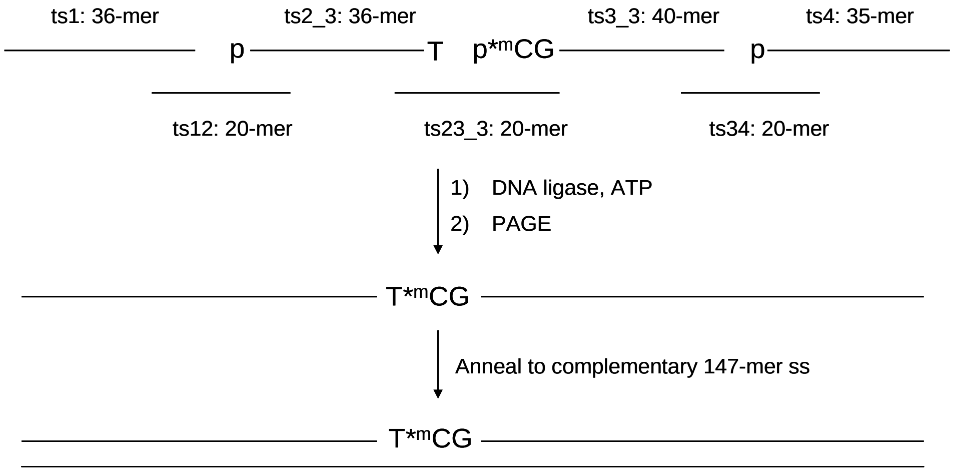

147-mer DNA duplex: NCP-3

Figure 4.2 Ligation strategy for assembly of the 147-mer NCP-3 and NCP-4 substrate.

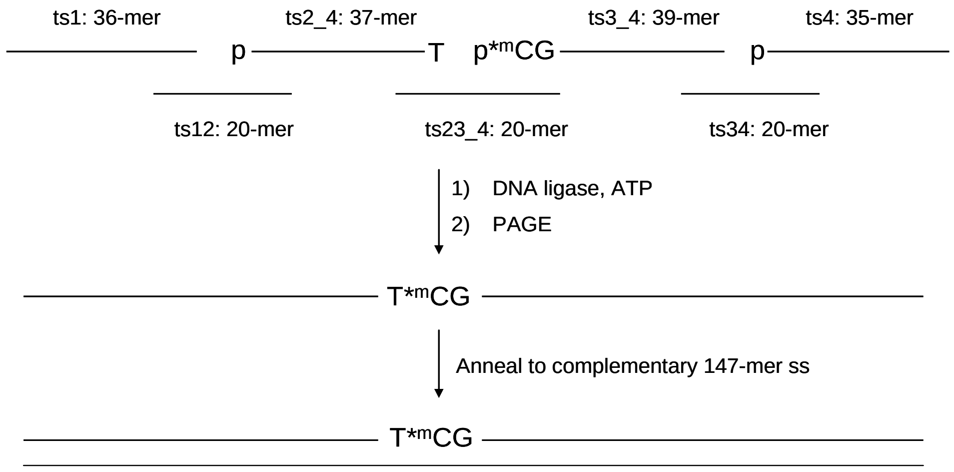

147-mer DNA duplex: NCP-4

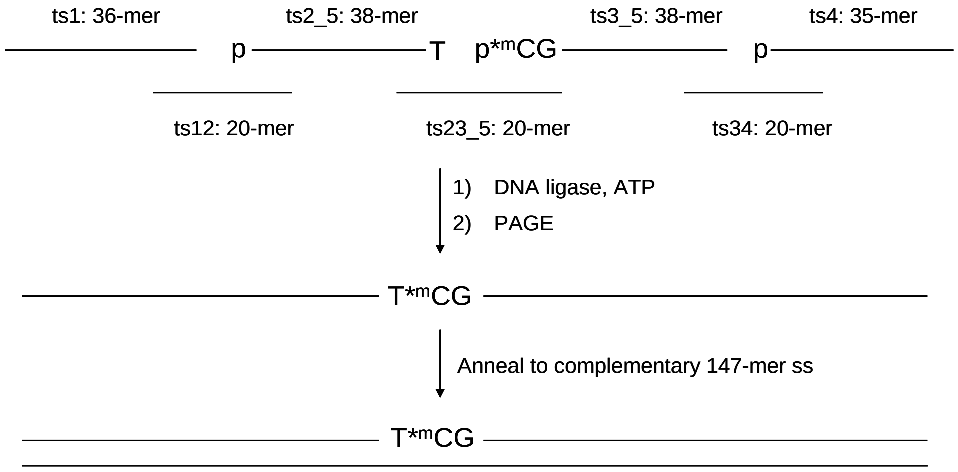

147-mer DNA duplex: NCP-5

Figure 4.3 Ligation strategy for assembly of the 147-mer NCP-5 and NCP-6 substrate.

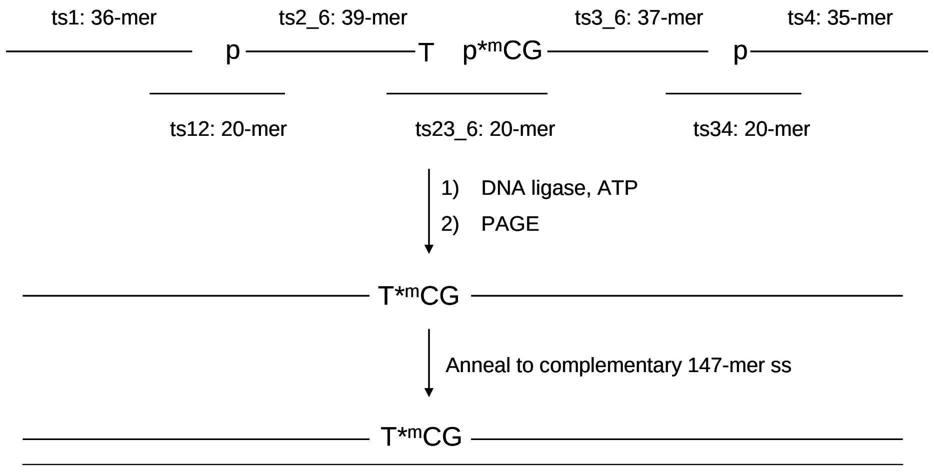

147-mer DNA duplex: NCP-6

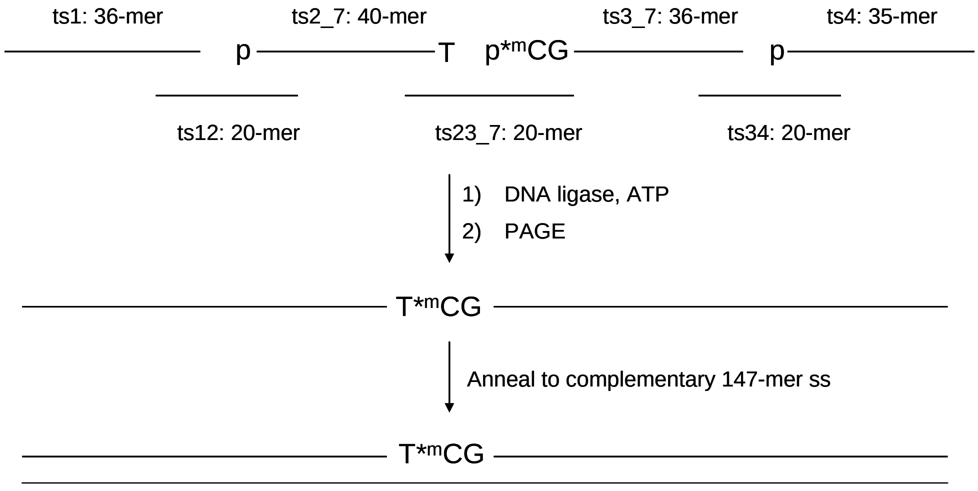

147-mer DNA duplex: NCP-7

Figure 4.4 Ligation strategy for assembly of the 147-mer NCP-7 and NCP-8 substrate.

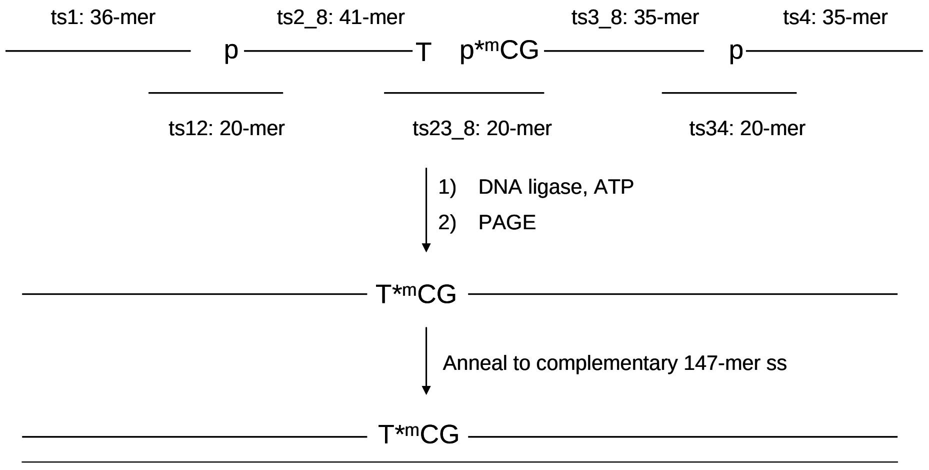

147-mer DNA duplex: NCP-8

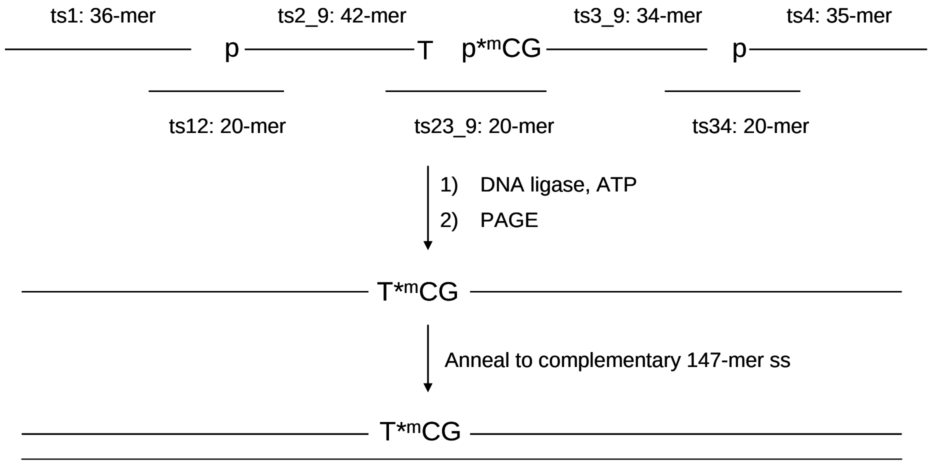

147-mer DNA duplex: NCP-9

Figure 4.5 Ligation strategy for assembly of the 147-mer NCP-9 and NCP-10 substrate.

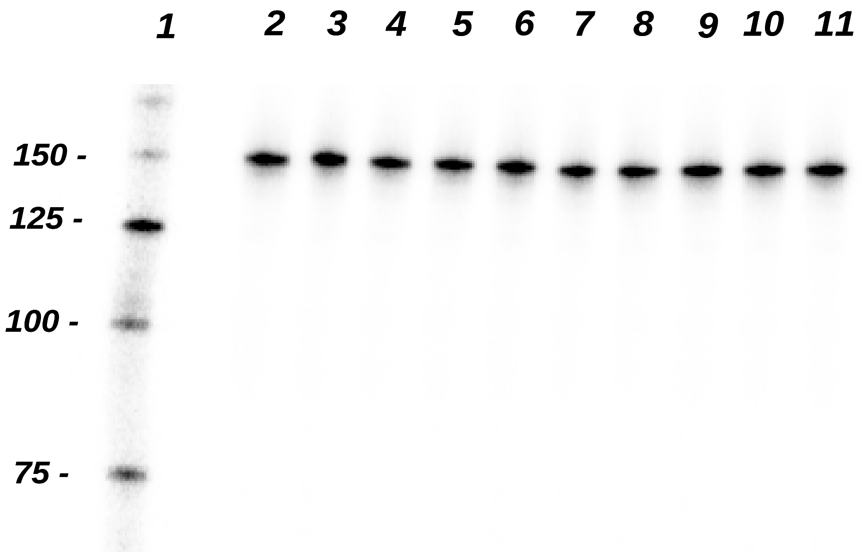

Lane 1: **25bp DNA ladder**

Lane 2-11: **147-mer NCP-1, NCP-2, to NCP-10**

Figure 4.6 Characterization and purification of the 147-mer DNA duplexes NCP-1, NCP-2 to NCP-10 by native PAGE. The PAGE-purified single strand 147-mer substrates were annealed together to form duplexes and characterized by native gel electrophoresis on a 10% acrylamide, 0.3% bisacrylamide polyacrylamide gel in TBE. Lane 1: 25 bp DNA ladder, lane 2-11: 147-mer NCP-1, NCP-2 to NCP-10. Each duplex substrate was isolated from the gel for further studies.

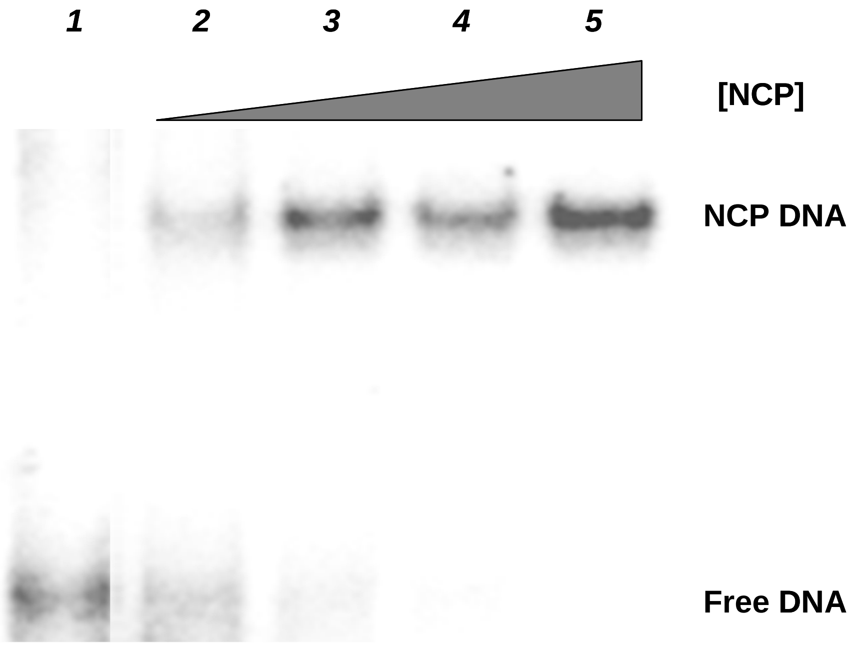

Figure 4.7 Reconstitution of the nucleosome core particles with equimolar ratio mixture of the ten 147-mer DNA duplexes ds-1, ds-2 to ds-10. The 147-mer DNA duplexes mixture (10nM total) were incubated with increasing amounts of chicken erythrocyte nucleosome core particles (NCP) (lanes 1-4: 100, 300, 500, 1000 nM) at room temperature in 2 M NaCl at pH 7.5 for 2 h followed by dialysis overnight at 4°C in 50 mM NaCl, with final equilibration at 55°C for 2 h. The reconstituted NCP were then electrophoresed on a native polyacrylamide gel (6% acrylamide, 0.2% bisacrylamide in TBE).

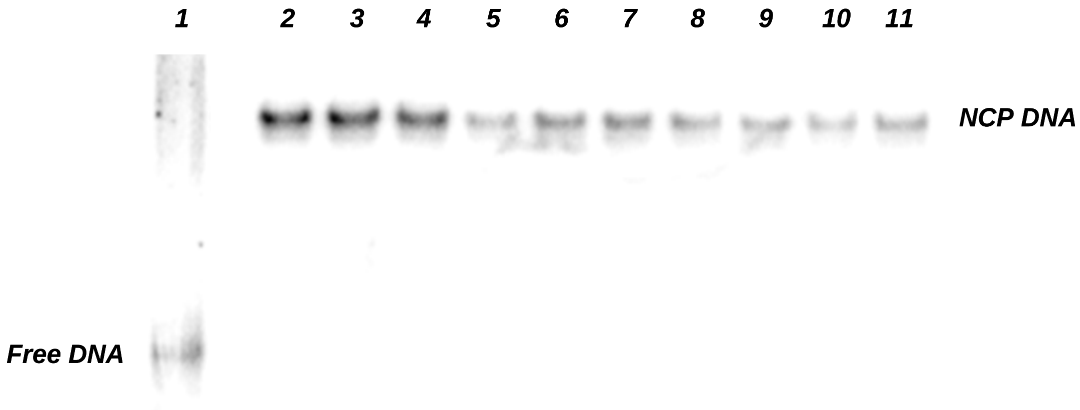

Figure 4.8 Reconstitution of the nucleosome core particles with individual 147-mer DNA duplex: NCP-1, NCP-2 to NCP-10. The 147-mer DNA duplexes (10nM each) were incubated with 1000nM chicken erythrocyte nucleosome core particles (NCP) at room temperature in 2 M NaCl at pH 7.5 for 2 h followed by dialysis overnight at 4°C in 50 mM NaCl, with final equilibration at 55°C for 2 h. The reconstituted NCP were then electrophoresed on a native polyacrylamide gel (6% acrylamide, 0.2% bisacrylamide in TBE). Lane 1: free 147-mer DNA duplex, Lane 2-11: reconstituted nucleosome-bound NCP-1, NCP-2 to NCP-10.

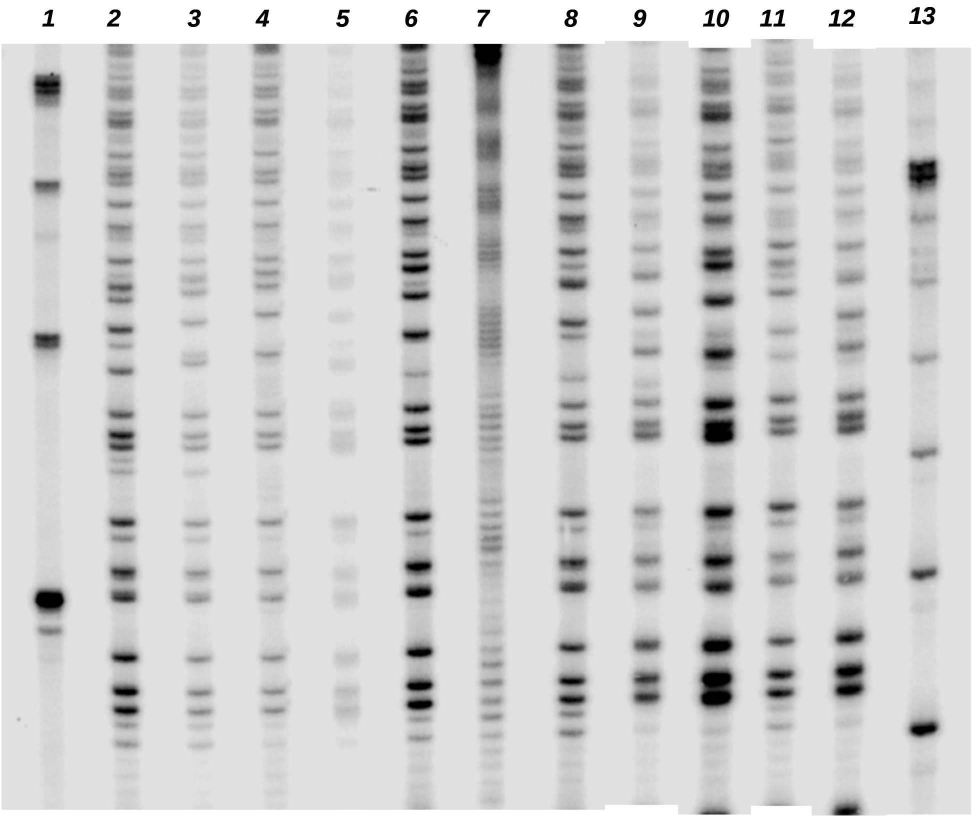

Figure 4.9 Hydroxyl radical footprinting of the reconstituted nucleosome core particle with equimolar ratio mixture of the ten 147-mer DNA duplexes ds-1, ds-2 to ds-10 and DMS mapping of ds-1, ds-2 to ds-10. The nucleosome core particle reconstituted with 5’-end-labeled 147-mer DNA duplexes ds-1, ds-2 to ds-10 was subjected to hydroxyl radical footprinting and electrophoresed on a 7 M urea, 10% acrylamide, 0.3% bisacrylamide denaturing gel. Lane 1, 25bp DNA ladder; lane 2 to 6, DMS mapping on ds-1 to ds-5; lane 7, hydroxyl radical footprinting of the reconstituted nucleosome core particle with the mixture of ten 147-mer DNA duplexes ds-1 to ds-10; lane 8 to 12, DMS mapping on ds-6 to ds-10; lane 13, 10bp DNA ladder. DMS, dimethyl sulfate.

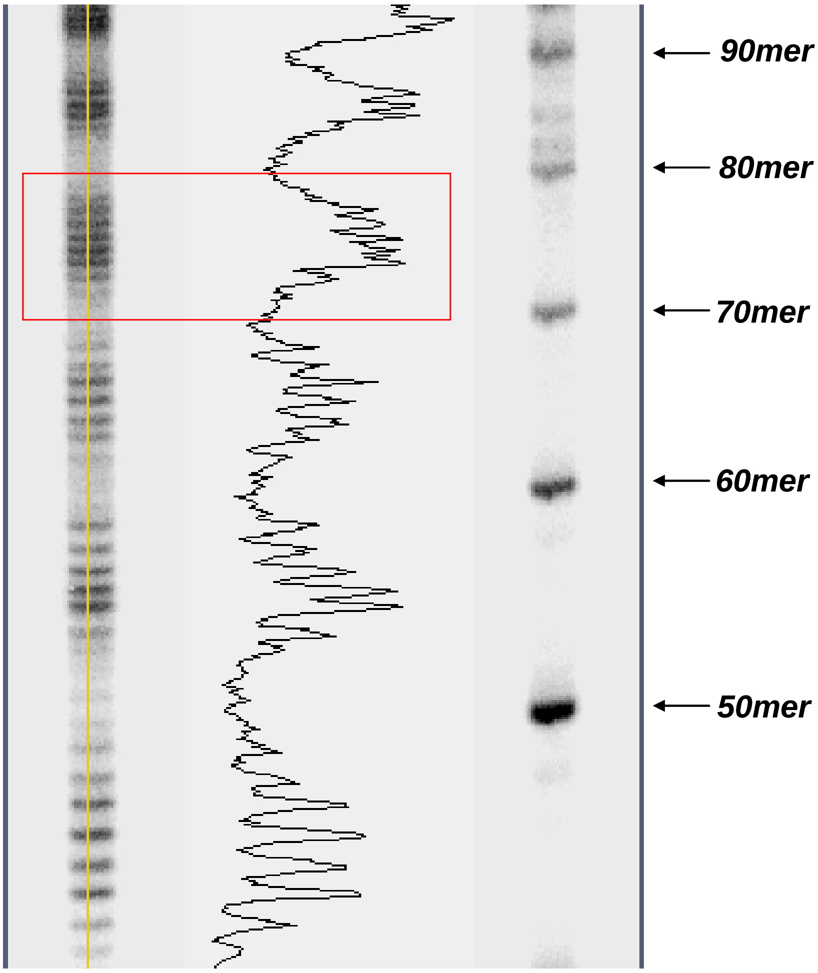

Figure 4.10 Hydroxyl radical footprinting of the reconstituted nucleosome core particle with equimolar ratio mixture of the ten 147-mer DNA duplexes ds-1, ds-2 to ds-10. The cleavage intensity was plotted up and the box region highlighted the ten positions of ^{m}C.

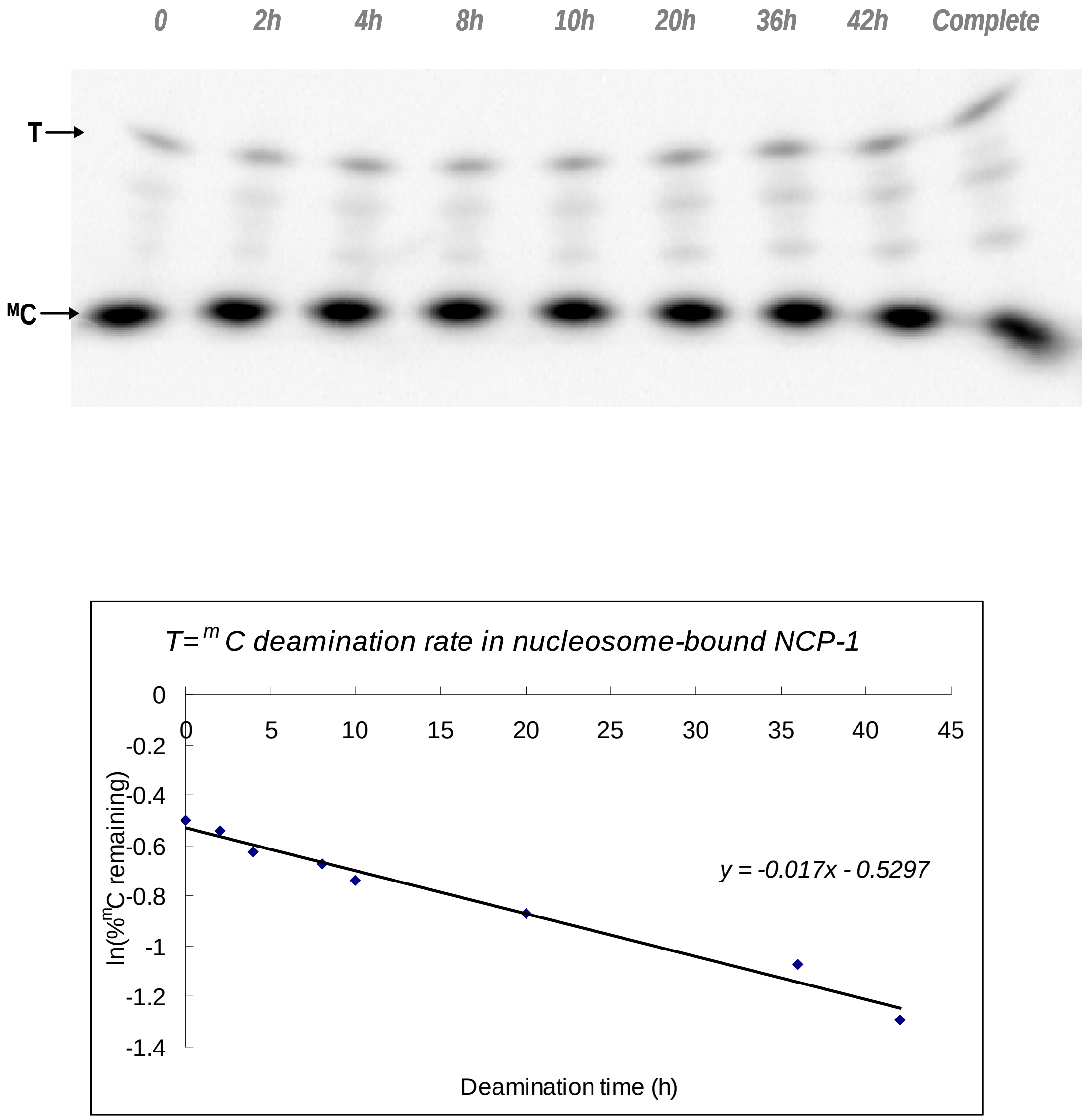

Figure 4.11 Deamination rate of T=^{m}C CPD in nucleosome-bound NCP-1 using two-dimensional gel electrophoresis (top) & Linear regression analysis of the deamination rate data (bottom). Plots of the individual deamination rate data as log (fraction T=^{m}C remaining) vs time.

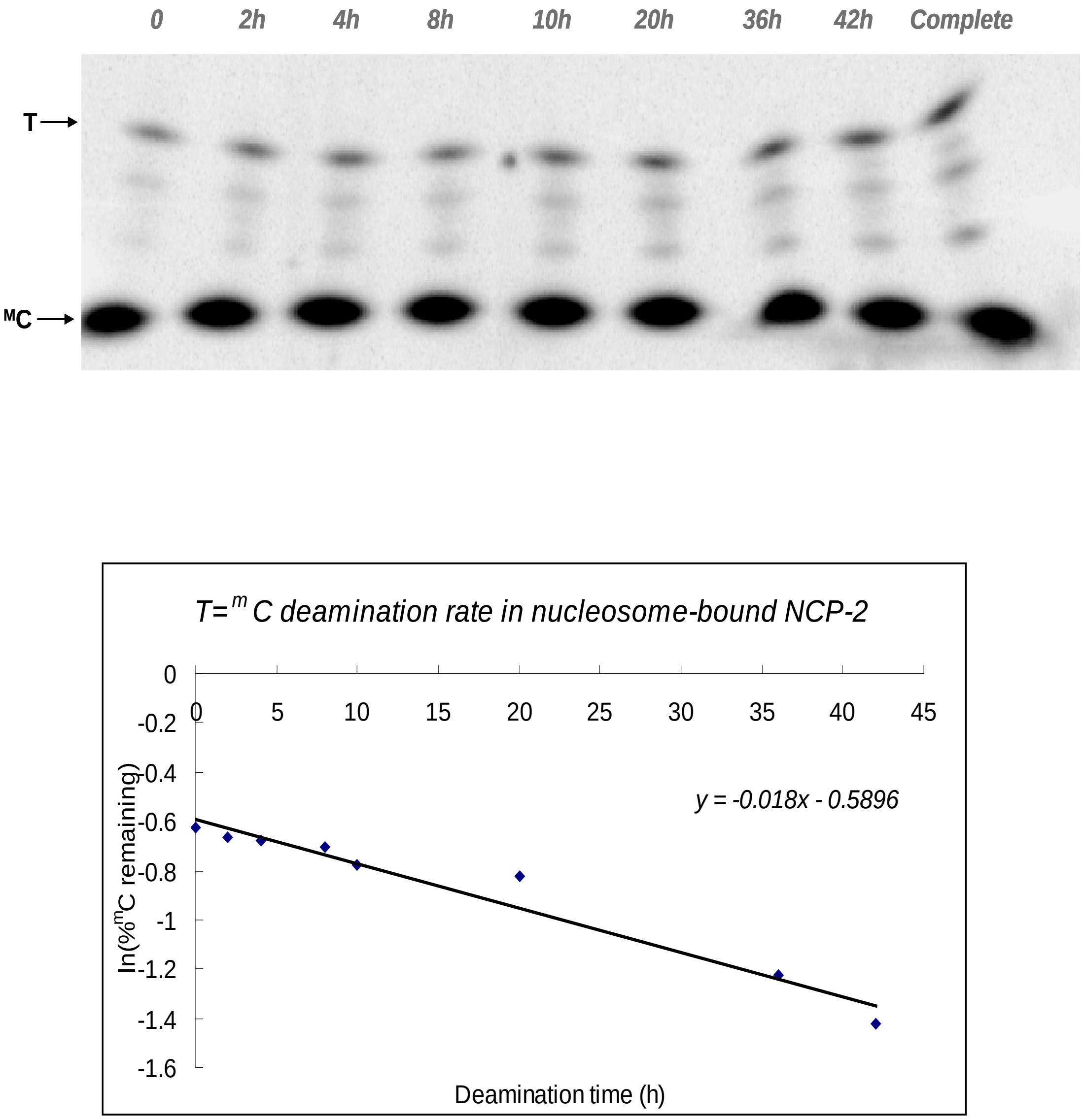

Figure 4.12 Deamination rate of T=^{m}C CPD in nucleosome-bound NCP-2 using two-dimensional gel electrophoresis (top) & Linear regression analysis of the deamination rate data (bottom). Plots of the individual deamination rate data as log (fraction T=^{m}C remaining) vs time.

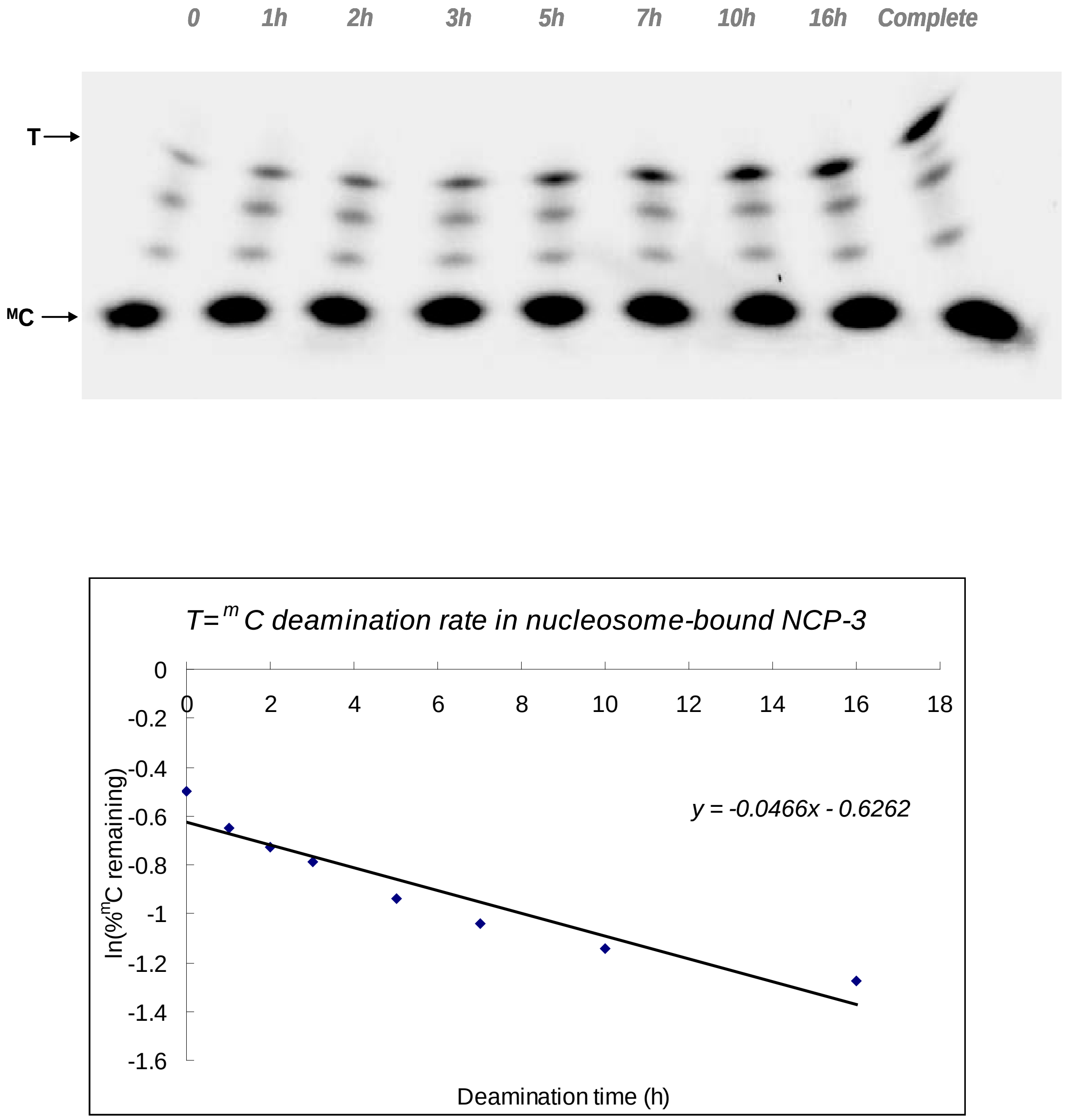

Figure 4.13 Deamination rate of T=^{m}C CPD in nucleosome-bound NCP-3 using two-dimensional gel electrophoresis (top) & Linear regression analysis of the deamination rate data (bottom). Plots of the individual deamination rate data as log (fraction T=^{m}C remaining) vs time.

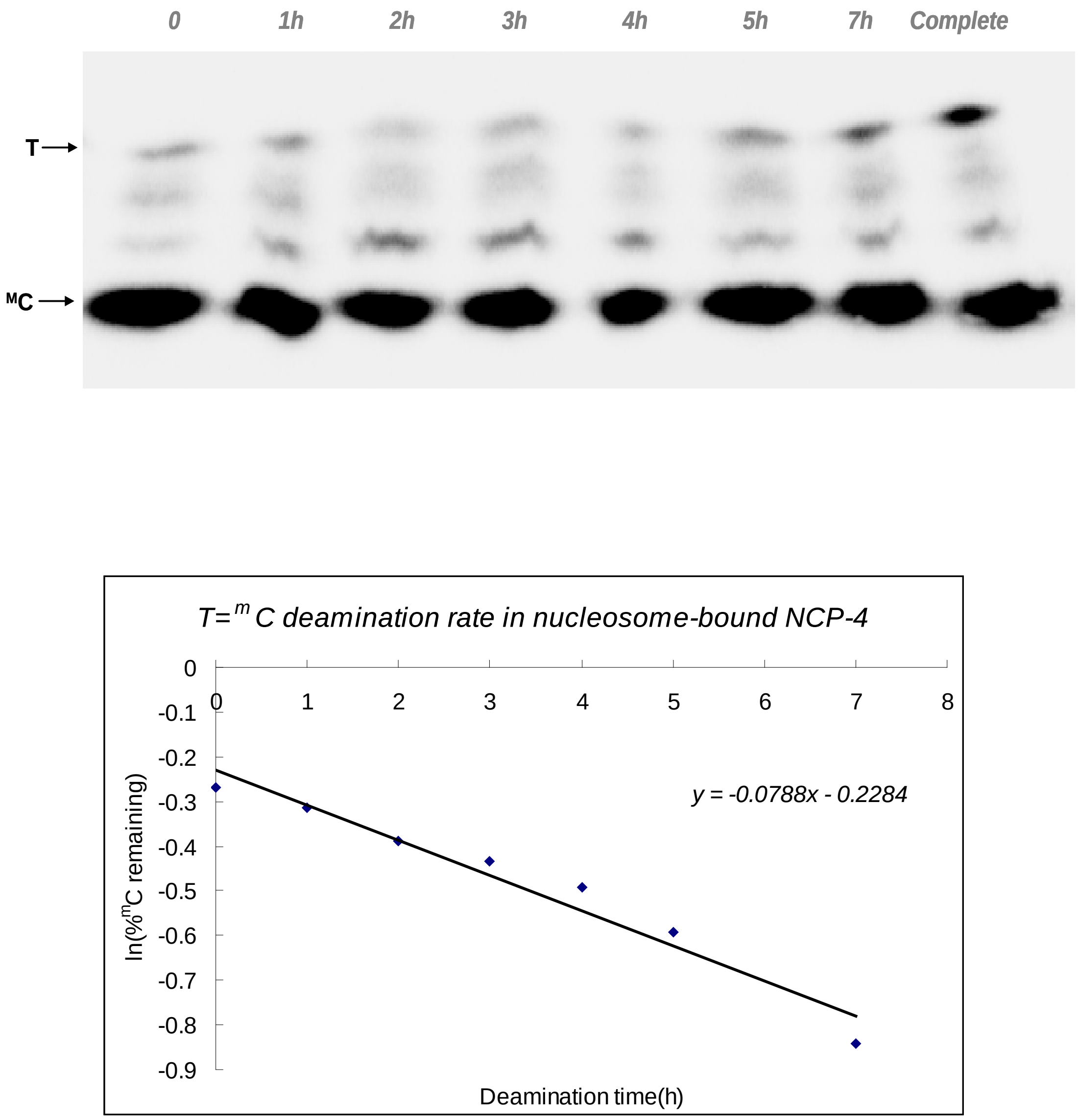

Figure 4.14 Deamination rate of T=^{m}C CPD in nucleosome-bound NCP-4 using two-dimensional gel electrophoresis (top) & Linear regression analysis of the deamination rate data (bottom). Plots of the individual deamination rate data as log (fraction T=^{m}C remaining) vs time.

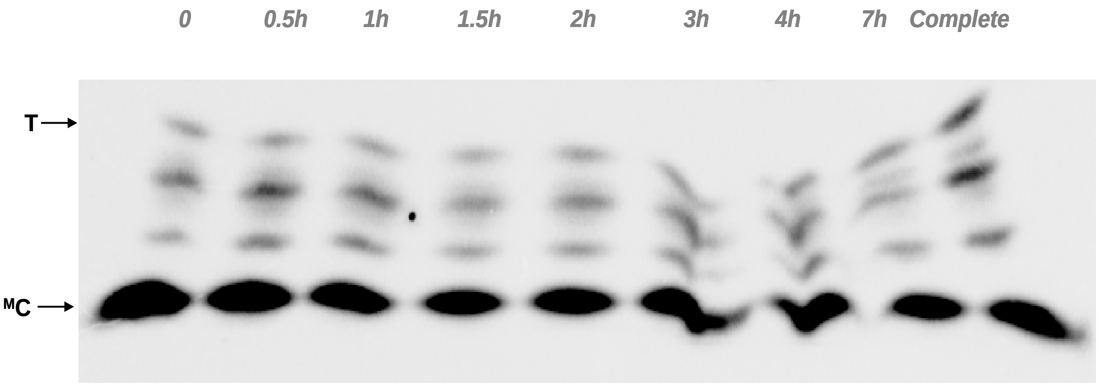

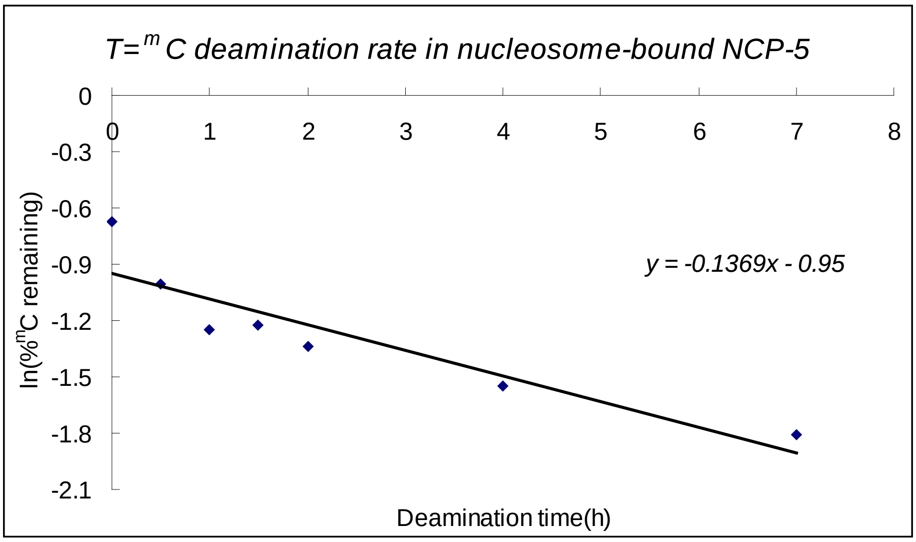

Figure 4.15 Deamination rate of T=^{m}C CPD in nucleosome-bound NCP-5 using two-dimensional gel electrophoresis (top) & Linear regression analysis of the deamination rate data (bottom). Plots of the individual deamination rate data as log (fraction T=^{m}C remaining) vs time.

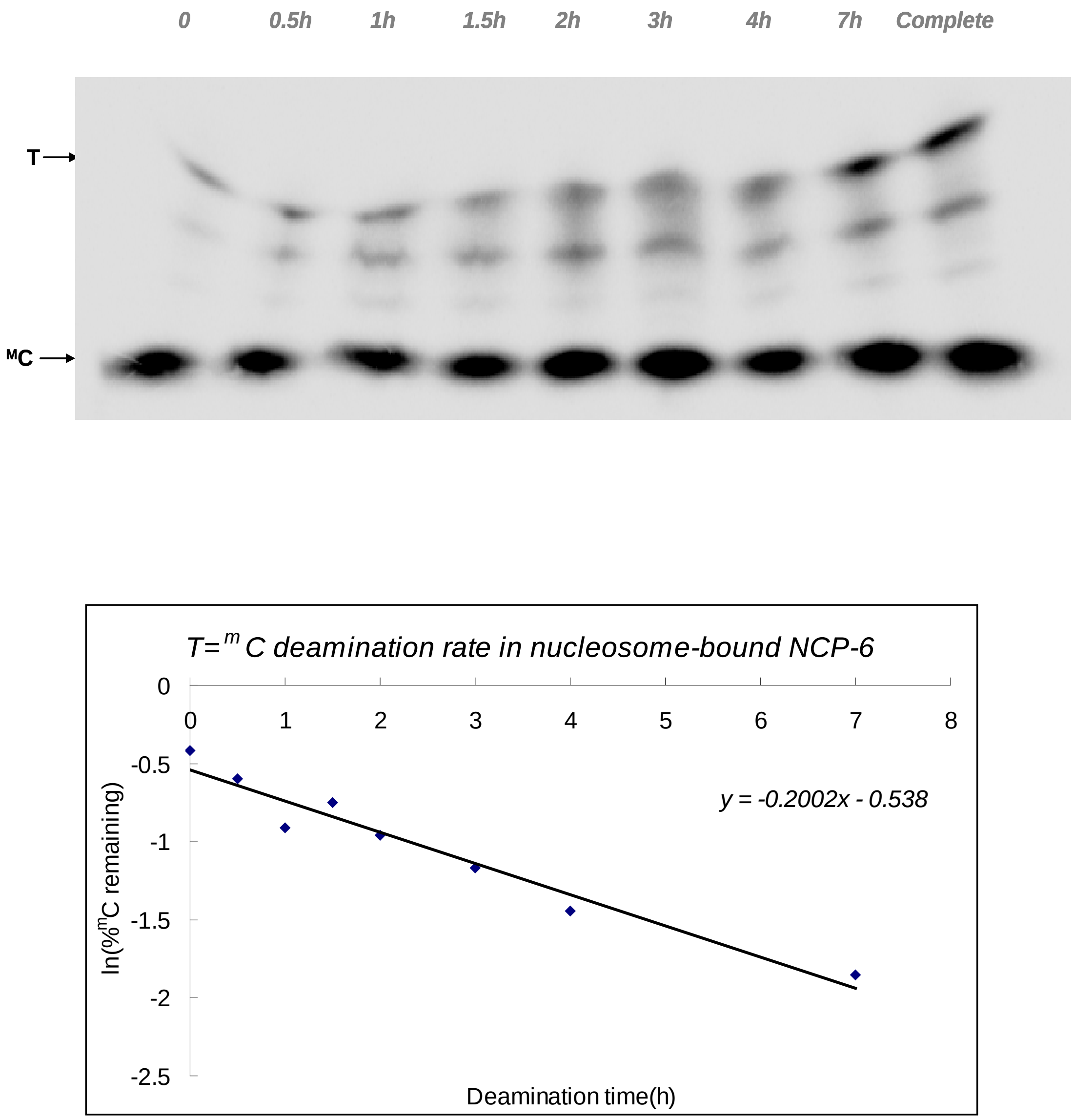

Figure 4.16 Deamination rate of T=^{m}C CPD in nucleosome-bound NCP-6 using two-dimensional gel electrophoresis (top) & Linear regression analysis of the deamination rate data (bottom). Plots of the individual deamination rate data as log (fraction T=^{m}C remaining) vs time.

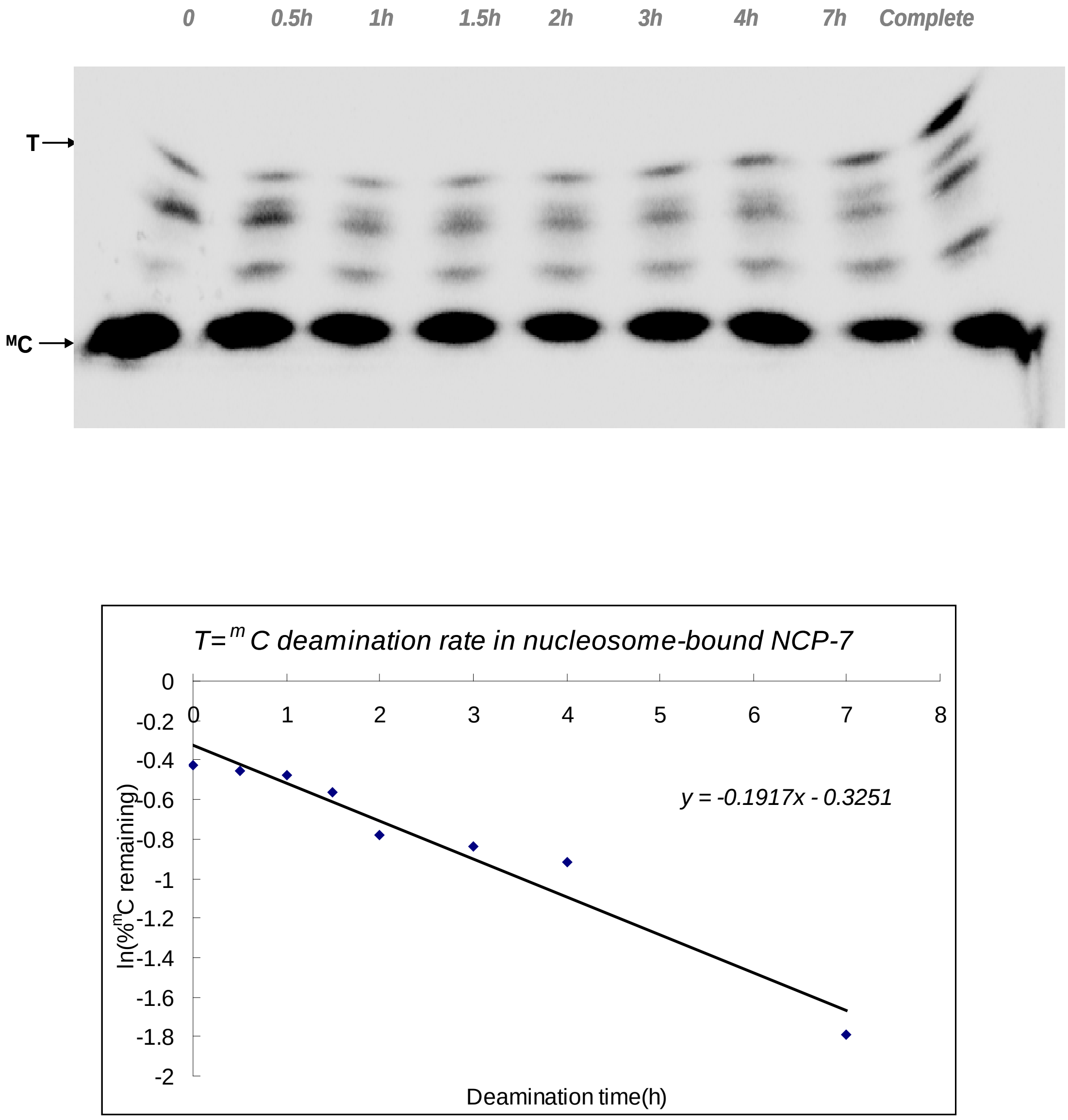

Figure 4.17 Deamination rate of T=^{m}C CPD in nucleosome-bound NCP-7 using two-dimensional gel electrophoresis (top) & Linear regression analysis of the deamination rate data (bottom). Plots of the individual deamination rate data as log (fraction T=^{m}C remaining) vs time.

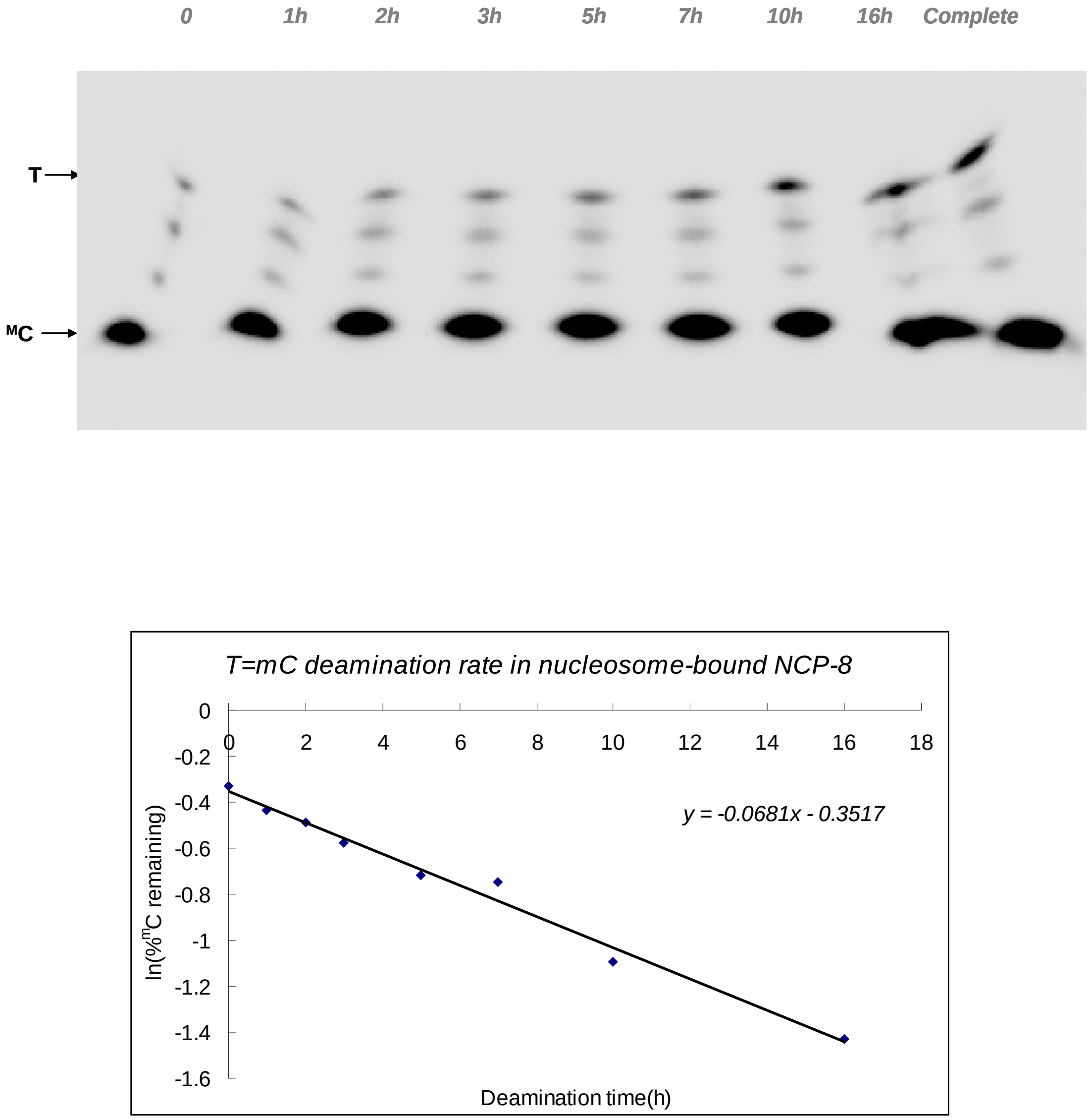

Figure 4.18 Deamination rate of T=^{m}C CPD in nucleosome-bound NCP-8 using two-dimensional gel electrophoresis (top) & Linear regression analysis of the deamination rate data (bottom). Plots of the individual deamination rate data as log (fraction T=^{m}C remaining) vs time.

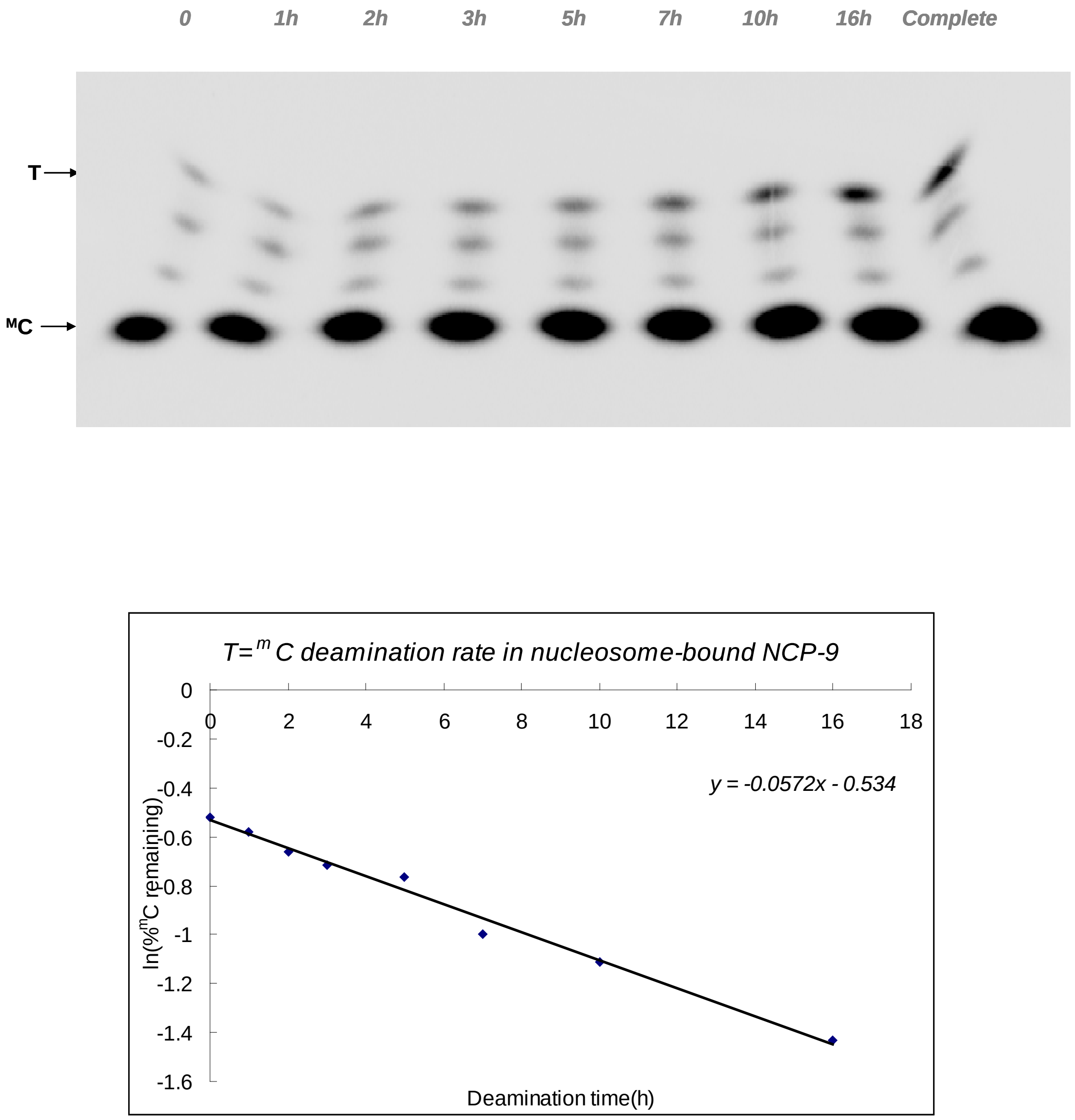

Figure 4.19 Deamination rate of T=^{m}C CPD in nucleosome-bound NCP-9 using two-dimensional gel electrophoresis (top) & Linear regression analysis of the deamination rate data (bottom). Plots of the individual deamination rate data as log (fraction T=^{m}C remaining) vs time.

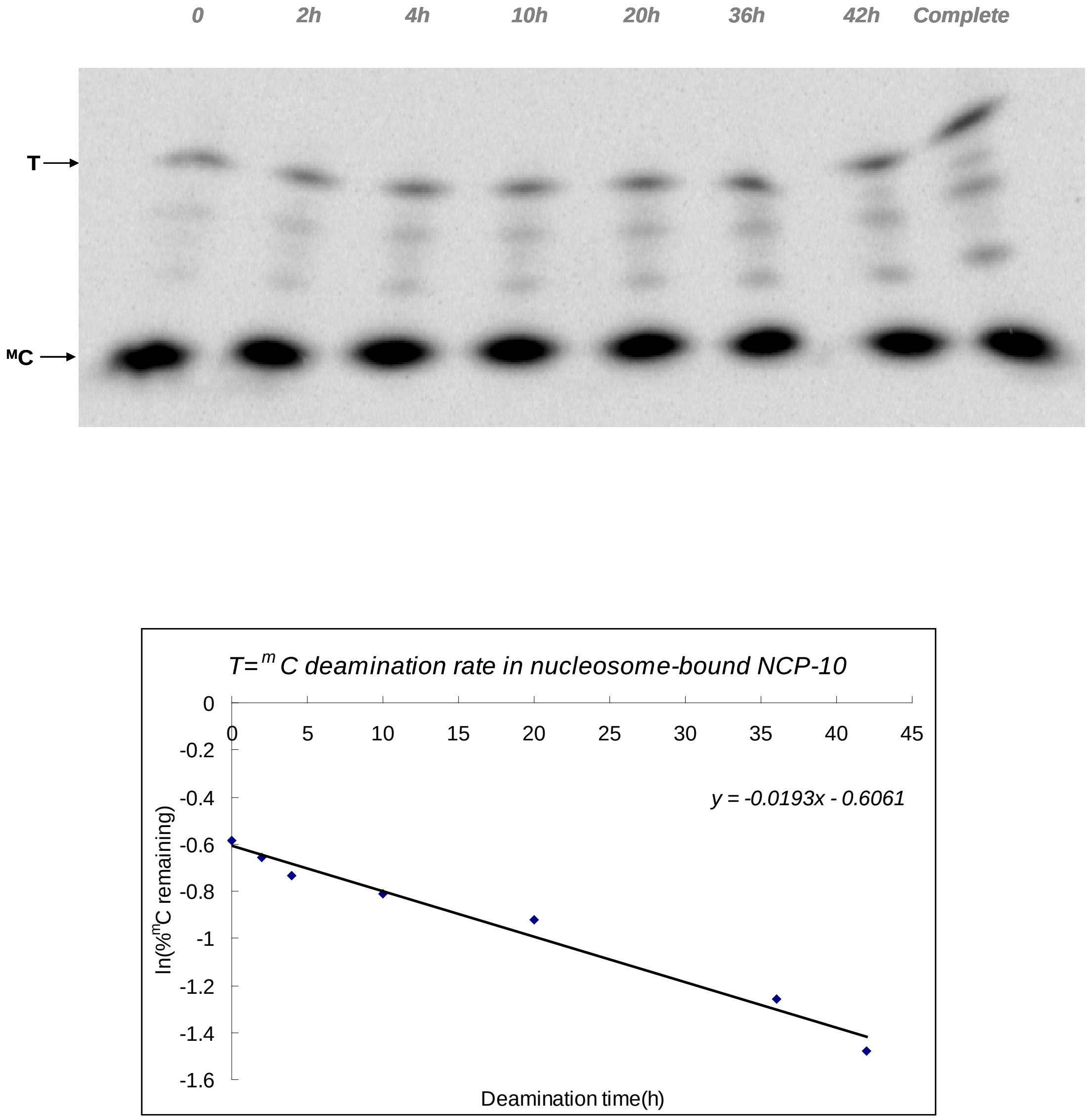

Figure 4.20 Deamination rate of T=^{m}C CPD in nucleosome-bound NCP-10 using two-dimensional gel electrophoresis (top) & Linear regression analysis of the deamination rate data (bottom). Plots of the individual deamination rate data as log (fraction T=^{m}C remaining) vs time.

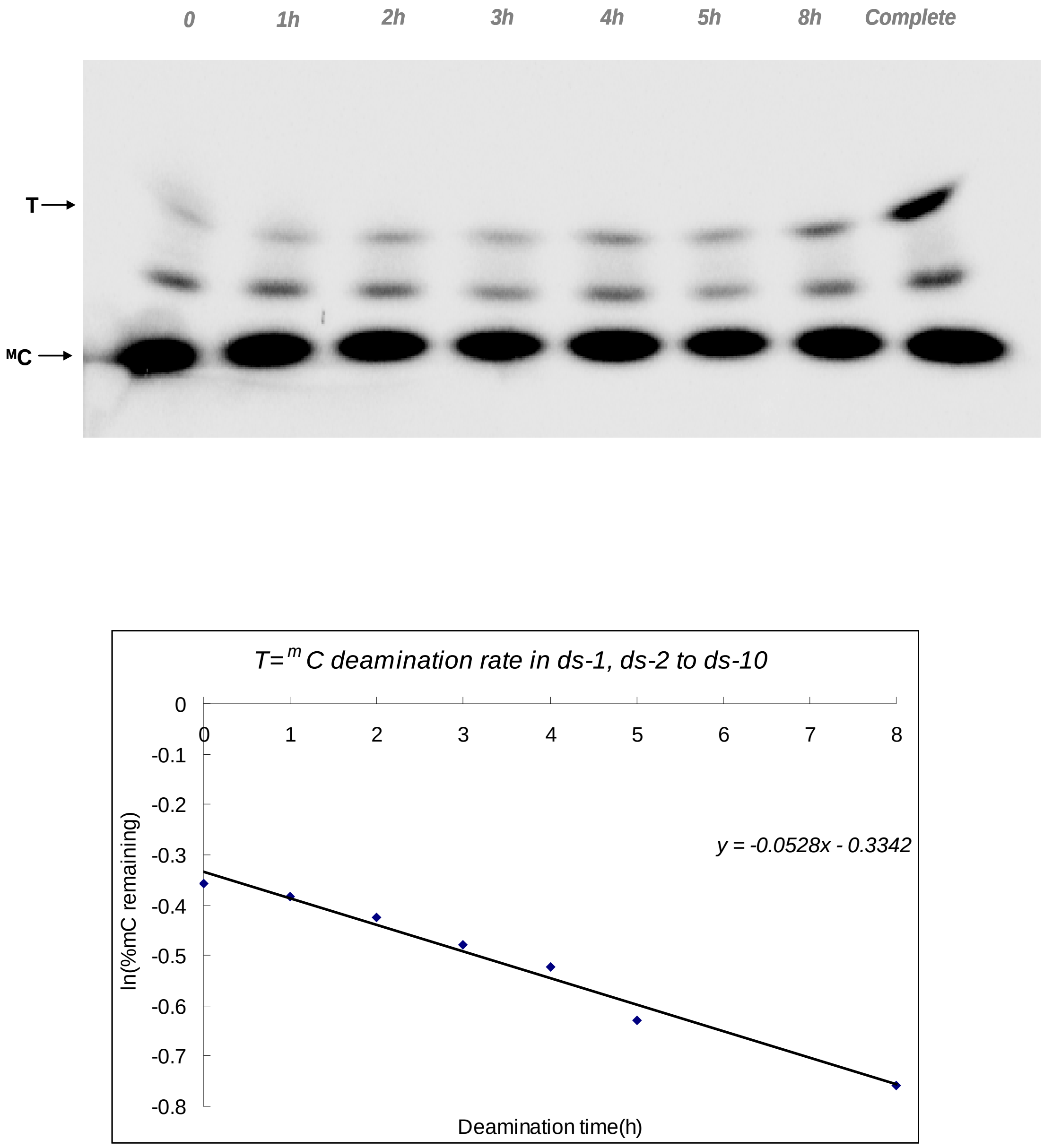

Figure 4.21 Deamination rate of T=^{m}C CPD in the mixture of ds-1, ds-2 to ds-10 using two-dimensional gel electrophoresis (top) & Linear regression analysis of the deamination rate data (bottom). Plots of the individual deamination rate data as log (fraction T=^{m}C remaining) vs time.

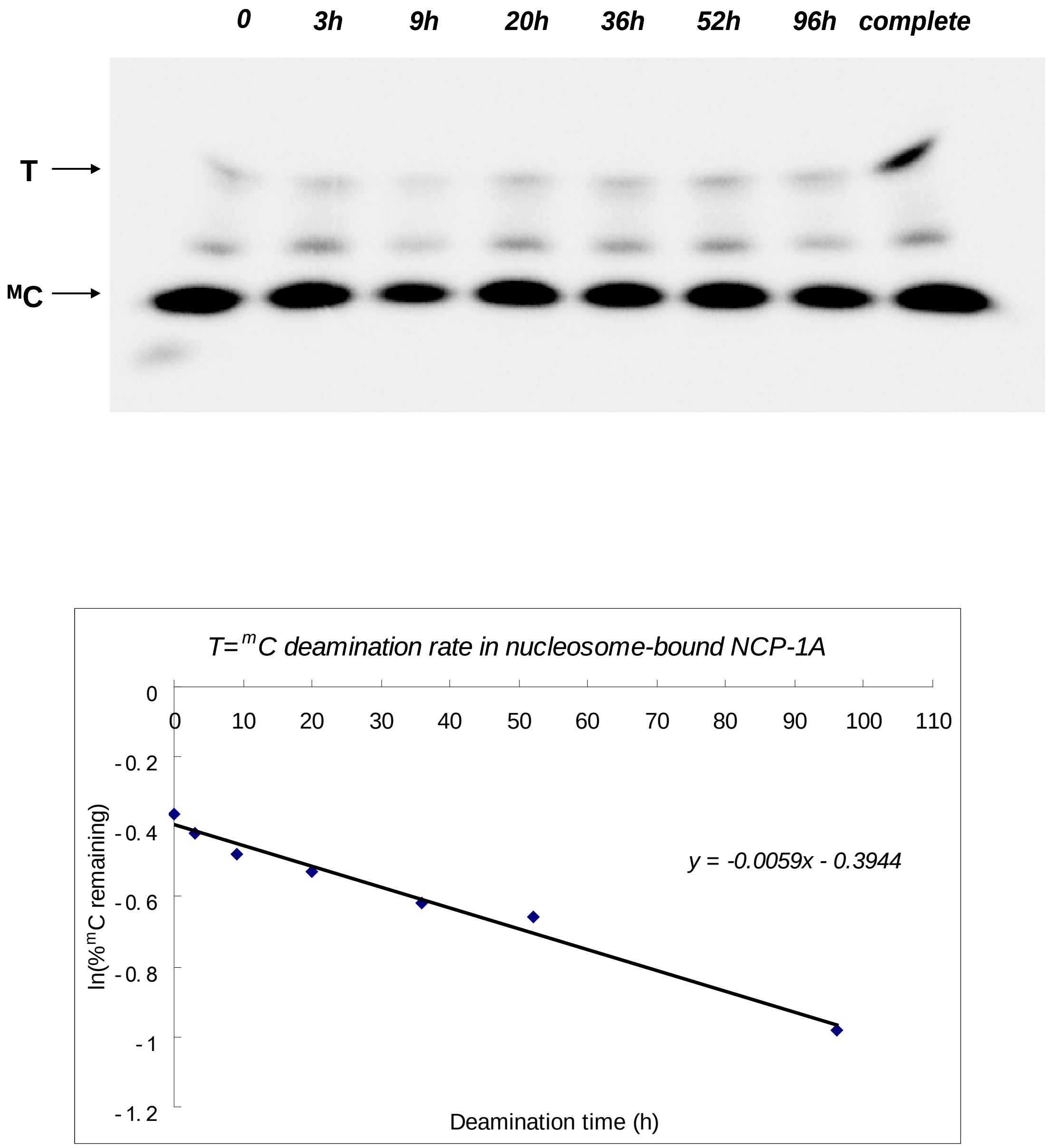

Figure 4.22 Deamination rate of T=^{m}CA CPD in nucleosome-bound NCP-1A using two-dimensional gel electrophoresis (top) & Linear regression analysis of the deamination rate data (bottom). Plots of the individual deamination rate data as log (fraction T=^{m}C remaining) vs time.

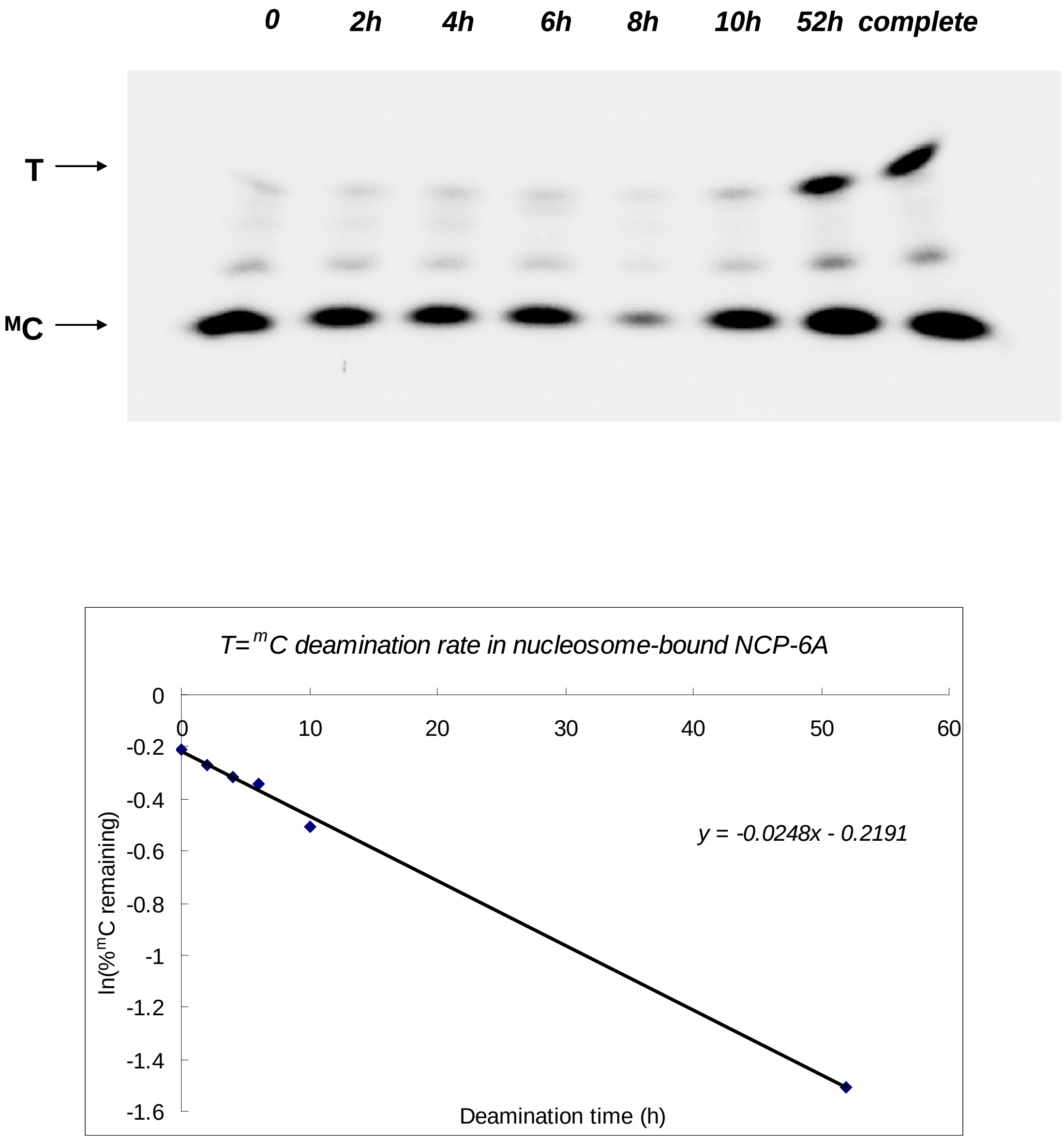

Figure 4.23 Deamination rate of T=^{m}CA CPD in nucleosome-bound NCP-6A using two-dimensional gel electrophoresis (top) & Linear regression analysis of the deamination rate data (bottom). Plots of the individual deamination rate data as log (fraction T=^{m}C remaining) vs time.

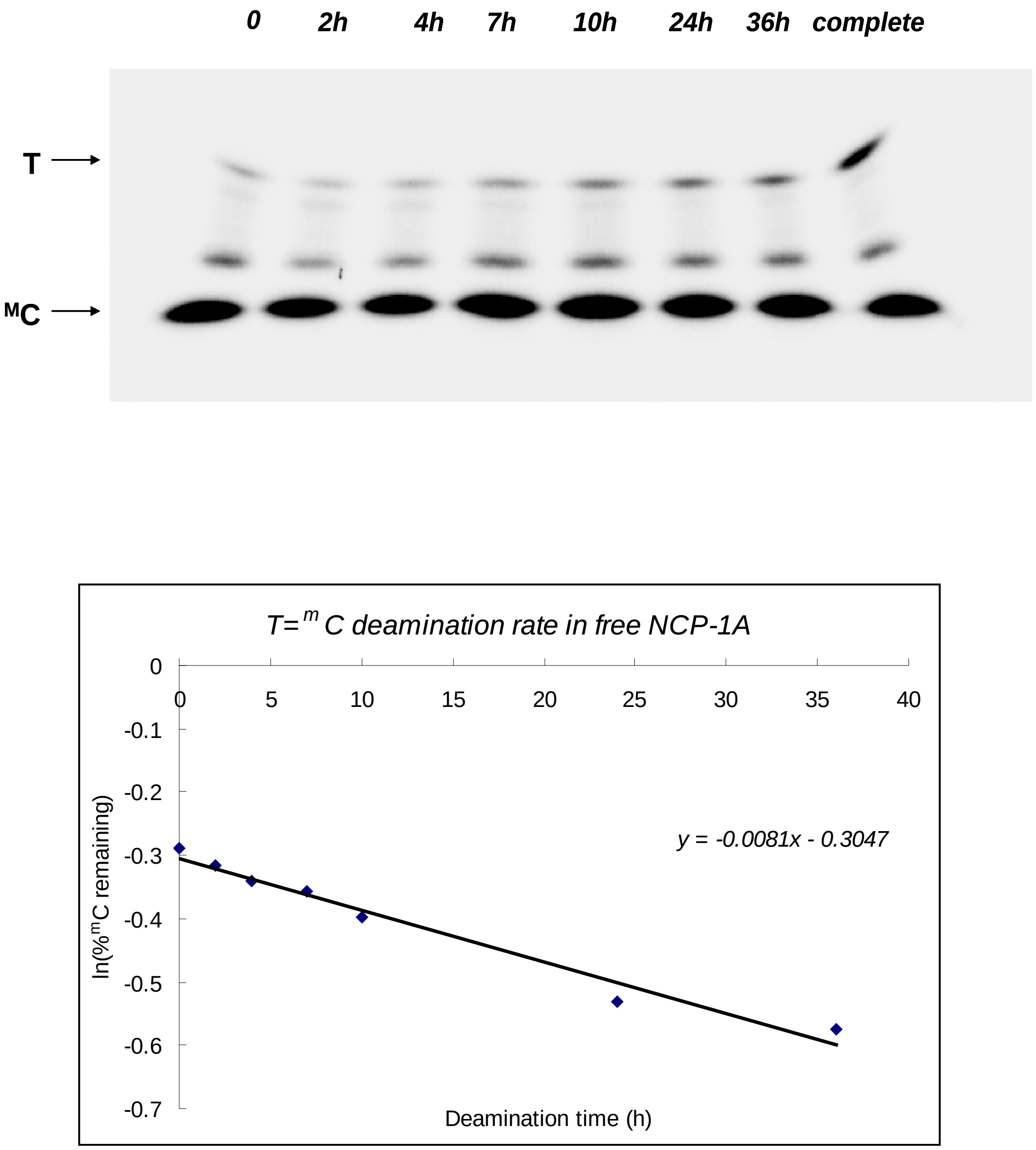

Figure 4.24 Deamination rate of T=^{m}CA CPD in free NCP-1A using two-dimensional gel electrophoresis (top) & Linear regression analysis of the deamination rate data (bottom). Plots of the individual deamination rate data as log (fraction T=^{m}C remaining) vs time.

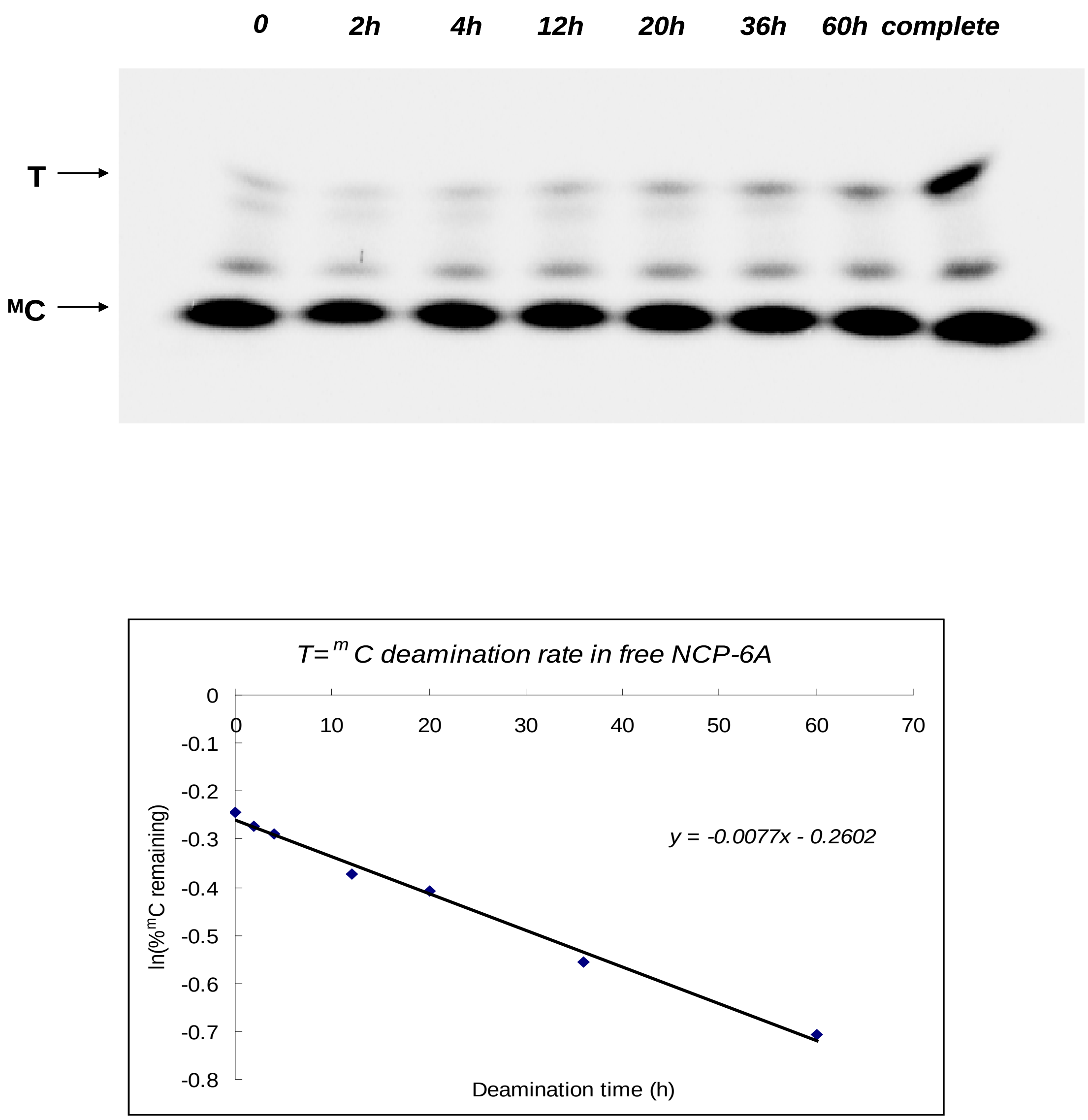

Figure 4.25 Deamination rate of T=^{m}CA CPD in free NCP-6A using two-dimensional gel electrophoresis (top) & Linear regression analysis of the deamination rate data (bottom). Plots of the individual deamination rate data as log (fraction T=^{m}C remaining) vs time.

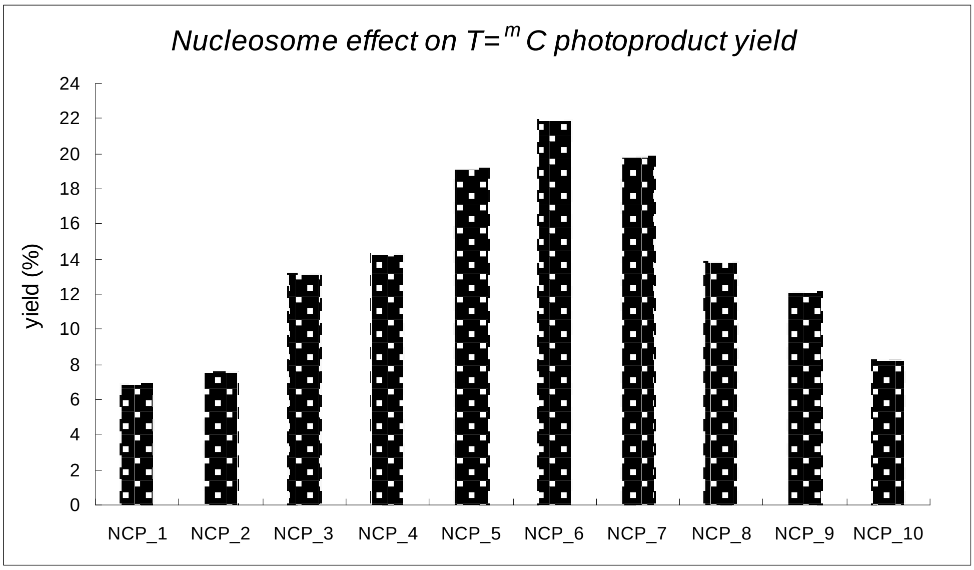

Figure 4.26 T=^{m}CG CPD photoproduct yield in NCP-1, NCP-2 to NCP-10.

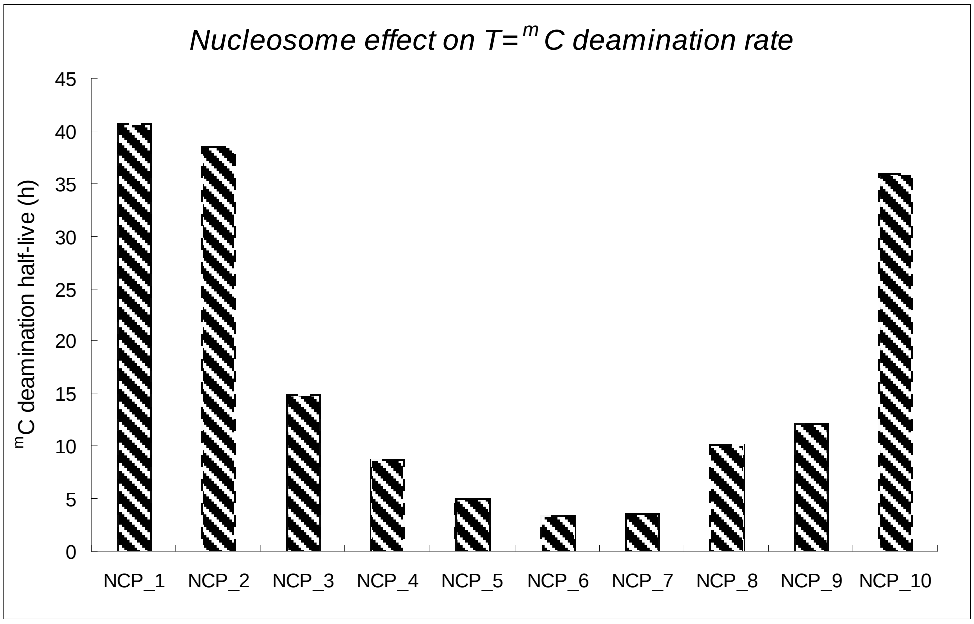

Figure 4.27 T=^{m}CG CPD photoproduct deamination half-life in NCP-1, NCP-2 to NCP-10.

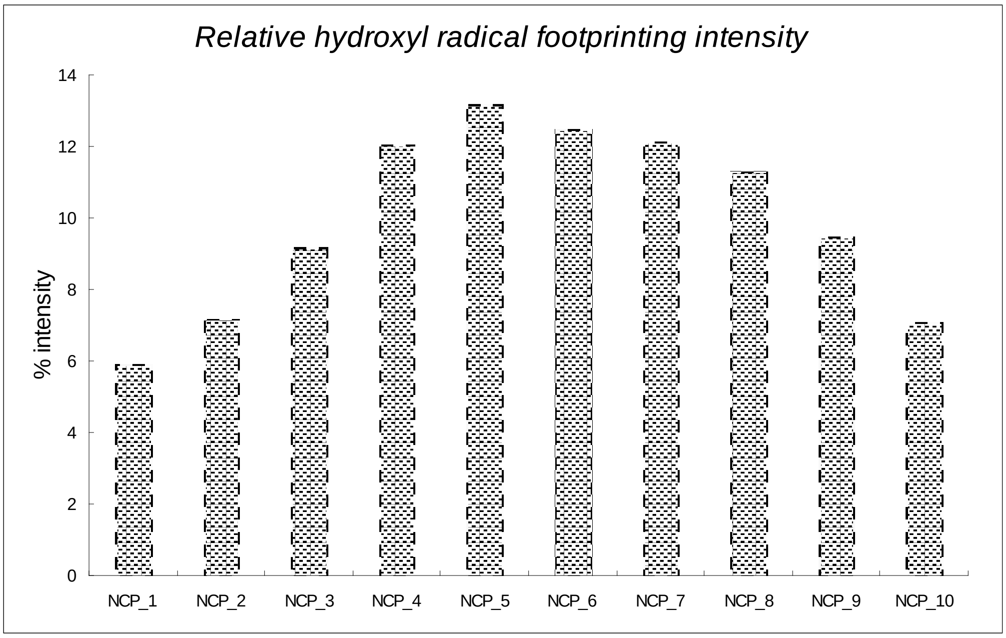

Figure 4.28 Relative hydroxyl radical foot-printing cleavage intensity for nucleosome-bound NCP-1, NCP-2 to NCP-10.

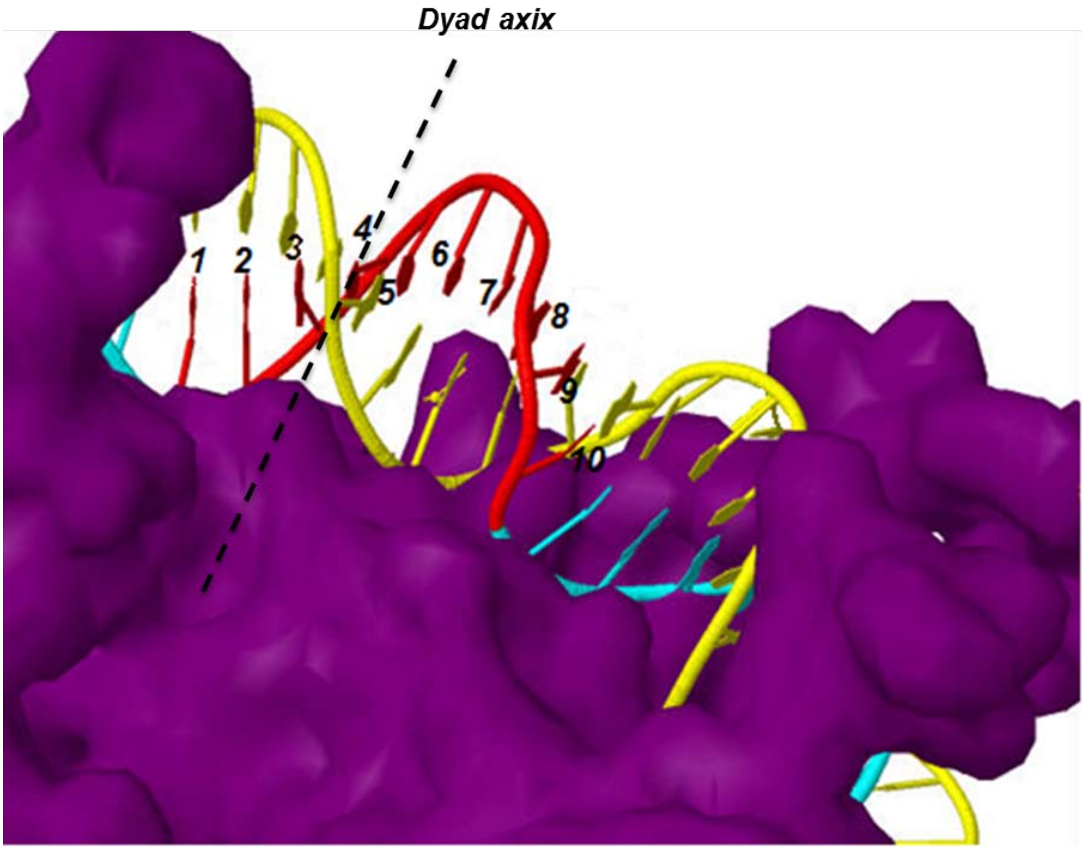

Figure 4.29 Nucleosome core particle structure highlighting the positions of the facing inside and outside T=^{m}CG CPD sites that are consistent with the hydroxyl radical foot-printing data. Purple color represents the histone proteins, yellow and blue color indicate the DNA duplex wrapping around the histone octamer surface. Black dashed line points out the dyad axis of the nucleosome core particle. Red color highlights the ten specific nucleosome rotational positionings of T=^{m}CG CPDs, with the number 1 to 10 indicating the ^{m}C sites relative the histone core surface.

Chapter 5

Reconstitution of Nucleosome Core particle from Recombinant Histones and Synthetic DNA

Abstract

Most of *in vitro* studies on nucleosome core particles (NCPs) or nucleosomes have generally been limited to the use of histone proteins isolated from chromatin, which although straightforward, has several inherited drawbacks. Among the various drawbacks, the procedure is generally time-consuming and the histone proteins obtained in this way are susceptible to degradation from contaminating proteases. Also, since the histones are obtained from a natural source they would exist as a mixture with various post-translational modifications which might have different effects on the property being studied. Most importantly, this method doesn't allow enable one to manipulate the sequence and properties of the histones in a straightforward manner. An alternate approach is to prepare nucleosome core particles (NCPs), or nucleosomal arrays, from recombinant histone proteins and synthetic DNA sequences. This approach has enabled researchers to study histone modifications, histone variants and histone site-mutagenesis. In this chapter, we report our efforts to assemble a histone octamer from recombinant histones expressed and purified from *E. coli*, based on a previously described protocol. We also describe reconstituting the recombinant histone octamer with our synthetic 147-mer DNA duplex, and show that the reconstituted protein rotationally position our 147-mer DNA, although with some differences compared with the chicken nucleome core particles.

Introduction

Most of *in vitro* studies on nucleosome core particles (NCPs) or nucleosomes have generally been limited to the use of histone proteins isolated from chromatin. Basically, the histone molecular aggregates (histone octamer, histone tetramer or histone dimer) are isolated from “long chromatin,” which could be extracted from the nuclei of different organisms. The histone aggregates could then be further separated into individual histone proteins. Although straightforward, there are several disadvantages with this approach. First of all, the procedure is generally time-consuming and highly dependent on the availability of fresh tissue or blood from the organism of choice. Second, histone proteins isolated from natural sources are often degraded by contaminating proteases (1). Third, depending on the specific source of the fresh tissue or blood, there could be different histone isotypes and post-translational modifications of histone proteins in the sample, which could give rise to heterogeneity in the purified histone proteins. The extent of heterogeneity and modifications will be strongly contingent on the type and developmental state of the tissue from which chromatin was isolated and could vary significantly between different batches. Last but not least, and also the most important, only naturally occurring histone proteins can be obtained by this method, if specific engineered histone proteins were in need, then these procedures were almost useless.

Given that, the ability to prepare nucleosome core particles (NCPs), or nucleosomal arrays, from recombinant histone proteins and defined-sequence DNA has become a requirement in many projects that could address the role of histone modifications, histone variants, or histone mutations in nucleosome and chromatin structure. Various reliable and well-established methods have been described in order to obtain single histone proteins in large quantities (2, 3). This approach offers many advantages, such as the ability to combine histone variants and tail deletion mutants, and the opportunity to study the effect of individual histone tail modifications on nucleosome structure and function. Also this approach enables histone engineering, which would enable researchers to investigate the relationship between histone structure and function, as well as nucleosome and chromatin function.

The availability of large quantities of naturally occurring mutants, or of new site-specific mutants of the highly conserved histone proteins, would be extremely valuable in attempts to resolve the observed functions and biophysical properties of the nucleosome core particles with the recently elucidated crystal structure (4). All four nucleosomal histone proteins have been successfully expressed in bacteria, which enabled methods to be developed for mapping of nucleosome core particles to base pair resolution (5). This also enabled the structure of nucleosome core particle to be determined at very high resolution (4). In comparison to yeast expression systems, the bacteria expression system gives relatively high yields, low protease activity, and does not require the presence of histidine-tags or other fusion tags (6, 7).

This chapter describes the over-expression of histones H2A, H2B, H3, and H4 in a bacterial system, both as full length proteins and the corresponding trypsin-resistant “globular domains” by a reported method (8). It also describes a relatively simple and efficient purification protocol in detail, that yields large amounts of homogenous protein in denatured form. Methods for refolding and purification of histone octamer, and for assembly of nucleosome core particles using a 5'-^{32}P-labeled 147-mer DNA duplex used previously in Chapter 4 are also detailed. We verified the formation of recombinant histone octamer, along with the reconstitution with 147-mer DNA duplex and hydroxyl radical foot-printing on the reconstituted particles.

Experimental Procedures

DNA Substrates

Oligodeoxynucleotides (ODN) with or without 5'-terminal phosphates were purchased from Integrated DNA Technologies and purified by denaturing gel electrophoresis prior to ligation with T4 DNA ligase and ATP in the presence of complementary 20-mer ligation scaffolds (Table 4.1 to 4.10, Figure 4.1 to 4.5). The 147-mer single strand products were purified by denaturing PAGE. Complementary 147-mers were then annealed to form the 150-mer duplexes and purified by native PAGE (Figure 4.6).

Histone Expression

Histone expression and isolation followed a previously described procedure with some modifications suited to our laboratory (9). BL21 (DE3) pLysS cells were transformed with 0.5 μg pET-Histone expression plasmid, the transformed competent cells were plated on AC agar plate, which contained 10% (w/v) bacto-tryptone, 5% (w/v) yeast extract, 8% (w/v) NaCl, and 1.5 % (w/v) Agar, supplemented with 100 μg/L ampicillin and 25 μg/L chloramphenicol. The plates were incubated at 37°C overnight. The next morning, 5 mL of 2X TY-AC media (16% (w/v) bacto-tryptone, 10% (w/v) yeast extract, and 5% (w/v) NaCl, supplemented with 100 μg/L ampicillin and 25 μg/L chloramphenicol) was inoculated with one single colony from the agar plate. The culture was shaken at 37°C for 4 h or until the OD_{600} was between 0.3 and 0.6. Then 0.5 mL of the culture was transferred into a sterile eppendorf tube, and 0.2 mL of sterile glycerol was added, the tube was mixed well and stored at –80°C, which served as the glycerol stock for large-scale expressions. Then 100 mL of 2X TY-AC media was inoculated with the histone glycerol stock. The culture was shaken at 37°C overnight. The next morning, 2 2-L Erlenmeyer flasks containing 1000 mL 2X TY-AC media were inoculated with 20 mL of the 100 mL starter culture per flask. The flasks were shaken at 200 rpm under 37°C, until the OD_{600} has reached 0.6, which could take about 3 h. Histone expression was induced by addition of 500 μL of 0.4 M IPTG (final concentration was 0.2 mM), and the culture was shaken for another 3 h (H2A & H2B) or 2 h (H3 & H4). The cells were harvested by centrifugation at 8,000 rpm (10,000 g) using SLA-3000 rotor at room temperature for 15 min. The cell pellet was resuspended homogeneously in 50 mL of wash buffer containing 50 mM Tris-HCl, pH 7.5, 100 mM NaCl, 1 mM Na-EDTA, 1 mM benzamidine and 5 mM 2-mercaptoethanol. The sample was immediately stored at -80°C.

Histone protein inclusion body preparation.

The cell suspension was thawed in a 37°C water bath with the cell suspension became extremely viscous as lysis occurs. The tube was inverted occasionally until completely thawed (20–30 min). The cell solution was transferred into a wide, short measuring cylinder and adjusted the volume with wash buffer to 75 mL. The solution was centrifuged immediately for 20 min at 4°C and 13,500 rpm (23,000 g), using and SS-34 rotor. The pellet contained inclusion bodies of histone protein. The pellet was resuspended completely in 75 mL TW buffer (wash buffer with 1% (v/v) Triton X-100), centrifuged for 15 min at 4°C at 12,000 rpm (17,240g) using SS-34 rotor. This washing step was repeated twice with TW buffer and twice with wash buffer. After the last wash, the drained pellet was stored at –20°C until further processing.

Histone gel filtration chromatography

A Sephacryl HR-200 gel filtration column (75 cm × 1.5 cm) was equilibrated with 2 L of filtered and degassed SAU-1000 buffer containing containing 7M urea (deionized with Amberlite MB3), 20 mM sodium acetate, pH 5.2, 1 M NaCl, 5 mM 2-mercaptoethanol, 1 mM Na-EDTA (passed through 0.4-µm filters before use). Controlled the flow rate around 0.3 mL/min. The equilibration could take overnight. The drained histone inclusion body pellet was transferred to a 50 mL centrifuge tube to which 0.5 mL of DMSO was added allowed to soak for 30 min at room temperature. After that, 10 mL of unfolding buffer containing 7M guanidinium HCl, 20 mM Tris-HCl, pH 7.5, 10 mM DTT (passed through 0.4-µm filters before use) was added dropwise and the solution was stirred gently for 1 h at room temperature. The cellular debris was removed by centrifugation at room temperature and 14,000rpm (23,000g) using SS-34 rotor. The supernatant contained the unfolded histone protein. The pellet was re-extracted with 10 mL of unfolding buffer, and combined with the other supernatant.

About 10 mL of the sample was loaded onto the equilibrated Sephacryl HR-200 column, and gel filtration chromatography was carried out with SAU-1000 buffer at a flow rate around 0.3 mL/min with 1.8 mL fractions. The histone elution profile was obtained by taking the absorbance of the fractions at a wavelength of 280 and 260 nm as shown in Figure 5.1 to 5.4. Then the fractions containing protein were analyzed by 15% SDS-PAGE. The first peak normally contained DNA and larger proteins, and sometimes merged with the histone peak. The second peak contained the histone protein, and eluted as a slightly smaller peak than the first peak. The fractions containing histone proteins were pooled together.

Histone ion-exchange chromatography

A Q-Sepharose cation-exchange column (1.5 cm × 1.5 cm) was equilibrated with SAU-1000 buffer, the column was drained and 2-3 mL of histone protein-DNA complex (about 5 mg) was loaded onto the column and mixed with Q-sepharose resin thoroughly by inverting the column repeatedly, then drained the SAU-1000 buffer. Then loaded 30 mL of SAU-DIL buffer containing 7 M urea (deionized), 20 mM sodium acetate, pH 5.2, 5 mM 2-mercaptoethanol, 1mM Na-EDTA (Pass through 0.4-μm filters before use). The solution was then mixed with the resin containing the histone protein-DNA complex thoroughly, as this salt dilution helps the histone protein bind tightly to the anion resin, instead of the contaminating DNA. The solution was drained andcontained most of the contaminating DNA. The column was washed with the SAU-DIL buffer until the A_{260} of the elution was close to background value. The histone protein was eluted by gradient salt elution (from

SAU-200 buffer containing containing 7M urea, 20 mM sodium acetate, pH 5.2, 0.2 M NaCl, 5 mM 2-mercaptoethanol, 1 mM Na-EDTA to SAU-1000 buffer containing containing 7M urea, 20 mM sodium acetate, pH 5.2, 1 M NaCl, 5 mM 2-mercaptoethanol, 1 mM Na-EDTA). Collected the eluting fractions under different salt concentration. Recorded the A_{260} and A_{280}.

The fractions with $A_{260}/A_{280} < 1.0$, which indicated the presence of pure histone protein, were pooled. Histones H2A & H2B were completely eluted with SAU-400 buffer which contained 0.4 M NaCl, histone H3 with 0.3 M NaCl, and histone H4 with 0.5 M NaCl. The pure histone proteins were dialyzed against dd H_2O, and lyophilized in eppendorf tubes. The final yield of each recombinant histone was 15 mg/L of initial culture (H2A), 18 mg/L (H2B), 23 mg/L (H3), 8 mg/L (H4).

Histone Octamer Assembly

About 4 mg of each histone aliquot was dissolved to a concentration of approximately 2 mg/mL in unfolding buffer containing 7M guanidinium HCl, 20 mM Tris-HCl, pH 7.5, 10 mM DTT (passed through 0.4 μm filters before use). A Pasteur pipet was used to scrape the side to ensure that any protein sticking to the sides of the tube was dissolved. It is important not to vortex the tube. Unfolding was allowed to proceed for at least 30 min and for no more than 3 h. The concentration of the unfolded histone proteins was determined by measuring the A_{276} of the undiluted solution against unfolding buffer, according to Table 5.1 (solid matterial was removed by centrifugation, if necessary). The four histone proteins were mixed in equimolar ratios and adjusted to a total final protein concentration of 1 mg/mL using unfolding buffer. The mixture was dialyzed at 4°C against three changes of 2 L of refolding buffer containing 2M NaCl, 10mM Tris-HCl, pH 7.5, 1 mM Na-EDTA, and 5 mM 2-mercaptoethanol. The second and third dialysis steps were performed overnight. The histone assembly solution was recovered from the dialysis tubing and concentrated to a final volume about 2 mL.

Gel filtration chromatography was performed at 4°C at a flow rate of 0.3 mL/min. The concentrated histone octamer was loaded onto the Sephacryl HR-200 gel filtration column previously equilibrated with refolding buffer. High-molecular weight aggregates eluted as the first peak, and the histone octamer as eluted as the second peak. The purity and stoichiometry of the fractions was analyzed by 15% SDS-PAGE. Each fraction was diluted by at least a factor of 4 before loading onto SDS-PAGE to reduce distortion of the bands resulting from the high salt concentration. The fractions containing equimolar amounts of the histone proteins were then pooled together.

The histone octamer concentration was determined by UV measurement (A_{276} = 0.45 for a solution of 1 mg/mL). The pure histone octamer solution was then used for nucleosome core particle reconstitution with DNA immediately, or concentrated to 3–15 mg/mL, adjusted to 50% (v/v) glycerol, and stored at –20°C.

Dynamic Light Scattering Measurement

The size of assembled histone s in the gel filtration fractions was measured by dynamic light scattering (DLS) on a Malvern Nano Sizer. Measurements were made with histone assembly concentrations from 0.2 mg/mL to 1 mg/mL, depending on the sepecific fraction, at 25 ± 1 °C. Scattered light was collected at a fixed angle of 173°.

Histone Octamer Reconstitution with 147-mer DNA duplexes

Reconstitution of histone octamer with 147-mer DNA duplex was accomplished using a modified salt gradient dialysis method described in chapter 4. Briefly, octamer and 10 nM 147-mer DNA was mixed at 2M KCl, and the salt concentration was reduced by dialysis to 0.2 M KCl over a period of 36 h. The histone octamer was added to the 5'-^{32}P-labeled 147-mer DNA duplex at a various molar ratios of octamer to DNA (0.5:1, 1:1, 2:1, 3:1, 5:1, and 10:1), with a final DNA concentration of 10 nM. Before adding the histone octamer, the salt concentration of the DNA solution was adjusted to 2 M KCl, and DTT was added to a final concentration of 5 mM. The histone octamer was always added last. The reconstitution samples were incubated at 4°C for 30 mins, then dialyzed against 300 mL of 2 M KCl, 10 mM Tris-HCl, 1 mM DTT, pH 7.5, at 4°C, for 1 h. Then 2.7 L of dialysis buffer containing 10 mM Tris-HCl, 1 mM DTT, pH 7.5, was gradually added to the 300 mL of the original buffer through a pump at flow rate of 1.5-2.0 mL /min, which slowly transfered the dialysis buffer into the original container used for the whole dialysis process. The pumping transfer and dialysis was carried out at 4°C, over a period of 36 h. The final salt concentration was about 0.2 M KCl. Finally, the reconstituted particles were recovered from the dialysis tubing and equilibrated at 50°C for 2 h to fix the nucleosome positioning.

The reconstituted particles were assayed by native PAGE (6% acrylamide, 0.2% bisacrylamide in TBE), and the ratio of nucleosome-bound DNA to free DNA was quantified by the Quantity One software.

Hydroxyl Radical Foot-printing of Reconstituted Recombinant Histone Octamer

After the reconstitution process, the nucleosome positioning of the 147-mer DNA duplex was determined by hydroxyl radical foot-printing experiment using the same reaction conditions as used before for the chicken nucleosome core particle. Briefly, a 15 uL aliquot of 10 mM sodium ascorbate, a 15 uL aliquot containing 1 mM $Fe(NH4)_2(SO4)_2 6H_2O$ and 2 mM EDTA, and 15 uL of a 0.12% (w/w) H_2O_2 solution were premixed and added within 5 s to 105 uL of the reconstituted histone octamer with 147-mer DNA duplexes. The reaction was incubated for 120 s at room temperature and stopped by the addition of 16 μL of 50% (v/v) glycerol and 4 μL of a 500 mM EDTA solution. The proteins were extracted with phenol: chloroform: isopropyl alcohol 25:24:1, and the DNA was precipitated with ethanol. The free ds-control was treated in a similar way, except that the reaction was quenched with a solution containing 1 M sodium acetate, 120 mM thiourea, 300 ug/mL salmon sperm DNA, and 60 mM EDTA at pH 6.5 and then ethanol-precipitated.

Results

Histone protein expression and purification

Based on previous research, expression levels of histones H2A and H2B appear to be insensitive to the sequence variant being expressed, but histone H3 expression levels vary a lot between different sequence variants or mutated genes. H4 expression is sensitive to amino acid substitutions and could drop to an undetectable level for certain point mutations. Typical reported yields for H2A, H2B, and H3 were 50–80 mg of pure protein per liter of bacterial cell culture, while the yield for H4 was 4–5 times lower (9). The pET-histone expression plasmids used in this research for the four histones were kindly provided by Professor Luger's lab.

After gel filtration chromatography, the A_{260}/A_{280} of the histone proteins were between 1.4 to 1.7, indicating there was a significant amount of DNA contaminating the histone proteins, so we utilized a modified ion-exchange chromatography to further purify the histone protein from the protein-DNA complex as described in details in experimental section. Using this modified ion-exchange chromatography method, we could obtain highly pure histones H2A, H2B, H3 and H4, as characterized by SDS-PAGE and mass spectrometry (Figure 5.5 to 5.9 and Table 5.2).

Histone Octamer Assembly

The protocol described in the experimental section works best for 6-15 mg of total protein, but for smaller amounts of protein the gel filtration column needs to be scaled down. After the gel filtration chromatography the absorbance at 276 nm was recorded for each fraction, which identified two big peaks and one small peak (Figure 5.10). Fractions corresponding to each peak were analyzed on a 15% SDS-PAGE, in order to determine the purity and stoichiometry of each peak. As shown in Figure 5.11, the first peak, with a larger molecular weight, was mainly made up with histone H3 and H4, however, for the second peak, as highlighted by the red box, we could clearly see the presence of all 4 kinds of histone proteins, indicating this peak contain the histone aggregate made up with the 4 histone proteins under a equimolar ratio of each other.

Besides the SDS-PAGE, we also carried out a dynamic light scattering (DLS) measurement of each histone aggregate eluting from the gel filtration chromatography, to further identify the histone octamer. As shown in Figure 5.12 to 5.13, and listed in Table 5.3, the size of the first peak of histone assembly after gel filtration chromatography exhibited a hydrodynamic diameter around 20 nm, which was about 3-fold larger than the ideal histone octamer assembly. However, the second peak exhibited a hydrodynamic diameter around 8.5 nm, which was almost the correct size of histone octamer assembly (7 nm). Since the hydrodynamic diameter normally gives a slightly bigger value than the actual size, we believed that the second peak was the desired histone octamer.

Histone Octamer Reconstitution with the 147-mer DNA Duplexes

Specific DNA fragments of desired length or sequence can be obtained by a number of methods (10, 11) for assembly with the recombinant histone octamer to form a nucleosome core particle. We used an electrophoretic mobility shift assay (Figure 5.14), to monitor the assembly of the recombinant histone core particle with the 147-mer DNA duplex. Below a molar ratio of 1:1 of recombinant histone core particle to DNA, we could still see free 147-mer DNA duplex (Figure 5.14, *Lane 1 to 3*). At a ratio of 3:1, we could see the disappearance of free 147-mer DNA duplex, and some histone-DNA complex which exhibited a slower electrophoretic mobility on the gel (Figure 5.14, *Lane 4*). At a ratio of 5:1, higher molecular aggregates appeared, as seen by a higher position on the gel, compared with that with a ratio of 3:1 (Figure 5.14, *Lane 5*), when the amount of recombinant histone core particle increased even more, no bands were detected on the gel, except the material in the well, indicating a super high molecular aggregate formed during the reconstitution process (Figure 5.14, *Lane 6*).

The reconstitution results proved that the recombinant histone core particle we prepared could successfully bind to the 147-mer DNA duplex containing a multiple repeat of nucleosome positioning sequence. When compared with the reconstitution of the nucleosome core particle isolated and purified from chicken blood cells (Figure 4.7 & 4.8, Chapter 4), we could see differences. During the assembly of the recombinant histone core particle, the nucleosome core particle band was not uniformly sized, unlike what we saw using the chicken nucleosome core particle. When the amount of recombinant histone core particle increased, higher and higher molecular weight aggregates were observed to form during the reconstitution process. When we used the chicken nucleosome core particle, however, the nucleosome core particle band did not change even when we increased the amount of chicken nucleosome core particle, which means only one kind of reconstituted product formed. Perhaps this was because this was an exchange reaction between free DNA and a properly formed nucleosome core particle. When it comes to the recombinant histone core particle, probably one or more reconstituted products can form during the salt gradient dialysis process.

Nucleosome rotational positisioning ability of 147-mer DNA on reconstituted histone *octamer.*

Since the 147-mer DNA duplex we used in chapter 4 has proved to have a strong nucleosome rotational positioning ability, we want to see whether this positioning ability would be observed with the recombinant histone octamer. Based on the hydroxyl radical foot-printing results shown in Figure 5.15, we plotted the intensity of the bands in each lane under different conditions as shown in Figure 5.16. From this figure we can see that although there was no uniform nucleosome core particle band, the 147-mer DNA duplex still exhibited strong nucleosome positioning on the recombinant histone core particle, as evidenced by the roughly 10-11 bp periodicity in the intensity of the hydroxyl cleavage bands. When the molecular ratio of recombinant NCP to DNA is 1:1, we could see a clear nucleosome pattern in Figure 5.16, although a part of the DNA sequence didn’t exhibit a perfect nucleosome positioning (highlighted in the red box). This imperfection was not observed in the previous study using the chicken nucleosome core particle. As we increased the ratio of recombinant NCP from 1:1 to 10:1, the nucleosome positioning ability did not change, which means although higher molecular weight DNA-histone aggregates formed as the ratio increased, the DNA still wrapped around the histone octamer with a defined rotational positioning.

Discussion

In previous chapters, we successfully utilized the nucleosome core particle isolated and purified from chicken blood cell to carry out the reconstitution experiment with 147-mer DNA duplexes. We were able to show that the nucleosome positioning of the 147-mer DNA duplexes by hydroxyl radical foot-printing and detect differences in deamination rates. While were were able to obtain valuable information from these particles, we desired a more general system that would allow for the introduction of probes, and site specific histone modifications. So in this chapter, we aimed to prepare the nucleosome core particles using recombinant histone proteins, which would allow us to manipulate the nucleosome core particle at the amino acid level, and investigate the structure and function of nucleosome more deeply and broadly.

Following the protocol developed in Professor Luger's lab (9), we expressed the four histone proteins H2A, H2B, H3 and H4 in bacteria system, using the pET-histone expression vector. The histone proteins were purified to a high degree of purity by gel filtration chromatography and ion-exchange chromatography in their denatured form. After that, we refolded the histone octamer using the purified H2A, H2B, H3 and H4 histone proteins. The histone octamer turned out to have the expected size and composition, and so we went on to reconstitute the nucleosome core particle with the previously designed 147-mer DNA duplex. To characterize the nucleosome core particle we used electrophoretic shift assays and hydroxyl radical foot-printing experiments.

Although we followed the procedure published before (9), we did see some variation in terms of the experiment outcome. During the gel filtration chromatography to purify the denatured histone proteins, we kept noticing the contamination of the protein sample with DNA, indicated by an A_{260}/ A_{280} around 1.6, which was not observed in the original experiment carried out by Luger’s lab using the same procedure. When we used the reported ion-exchange chromatography method, however, we couldn’t separate the protein from the protein-DNA mixture cleanly, so we modified the ion-exchange chromatography method. Our modification used a salt dilution step, which was proved to be highly effective in separating the histone proteins from the contaminating DNA. By taking advantage of this modification, we were able to purify the histone protein much better than the original reported method.

In the complexation step of recombinant histone octamer and 147-mer DNA, we saw a clear evidence of binding between them, although the nucleosome particle formed was not as uniform as what we got previously using the chicken nucleosome core particle. One possible explanation is that the chicken nucleosome core particle was already wrapped by chicken nucleosomal DNA, which could help to stabilize the core particle as the mono-nucleosome at low salt concentration (50 mM NaCl). The recombinant histone octamer, however, did not contain DNA, and although it was stored at high salt concentration (2M NaCl), it may have formed aggregates during storage or during the salt gradient dialysis. The histone octamer aggregates might still be expected to bind to the 147-mer DNA duplex, but the bound complex might be non-uniform in terms of size and shape, exhibiting slower gel electrophoresis ability, as shown in Figure 5.14. Also these histone octamer aggregates could interfere with the nucleosome positioning ability of the 147-mer DNA duplex, since the octamer aggregate might have a bigger size and a different shape. The DNA might wrap in a different way compared with the histone mono octamer, which could lead to a different hydroxyl radical foot-printing results, as could be seen from Figure 5.15 and 5.16, the red box indicate the partial footprinting results that was not consistent with the 10-11 bp periodicity of nucleosome pattern. When compared with the hydroxyl radical foot-printing of the chicken nucleosome core particle (Figure 5.17). We could see that the hydroxyl radical cleavage pattern was not as good as for the chicken nucleosome, as highlighted in the blue box in Figure 5.17, indicating the partial structure of the recombinant histone core particle around 50-60 bp DNA region (from 5' end) was probably different than the chicken histone core particle.

Another possibility for the differences in the reconstitution and hydroxyl radical foot-printing assay could be due to difference in the sequences of the four histone proteins of chicken and xenopus. As shown from Table 5.4 to 5.7, there are a number of amino acid variants in the histone protein sequences. For example, there are 30 amino acid differences between the xenopus H2A sequence compared with that of the chicken (about 25% difference). There were 10 amino acid different in xenopus H2B compared with chicken H2B, while the sequence variations between H3 and H4 are relatively small between xenopus and chicken. These major sequence alterations could causes differences in the protein size, shape, hydrophobicity or charge. According to the crystal structure of the nucleosome, the amino acids from 76 to 80 of the H2A loop region (L2) directly contact the 50-60 bp region in the 147-mer DNA duplex (4). The Arg_{78} of chicken H2A can insert its side chain into the minor groove of the DNA to help the binding and orientation of the DNA onto the histone core surface. However, the same position on H2A from xenopus is replaced with Pro, which eliminates the direct interaction between the DNA and histone H2A. Also we can see the amino acids sequence in this loop region differ a lot between these two species, five out of the six are different, which probably cause a lot of structural change in this L2 loop region of H2A, hence changing the direct contact between the DNA and histone core surface at this area, making the corresponding histone octamer could differ a lot in the ability to complex with the 147-mer DNA duplex, leading to different binding products and foot-printing results.

Conclusions

We successfully expressed and purified all four histone proteins H2A, H2B, H3 and H4 utilizing a modification of a protocol described previously (9). By using the published procedure, we were able to assemble the recombinant histone octamer from these four pure histone proteins. Through the assembly process, we could wrap our synthetic 147-mer DNA duplex onto the histone octamer to form a nucleosome core particle. Although not completely the same as using nucleosome core particle from chicken blood cells, the hydroxyl radical foot-printing of the nucleosome core particle assembled from recombinant histone octamer did show a clear nucleosome positioning pattern with a 10-11 bp periodicity. The differences in size and footprinting between chicken nucleosome core particle and recombinant histone octamer could probably be due to several reasons: the size and shape of DNA-recombinant histone octamer aggregate was different from reconstituted chicken nucleosome core particle; the interactions between DNA and histone octamer could be different due to variations in the amino acid sequence between these two species.

Acknowledgment

We thank Professor Luger’s Lab kindly providing the pET-histone expression plasmids used in this research for the four histones.

References

1. Mellado, R. P. and Murray, K. Synthesis of yeast histone 3 in an Escherichia coli cell-free system. *J. Mol. Biol.* **1983,** *168,* 489–503.

2. Von Holt, C., Brandt, W. F., Greyling, H. J., Lindsey, G. G., Retief, J. D., Rodrigues, J. D., Schwager, S., and Sewell, B. T. Isolation and characterization of histones. *Meth. Enzymol.* **1989,** *170*, 431–523.

3. Luger, K., Rechsteiner, T., and Richmond, T. J. Characterization of nucleosome core particles containing histone proteins made in bacteria. *J. Mol. Biol.* **1997,** *272*, 301–311.

4. Luger, K., Maeder, A. W., Richmond, R. K., Sargent, D. F., and Richmond, T. J. X-ray structure of the nucleosome core particle at 2.8 A resolution. *Nature.* **1997,** *389*, 251–259.

5. Flaus, A., Luger, K., Tan, S., and Richmond, T. J. Mapping nucleosome position at single base-pair resolution by using site-directed hydroxyl radicals. *Proc. Natl. Acad. Sci. USA*, **1996,** *93*, 1370–1375.

6. Fukuma, M., Hiraoka, Y., Sakurai, H., and Fukasawa, T. Purification of yeast histones competent for nucleosome assembly in vitro. *Yeast*, **1994**, *10,* 319–331.

7. Pilon, J., Terrell, A., and Laybourn, P. J. Yeast chromatin reconstitution system using purified yeast core histones and yeast nucleosome assembly protein-1. *Protein Expr. Purif.* **1997,** *10*, 132–140.

8. Bohm, L. and Crane-Robinson, C. Proteases as structural probes for chromatin: the domain structure of histones. *Biosci. Rep.* **1984,** *4*, 365–386.

9. Luger, K., Rechsteiner, T. J., and Richmond, T. J. Expression and purification of recombinant histones and nucleosome reconstitution. *Methods. Mol. Biol.* **1999,** *119,* 1–16.

10. Simpson, R. T., Thoma, F., and Brubaker, J. M. Chromatin reconstituted from tandemly repeated cloned DNA fragments and core histones: a model system for study of higher order structure. *Cell.* **1985,** *42*, 799–808.

11. Richmond, T. J., Searles, M. A., and Simpson, R. T. Crystals of a nucleosome core particle containing defined sequence DNA. *J. Mol. Biol.* **1988,** *199*, 161–170.

Table 5.1 Molecular Weights and Molar Extinction Coefficients (ε) for Full-Length and Trypsin Resistant Globular Domains of Histone Proteins.

Full-length protein			Globular domains		
Histones	Mol. wt	ε (cm/*M*), 276nm	Amino Acid	Mol. wt	ε (cm/*M*), 276nm
H2A	13,960	4050	19-118	11,862	4050
H2B	13,774	6070	27-122	11,288	6070
H3	15,273	4040	27-135	12,653	4040
H4	11,236	5400	20-102	9,521	5400

Table 5.2 Calculated mass and experimental mass obtained for histone Proteins.

Histones	**Calculated Mass**	**Experimental Mass**
H2A	13,960	14,063
H2B	13,774	13,574
H3	15,273	15,405
H4	11,236	11,304

Table 5.3 DLS measurement of histone assembly fractions after gel filtration chromatography.

Fraction No.	Hydrodynamic diameter (nm)
15	**22**
16	**21**
19	**8.8**
20	**8.5**
21	**8.4**

Table 5.4 Sequence alignment of histone H2A between chicken and xenopus.

H2A amino acid sequence alignment	
Chicken Xenopus	MSGRGKQGGK ARAKAKSRSS RAGLQFPVGR VHRLLRKGNY MSGRGKQGGK TRAKSKTRSS RAGLQFPVGR VHRLLRKGNY
Chicken Xenopus	AERVGAGAPV YLAAVLEYLT AEILELAGNA ARDNKKTRII AERVGAGAPV YLAAVLEYLT AEILELAWER LPEITKRPVL
Chicken Xenopus	PRHLQLAIRN DEELNKLLGK VTIAQGGVLP NIQAVLLPKK TDSHKAKAK SPGTCNSLCN DEELNKLLGG VTIAQGGVLP NIQSVLLPKK TESSKSTKSK

Table 5.5 Sequence alignment of histone H2B between chicken and xenopus.

H2B amino acid sequence alignment	
Chicken Xenopus	MPEPAKSAPA PKKGSKKAVT KTQKKGDKKR KKSRKESYSI MPEPAKSAPA PKKGSKKAVT KTPKKDGKKR RKSRKESYAI
Chicken Xenopus	YVYKVLKQVH PDTGISSKAM GIMNSFVNDI EIRIAGEASR YVYKVMKQVH PDTGISSKAM GIMNSFVNDI FERIAGEASR
Chicken Xenopus	LAHYNKRSTI TSREIQTAVR LLLPGELAKH AVSEGTKAVT KYTSSK LAHYNKRSTI TSREIQTAVR LLLPGELAKH AVSEGTKAVT KYTSAK

Table 5.6 Sequence alignment of histone H3 between chicken and xenopus.

H3 amino acid sequence alignment	
Chicken Xenopus	MARTKQTARK STGGKAPRKQ LATKAARKSA PATGGVKKPH MARTKQTARK STGGKAPRKQ LATKAARKSA PATGGVKKPH
Chicken Xenopus	RYRPGTVALR EIRRYQKSTE LLIRKLPFQR LVREIAXDFK TDLRFQSSAV RYRPGTVALR EIRRYQKSTE LLIRKLPFQR LVREIAQDFK TDLRFQSSAV
Chicken Xenopus	MALQEASEAY LVGLFEDTNL CAIHAKRVTI MPKDIQLARR IRGERA MALQEASEAY LVGLFEDTNL CAIHAKRVTI MPKDIQLARR IRGERA

Table 5.7 Sequence alignment of histone H4 between chicken and xenopus.

H4 amino acid sequence alignment	
Chicken Xenopus	MSGRGKGGKG LGKGGAKRHR KVLRDNIQGI TKPAIRRLAR MSGRGKGGKG LGKGGAKRHR KVLRDNIQGI TKPAIRRLAR
Chicken Xenopus	RGGVKRISGL IYEETRGVLK VFLENVIRDA VTYTEHAKRK RGGVKRISGL IYEETRGVLK VFLENVIRDA VTYTEHAKRK
Chicken Xenopus	TVTAMDVVYA LKRQGRTLYG FGG TVTAMDVVYA LKRQGRTLYG FGG

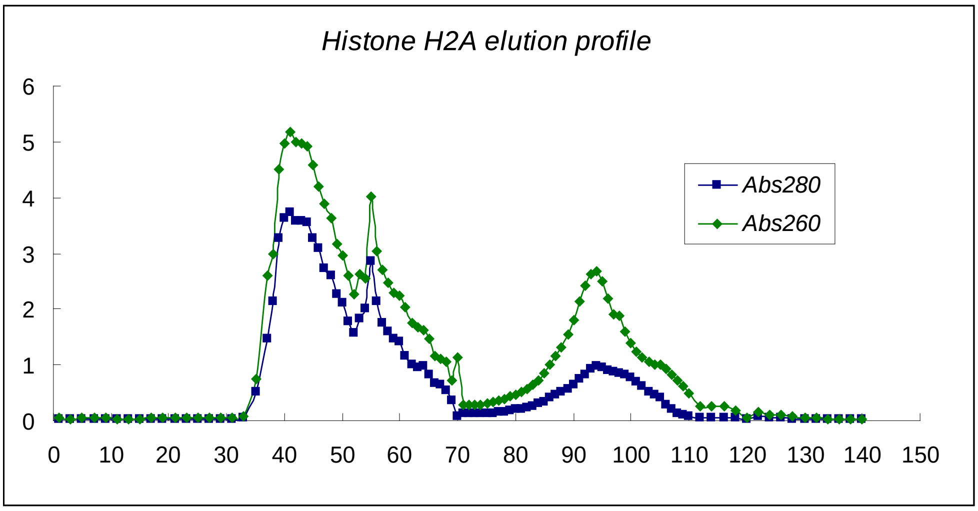

Figure 5.1 Histone H2A elution profile from Sephacryl HR-200 gel-filtration chromatography. Both A_{260} and A_{280} were recorded.

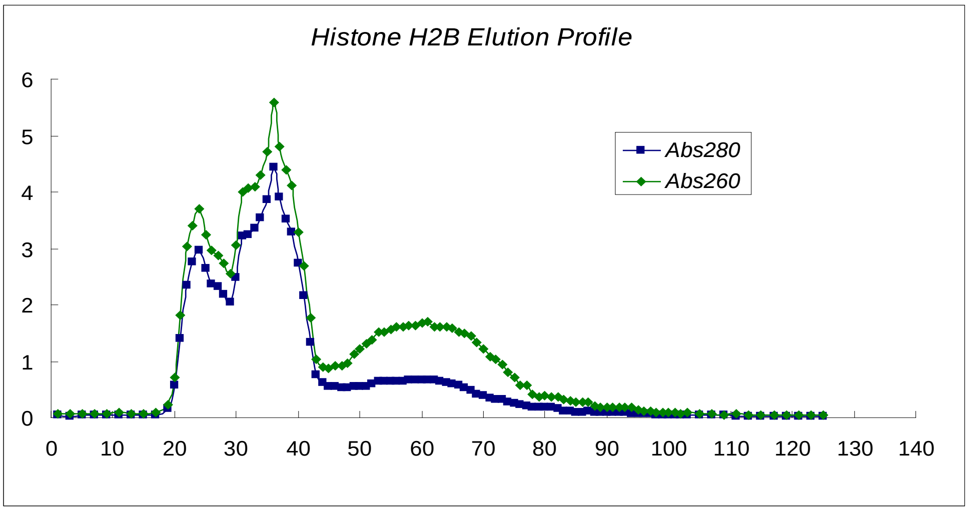

Figure 5.2 Histone H2B elution profile from Sephacryl HR-200 gel-filtration chromatography. Both A_{260} and A_{280} were recorded.

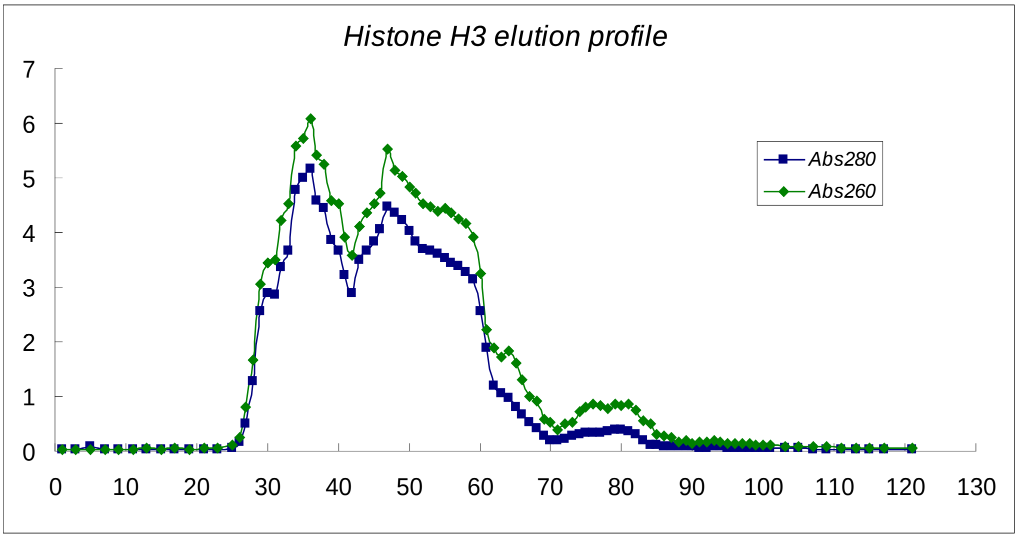

Figure 5.3 Histone H3 elution profile from Sephacryl HR-200 gel-filtration chromatography. Both A_{260} and A_{280} were recorded.

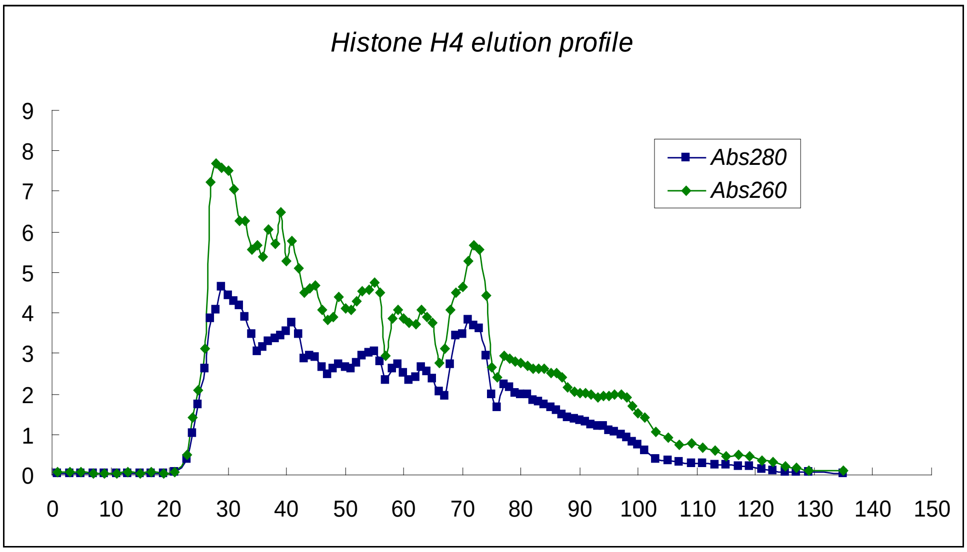

Figure 5.4 Histone H4 elution profile from Sephacryl HR-200 gel-filtration chromatography. Both A_{260} and A_{280} were recorded.

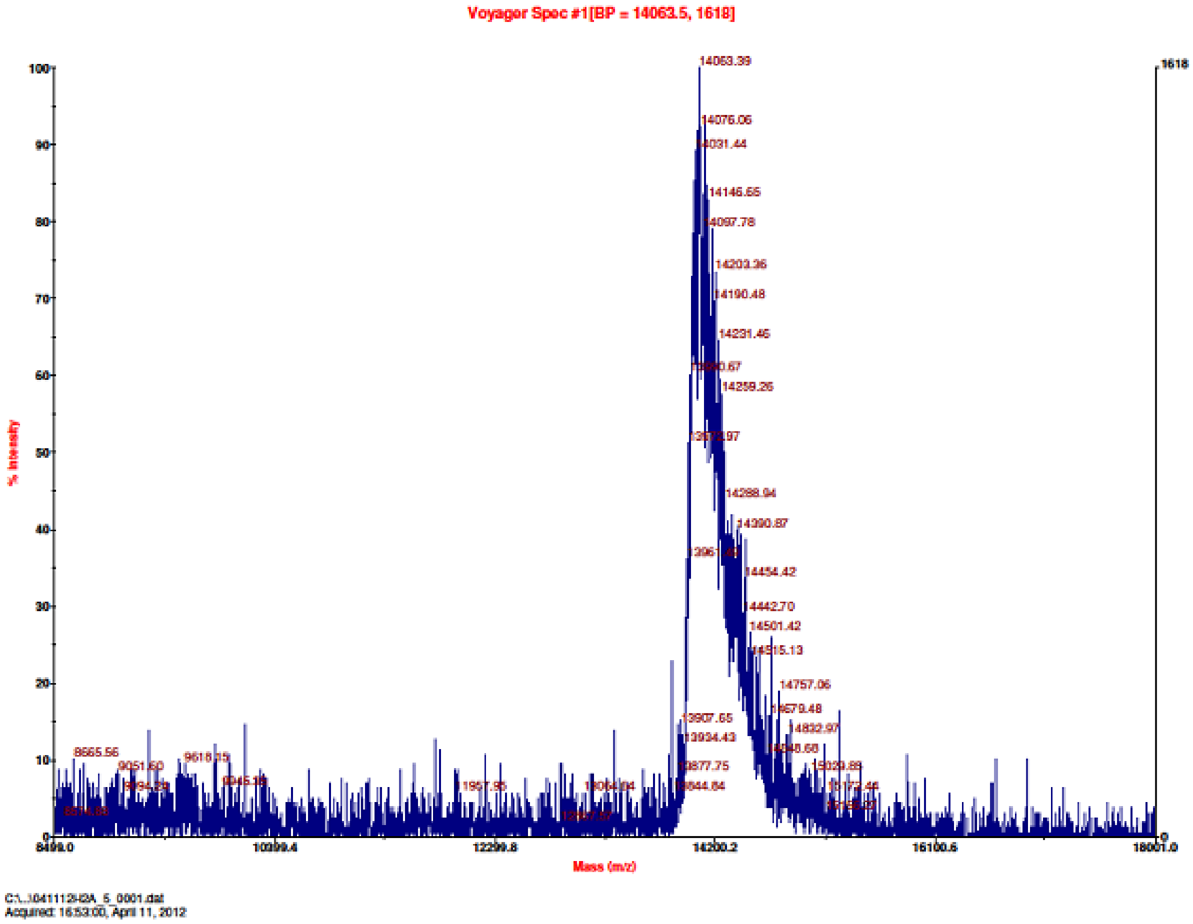

Figure 5.5 Characterization of histone protein H2A by MALDI-TOP Mass Spectrometry.

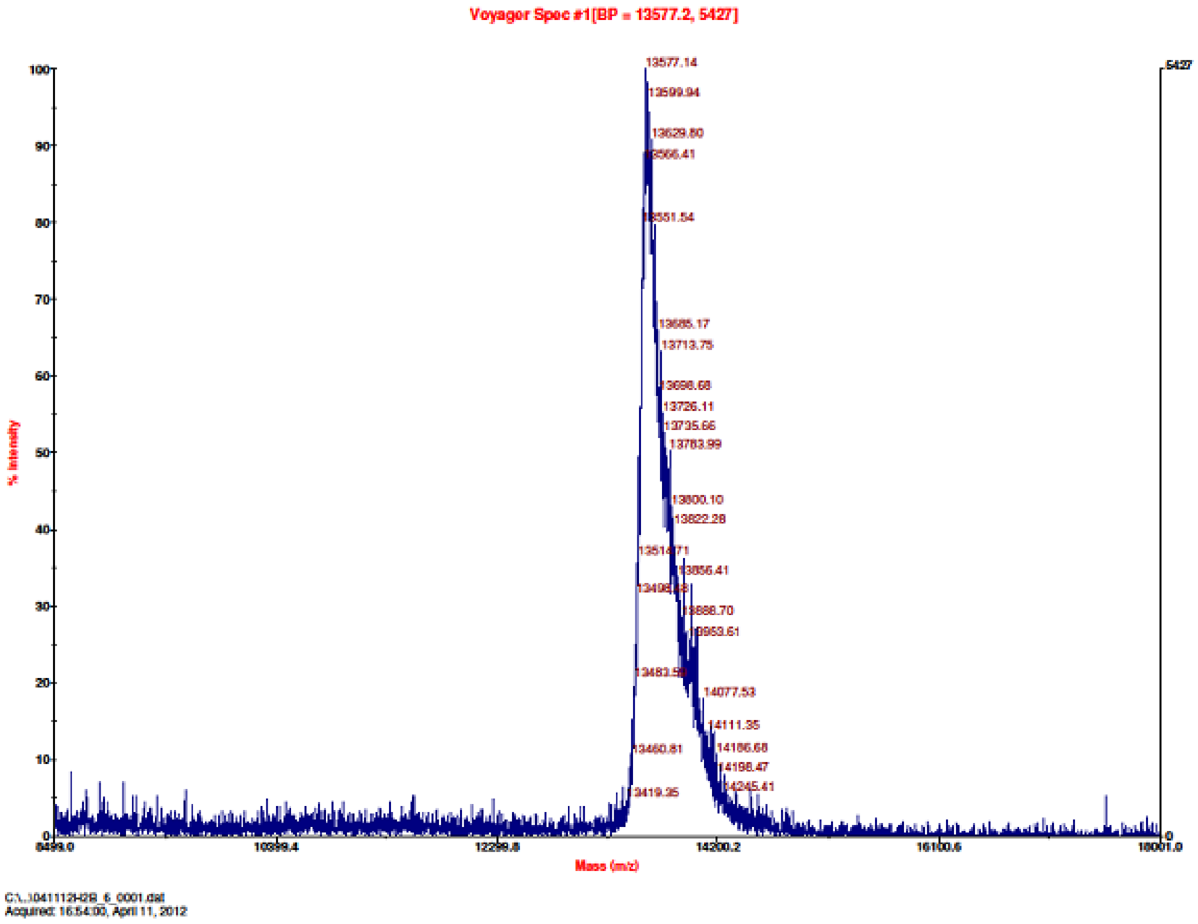

Figure 5.6 Characterization of histone protein H2B by MALDI-TOP Mass Spectrometry.

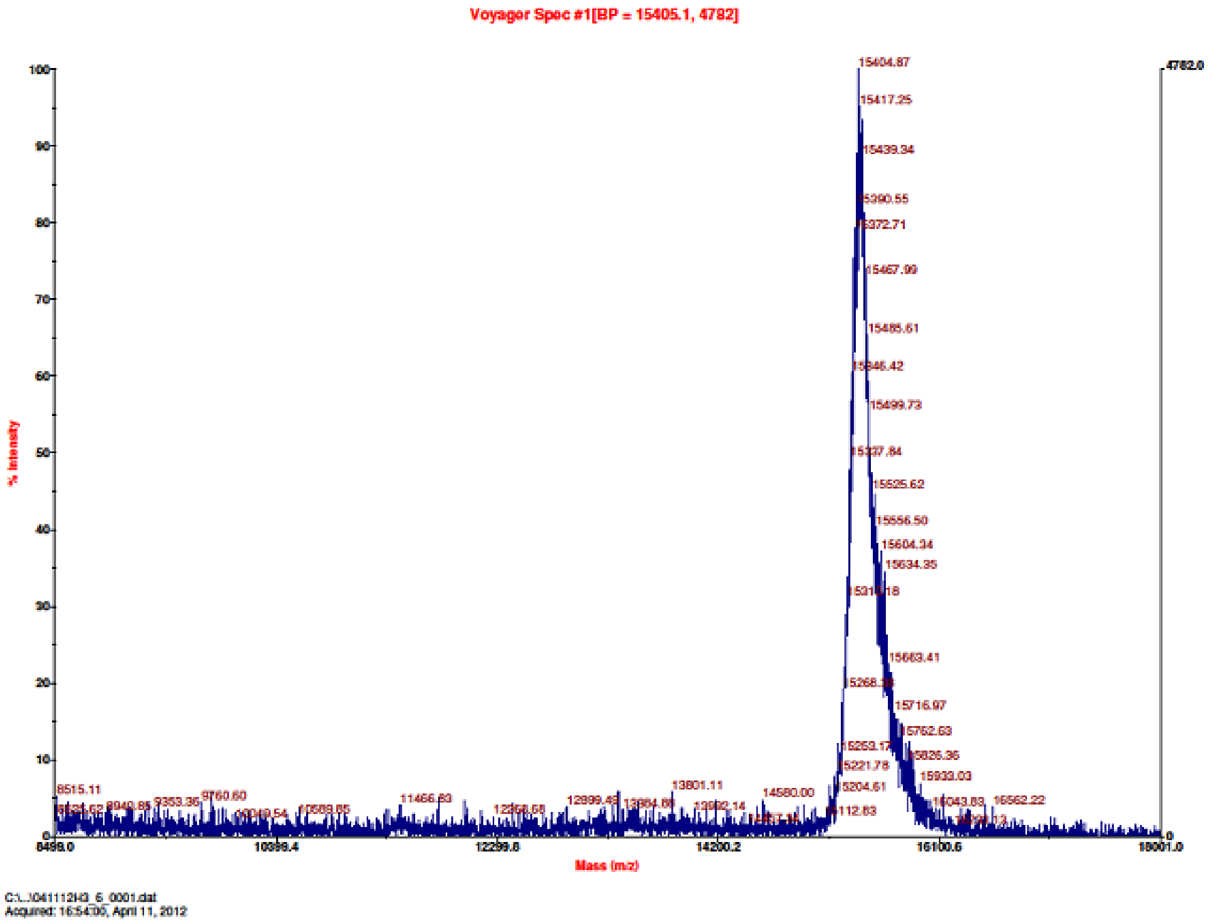

Figure 5.7 Characterization of histone protein H3 by MALDI-TOP Mass Spectrometry.

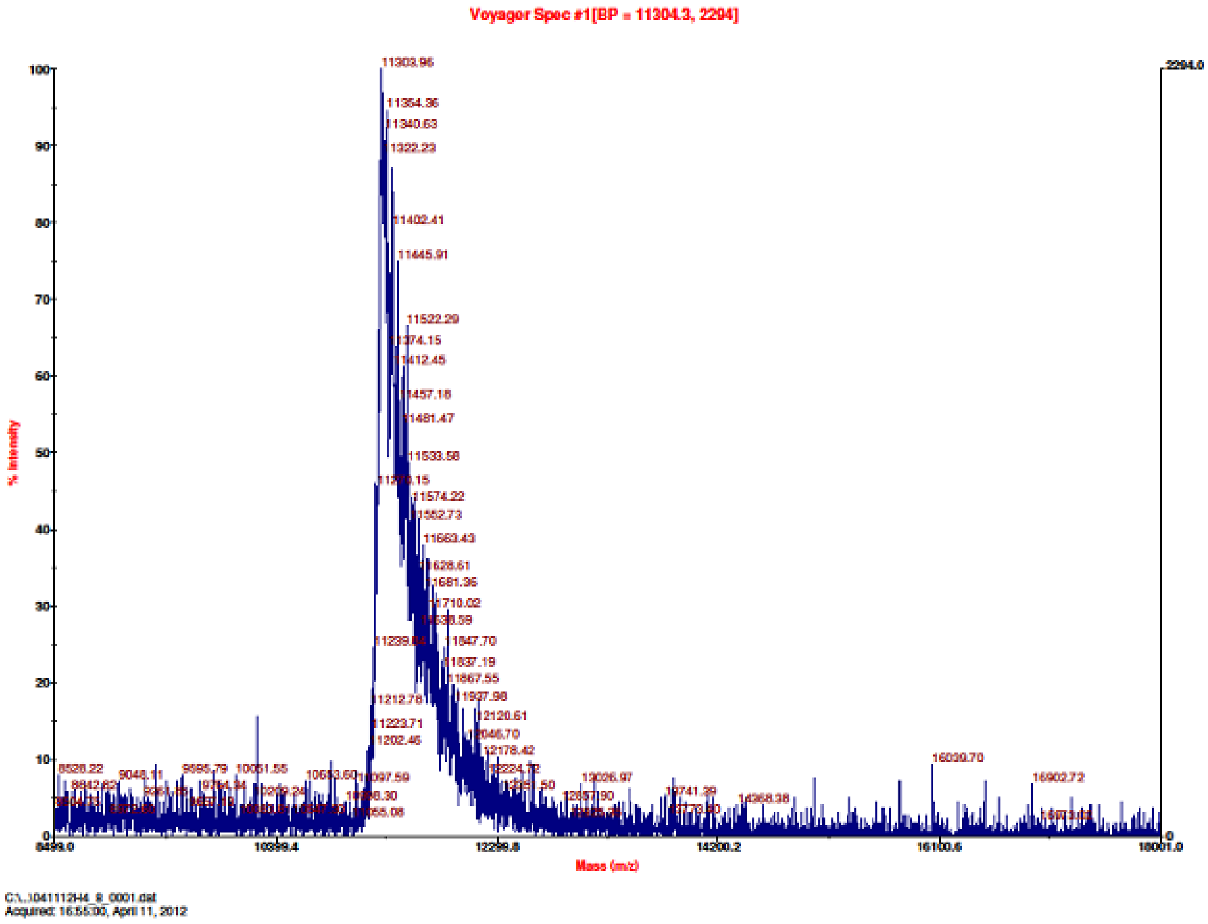

Figure 5.8 Characterization of histone protein H4 by MALDI-TOP Mass Spectrometry.

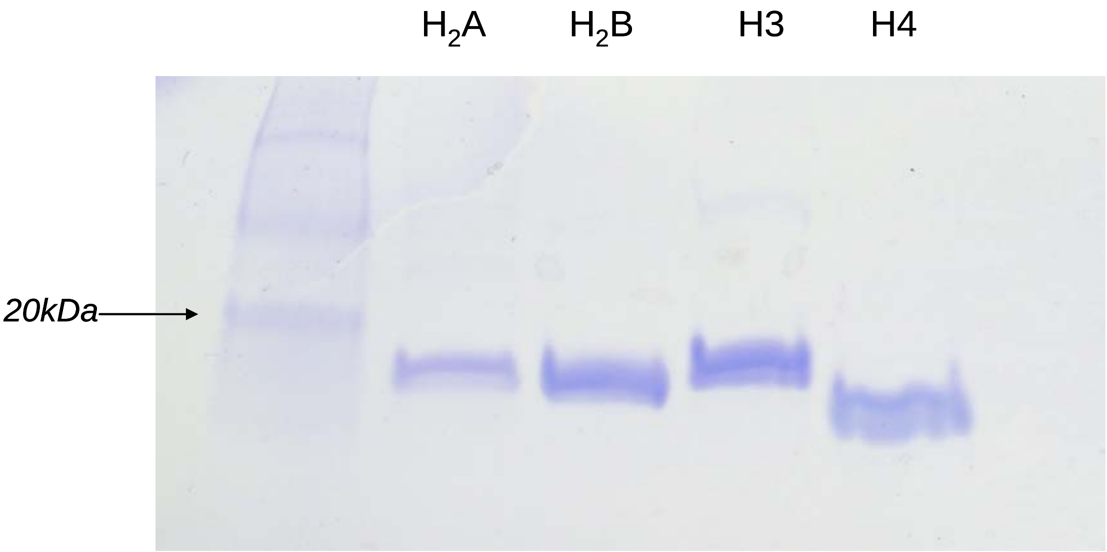

Figure 5.9 Characterization of purified histones H2A, H2B, H3 and H4 on 15% SDS-PAGE.

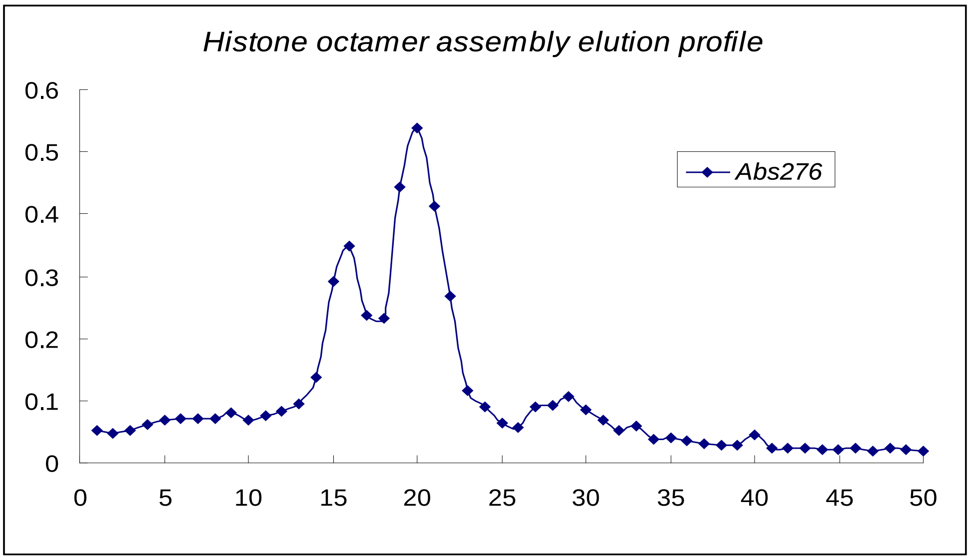

Figure 5.10 Histone octamer assembly elution profile from Sephacryl HR-200 gel-filtration chromatography.

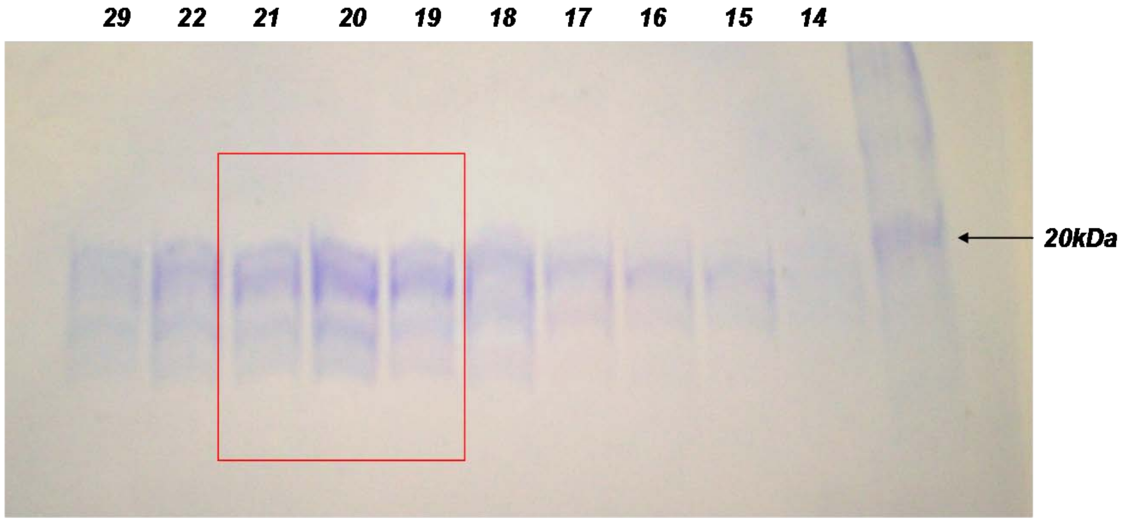

Figure 5.11 Characterization of the purity and stoichiometry of histone assembly fractions on a 15% SDS-PAGE.

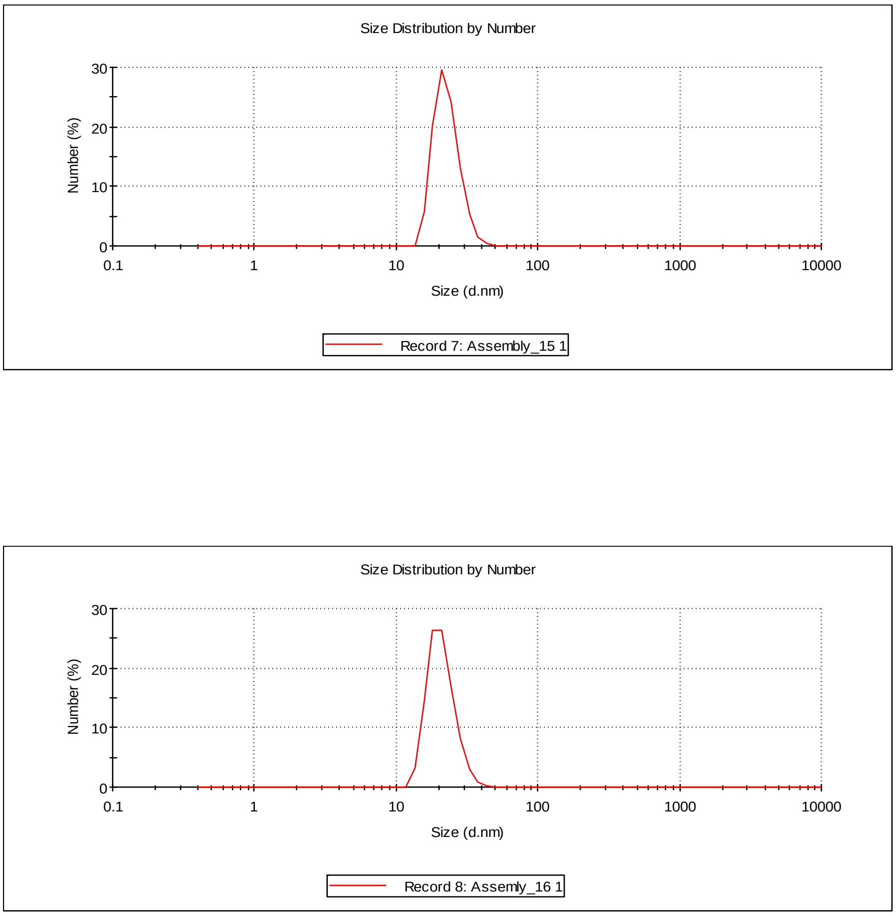

Figure 5.12 DLS measurement of histone assembly fraction 15 & 16 after gel filtration chromatography.

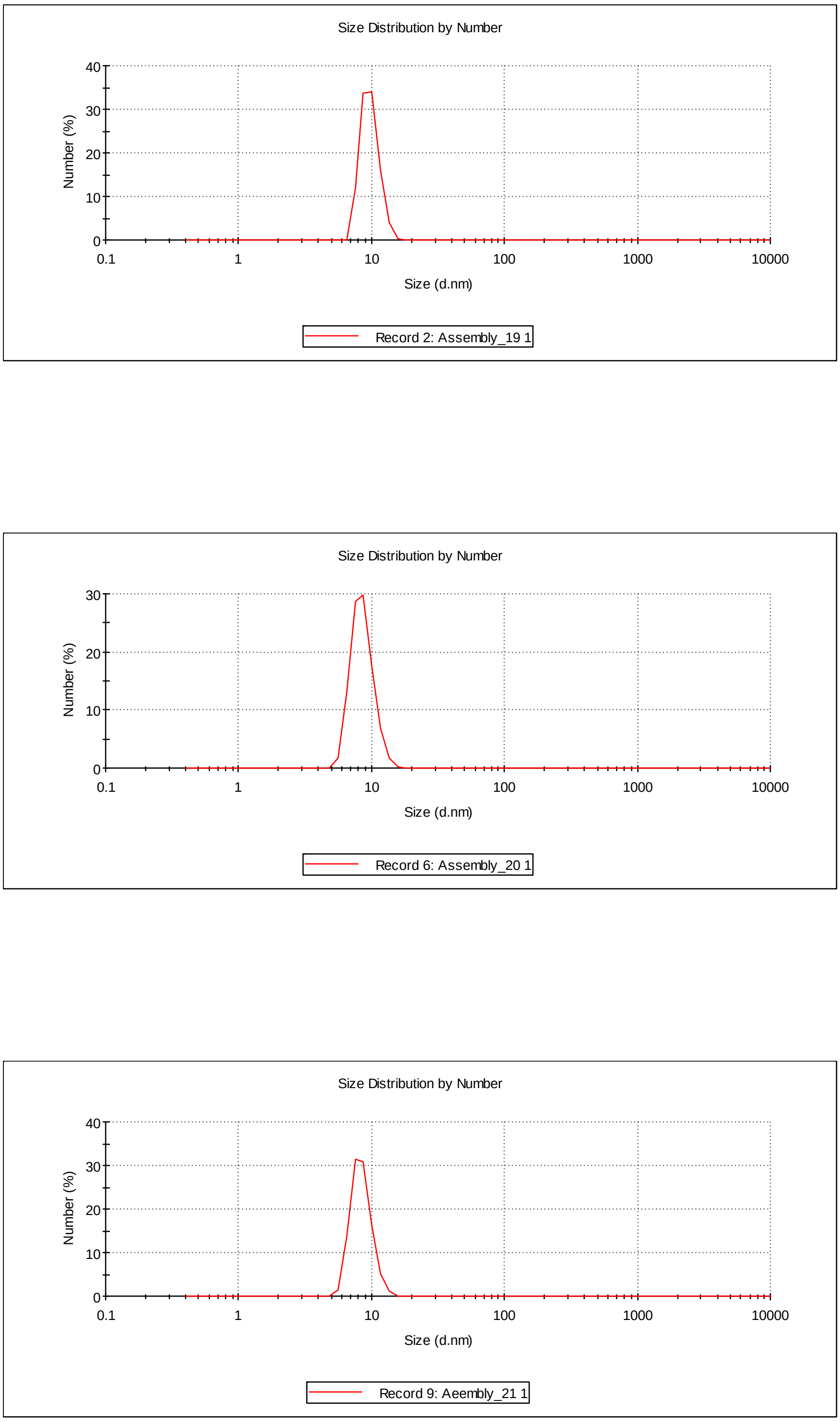

Figure 5.13 DLS measurement of histone assembly fraction 19, 20 and 21 after gel filtration chromatography.

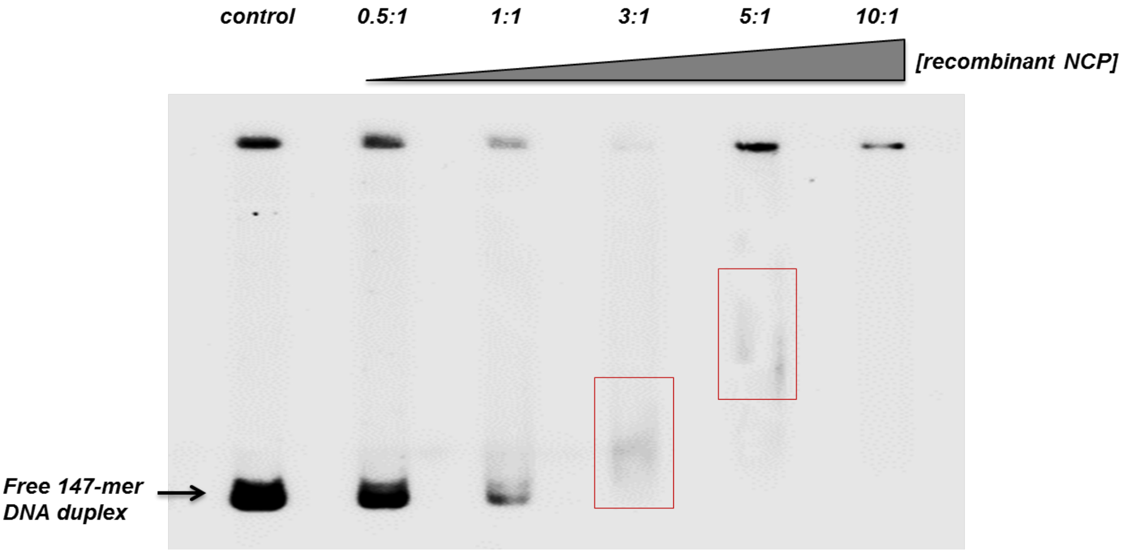

Figure 5.14 Reconstitution between recombinant nucleosome core particle (NCP) and 147-mer DNA duplex. The 147-mer DNA duplex (10nM) was incubated with increasing ratio of recombinant nucleosome core particles (NCP) to free DNA(lanes 2-6: 0.5:1, 1:1, 3:1, 5:1, 10:1) incubated at 4°C for 30 mins, then first dialyzed against 300 mL of 2 M KCl, 10 mM Tris-HCl, 1 mM DTT, pH 7.5, at 4°C, for 1 h, then 2.7 L dialysis buffer containing 10 mM Tris-HCl, 1 mM DTT, pH 7.5, was gradually added to the 300 mL original buffer through a pump at flow rate of 1.5-2.0 mL /min, which can slowly transfer the dialysis buffer into the original container used for the whole dialysis process. The pumping transfer and dialysis was carried out at 4°C, over a period of 36 h. The final salt concentration would be 0.2 M KCl. The reconstituted products were then electrophoresed on a native polyacrylamide gel (6% acrylamide, 0.2% bisacrylamide in TBE).

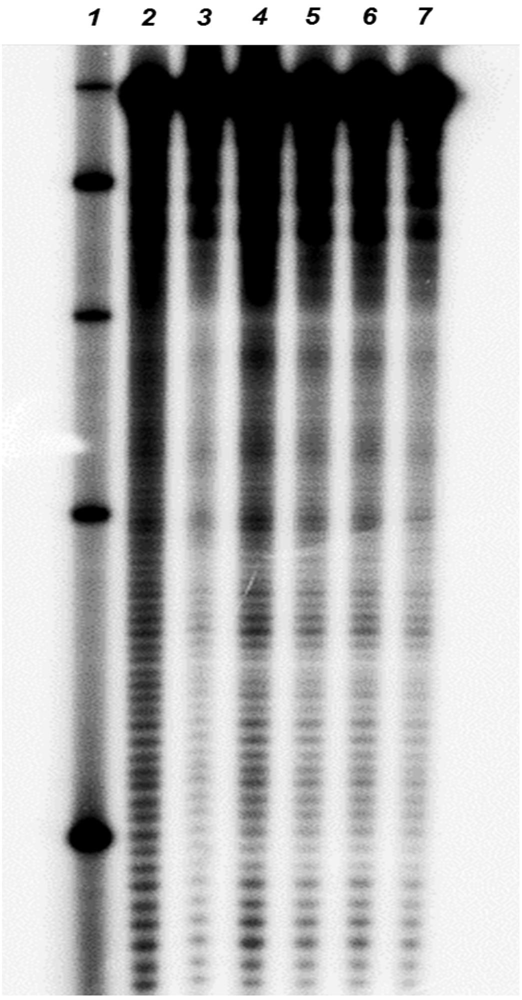

Figure 5.15 Hydroxyl radical foot-printing of the reconstituted histone octamer. The histone octamer reconstituted with 5'-^{32}P-labeled 147-mer duplex DNA was subjected to hydroxyl radical foot-printing and electrophoresed on a 7 M urea, 10% acrylamide, 0.3 % bisacrylamide denaturing gel. *Lane 1:* 25-bp DNA ladder, *Lane 2*, hydroxyl radical foot-printing of the free 147-mer DNA duplex; *Lane 3*, hydroxyl radical foot-printing of the reconstituted 147-mer DNA duplex under ratio of recombinant NCP to DNA at 0.5:1; *Lane 4*, hydroxyl radical foot-printing of the reconstituted 147-mer DNA duplex under ratio of recombinant NCP to DNA at 1:1;

Lane 5, hydroxyl radical foot-printing of the reconstituted 147-mer DNA duplex under ratio of recombinant NCP to DNA at 3:1; *Lane 6*, hydroxyl radical foot-printing of the reconstituted 147-mer DNA duplex under ratio of recombinant NCP to DNA at 5:1; *lane 7*, hydroxyl radical foot-printing of the reconstituted 147-mer DNA duplex under ratio of recombinant NCP to DNA at 10:1.

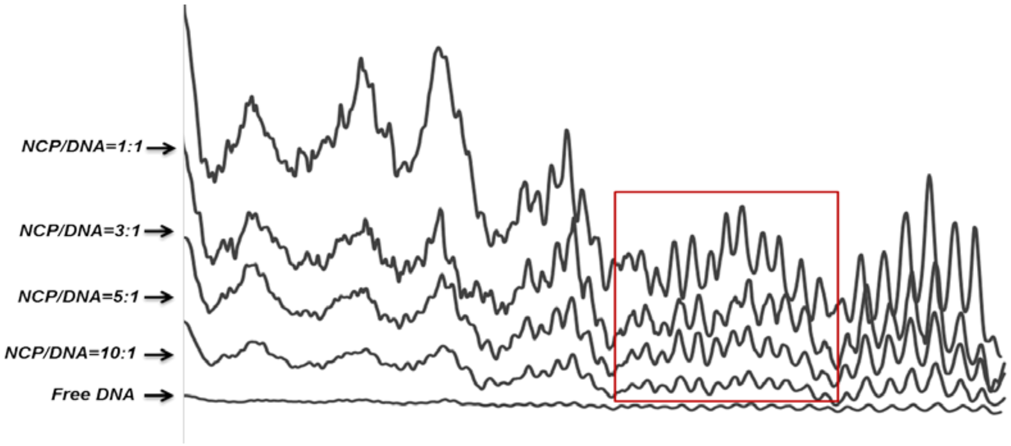

Figure 5.16 Intensity plot of hydroxyl radical foot-printing of the reconstituted nucleosome core particles.

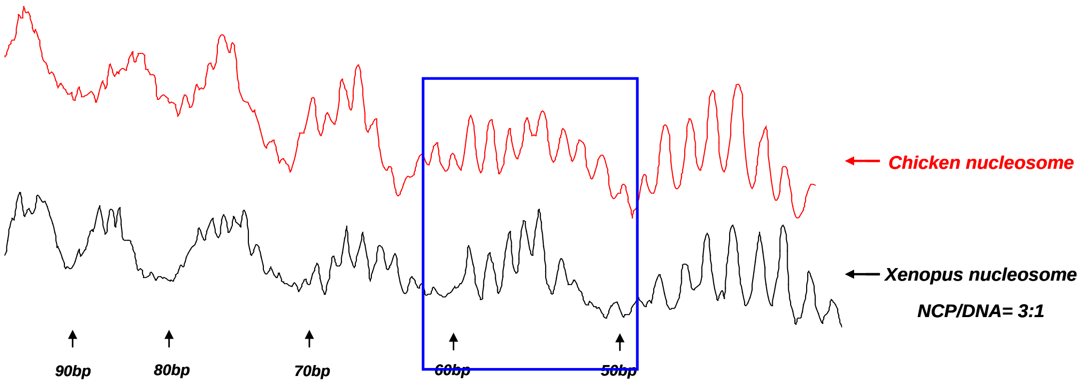

Figure 5.17 Intensity plot of hydroxyl radical foot-printing of the reconstituted nucleosome core particles, chicken erythrocyte vs xenopus oocyte.

Chapter 6

Conclusions and Future Directions

6.1 Conclusions

In chapter 2, we reported the preparation and characterization of a *cis-syn* T=^{m}CG CPD photoproduct in a 14-mer DNA oligodeoxynucleotide as a template for DNA polymerase bypass studies. This CPD site is a known hotspot for C methylation, CPD formation, and UV light-induced C-to-T mutations found in the p53 gene of basal and squamous cell cancers (1-4). By use of both single-hit and multiple-hit competitive nucleotide insertion assay, we showed that both yeast and human DNA polymerase η could synthesize past the 3'-^{m}C in the T=^{m}C CPD in a >99% error-free manner. The results are consistent with the highly water-exposed nature of the active site of the enzyme which would be expected to stabilize the amino tautomeric form of the ^{m}C, which might have led to its evolution (5). These results also demonstrate that the 3'-^{m}C in the T=^{m}C CPD is non-mutagenic when bypassed by polymerase η, but would become highly mutagenic after deamination to a T which would direct the insertion of an A. Thus our study provides strong evidence for the deamination-bypass mechanism for the origin of C to T transition mutations in UV light.

Since in eukaryotic cells, genomic DNA is packaged into chromatin through the repeating structural unit of nucleosomes, it would be important to consider the effect of the nucleosome on photoproduct formation and deamination when trying to understand the molecular basis of UV-induced C→T mutations. In Chapter 3 we compared the photoreactivity and deamination rates of two T=^{m}C CPDs in different rotational positions in a reconstituted nucleosome core particle. One site facing IN and one facing OUT, and in Chapter 4 in all ten positions of a full helical turn. As a result of these studies, we found that that the rotational position of a T^{m}CG site in a nucleosome greatly affects the photoproduct yield and deamination rate of the resulting CPD. Inside facing positions decrease the photoproduct yield and slowed down the deamination rate of the CPD, whereas outside facing sites enhanced the yield and the deamination rate. This discovery may explain at least in part the origin of UV mutation hotspots and coldspots in phased nucleosomes in living cells, with outside facing positions being hotspots, and inside facing inside positions being coldspots. Due to the dynamics of nucleosomes (6-9), deamination of CPDs may also be accelerated in unphased nucleosomes if the CPDs are in exchange with outside positions. The observation that the effect of rotational position on the deamination rate of an ^{m}C in a CPD flanked by a 3'-A is less than for G is consistent with our previous observation that the deamination rate is most sensitive to the C6 carbonyl group of a G. It suggests that the G is not optimally aligned in an inside position, but is in an outside position. We therefore expect that the greatest modulation of CPD deamination will be at sites flanked by a 3'-G.

6.2 Future directions

Although we have already measured the effect of rotational position on the ^{m}C deamination rate in a T=^{m}C CPD around the dyad axis of a phased nucleosome , it remains to be investigated how the nucleosome would affect the deamination rate of C^{m}CG CPDs, which are another hotspot for UV-induced mutations found in the p53 gene of skin cancer cells. C^{m}CG CPDs deaminate much more slowly than T^{m}CG

CPDs in free DNA, so we expect that it might deaminate much faster if located in the facing outside regions in a phased nucleosome. There are also other types of DNA photoproducts, like (6-4) and Dewar photoproducts that could be formed at these hotspot mutation sites and could also deaminate. Nucleosome rotational positioning is also expected to affect the spontaneous deamination of C and ^{m}C and their more readily deaminated oxidized products, such as 5,6-dihydroxy cytosine. In addition to deamination, we could also investigate repair of these CPDs. It is known that CPD become much more susceptible to excision repair following deamination because a mismatch is produced that destabilizes the duplex, and so while outside facing positions may deaminate faster, they might also be repaired faster.

Besides the effect of rotational position, there is also the effect of translational position to be investigated. So far we have focused on one particular translational position at the peudodyad axis, and know nothing of the rates of photoproduct formation, deamination and repair at other translational positions. Greenberg and coworkers have shown interesting effects of superhelix position 1.5 on strand cleavage at abasic sites, suggesting that this would be a good place to start (10). Beyond that, we can expand our insight to nucleosome arrays, not just a mononucleosome, and eventually mini-chromosome to investigate the effect of chromatin structure on DNA photomutagenesis.

It will also be important to determine whether the effects observed in model systems in vitro can also be detected in chromatin structure *in vivo*. As shown in Appendix, we already developed a method to probe the nucleosome phasing along the p53 gene in both HeLa cell and human primary keratinocytes, and found five CPD sites with different nucleosome positioning. Another member of the group has begun to measure the deamination rate of these five CPDs and compare the observed effects of nucleosome position with our *in vitro* data with nucleosome core particles. It will be extremely exciting if we can explain the origin of UV-induced C to T mutations hotspots in human primary keratinocytes by their position within a nucleosome.

In chapter 5, we successfully expressed and purified all four histone proteins H2A, H2B, H3 and H4 utilizing a modified protocol described previously (11) and showed that we could assemble our synthetic 147-mer DNA duplex onto a histone octamer formed from these proteins. Based on this approach, we could further investigate the effect of the nucleosome on deamination at an amino acid level by site-directed mutagenesis. We could also study the effect of post-translational modifications of histones (the "histone code") which might also play a important role in carcinogenesis (12-15).

References

1. Brash, D. E., Rudolph, J. A., Simon, J. A., Lin, A., McKenna, G. J., Baden, H. P., Halperin, A. J., and Pontén, J. A role for sunlight in skin cancer: UV-induced p53 mutations in squamous cell carcinoma. *Proc. Natl. Acad. Sci. U.S.A.* **1991,** *88,* 10124–10128.

2. Ziegler, A., Leffell, D. J., Kunala, S., Sharma, H. W., Gailani, M., Simon, J. A., Halperin, A. J., Baden, H. P., Shapiro, P. E., and Bale, A. E. Mutation hotspots due to sunlight in the p53 gene of non-melanoma skin cancers. *Proc. Natl. Acad. Sci. U.S.A.* **1993***, 90*, 4216–4220.

3. You, Y. H., Li, C., and Pfeifer, G. P. Involvement of 5-methylcytosine in sunlight-induced mutagenesis. *J. Mol. Biol.* **1999,** *293*, 493–5034.

4. You, Y. H., Szabó, P. E., and Pfeifer, G. P. Cyclobutane pyrimidine dimers form preferentially at the major p53 mutational hotspot in UVB induced mouse skin tumors. *Carcinogenesis.* **2000,** *21,* 2113–2117.

5. Song, Q., Sherrer, S. M., Suo, Z., Taylor, J. S. Preparation of site specific T=^{m}C *cis-syn* cyclobutane dimer-containing template and its error-free bypass by yeast and human polymerase *η*. *J. Biol. Chem*. **2012,** *287,* 8021–8028.

6. Luger, K. Dynamic nucleosomes. *Chromosome Res.* **2006,** *14,* 5–16.

7. Luger, K., Ma¨der, A. W., Richmond, R. K., Sargent, D. F., and Richmond, T. J. Crystal structure of the nucleosome core particle at 2.8 A resolution. *Nature.* **1997,** *389*, 251–260.

8. Duan MR, Smerdon MJ. UV damage in DNA promotes nucleosome unwrapping. *J. Biol. Chem*. **2010,** *285,* 26295–26303.

9. Hinz JM, Rodriguez Y, Smerdon MJ. Rotational dynamics of DNA on the nucleosome surface markedly impact accessibility to a DNA repair enzyme. *Proc. Natl. Acad. Sci. U.S.A.* **2010,** *107,* 4644–4651.

10. Zhou, C. and Greenberg, M. M. Histone-catalyzed cleavage of nucleosomal DNA containing 2-deoxyribonolactone. *J. Am. Chem. Soc.* **2012,** *134,* 8090-8093.

11. Luger, K., Rechsteiner, T. J., and Richmond, T. J. Expression and purification of recombinant histones and nucleosome reconstitution. *Methods. Mol. Biol*. **1999,** *119,* 1–16.

12. Wang Z, Patel DJ. Combinatorial readout of dual histone modifications by paired

chromain-associated modules. *J. Biol. Chem*. **2011,** *286,* 18363–18368.

13. Fullgrabe J, Hajji N, Joseph B. Cracking the death code: apoptosis-related histone modifications. *Cell. Death. Differ.* **2010,** *17*, 1238–1243.

14. Chapman-Rothe N, Brown R. Approaches to target the genome and its epigenome in cancer. *Future. Med. Chem.* **2009,** *1,* 1481–1495.

15. Lawless MW, Norris S, O'Byrne KJ, Gray SG. Targeting histone deacetylases for the treatment of disease. *J. Cell. Mol. Med.* **2009,** *13*, 826–852.

Appendix

Nucleosomal positioning of DNA photoproduct sites along human p53 gene in living cells

Introduction

In eukaryotic cells, genomic DNA is organized into chromatin, where nucleosomes and non-histone proteins can regulate many DNA-dependent processes (1). Under most circumstances the modulation is believed to be negative, i.e., nucleosome structures block access of DNA-binding or DNA-modifying proteins. Regulatory sequences are commonly found in nucleosome-free regions, and transcription factors are often excluded from sequences that are associated with nucleosomes (1, 2) although there are a few examples in which transcription factors can bind to DNA in a positioned nucleosome (3).

When cells are exposed to a DNA-damaging agent, i.e. UV light, the presence of nucleosomes could interfere with the formation, recognition, and repair of specific DNA lesions (4-6). The p53 tumor suppressor gene 53 gene is inactivated by bearing various mutation or deletion in many types of human malignancies (7-10). Most p53 mutations are localized within the four evolutionarily conserved domains of the gene between exons 5-8 (8), and there are six mutational hot-spots located in this region that are found in many types of human cancer. They include codons 175,245,248,249,273 and 282 (10). Five of these six p53 mutation hot-spot codons contain CpG dinucleotides (175,245,248,273, and 282). Previous work showed that the distribution of mutations in the p53 gene in skin cancers is related to slow repair of DNA cyclobutane pyrimidine dimers (CPD) at specific sequence positions (11), with the repair rates for these UV-induced lesions highly sequence specific. In this case, it might be possible that these DNA mutagenesis along the p53 gene could be regulated by the particular chromatin or nucleosome structure at those mutational sites in p53 gene.

To determine the structure of the chromatin at a specific site we developed a hydroxyl radical foot-printing method to determine the phasing and positioning of nucleosome along the p53 gene in living cells. In this method, the short-lived hydroxyl radical was generated inside living cells from a fenton reagent that introduced by permeabilizing the cell membrane of HeLa cells and human primary keratinocytes. The hydroxyl radicals then cleave the genomic DNA at different chromosomal positions, depending on the relative accessibility of genomic DNA. To characterize and amplify the hydroxyl radical cleavage site along the p53 gene, we utilized ligation-mediation PCR with some modifications of the protocol described previously (12). Our foot-printing results were consistent with earlier data using DNase I footprinting showing that there was a clear nucleosome association pattern in exon 5 and 6 region along p53 gene (13), although the cell model we used were HeLa cells and human primary keratinocytes. In this appendix we describe our method for hydroxyl radical footprinting of DNA in vivo to determine phasing and positioning of nucleosomes along specific genes.

Experimental procedures

Cell culture

HeLa cells or human primary keratinocytes were seeded at 1× 10^6 cells per 100 mm cell culture plate, and were grown to approximately 80% confluence with 10 mL DMEM media (for HeLa) or KSFM (for keratinocytes) after 48h.

Cell membrane permeabilization

HeLa cells or human primary keratinocytes monolayers were washed twice with 10 mL PBS buffer, then permeabilized by treatment with 0.05% lysolecithin (type I; Sigma Chemical Co., St. Louis, MO) in permeabilization buffer containing 150 mM sucrose, 80 mM KCl, 35 mM NaHEPES, pH 7.4, 5 mM K_2HPO_4, 5 mM $MgCl_2$ and 0.5 mM $CaC1_2$ for 1 min at room temperature. After that, the permeabilization buffer was removed and the cells were washed once with 10 mL PBS buffer.

Hydroxyl radical cleavage in living cells

After the cell membrane permeabilization, the HeLa cells or human primary keratinocytes were immediately subjected to hydroxyl radical cleavage with 50 mM sodium ascorbate, 5 mM $Fe(NH_4)_2(SO4)_2{\cdot}6H_2O$ + 10 mM EDTA and 0.6 % H_2O_2 that were added to 10 mL DMEM (HeLa) or KSFM (human primary keratinocyte) media in a 37°C incubator for 15 mins.

Cell lysis, DNA isolation and purification

The HeLa or human primary keratinocyte cells were released from the cell culture plate by scraping directly into the corresponding growth media and transferred to a 15 mL conical tube and immediately cooled on ice before centrifugation at 4°C.

After centrifugation, the media was removed with a Pasteur pipette and the cell pellet was taken up in 0.9 mL lysis buffer containing 0.3 M NaCl, 10 mM EDTA and 10 mM Tris-HCl pH 8.3, and the cell lysis started by the addition of 100 μL of 10% SDS. After incubating for a few minutes at room temperature, 50 μg proteinase K was added to the cell lysates and allowed to react with the cell lysates for 30 mins at 37°C at pH 8.4. This was followed by two phenol-chloroform-isopropanol extractions (saturated with 0.2 M NaCl and 30 mM Tris-HCl, pH 8.5). After that, sodium acetate (0.3 M), 20 mM Tris-HCl pH 8.3 and 200 μg of glycogen were added to the samples before the addition of 3 volumes of ethanol. The samples were then quickly frozen at -80°C for 20 mins, thawed on ice and centrifuged to pellet the DNA. The supernatant was removed and the pellet was resuspended in 300 μL of 0.3 M sodium acetate (with 20 mM Tris-HCl, pH 8.3) and re-precipitated with ethanol. The pellets were then washed with 95% ethanol and air dried. Each pellet corresponding to one cell culture plate (about 40 μg DNA) was re-suspended in 400 μL of 50 mM NaCl and centrifuged at high speed to pellet any un-dissolved sample prior to further purification with the Qiagen PCR clean up kit to remove RNA. Three washes with the chaotropic salts at pH 5.5 were required to remove the RNA. After the final elution of the DNA in 10 mM Tris-HCl, pH 8.5 (100 μL per column), sodium acetate was added to 300 mM in addition to 200 μg glycogen before ethanol precipitation followed by an ethanol wash. After centrifugation, the DNA was air dried, re-suspended in 50 mM NaCl and then stored at -80°C. DNA samples were quantified by OD_{260} measurements.

Before the detection of hydroxyl radical cleavage by ligation-mediated PCR (LMPCR), the DNA fragments were run at 1% agarose gel to test the size range after the hydroxyl radical cleavage, as showed in Figure A.3, we could see that after the hydroxyl radical cleavage, both DNA in HeLa cells and human primary keratinocytes were fragmented down to size range between 200 bp to 1000 bp.

Detection of hydroxyl radical cleavage site by ligation-mediated PCR (LMPCR)

Blunt-end synthesis

Blunt end synthesis was carried out in a 30 μL reaction buffer mix containing 2 μg DNA, 1X Vent polymerase mix and an additional 3 mM $MgSO_4$ (both supplied by the manufacturer), 50mM NaCl, 0.01% gelatin, and 1 pmol of the P1 primer. After heating this mixture for 10 min, the samples were immediately chilled on ice-water bath, then 0.7 μL of dNTPs (25 mM each) was added to the samples before adding 0.7 μL of the Vent polymerase. Samples were transferred to a 94°C water bath for 4 min before transferring again to a 58°C water bath for the annealing-synthesis reactions. The annealing-synthesis reactions were continued for 40 min before transferring the samples to a 76°C water bath for 10 min to complete the synthesis reaction. The samples were then immediately put on an ice-water bath and 270 μL of cold 0.2 M NaCl was added to each sample and quickly mixed by vortexing. This was followed by the immediate addition of about 1 mL of phenol-chloroform-isopropanol. The samples were extracted by 5 min of inversions and then centrifuged to separate phases. Most of the bottom phenol layer was first removed by Pasteur pipette and the remaining phenol by a 200 μL Eppendorf tip. After a second centrifugation the top aqueous layer was removed by a 200 μL tip. 3M sodium acetate was added to the sample to a final concentration of 0.3 M, along with 150 μg glycogen, followed by addition of three volumes of ethanol for DNA precipitation. After centrifugation, the pellet was washed, air dried and then taken up in 45 μL of 50 mM NaCl.

Ligation

To the 45 μL sample incubating on ice-water batch, 5.6 μL of 10X T4 DNA ligase mix (from manufacturer) and 6.25 μL of the P4/P5 duplex (100 pmoles in 50 mM NaCl) were added for ligation. The P4/P5 duplex was stored frozen, thawed before use in a water bath at 14°C and then kept on ice to avoid duplex dissociation before addition to the cold reaction mix. 2 μL of T4 DNA ligase was added to each sample and the reaction was incubated at 14°C overnight. After ligation, the samples were heated at 100°C for ten minutes, ethanol precipitated with sodium acetate omitting the glycogen, washed with ethanol. The pellet was air dried and taken up in 50ul dd-water.

PCR

50 μL of a PCR mix containing 100 mM NaCl, 2X PCR mix, 0.02% gelatin, 6 mM $MgSO_4$, 10 pmoles of P2 and P4 primers was added to each 50 μL DNA sample and heated at 100°C for 5 min. After that, the samples were immediately chilled on ice-water bath, and then 0.9 μL of dNTPs (25 mM each) was added before adding 1μL Vent polymerase. Samples were then transferred to PCR tubes and kept on ice before incubation at 95°C in a water bath next to the PCR cycler. After 3 min in the 95°C water bath, the samples were transferred to the PCR cycler set at 95°C for 8 min.

One sample at a time was transferred quickly to avoid cooling down of the sample. Samples were amplified by 25 cycles with settings of 95°C for 2 min, 65°C for 2 min and 76°C for 5min before a single 76°C cycle set at 13 min. Samples were removed after 10 min from this final cycle one at a time and placed directly into a rack on ice water to cool the samples quickly. The PCR samples were centrifuged briefly to remove condensation from the caps at 4°C. Samples were placed into the rotor containing the 1.5 mL tubes with the caps removed. These 1.5 mL tubes each contained 600 μL of ice cold water to insure no heating of the samples. After centrifugation the samples were transfer to ice and then transferred again to 1.5 mL Eppendorf tubes to prepare the labeling mix.

End-Labeling

Toward the labeling mix, 0.7 μL dNTPs (25mM each), 0.7 Vent polymerase and 2 μL (5 pmol) of the 5’-^{32}P-labeled P3 primer were added in order. Samples were briefly mixed after each addition. After completion, each sample was transferred back into new PCR tubes and kept on ice. The rack containing the PCR tubes was put quickly into a 96°C water bath next to the PCR instrument for 3 min and then each sample transferred into the PCR instrument set at 96°C for 8 min. Two linear PCR cycles were done with settings at 96°C for 4 min, 71°C for 2 min and 76°C for 10 min. This was followed by a single cycle at 76°C set for 10 min. Samples were again removed one at a time into a rack on ice water after 2 min and centrifuged again in Eppendorf tubes containing ice cold water. Samples were then transferred to a tube containing 200 μL of 0.2 M NaCl and 1% SDS at room temperature, mixed by vortex and incubated for 5 min before phenol-chloroform-isopropanol extraction. After extraction for 5 min, the samples were centrifuged and the bottom phenol layer removed by Pasteur pipette and finally by a 200 μL pipette tip. After a second centrifugation, the top ^{32}P-labeled sample layer was removed by a 200 μL tip and transferred to a tube containing 150 μg of glycogen and 40 μL of 3 M sodium acetate. 3 volumes of ethanol were added for precipitation. After freezing the sample on dry ice, the samples were brought to room temperature in a water bath. Centrifugation was at 18°C to avoid some precipitation of residual SDS. This was followed by an ethanol wash. Pellets were air-dried and then resuspended in 20 μL formamide containing the xylene-cyanol dye maker. Resuspension of the DNA pellet was a little problematic. The samples were heated for one min and mixed manually for four separate times before a final 10min heating prior to electrophoresis.

After heating, the samples were loaded onto a 10% denaturing PAGE containing TBE and 7 M urea. The gel was aged briefly (1 h) and pre-run 45 min at 1100 V to reach an external temperature of about 50°C before loading the sample. After running at 1100 V for 2 h, the voltage was increased to 1300 V to maintain temperature.

Results

We chose HeLa cells and human primary keratinocytes as our cell model, and developed the hydroxyl radical foot-printing method by the fenton reaction in these living cells. As shown in Figure A.1, the cells were first permeabilized by lysolecithins, which are phospholipids that can penetrate and become incorporated into the cell membrane, and help permeabilize the both the cellular and nuclear membranes. The hydroxyl radical was generated by the reaction between sodium ascorbate, Fe $(NH_4)_2(SO4)_2{\cdot}6H_2O$+ EDTA, and H_2O_2. Due to the short life-time of hydroxyl radical, the three reagents were freshly made right after the membrane permeabilization, and quickly mixed into the growth media within 5 s. After the hydroxyl radical cleavage**,** the cells were lysed, and genomic DNA was collected and identified by LMPCR.

The hydroxyl radical cleavage generated DNA fragments with size ranges between 200 bp to 1000 bp, as shown in Figure A.3. LMPCR was carried out on the DNA fragments after hydroxyl radical cleavage in both cell types, together with human genomic DNA after Maxam-Gilbert reaction to generate the G ladder along the p53 gene sequence. As shown in Figure A.4, the hydroxyl radical cleavage patterns in HeLa cells and human primary keratinocytes were almost the same, indicating that this part of p53 gene (Exon 5) had the same nucleosome positioning ability in both HeLa cell and human primary keratinocytes.

To detect the specific nucleosome positioning ability of different DNA photoproducts along p53 gene in HeLa cells, we aligned the LMPCR results of DNA photoproduct mapping, DMS mapping together with the hydroxyl radical foot-printing on one sequencing gel, as shown in Figure A.5. The partial sequence in Exon 5 and Exon 6 along p53 showed a clear nucleosome pattern, with roughly 10-11 bp as a periodicity. The blue arrow indicates the maximum clevage intensity of each 10-11 bp nucleosome turn along the DNA. As for the three $T{=}^{m}C$ DNA photoproducts, the first one, CT=^{m}CG, which was located at G_{46} position, exhibited an inside facing nucleosome position, as highlighted by the red arrow. The second T=^{m}C DNA photoproduct, GT=^{m}CG, which was located at G_{16} position, however, exhibited an outside facing nucleosome position. The last T=^{m}C DNA photoproduct, AT=^{m}CG, which was located at G_{12} position, unlike the other two photoproducts, exhibited a nucleosome positioning ability between inside and outside, leaning more towards out. So basically, we had three T=^{m}C DNA photoproducts in three different nucleosome positions. When it comes to other DNA photoproducts, we could also find that one T=C DNA photoproduct, TC=TC, which was located between G_{15} and G_{16}, exhibited an inside facing position, as highlighted by the red arrow, and there was another C=T DNA photoproduct, CT=CA, located between G_{13} and G_{12}, that exhibited an outside facing position. These five different DNA photoproducts exhibited specific nucleosome positioning abilities that are summarized in Table A.2. These mapping results will allow us to interpret the results of LMPCR-based deamination studies being carried out by Vincent Cannistraro.

References

1. Wolffe AP. Chromatin: Structure and Function. Academic Press. **1992**

2. Pfeifer GP, Riggs AD. Chromatin differences between active and inactive X chromosomes revealed by genomic footprinting of permeabilized cells using DNasel and ligation-mediated PCR. *Genes Dev*. **1991,** *5*, 1102–1113.

3. McPherson CE, Shim E-Y, Friedman DS, Zaret KS. An active tissuespecific enhancer and bound transcription factors existing in a precisely positioned nucleosomal array. *Cell.* **1993,** *75*, 387–398.

4. Smerdon MJ, Thoma F. Site-specific DNA repair at the nucleosome level in a yeast minichromosome. *Cell.* **1990**, *61*, 675–684.

5. Smerdon MJ. DNA repair and the role of chromatin structure. *Curr Opin Cell Biol.* **1991,** *3*, 422–428.

6. Tornaletti ***S,*** Pfeifer GP. UV damage and repair mechanisms in mammalian cells. *Bioessays*. **1996,** *18*, 221–228.

7. Jones PA, Buckley JD, Henderson BE, Ross RK, Pike MC. From gene to carcinogen: A rapidly evolving field in molecular epidemiology. *Cancer Res.* **1991,** *51*, 3617–3620.

8. Caron de Fromentel C, Soussi T. TP53 tumor suppressor gene: A model for investigating human mutagenesis. *Genes Chromosome Cancer.* **1992,** *4*, l–15.

9. Harris CC. p53: At the crossroads of molecular carcinogenesis and risk assessment. *Science.* **1993,** *262*, 1980–1981.

10. Greenblatt MS, Bennett WP, Hollstein **M,** Harris CC. Mutations in the ***p53*** tumor suppressor gene: Clues to cancer etiology and molecular pathogenesis. *Cancer Res.* **1994,** *54*, 4855–4878.

11. Tornaletti S, Pfeifer GP. Slow repair of pyrimidine dimers at p53 mutation hotspots in skin cancer. *Science.* **1994,** *263*, 1436–1438.

12. Mueller PR, Wold B, Garrity PA. Ligation-mediated PCR for genomic sequencing and footprinting. *Curr Protoc Mol Biol.* **2001,** *Chapter 15*, Unit 15.3.

13. Tornaletti S, Bates S, Pfeifer GP. A High-resolution analysis of chromatin structure along p53 sequences. *Mol Carcinog.* **1996,** *17*, 192–201.

Table A.1 Primer sequences used for ligation-mediated PCR (LMPCR)

Primers used in LMPCR		
ODN	Definition	Sequence
P1	upstream primer for blunt end synthesis	GCG CCA TGG CCA TCT ACA AG
P2	specific amplification primer in PCR	CAG TCA CAG CAC ATG ACG GAG GTT GTG AG
P3	p^{32} end- labeling primer	GTC ACA GCA CAT GAC GGA GGT TGT GAG GCG C
P4	nonspecific primer ligated to the target phosphate at 5' end	GCG GTG ACC CGG GAG ATC TGA ATT C
P5	short sequence to form heat labile duplex needed for blunt end ligation	GAA TTC AGA TCT CC

Table A.2 Position of CPD photoproducts that were mapped along the p53 gene in HeLa cells and their specific nucleosome positioning.

DNA photoproduct	Nucleosome positioning ability
CT=^{m}CG	**In**
GT=^{m}CG	**Out**
AT=^{m}CG	**Intermediate-out**
TC=TC	**In**
CT=CA	**Out**

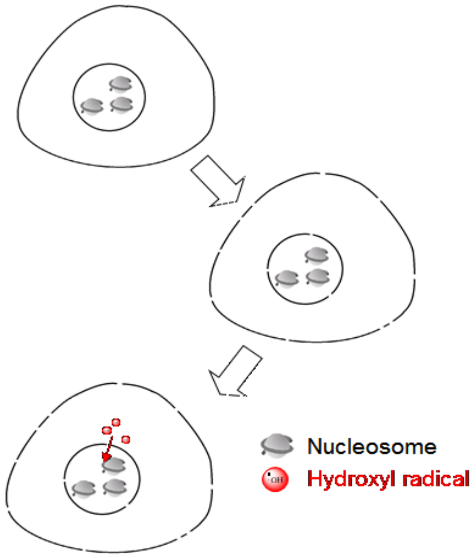

Figure A.1 Strategy for hydroxyl radical foot-printing in HeLa cells and human primary keratinocytes.

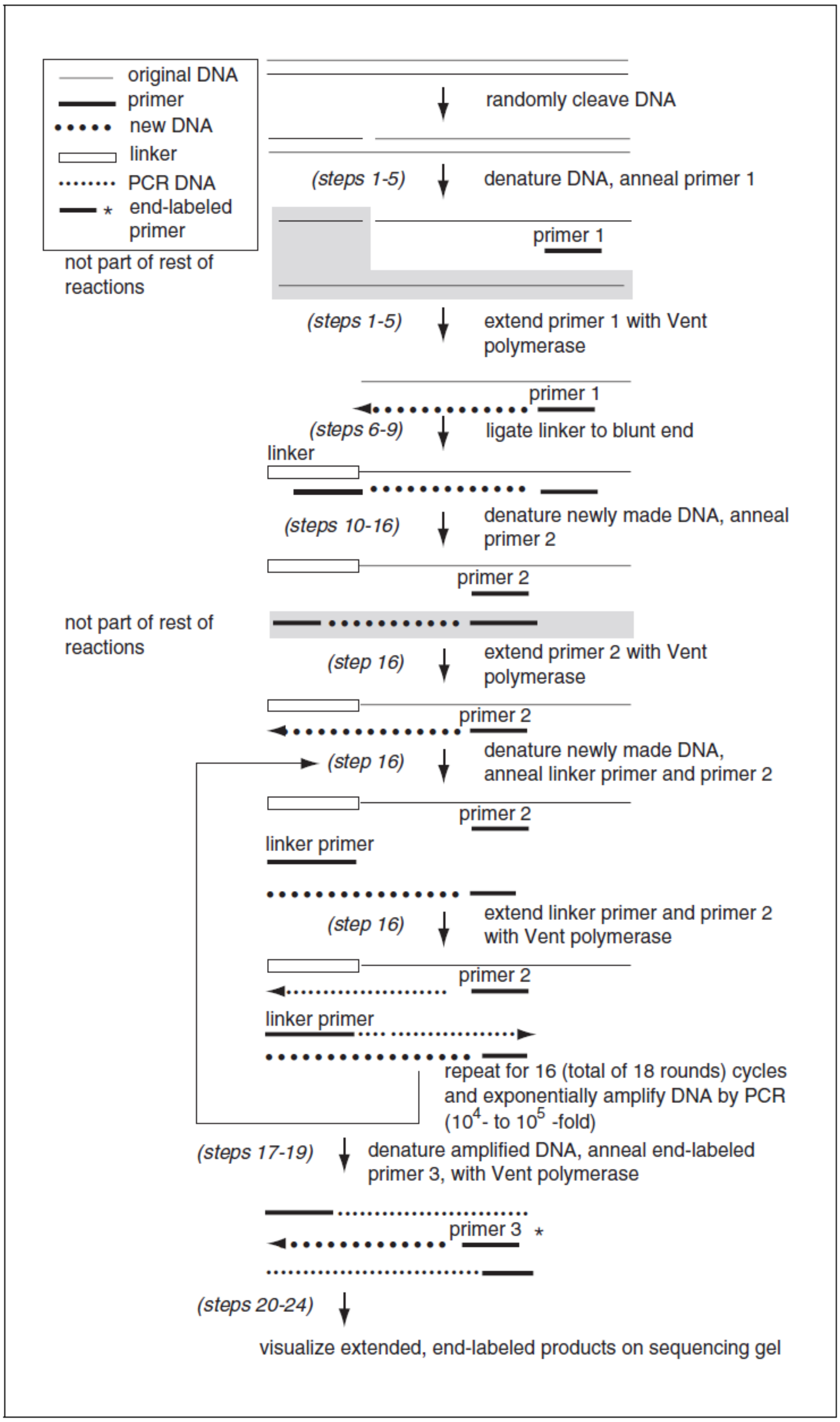

Figure A.2 Flow chart of the ligation-mediated PCR protocol

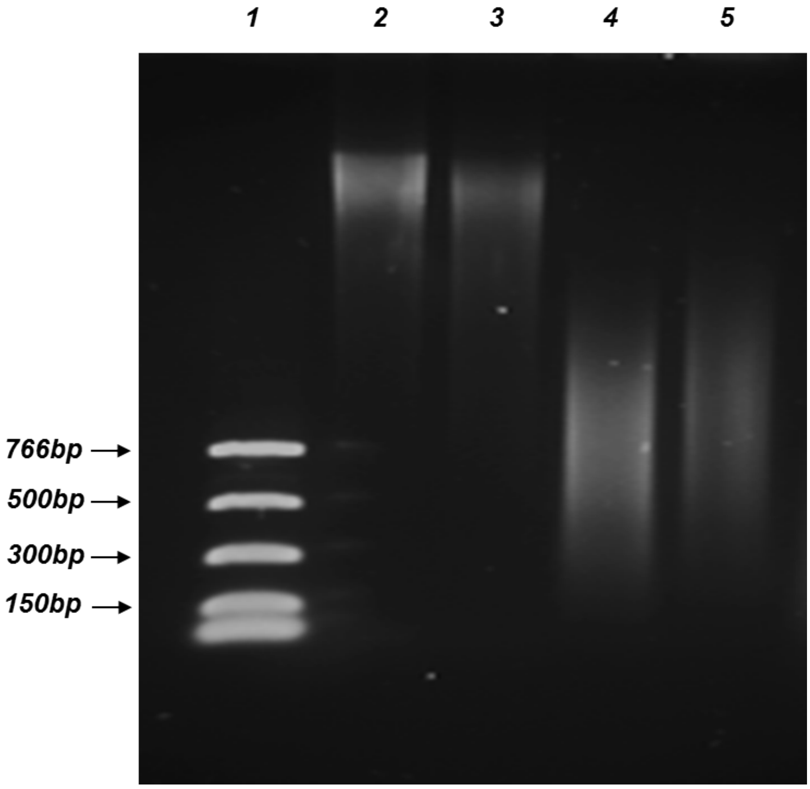

Figure A.3 Testing the efficiency of hydroxyl radical cleavage of the DNA in HeLa cells and human primary keratinocytes. Lane 1: PCR marker. Lane 2: control HeLa cell DNA after cell membrane permeabilization, but no hydroxyl radical cleavage. Lane 3: control human primary keratinocytes DNA after cell membrane permeabilization, but hydroxyl radical cleavage. Lane 4: DNA fragment after hydroxyl radical cleavage in HeLa cells. Lane 5: DNA fragment after hydroxyl radical cleavage in human primary keratinocytes.

3′ ACG$_{1}$GGGGTG$_{6}$G$_{7}$TACTCG$_{8}$CG$_{9}$ACG$_{10}$AG$_{11}$TCTATCG$_{12}$C^{m}TACCACTCG$_{13}$TCG$_{14}$
ACCCCG$_{15}$ACCTCTCTG$_{16}$C^{m}TG$_{17}$TCG$_{18}$ACCAACGG$_{20}$GTCCCAG$_{22}$GGG$_{25}$TCC *5′*

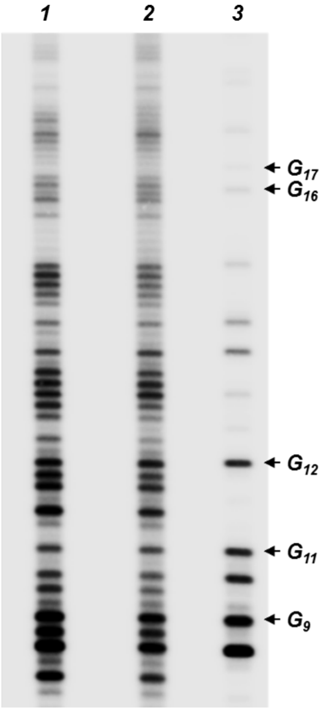

Figure A.4 Hydroxyl radical foot-printing of exon 5 along p53 gene in HeLa cells and human primary keratinocytes. Lane 1: hydroxyl radical foot-printing of exon 5 along p53 gene in HeLa cells. Lane 2: hydroxyl radical foot-printing of exon 5 along p53 gene in human primary keratinocytes. Lane 3: DMS mapping of the Gs along the p53 gene using human genomic DNA. On top is the DNA sequence of exon 5 that was amplified by LMPCR.

3′ ACG$_1$GGGGTG$_6$GTACTCGCGACG$_{10}$AGTCTATCG$_{12}$C^m=TACCAC=TCGTCGACCCCG$_{15}$A
CCT=CTCTG$_{16}$C^m=TGTCGACCAACGG$_{20}$GTCCCAGGGG$_{25}$TCCGGAGACTAAGG$_{30}$AGTG
ACTACGAGAATCCAG$_{35}$ACCGGGGAG$_{40}$GAGTCGTAGAATAGG$_{46}$C^m=TCCCTTCCTTTAA5′

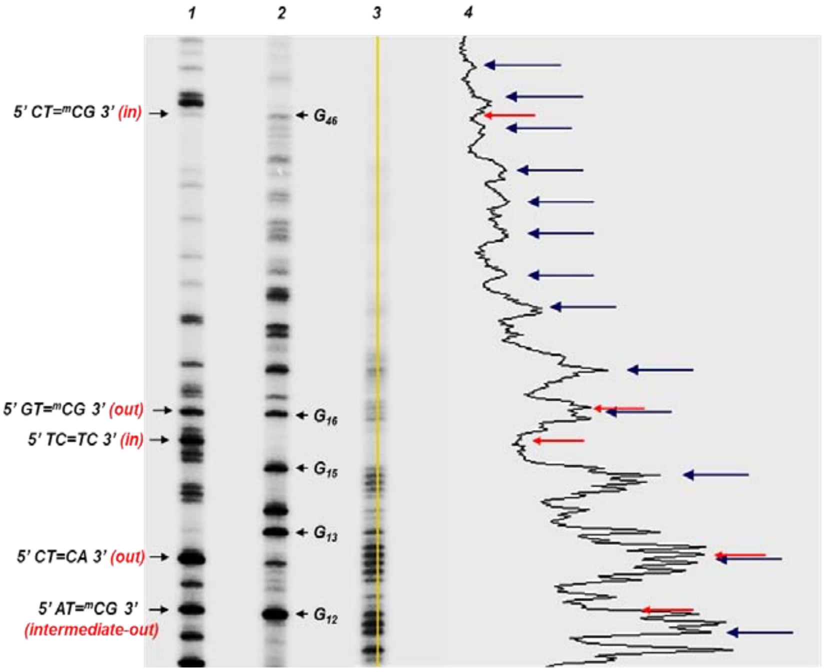

Figure A.5 Hydroxyl radical foot-printing of exon 5 and exon 6 of the p53 gene in HeLa cells.* Lane 1: T4 endo V mapping of CPD photoproduct sites in UVB-irradiated HeLa cells. Lan2: DMS mapping of G's along p53 gene using human genomic DNA. Lane 3: hydroxyl radical foot-printing of exon 5 and exon 6 along the p53 gene in HeLa cells. Lane 4: cleavage band intensity plot of lane 3. On top is the DNA sequence of exon 5 along p53 gene that was amplified by LMPCR.

---

* DNA photoproduct mapping was carried out by Dr. Vincent Cannistraro.